CYCLIC AND POST-CYCLIC BEHAVIOUR OF SOFT CLAYS

HO JIAHUI

(B.Eng. (Hons.), National University of Singapore)

A THESIS SUBMITTED FOR THE DEGREE OF DOCTOR OF PHILOSOPHY

DEPARTMENT OF CIVIL AND ENVIRONMENTAL ENGINEERING

NATIONAL UNIVERSITY OF SINGAPORE

2013

DECLARATION

I hereby declare that this thesis is my original work and it has been written by me in its entirety. I have duly acknowledged all the sources of information which have been used in the thesis.

This thesis has also not been submitted for any degree in any university previously.

Ho Jiahui

01 January 2014

Acknowledgements

The author would like to express her heartfelt gratitude to the following people who have offered their help in making this dissertation possible:

First and foremost, I will like to thank my supervisor, **Professor Lee Fook Hou**, for all of his invaluable guidance. A big thank you for all of his precious time and effort in patiently teaching me almost everything – from theories to experimental techniques to even electrical circuitry; the list is endless. I will always remember his kindness in giving me the opportunity to learn and inspire me to become a researcher.

I am also extremely grateful to my co-supervisor, **Assistant Professor Goh Siang Huat**, for his continuous support and valuable advices rendered throughout the entire PhD journey. Despite his busy schedule, he always set aside many hours helping me for which I am deeply appreciative.

Most importantly, I want to grab this opportunity to thank my family for their unconditional love, concern and support showered upon me during this arduous yet rewarding part of my life. A special thank you to my husband, **Shang Jia Shun**, for always being there for me every step of the way. I would also like to extend my gratitude to my sister, **Grace Ho Minghui**, for being my emotional pillar and taking care of our cute bunnies. I am also thankful towards my parents, **Steven and Jennifer Ho**, for being understanding and supportive to my pursuit of higher education. It is with deepest sentiment that I thank my grandmother, **Yuen Wai Har**, for your never-ending love and encouragement. Although you had moved on to a better place, you will always live in my heart.

Last but not least, I wish to thank all of the final year students – **Puvaneswary Rajarathnam**, **Quek Xian Xue**, **Grace Christine Hangadi**, **Kenneth Ang Seh Hai** and **Kho Yiqi** for all of your assistance and sharing the laughter and suffering with me. Finally, I would like to express my appreciation to my fellow graduate students and friends, of whom **Tran Huu Huyen Tran**, **Cisy Joseph**, **Hartono Wu**, **Yang Yu**, **Zhang Lei**, **Lu Yitan**, **Zhao Ben**, **Subhadeep Banerjee** and **Ma Kang** need special mention.

Table of Contents

Summary

During undrained cyclic loading of clayey soils, continuous pore pressure build-up changes the effective stresses and decreases the stiffness and strength of the soil (e.g. Vucetic and Dobry 1988; Ishihara 1993; Cavallaro and Maugeri 2004; Banerjee 2009). In the local context, Singapore faces dynamic problems arising from far-field earthquakes and construction vibrations. Despite the pressing need for the dynamic behaviour of local clays to be examined, previous characterization studies on Singapore Marine Clay have been largely restricted to monotonic loading behaviour (e.g. Tan 1983; Dames and Moore 1983; Tan et al. 1999; Tan et al. 2002; Chu et al. 2002; Chong 2002). In general, there exists a major lack of understanding in the behaviour of Singapore clays under dynamic loadings.

In this study, the cyclic and post cyclic behaviour of reconstituted Singapore Upper Marine Clay and Kaolin Clay are examined through a series of two-way strain-controlled cyclic triaxial and resonant column tests. Kaolin clay is used herein as a "reference" soil against which the behaviour Singapore Marine Clay can be compared. Cyclic triaxial tests at various loading rates were first performed to investigate the effect of pore pressure equilibration on the effective stress paths and stress-strain relationships for both clays. One key finding is the higher initial shear modulus of clays measured when pore pressure uniformity is not achieved. Upon achieving pore pressure equilibration, the clay specimens exhibit similar effective stress paths and stress-strain relationships, indicating that strain rate effects are insignificant. Consequently, the effect of strain rate (i.e. loading frequency) on the stiffness degradation and damping characteristics of clays becomes negligible compared to the effect of strain magnitude. Based on the experimentally-derived strain rates required for pore pressure equilibration, modifications were made to BS1377 and Eurocode strain rate specifications for monotonic compression triaxial tests to cater to cyclic loading. Subsequently, all triaxial tests are conducted using the proposed strain rates sufficiently slow for pore pressure equilibration within each specimen to facilitate reliable effective stress analyses.

Apart from examining frequency effects, a detailed characterization of the dynamic properties of Marine Clay and kaolin was conducted. Their normalized shear modulus and damping curves fall within a well-defined band together with published data from various past researchers (e.g. Kokusho et al., 1982; Idriss 1980; Kagawa 1993;

Zanvoral and Campanella 1994; Darendeli 2001; Banerjee 2009). Comparisons are drawn between the experimentally derived shear modulus and damping curves against the Hyperbolic, Ramberg-Osgood and Modified Hyperbolic models. Results herein reveal good correlations for strain-dependent shear modulus degradation curve. However, for strain-dependent damping curve, these models are applicable only at small strains of less than 0.3%. For larger strain magnitudes, the Ramberg-Osgood Model tends to under-predict while the other two models over-predict damping ratios of both clays. It should also be noted that none of these models predict pore pressure generation; all of them are total stress models.

In order to better understand the behaviour of clays under cyclic loading, an effective stress approach to the interpretation of cyclic test results is essential. Based on the effective stress paths of Marine Clay and kaolin, dilation of the clay structure was observed to occur during cyclic loading once their stress ratio reaches 0.6 times the critical state parameter (M), defining the phase transformation line. As cyclic loading progresses, the cyclic oscillations in the effective stress and stiffness for both clay types resulted in distinctive “butterfly” profile in their effective stress paths and their hysteretic stress-strain loops gradually collapse in size to form S-shapes. Such behaviour is analogous to that reported for dense sands under cyclic loading. Based on the experimental findings, a three-surface hardening model of the bounding surface type is developed. This proposed effective stress model can reasonably model the effective stress paths of normal and overconsolidated specimens of Marine Clay and kaolin. In addition, the model also shows good qualitative agreement with the monotonic and post-cyclic behaviour for both clays. The predicted undrained shear strengths are generally on the conservative side.

List of Tables

List of Figures

List of Symbols

α	Dimensionless material constant for plastic strain interpolation from Modified Cam Clay yield surface
A	Applied displacement/strain amplitude
$AOCR$	Cyclic-induced apparent overconsolidation ratio
β	Dimensionless material constant for the unloading phase
B	Pore pressure coefficient
C_{BS}	Parameter related to the number of points required for equalization (BS1377)
C_{ISO}	Parameter related to the number of points required for equalization (TS17892)
$d\varepsilon^{p}$	Plastic strain increment vector
$d\varepsilon_{v}^{p}$	Plastic volumetric strain increment
$d\varepsilon_{s}^{p}$	Plastic shear strain increment
D	Damping ratio
ε	Generalized shear strain
ε_{1f}	Significant strain interval specified in TS17892
ε_{f}	Significant strain interval specified in BS1377
$\dot{\varepsilon}_{avg}$	Average strain rate in cyclic triaxial tests
$\dot{\varepsilon}_{BS}$	Maximum strain rate specified in BS1377
$\dot{\varepsilon}_{cyclic}$	Experimental cyclic strain rate for pore pressure equilibration
$\dot{\varepsilon}_{ISO}$	Maximum strain rate specified in TS17892
$\dot{\varepsilon}_{\max}$	Maximum strain rate in cyclic triaxial tests
e	Void ratio
e_{0}	Initial void ratio at the start of cyclic loading
f_{T}	System resonant frequency
F	Factor depending on type of test and drainage conditions (BS1377 and TS17892)
F_{T}	Dimensionless frequency factor (ASTM D4015-07)
γ	Torsional shear strain

G	Secant shear modulus
G'	Effective shear modulus
$G_{\max}$	Small-strain shear modulus
$G / G_{\max}$	Normalized shear modulus
κ	Slope of elastic unloading-reloading line / Swelling index
K'	Effective bulk modulus
λ	Slope of the normal consolidation line / Compression index
L	Specimen length
L_c	Specimen length after consolidation
m	Exponential factor of overconsolidation ratio
M	Critical state friction coefficient
M_{peak}	Peak friction coefficient
η	Stress ratio
η_{PT}	Stress ratio of the phase transformation line
η_r	Reversal stress ratio
n	Exponential factor of effective mean principle stress
N	Number of points required for pore pressure equalization
N	Cycle number
OCR	Overconsolidation ratio
ϕ'	Effective friction angle
ϕ_{crit}'	Critical state friction angle
ϕ_{peak}'	Peak friction angle
ϕ_{PT}'	Phase transformation angle
ψ	Angle of dilation
p'	Mean effective stress
p_0'	Effective confining pressure
p_c'	Preconsolidation pressure
p_r	Reference pressure
p_r'	Mean effective stress corresponding to stress reversal point
PI	Plasticity index
q	Deviator stress

ρ	Soil mass density
t_{50}	Projected time required for 50% consolidation
t_{100}	Projected time required for 100% consolidation
t_f	Significant testing time
T	Cyclic period
μ	Dimensionless material constant for plastic strain interpolation from unloading yield surface
Δu	Excess pore pressure
υ'	Effective Poisson's ratio
v_λ	Specific volume axis intercept for normal consolidation line
v_κ	Specific volume axis intercept for elastic unloading-reloading line

Chapter 1 – Introduction

1.1 Overview

1.1.1 Background

Many cities, including Singapore, Taipei, Bangkok, Mexico and Shanghai, are situated on thick deposits of soft clays. During dynamic events such as earthquakes, ocean wave storms, traffic vibrations and construction-related vibration, the soft clay deposits will be subjected to undrained cyclic loading conditions. Cyclic loading of significant amplitude will generate excess pore water pressure and decreases the stiffness and strength of the soil (e.g. Vucetic and Dobry 1988; Ishihara 1993; Cavallaro and Maugeri 2004; Banerjee 2009). The concern with liquefaction of sands under cyclic loading has led to extensive cyclic loading studies into the sandy soils (e.g. Wood 1982; Frost 1989; Yin et al. 2010; Chiaro et al. 2011; Monkul and Yamamuro 2011, Yang and Sze 2011). Compared to sand, soft clay does not liquefy and has, to date, elicited much less concern. Nonetheless, the severity of the damages suffered by structures lying atop soft clay strata during the 1906 San Francisco Earthquake, 1985 Mexico Earthquake, 1995 Kobe Earthquake and many more stressed the importance of investigating cyclic clay behaviour (Idriss et al. 1978; Romo et al. 1988; Towhata 2008).

Geological deposits in mainland Singapore can be divided into six major formations: Kallang Formation, Old Alluvium, Jurong Formation, Bukit Timah Granite, Gombak Norite and Sahajat Formation (Pitts, 1992). Singapore Marine Clay is the main constituent of the Kallang Formation. It is a weakly flocculated, kaolinite-rich clay with moderate contents of montmorillonite and illite (Tan, 1983). Kaolinite has been further verified as the dominant component by Tan et al. (1999), Tanaka et al. (2001) and Tan et al. (2002). Pitts (1992) estimated that the Kallang Formation constitutes one quarter of the Singapore land area. Much of the old urban areas, such as Chinatown, Little India and Arab Street are built over Singapore Marine Clay (Shirlaw et al., 2006). In addition, land reclamation in coastal areas has resulted in developments being built over Singapore Marine Clay deposits. Singapore Marine Clay has been found to have a thickness of 10 m to 15 m near estuaries, and more than 40 m at some locations (Low, 2004). At regions of thick Singapore Marine Clay deposits, the soil profile can be divided into three layers comprising the Upper Marine Clay, the intermediate layer and the Lower Marine Clay. In general, Upper

Marine Clay is very soft to medium stiff with undrained shear strength value in the range of 10kPa to 30kPa and is usually overconsolidated. The overconsolidation ratio can be up to 8 near the Upper Marine Clay surface (Chu et al., 2002).

Singapore is around 600 km from the Sunda Arc seabed subduction trench, which has generated 5 major earthquake events of magnitude ranging from 7.9 to 9.3 in the past decade (Lam et al., 2009). Tremors from these events could be felt in Singapore, in particular the Nias-Simeulue Earthquake in 28 March 2005 with moment magnitude M_w of 8.7 (Pan et al., 2006). Although the epicenter was about 760 km from Singapore, tremors were felt in more than 200 buildings across Singapore. Many of these buildings are situated within the Kallang formation. This is attributed to the dynamic amplification of the far-field earthquake motion as it propagates upward through the soft Singapore Marine Clay strata. During the 1 April 1998 earthquake, accelerometers at the KAP seismic station recorded motions that had predominant frequencies of 0.9 Hz and 0.6 Hz (Pan et al., 2007). During the 26 December 2004 earthquake, ground motion recorded by accelerometers in the basement of the Singapore Republic Plaza had a frequency range of 0.04 to 0.1 Hz (Pan et al., 2006). Although there has been no reported structural damage in Singapore due to induced tremors, there are also no design criteria assessing the impact of seismic actions on buildings. The only relevant design requirement is that buildings have to withstand a 0.015g horizontal acceleration (Lam et al., 2009). In view of the history of local ground motions induced by major earthquakes from Sumatra, Pan et al. (2006) suggested that larger and nearer earthquakes could have a damaging effect on Singapore. Therefore, there is a pressing need for the dynamic behaviour of Singapore Marine Clay to be examined

1.1.2 Overview of Cyclic Loading Studies on Soft Clays

Most investigations up till now focused on specific aspects of constitutive behaviour of soft clays under cyclic loading. These aspects include very small strain shear modulus (Hardin and Black 1968; Anderson and Richart 1976; Kokusho et al. 1982; Viggiani and Atkinson 1995; Dasari 1996), strain-dependent shear modulus and damping ratio (Hardin and Drnevich 1972a and 1972b; Vucetic and Dobry, 1991; Kagawa, 1993; Ishibashi and Zhang 1993; Ishihara 1996; Towhata 2008), stiffness and strength degradation under cyclic loading (Vucetic & Dobry, 1988) as well as effective stress and pore pressure response (Kagawa 1993; Zergoun and Vaid 1994; Matasovic and Vucetic 1995).

Published findings on the behaviour of soft clays under cyclic loading vary significantly. For instance, Zanvoral and Campanella (1994) and Thammathiwat and Weeraya (2004) found that damping in clays increases with loading frequency while Shibuya et al. (1995) and Teachavorasinskun et al. (2002) reported a decrease in damping with increasing loading frequency. On the other hand, Ishihara (1996) and Towhata (2008) concluded that the dissipated energy per cycle is mostly frequency-independent and hence of a hysteretic nature.

These discrepancies may be partially attributed to the differences in the behaviour of different soft clays. However, it is also possible that pore pressure equilibration issues could have played a role. Many soft clays have low permeability and therefore require low loading rates to ensure that excess pore pressure is uniform within the sample. Reliability in excess pore pressure measurements is a fundamental requirement for accuracy in effective stress approach to cyclic test results (Crawford 1959; Wilson and Greenwood 1974; Germaine and Ladd 1988). Many studies in the past involve relatively high cyclic loading rates, which typically ranges from 0.05Hz to 2Hz (e.g. Ansal et al. 2001; Zhou and Gong 2001; Moses et al. 2003; Matesic and Vucetic 2003; Yamada et al. 2008; Banerjee 2009). At such loading rates, equilibration of excess pore pressure within the sample may not be fully achieved under undrained triaxial conditions, leading to non-uniformities in pore pressure and strain within specimens, and thus affecting the test results (e.g. Wood 1982; Zergoun and Vaid 1994). This may affect the reliability of pore pressure measurements during cyclic loading.

Where failure did not occur, cyclic loading often resulted in residual excess pore pressures and residual shear strains within clayey soils (Li et al. 2011). Consequently, an important consideration in seismic design of foundation in clays is the undrained shear strength of clays after cyclic loading. Thus, efforts were made to evaluate the post-cyclic shear strength of clays as well. However, pore pressure non-uniformity has been known to affect the reliability of the published data on post-cyclic undrained shear strength of clays (e.g, Andersen et al. 1980; Wood 1982; Diaz-Rodriguez et al. 2000). Many previous post-cyclic studies also used relatively fast cyclic loading rates ranging 0.01Hz to 10Hz (e.g. Taylor and Bacchus 1969; Thiers and Seed 1969; Sangrey and France 1980; Yasuhara et al. 1983; Yasuhara et al. 1992; Erken and Ulker 2007; Li et al. 2011). As such, pore pressure equilibration may not be achieved during the cyclic loading phase. Some attempts had been made to mitigate the issue

of unequalized pore pressures during cyclic loading. For instance, Koutsoftas (1978), Diaz-Rodriguez et al. (2000) and Pillai et al. (2011) allowed the specimen to cure in an undrained state under zero deviator stress prior to post-cyclic compression test to achieve equalization of cyclic-induced pore pressures. On the other hand, Andersen et al. (1980) allow the specimens to cure periodically during the cyclic loading phase. Another approach is to introduce drainage either intermittently during cyclic loading (e.g. Sangrey and France 1980) or after cyclic loading (e.g. Andersen et al. 1980; Yasuhara et al. 1983 and 1992; Yasuhara 1994) to allow equilibration of cyclic-induced pore pressures within the specimens. However, these two methods not only results in pore pressure equilibration but also pore pressure dissipation, leading to discontinuities in effective stress paths between the cyclic loading and post-cyclic loading phases. Intuitively, the effective stress response of clay undergoing cyclic loading should be indicative of its post-cyclic behaviour if post-cyclic monotonic loading is conducted immediately after cyclic loading. Because of possible pore pressure non-uniformity and discontinuities between cyclic and post-cyclic effective stress paths, a direct comparison between the cyclic and post-cyclic behaviour of clays was difficult to achieve.

1.2 Research Motivations

The motivations for this research can be summarized as follows:

(i) Lack of studies on the cyclic loading behaviour of local clays. Previous characterization studies on Singapore Marine Clay (e.g. Tan 1983; Dames and Moore 1983; Tan et al. 1999; Tan et al. 2002; Chu et al. 2002; Chong 2002) have been largely restricted to monotonic loading behaviour.

(ii) Findings of previous studies on different clays (e.g. San Francisco Bay Mud, Venezuelan Clay, Bangkok Clay, Vancouver Marine Clay etc.) may not be applicable to Singapore Marine Clay. In addition to the differences in plasticity and mineralogy, conflicting conclusions in previous studies (to be further discussed in Chapter 2) makes their findings difficult to apply directly to Singapore Marine Clay.

1.3 Research Objectives

The preceding paragraphs provide a glimpse at the fundamental goal of this research: to examine the cyclic and post-cyclic response of Singapore Marine Clay and present

a detailed characterization of its dynamic properties (e.g. small-strain shear modulus and damping ratio, variations in strain-dependent modulus degradation and damping behaviour), while ensuring adequate equilibration of excess pore pressure. In order to fulfil this objective, resonant column and cyclic triaxial tests will be performed on normal and overconsolidated reconstituted specimens. A comparison with existing literature shall serve as a means to verify the reliability of the experimental data in this study. Apart from Singapore Marine Clay, commercially available Kaolin Clay was also used for ease of comparison with past studies. Kaolin clay is used herein as a "reference" soil against which the behaviour Singapore Marine Clay can be compared.

1.4 Organization of Dissertation

The outline of this dissertation is as follows:

Chapter 2 – Literature Review

Chapter 2 provides a detailed literature review on available experimental information on cyclic and post-cyclic response of clays. Conclusions drawn by various researchers are compared and evaluated. The available stress-strain models for clays undergoing cyclic loadings are examined as well.

Chapter 3 – Experimental Methodology

Chapter 3 introduces the methodology of the resonant column and consolidated undrained cyclic triaxial tests conducted. This includes the sample preparation, experimental procedure and the method used for processing of experimental data.

Chapter 4 – Effect of Cyclic Strain Rate on Pore Pressure Measurement

As previously highlighted, one possible limitation in past studies is the relatively fast rates of cyclic loading used (typically 0.05Hz to 2Hz) such that pore pressure equilibration was not ensured and the reliability of pore pressure measurements became doubtful. Inconsistencies in strain rates used in these studies may be attributed to the fact that the specifications for cyclic loadings are unclear and ill defined. Thus, Chapter 4 seeks to investigate the minimum strain rate required for pore pressure equilibration within Singapore Upper Marine Clay and Kaolin Clay specimens in undrained cyclic triaxial testing. In addition, modifications were made to BS1377: 1990 and Eurocode ISO/TS 17892: 2004 guidelines for undrained monotonic triaxial testing to include specifications for cyclic tests.

Chapter 5 – Shear Modulus and Damping Ratio

As shear modulus and damping ratio are perhaps the two most common parameters considered for cyclic soil behaviour, Chapter 5 presents the cyclic characteristics of Singapore Upper Marine and Kaolin clays with emphasis on these two parameters. Although previous studies had demonstrated that no pore pressure generation occurs during small strain cyclic loading (Jardine 1992; Vucetic 1994; Díaz-Rodríguez and López-Molina 2008) with amplitudes lesser than 0.001% to 0.01% (Georgiannou et al. 1991), most of these studies did not check for possible build-up after cyclic loading. As there have been unconfirmed indications from several local railway projects that excess pore pressure may be generated around train tracks after the soil was subjected to train-induced vibrations, this chapter also seeks to verify if pore pressure build-up occurs after an episode of small strain cyclic loading.

Chapter 6 – Cyclic and Post-Cyclic Behaviour

Chapter 6 summarizes the cyclic and post-cyclic experimental results obtained in this study. The salient features of the observed clay behaviour in terms of effective stress path and stress-strain response will be discussed in details. The observations made are compared against relevant literature data to assess the reliability of the current results.

Chapter 7 – Constitutive Model for Cyclic Loading

Chapter 7 introduces the available constitutive models for clays undergoing cyclic loadings and evaluates the applicability of these models to the current experimental results. Due to the shortcomings of these models in describing the behaviour of Singapore Marine Clay and Kaolin Clay, a new constitutive model for describing the behaviour of soft clays under cyclic loading will be proposed. Since the key characteristics of cyclic clay behaviour to be modelled are based on current experimental data, the proposed three-surface hardening model is essentially phenomenological in nature.

Chapter 8 – Conclusion

Lastly, key findings in the current study are summarized.

Chapter 2 – Literature Review

In this chapter, available experimental information on the cyclic and post-cyclic behaviour of clays is evaluated in terms of the effective stress paths and stress-strain relationships obtained in past studies. In addition, simple stress-strain models which have been used to model the undrained cyclic behaviour of clays (e.g. Hyperbolic Model, Ramberg-Osgood Model and Modified Hyperbolic Model) are discussed.

2.1 Cyclic Effective Stress Paths

2.1.1Experimental Observations on Cyclic Effective Stress Paths

For stress-controlled and strain-controlled cyclic loading tests on clays, the permanent densification or contraction due to gradual development of positive excess pore pressure (for undrained cases) caused the effective stress paths to migrate either to failure or to equilibrium without failure (Sangrey and France 1980; Hyde and Ward 1985; Wood 1982; Yasuhara et al. 1992; Yu et al. 2007). The latter occurs when the amplitude of the applied stress or strain is sufficiently small such that stiffness and strength degradation is insignificant. Due to this phenomenon, researchers proposed varying cyclic failure criterions as follows:

(i) Based on Sangrey et al.'s (1969) study on clays, Sangrey and France (1980) postulated that non-failure equilibrium condition is achieved when the applied stress levels lie below a critical level for failure to occur. Thus, cyclic failure can only occur when the deviator stress in a clay specimen reaches a failure stress level under cyclic loading, as illustrated in Figure 2.1.

(ii) Hyde and Ward (1985) proposed that cyclic failure occurs when the accumulation of positive pore pressure cause the stress state of the clay specimen to cross the Hvorslev surface to the dry side of critical. Yasuhara et al. (1992) adopted a similar definition for cyclic failure but using the critical state line as the criterion (refer to Figure 2.2).

(iii) More recently, Hyodo et al. (1994) and Li et al. (2011) defined cyclic failure in terms of the number of loading cycles required for the accumulated axial strain to reach a prescribed value in two-way stress-controlled tests.

Wood (1982) noted that the resistance of clays to cyclic failure is directly related to its mineralogy and plasticity that govern the amount of increase in excess pore pressure during cyclic loadings. For instance, resistance to cyclic failure in cohesive soils was observed to increase with plasticity index due to the lower excess pore pressure and shear strain accumulation in highly plastic clays (Erken and Ulker 2006). Hyodo et al. (1994) studied the effects of anisotropy on Itsukaichi clay by applying sinusoidal axial loads at a fixed frequency of 0.02Hz which was verified to be slow enough for pore pressure equilibration. He reported that the effective stress path of an isotropic-consolidated specimen migrates to the critical state line on both compression and extension sides while the effective stress path of the anisotropically consolidated specimen only touched the critical state line on the compression side at the final stage of loading (Figure 2.3). Other researchers (e.g. Koutsoftas 1978; Sangrey et al. 1969; Brown et al. 1975) have reported that the accumulation of positive excess pore pressure during cyclic loading was higher in normally consolidated than overconsolidated clays.

2.1.2 Effect of Strain Rate on Effective Stress Paths

The effect of pore pressure changes on cyclic-induced degradation in stiffness and strength of clays is well-established (e.g. Vucetic and Dobry 1988; Ishihara 1993; Cavallaro & Maugeri, 2004; Banerjee, 2009). The use of fast loading rates in undrained cyclic triaxial tests prevents equilibration of excess pore pressure leading to non-uniform pore pressure and strain distributions within specimens (Wood 1982; Zergoun and Vaid 1994). Researchers such as Hirschfeld (1958), Crawford (1959), Bishop et al. (1962) and Germaine and Ladd (1988), amongst others, had attributed the cause of high pore pressure concentration in the middle one-third portion of specimen to the time required for pore pressure re-distribution throughout the specimen. This is consistent with the reported increase in pore pressure measured at the specimen base as cyclic strain rate is reduced (e.g. Bjerrum et al. 1958; Crawford 1959; Whitman 1960; O'Neill 1962; Richardson 1963; Richardson and Whitman 1963; Matsui et al. 1980; Zhou and Gong 2001).

In the event when equilibration of pore pressure was not achieved, the pore pressure measured at the ends or the centre of the specimen may be lower than the average value of the specimen (Zergoun and Vaid 1994). As illustrated in Figure 2.4, the effect of this is to cause the effective stress path to drift closer to the total stress path. For this reason, the importance of having a strain rate sufficiently slow to ensure pore

pressure equilibration has been emphasized by Sangrey et al (1969), Wood (1982), Zergoun and Vaid (1994), amongst others. Nonetheless, as Table 2.1 shows, recent experimental investigations into strain rate (or frequency) effects were still conducted at fast cyclic loading rates, which typically range from 0.05Hz to 2Hz, and pore pressure equalization did not appear to be given due importance in these studies. Intuitively, studies on frequency effects on cyclic behaviour of clays have to take into account whether pore pressure equilibration has occurred, before evaluating if intrinsic strain rate effects are present. One possible reason to account for the use of relatively fast cyclic loading rates is the lack of clear specifications for cyclic testing.

2.1.2.1 BS1377:1990

BS1377 does not provide specifications for cyclic triaxial testings. Guidelines are only available for strain-controlled monotonic triaxial compression tests. As stipulated in BS1377, during a consolidated-undrained triaxial compression test with measurement of pore pressure, the rate of applied axial deformation must be sufficiently slow to ensure adequate equalization of excess pore pressures. The maximum rate of axial displacement is prescribed by

$$d_r = \frac{\varepsilon_f \times L_c}{t_f} \qquad [2.1]$$

Where:

d_r = Rate of axial displacement (mm/min),

ε_f = Significant strain interval,

L_c = Length of consolidated specimen (mm),

t_f = Significant testing time (min) (≥ 2 hours).

The significant strain interval is a user-prescribed parameter; it depends on the strain increment over which pore pressure equilibration is required. For example, when equalization of pore pressure is only needed at the point of failure, the significant strain interval is the estimated strain at which failure is expected to occur. On the other hand, the significant testing time is governed by the consolidation properties of the test specimen and is thus defined as follows:

$$t_f = F \times t_{100} \qquad [2.2]$$

Where:

F = A coefficient which depends on the drainage conditions and the type of compression test (i.e. undrained or drained) (refer to Table 2.2),

t_{100} = A projected time corresponding to intersection of the initial linear portion of the square-root time settlement curve and the settlement at 100% consolidation, as shown in Figure 2.5.

Using Equation 2.2, highly permeable soils can produce unrealistically short significant testing times. Hence, a minimum duration of 2 hours was specified by BS1377.

2.1.2.2 ISO/TS 17892:2004

TS17892 also does not contain guidelines for cyclic triaxial tests. Specifications are only provided for strain-controlled monotonic triaxial compression tests. In TS17892, the maximum rate of vertical displacement allowed in undrained triaxial tests is given by

$$v_{\max} = \frac{\left(H_i - \Delta H_c\right) \times \varepsilon_{1f}}{F \times t_{50}} \qquad [2.3]$$

Where:

$v_{\max}$ = Rate of displacement of the loading platen,

H_i = Initial specimen height prior to consolidation,

ΔH_c = Change in specimen height during consolidation,

ε_{1f} = Expected vertical strain at failure,

F = Factor depending on type of test and drainage conditions (refer to Table 2.3),

t_{50} = Projected time required for 50% consolidation, to be determined using the Casagrande's logarithmic time method.

Apart from using t_{50} instead of t_{100}, the values of the factor F are also different in TS17892 and BS1377. In TS17892, the value of F also accounted for the specimen length, specimen permeability and location of pore pressure transducer.

2.1.2.3 ASTM D-3999-91 (Reapproved 2003)

In contrast to the two aforementioned codes, ASTM contains specifications for the determination of the modulus and damping properties of soils using the cyclic triaxial apparatus. However, ASTM does not provide clear recommendations on suitable strain rates for reliable excess pore pressure measurements. The code merely states that the equipment "must be capable of applying a uniform sinusoidal load at a frequency within the range of 0.1 to 2Hz". The frequency of test, however, is dependent on (i) the specimen length (Whitman, 1960), (ii) the specimen permeability (Blight, 1964), (iii) the location of pore pressure measuring device (Wood, 1982), and (iv) the load amplitude. Apart from these recommendations, the precise specification for strain rate remains ambiguous.

2.2 Cyclic Stress-Strain Curves

Apart from the effective cyclic stress paths, experimental information on the cyclic stress-strain relationships is also vital for understanding cyclic clay behaviour. The shear modulus is often defined as the gradient of a line joining the points of maximum and minimum shear stresses. Similarly, the damping ratio is often defined as a ratio between the area enclosed by the hysteresis loop and the maximum elastic energy that can be accumulated per cycle (Figure 2.6). This definition of damping is based on the assumption of viscoelastic behaviour (Wood 1982; Ishihara 1993; Towhata 2008). According to Wood (1982), this assumption does not consider the number of cycles and thus should be restricted to a small number of cycles with ideal hysteresis loops. As cyclic loading progresses, the hysteresis loops tend to collapse in shape to S-shapes (Figure 2.7) where the clay is no longer exhibiting the assumed ideal viscoelastic behaviour and characterization simply in terms of shear modulus and damping ratio becomes flawed (Wood 1982). Furthermore, the stress-strain-strength response of clay is governed by inter-granular friction, chemical bonding and electrical interaction which are primarily rate-independent (Towhata 2008). Many studies have shown that cyclic stress-strain behaviour of clays is only rate-dependent to a very limited extent (Brown et al. 1975; Vucetic and Dobry 1991; Ishihara 1996; Shibuya et al. 1995; Matesic and Vucetic 2003; Towhata 2008). A plausible reason for the observed frequency effects in some experimental investigations (e.g. Figure 2.8) can be attributed to the use of relatively fast strain rates such that non-uniformities in pore pressure (and strain) are present as discussed in the earlier Section 1.1.

Notwithstanding this, a considerable amount of research efforts had been dedicated towards evaluating the influences of different variables affecting shear modulus and damping of clays (Hardin and Black, 1968; Zen et al., 1978 and Kokusho et al., 1982; Vucetic and Dobry 1991).). The variables explored are:

(i) Strain amplitude,
(ii) Plasticity,
(iii) Effective mean principal stress (p'),
(iv) Overconsolidation ratio,
(v) Frequency, and
(vi) Void ratio.

A brief summary of their findings on shear modulus and damping ratio will be discussed in this section considering that the past conclusions drawn will serve as a useful comparison to assess the reliability of the experimentally-derived dynamic characteristics of the clays used in the present study.

2.2.1Small-strain Shear Modulus, G_{max}

Clay behaviour within a very small strain regime is essentially elastic and its shear modulus reaches a nearly constant limiting value (Figure 2.9). Available empirical data indicates that this strain regime is smaller than a threshold value ranging from 0.001% to 0.01% (e.g. Hardin and Black 1968; Anderson and Richart 1976; Stokoe and Lodde 1978; Kokusho et al. 1982; Georgiannou et al. 1991; Viggiani and Atkinson 1995; Diaz-Rodriguez and Lopez-Molina 2008).

Most empirical expressions for small-strain shear modulus involve stress parameter, such as mean effective stress, and a parameter for stress history, such as overconsolidation ratio, or packing density, such as void ratio. Examples of the proposed empirical correlations in terms of void ratio and overconsolidation ratio are summarized in Tables 2.4 and 2.5 respectively, where mean effective principal stress, p', is expressed in kPa.

Vucetic and Dobry's (1991), Hardin and Black's (1968), Hardin's (1978) and Ishihara's (1996) observations indicate that the small-strain shear modulus of normally consolidated clays appears to remain approximately constant even if their plasticity indices are different (Figure 2.10). By considering the influence of plasticity

index on various normally and overconsolidated clays, Viggiani and Atkinson (1995) proposed a more generalized empirical expression for small-strain shear modulus:

$$\frac{G_{\max}}{p_r} = A\left(\frac{p'}{p_r}\right)^n (OCR)^m \qquad [2.13]$$

Where:

A = Empirically derived constant,

p_r = Reference pressure required to make Equation 2.13 dimensionally consistent,

n = Exponential factor of effective mean principle stress (p'),

m = Exponential factor of overconsolidation ratio (OCR).

They also proposed some empirical charts for the stiffness parameters *A*, *n* and *m*, Figure 2.11. Their suggested values of *m* for plasticity index in the range 10 to 50 agree reasonably well with those proposed by Hardin and Black (1968) and Hardin (1978) (Figure 2.12). By applying the estimated values of *A* and *n* from Figure 2.11 into Equation 2.13, plasticity index is observed to influence the value of small-strain shear modulus for a normally consolidated clay (Figure 2.13). For a given effective mean stress, the small-strain shear modulus increases with plasticity index when plasticity index ranged from 0 to 25 beyond which the small-strain shear modulus decreases with further increase in plasticity index. This observed effect of plasticity index on small-strain shear modulus contrast the aforementioned independence of small-strain shear modulus on plasticity index for normally consolidated clays demonstrated earlier in Figure 2.10. This dependence of small-strain shear modulus on plasticity index for normally consolidated clays is also observed to be more pronounced at higher mean effective stresses.

2.2.2 Normalized Shear Modulus (G / G_{max}) and Damping Ratio

Numerous studies in the literature have demonstrated that soft clays undergoing monotonic and cyclic loading typically exhibits a relationship between generalized shear strain and shear modulus that has the form of a reverse S-curve. The damping ratio, on the other hand, usually increases with strain level, forming a S-shaped curve as illustrated in Figure 2.14 (e.g. Vucetic & Dobry 1991; Kagawa 1992; Hardin and Drnevich 1972a and 1972b; Ishibashi and Zhang 1993; Kokusho et al., 1982).The influence of various factors on the normalized shear modulus and damping curves

had been well-documented in literature (Seed and Idriss 1970; Vucetic and Dobry 1988 and 1991; Ishihara 1996; Towhata 2008).

2.2.2.1 Effects of Plasticity Index

Vucetic and Dobry (1991) presented data on the impact of plasticity index on dynamic characteristics of clays. They concluded that the plasticity index (PI) is the principal factor controlling the shape of the modulus degradation and damping curves. As the PI increases, the normalized modulus curve gradually moves to the right indicating a slower rate of attenuation with increasing shear strain. Similarly, for a given strain level, the damping ratio tends to trend downwards as PI increases, as illustrated in Figure 2.15 (Kokusho et al. 1982; Vucetic and Dobry 1991; Okur and Ansal 2007). Towhata (2008) attributed these changes to the level of microscopic interactions within clays. For an ideal elastic material, the shear modulus is independent of strain amplitude and the material does not exhibit damping characteristics. According to Towhata (2008), the nonlinearities in clays cause its shear modulus and damping ratio to vary with strain amplitude and the extent of nonlinearity is influenced by the discreteness of the soil particles (i.e. the level of separation between particles). High plasticity clays are less discrete compared to low plasticity clays due to the increased electric and chemical interactions between particles, resulting in reduction of nonlinearities with higher plasticity (Towhata 2008). Consequently, clays with higher plasticity index tend towards the ideal elastic behaviour (Figure 2.16).

2.2.2.2 Effects of Void Ratio

Results obtained from numerous studies (e.g. Stokoe and Lodde 1978; Lodde 1980; Sun et al. 1988) indicate that the higher the void ratio the higher is the position of the normalized shear modulus versus strain curve, i.e. the slower the rate of decrease in normalized shear modulus as shown in Figure 2.17. However, the modulus degradation curves reported by Isenhower (1978) , Isenhower and Stokoe (1981) and Guha (1995) for San Fransico Bay mud and Old Bay clay specimens fail to reflect any distinct influence of void ratio on the position of the normalized modulus degradation curves (Figure 2.18). In contrast to the conflicting trends reported for shear modulus, the influence of void ratio on damping ratio of cohesive soils is generally better understood and more widely accepted. Several studies concluded that damping ratio decreases with increasing void ratio (Hardin and Drnevich 1972a and 1972b; Vucetic and Dobry 1991; Guha 1995). Intuitively, void ratio should exert a

similar influence on shear modulus and damping as plasticity index because both factors are correlated, i.e. soils with higher plasticity index have a more open structure and thus a larger void ratio (Yoon 2007).

2.2.2.3 Effects of Mean effective stress and Consolidation Stress History

Past experimental works showed that cyclic properties of clays are dependent on mean effective stress to a limited extent (Kokusho 1980; Isenhower and Stokoe 1981; Kim and Novak 1981; Sun et al. 1988; Guha 1995; Towhata 2008). According to Sun et al. (1988), the influence of mean effective stress on the normalized modulus degradation curves gradually decreases as plasticity increases. Using Towhata's postulations regarding the effect of particle discreteness on cyclic properties (Figure 2.16), clays with greater plasticity index has stronger inter-particle bonds which is less susceptible to possible breakage induced by higher mean effective stress. Thus, Kokusho et al.'s (1982) study on four different undisturbed cohesive soils having plasticity index of 38 to 56 showed practically no influence of mean effective stress on normalized modulus degradation versus shear strain curve despite varying the mean effective stress between 45 to 500kPa (Figure 2.19). In addition, based on Vucetic and Dobry's (1991) compilation of 21 past experimental studies, an increase in mean effective stress may lead to a corresponding increase in modulus degradation curve with a decrease in damping ratio. This further supports the justification that higher effective stresses may destroy the inter-particle bonds such that the clay becomes less discrete and exhibits cyclic characteristics illustrated in Figure 2.16 (Towhata 2008).

Similarly, effects of consolidation histories, such as normal or overconsolidation or long-term application of consolidation pressure, has practically no effect on the positions of the normalized shear modulus and damping curves (Figure 2.20) (Kokusho et al. 1982; Vucetic and Dobry 1991; Ishihara 1996).

2.2.3 Available Stress-Strain Models

Researchers had proposed various empirical or semi-empirical models for the cyclic stress-strain relationship. Stress-strain relationships which have been assumed include bilinear (Penzien et al. 1964; Parmelee et al. 1964; Thiers & Seed 1968), hyperbolic (Duncan and Chang 1970; Hardin and Drnevich 1972b; Pyke 1979; Puzrin et al. 1995; Rao and Panda 1999; Liu and Ling 2006) and Ramberg-Osgood type (Richart 1975; Streeter et al. 1975; Idriss et al. 1978; Andrianopoulos 2006). Amongst the available

models, the hyperbolic (Figure 2.21) and Ramberg-Osgood models are shown to be moderately conservative (Ejezie and Harrop-Williams 1987). Table 2.6 provides a summary on the hyperbolic, Ramberg-Osgood and the more recent modified hyperbolic (Banerjee 2009) models.

Banerjee's (2009) modified hyperbolic model incorporated nonlinear elasticity at small strain, hysteretic stress-strain behaviour and cyclic degradation of backbone curve. He modelled nonlinear elasticity at small strain by setting the shear and bulk moduli as functions of the mean effective stress, overconsolidation ratio and strain history. Hysteretic stress-strain behaviour during cyclic loading is determined using the Masing rule (Masing, 1926). Lastly, the degradation of the backbone curve under cyclic loading is modelled with the use of degradation index (Idriss, 1978).

Figures 2.22 and 2.23 compare the available empirical data against the three aforementioned models. The model parameters used to provide the best fit curves are summarized in Table 2.7. From Figure 2.22, all three models are able to reasonably approximate the values of normalized shear modulus. The same is observed for damping ratio models at low shear strains (< 0.1%) (Figure 2.23). However, when the applied cyclic strain exceeds 0.1%, the hyperbolic and modified hyperbolic models over-predict while the Ramberg-Osgood model under-predicts the damping ratio. According to Towhata (2008), hyperbolic models should not be used for large strains. This is due to the theoretical limiting value of 0.637 (i.e. $2 / \pi$) for damping ratio at high strain levels which exceeds the typical experimental values (Towhata 2008; Banerjee 2009).

2.3 Post-Cyclic Behaviour

2.3.1 Testing Techniques of Past Studies

Table 2.8 summarizes previous studies on the post-cyclic behaviour of clays. As highlighted previously in Section 1.1.2, the limitations in these past studies lie in their experimental techniques. There are essentially three methods of conducting post-cyclic compression tests on clay specimens:

(i) The post-cyclic strain-controlled or stress-controlled undrained compression tests were conducted immediately after an episode of undrained cyclic loading to measure the deviator stress of the specimen at failure (Taylor and

Bacchus 1969; Thiers and Seed 1969; Sangrey and France 1980; Yasuhara et al. 1983; Yasuhara et al. 1992; Erken and Ulker 2007; Li et al. 2011). As Table 2.8 shows, the cyclic loading phase of these experimental studies was conducted at relatively fast loading frequencies ranging 0.01Hz to 10Hz without ensuring pore pressure equilibration. Due to the possible non-uniformities in pore pressure and strain within the test specimens, the interpretations provided on the influence of cyclic stress or strain history on the subsequent post-cyclic characteristics of clays become complicated and possibly unreliable.

(ii) After cyclic loading and prior to post-cyclic monotonic shearing, the specimen was left to stand in an undrained state under zero deviator stress to allow for equalization of cyclic-induced excess pore pressures (Koutsoftas 1978; Diaz-Rodriguez et al. 2000; Pillai et al. 2011). This process, commonly known as curing, was also introduced intermittently during cyclic loading in some cases (Andersen et al. 1980). Andersen et al. (1980) justified their use of intermittent curing by assuming that the permanent cyclic-induced pore pressure is not easily susceptible to lags in the system since its accumulation occurs gradually. In cases when curing was introduced after cyclic loading, either negligible changes (Pillai et al. 2011) or slight increments (Koutsoftas 1978) in pore pressure measurements were observed. Koutsoftas (1978) attributed the increase in pore pressure measurement to possible undrained creep at zero deviator stress. Although undrained creep can happen, given that the cyclic tests were conducted at a relatively fast loading rate of 1Hz, there is a high likelihood that this increase in pore pressure during "curing" occurred because some of the cyclic-induced pore pressure concentrated in the middle of the specimen propagated to the ends of the specimen where pore pressure readings are measured and recorded.

(iii) Prior to post-cyclic compression test, drainage was introduced either intermittently during cyclic loading (Sangrey and France 1980) or after cyclic loading (Andersen et al. 1980; Yasuhara et al. 1983 and 1992; Yasuhara 1994) to allow for complete dissipation of cyclic-induced excess pore pressure within the specimen. The effect of drainage was found to increase and decrease the post-cyclic undrained strength of normally consolidated (Figure 2.24) and overconsolidated clays respectively (Taylor and Bacchus 1969; Andersen et al. 1980; Sangrey and France 1980). For normally consolidated clays that are contractive, cyclic shearing causes the

realignment of clay particles into a more efficient structure which leads to an increase in pore pressure under undrained conditions (Taylor and Bacchus 1969). With drainage, the equilibrium would be re-established at a lower void ratio accompanied by a decrease in water content resulting in an increased shearing resistance in normally consolidated clays (Taylor and Bacchus 1969; Sangrey and France 1980). Conversely, overconsolidated clays exhibiting dilative behaviour will take in water once drainage is permitted, and the clay softens. As such, the introduction of drainage can be viewed as an additional variable into the assessment of post-cyclic behaviour of clays. Sangrey and France (1980) justified the use of drainage during cyclic loading by assuming that pore pressure dissipation is allowed in field conditions prior to application of loads that would mobilize the peak strength; this is analogous to the situation whereby pre-cast piles are driven by repeated loading and drainage precedes working load. However, applicability of these experimental data to actual scenarios is questionable since clays have low permeabilities and short-term cyclic loadings such as earthquakes do not provide sufficient time for excess pore pressure to dissipate.

2.3.2 Experimental Observations on Post-Cyclic Clay Behaviour

Previous studies have demonstrated that, during undrained compression tests, the post-cyclic effective stress paths of clays with cyclic-induced apparent overconsolidation are similar to those of clays overconsolidated by actual unloading (Figure 2.25). From Figures 2.25a and 2.25b, the post-cyclic effective stress paths of the clays are observed to migrate towards the critical state line (CSL) just as clays without a previous cyclic history do. However, Andersen et al. (1980) presented contrasting results wherein the post-cyclic effective stress paths for normally consolidated Drammen clay cross the critical state line for normally consolidated specimens without a previous cyclic history and tend towards the critical state line for overconsolidated specimens (Figure 2.25c). From Figure 2.25c, both experimentally-derived critical state lines for normally consolidated and overconsolidated undisturbed specimens without prior cyclic loading fall closely together. However, Andersen et al.'s (1980) assertion of there being multiple critical state line is anomalous to say the least, since this violates the basic premise of the critical state soil mechanics. Hence, the strength parameters (i.e. cohesion and effective angle of friction) and critical state parameter M are concluded to be independent of cyclic

history (Yasuhara et al. 1992). The same is observed for overconsolidated clays subjected to cyclic loadings (Figure 2.26).

In contrast, the shape of the post-cyclic effective stress path is clearly influenced by the undrained cyclic loading in the same way as overconsolidated clays produced by actual unloading. For this reason, Yasuhara et al. (1992 and 1994) proposed an empirical relation for predicting the changes in undrained strength of normally consolidated clays subjected to cyclic loading without prior drainage as follows:

$$\frac{(c_u)_{cy}}{(c_u)_{NC}} = (AOCR)\exp\left(\frac{\Lambda_0}{1-C_c/C_r}-1\right) \qquad [2.14]$$

Where:

$(c_u)_{cy}$ = Undrained strength after cyclic loading,

$(c_u)_{NC}$ = Undrained strength before cyclic loading,

$AOCR$ = Apparent overconsolidation ratio,

Λ_0 = Material constant,

C_c = Compression index,

C_r = Re-compression / Swelling index.

The definition of apparent overconsolidation ratio in Equation 2.14 is the ratio of the effective mean stress at the start of cyclic loading (i.e. Point A in Figure 2.27) to the effective mean stress at the end of cyclic loading (i.e. Point B in Figure 2.27). In mathematical form, the apparent overconsolidation ratio is expressed as:

$$AOCR = \frac{p_A'}{p_B'} = \frac{1}{1-\frac{(\Delta u)_{cy}}{p_{NC}'}} \qquad [2.15]$$

Where:

$(\Delta u)_{cy}$ = Cyclic-induced excess pore pressure,

p_{NC}' = Mean effective stress before cyclic loading.

Conceptually, the above definition of overconsolidation ratio is inconsistent with the standard definition of overconsolidation ratio which uses the effective mean stress at point D (Figure 2.27) as the preconsolidation pressure. The use of Equation 2.15 will result in an unloading from stress state at A to swell along the unload-reload line and reach stress state at B' with a specific volume larger than point B. Nonetheless, this

conceptually incorrect definition of overconsolidation ratio in Equation 2.15 does not affect Yasuhara et al.'s (1992 and 1994) derivation of Equation 2.14 because they also assumed that the stress state at point B produced by undrained cyclic loading is equivalent to the condition produced by a stress release from point D (Figure 2.27) in their deduction of post-cyclic undrained strength. As such, the apparent overconsolidation ratio can be viewed as a variable in their proposed relationship that does not necessarily have a physical meaning.

An alternative framework in the analysis of the post-cyclic undrained shear strength of clays is to establish the correlations between the reduction in undrained shear strength after cyclic loading (for normally consolidated and lightly overconsolidated clays) and the ratio of the peak cyclic shear strain to the critical or failure strain in a stress-controlled static test as illustrated in Figure 2.28 (Thiers and Seed 1969; Sangrey and France 1980; Yasuhara et al. 1983). Likewise, Yasuhara (1994) presented the reduction in undrained strength after cyclic loading against the normalized values of cyclic-induced pore pressures (Figure 2.29). It should be noted that both Figures 2.28 and 2.29 are based on post-cyclic compression tests conducted without prior drainage. Based on Figure 2.29, the reduction in undrained strength for normally consolidated or slightly overconsolidated clays subjected to cyclic loadings is typically less than 20%. A more drastic reduction is observed for the clays studied by Thiers and Seed (1969) (Figure 2.28). However, aside from the relatively fast cyclic loading rate of 1 Hz used in Thiers and Seed's (1969) experiments, the post-cyclic compression tests were conducted at 3%/min which is much faster than the rates commonly used by other researchers (Table 2.8). There is a high possibility that non-uniform distributions of pore pressures and strains within specimens could have affected their results. In contrast, the consistency observed in the compiled data by Yasuhara (1994) provides a more accurate description on the undrained strength reduction due to cyclic loading.

Nonetheless, the reliability of the aforementioned observations on the post-cyclic behaviour of clays drawn from various researchers remains to be validated due to limitations in their experimental techniques as discussed in Section 2.3.1.

Table 2.1 Strain rates used in recent experimental studies.

Clay	Effective Confining Pressure (kPa)	Test Frequency (Hz)	Reference
Undisturbed Golden Horn Clay	> Preconsolidation stress determined from oedometer tests	Varying amplitudes with same frequency of 0.1Hz	Ansal et al. 2001
Undisturbed Clay extracted from construction site of Hangzhou Telecommunication Bureau, Dongxing Branch	110, 117, 140, 150, 158	0.01, 0.05, 0.1, 0.5	Zhou and Gong 2001
Undisturbed Clay extracted from Vishakapatnam	50, 75, 100, 200	0.166, 0.083, 0.05	Moses et al. 2003
Undisturbed Augusta Clay, Undisturbed La Cienega Clay, Remoulded Kaolinite Clay	300 to 857	0.0066 to 111	Matesic and Vucetic 2003
Remoulded Onoda Clay, Remoulded Ariake Clay C, Remoulded Dejima Clay	66.7, 100, 133.3	0.1 , 1 , 2	Yamada et al. 2008
Remoulded Kaolinite Clay	150, 200	0.05, 0.1, 0.25, 0.5, 1, 3, 5	Banerjee 2009

Table 2.2 Recommended values for coefficient F based on 95% dissipation of excess pore pressure induced by shear (Edited from: BS1377: 1990).

Drainage conditions during consolidation	Values of F	
	Drained test	Undrained test
From one end	8.5	0.53
From both ends	8.5	2.1
From radial boundary and one end	14	1.8
From radial boundary and two ends	16	2.3

Table 2.3 Recommended values for factor F corresponding to 95% pore pressure dissipation (Edited from: Eurocode ISO/TS 17892:2004).

Drainage conditions during consolidation	Values of F	
	Drained test	Undrained test
From one end	34	2.1
From both ends	34	8.4
From radial boundary and one end	56	7.2
From radial boundary and two ends	64	9.2

Table 2.4 Proposed empirical expressions for small-strain shear modulus and void ratio.

Equation No.	Clay Material	Range of *e* applicable	Proposed Correlation	Reference
2.4	Kaolinite PI = 21	0.6 to 1.5	$G_{\max} = 3300\frac{(2.97-e)^2}{1+e}(p')^{0.5}$	Hardin and Black 1968
2.5	Kaolinite PI = 35	< 1.5	$G_{\max} = 4500\frac{(2.97-e)^2}{1+e}(p')^{0.5}$	Marcuson and Wahls 1972
2.6	Bentonite PI = 60	1.5 to 2.5	$G_{\max} = 450\frac{(4.4-e)^2}{1+e}(p')^{0.5}$	Marcuson and Wahls 1972
2.7a	Remoulded Clays PI = 0 to 50	< 2.0	**Lower bound:** $G_{\max} = 2000\frac{(2.97-e)^2}{1+e}(p')^{0.5}$	Zen et al. 1978
2.7b			**Upper bound:** $G_{\max} = 4000\frac{(2.97-e)^2}{1+e}(p')^{0.5}$	
2.8	Undisturbed Clays PI = 40 to 100	1.5 to 4.0	$G_{\max} = 90\frac{(7.32-e)^2}{1+e}(p')^{0.6}$	Kokusho et al. 1982

Table 2.5 Proposed empirical expressions for small-strain shear modulus and overconsolidation ratio.

Equation No.	Clay Material	Range of *OCR* applicable	Proposed Correlation	Reference
2.9	Speswhite Kaolin	1 to 4	$\frac{G_{\max}}{p_r} = 1964\left(\frac{p'}{p_r}\right)^{0.653}(OCR)^{0.196}$	Viggiani and Atkinson 1995
2.10	Malaysian Kaolin	1	$\frac{G_{\max}}{p_r} = 2060\left(\frac{p'}{p_r}\right)^{0.653}$	Banerjee 2009
2.11a	Gault Clay	1 to 70	**Normally Consolidated:** $G_{\max} = 886(p')^{0.79}$	Dasari 1996
2.11b			**Overconsolidated:** $G_{\max} = 4545(p')^{0.59}$	
2.12	Singapore Lower Marine Clay	1 to 2.5	$G_{\max} = 425(p')^{0.9}$	Chong 2002

Table 2.6 Stress-strain models (Kagawa 1993; Ishihara 1996; Towhata 2008; Banerjee 2009).

Models	Mathematical Expressions
Hyperbolic	**Skeleton curve**: $\tau = \dfrac{G_{\max}\gamma}{1+\lvert\gamma/\gamma_r\rvert}$ **Normalized shear modulus**: $\dfrac{G}{G_{\max}} = \dfrac{1}{1+\lvert\gamma_A/\gamma_r\rvert}$ **Damping ratio**: $D = \dfrac{2}{\pi}\left\{\left(1+\dfrac{2}{\gamma_A/\gamma_r}\right) - 2\dfrac{1+\gamma_A/\gamma_r}{(\gamma_A/\gamma_r)^2}\ln(1+\gamma_A/\gamma_r)\right\}$ Where: $G_{\max}$ = Small-strain shear modulus, γ = Shear strain, γ_r = Reference shear strain at which $G/G_{\max}$ = 0.5, γ_A = Applied strain amplitude.
Ramberg-Osgood	**Skeleton curve**: $\dfrac{\gamma}{\gamma_r} = \dfrac{\tau}{\tau_r}\left\{1+\alpha\left(\dfrac{\tau}{\tau_r}\right)^{r-1}\right\}$ **Normalized shear modulus**: $\left(\dfrac{\gamma_A}{\gamma_r}\right)^{r-1} = \dfrac{1-\dfrac{G}{G_{\max}}}{\alpha\left(\dfrac{G}{G_{\max}}\right)^{r} C_1^{r-1}}$ **Damping Ratio**: $D = \dfrac{2}{\pi}\left(\dfrac{r-1}{r+1}\right)\left(1-\dfrac{G}{G_{\max}}\right)$ Where: τ_r = Ultimate shear resistance, α, C_1 and r = Model parameters.
Modified Hyperbolic	**Skeleton curve**: $q = q_f - \dfrac{1}{\dfrac{3G_{\max}}{q_f}}\left\{\dfrac{3G_{\max}}{1+\dfrac{3G_{\max}\lvert\varepsilon_s\rvert}{q_f}}\right\}$ **Normalized shear modulus**: Denoting $R = G_{\max}/q_f$ $\dfrac{G}{G_{\max}} = \dfrac{1}{1+3R\varepsilon_r}$ **Damping Ratio**: $D = \dfrac{2}{\pi}\left\{\dfrac{2+3R\varepsilon_r - \dfrac{2(1+3R\varepsilon_r)}{3R\varepsilon_r}\ln(1+3R\varepsilon_r)}{3R\varepsilon_r}\right\}$ Where: q = Deviator stress, q_f = Deviator stress at failure, ε_s = Generalized shear strain, ε_r = Reloading shear strain.

Table 2.7 Material parameters used for the available stress-strain models.

Model	Parameters	Assumed Values
Hyperbolic	γ_r	0.2
Ramberg-Osgood	γ_r	0.2
	α	6
	C_1	0.6
	r	2.5
Modified Hyperbolic	R	120

Table 2.8 Past investigations on post-cyclic behaviour.

Clay Material	Plasticity Index	Cyclic Frequency	Post-cyclic loading rate	Immdiate / Curing / Drainage	Confining Pressure (kPa)	Reference
Commercial Halloysite	26	0.2 Hz (100 cycles)	1%/min	Immediate	26 - 413	Taylor and Bacchus 1969
San Francisco Bay Mud; Anchorage Silty Clay (from 2 sites)	45; 14	1 Hz (200 cycles)	3%/min	Immediate	Not available	Thiers and Seed 1969
Holocene Clay	40	1 Hz (70 - 540 cycles)	10%/hr	Curing (1 day)	120 - 479	Koutsoftas 1978
Drammen Clay	27	0.1Hz (1000 cycles)	3%/hr or 4.5%/hr	Curing (20min rest periods during cyclic loading); Drainage after cyclic	8 - 400	Andersen et al. 1980
Ariake Clay	69	0.1 - 3Hz (3600 - 172,800 cycles)	0.1%/min	Immediate; Drainage after cyclic	Not available	Yasuhara et al. 1983
Ariake Clay (2 types)	69; 72	0.1 Hz (6 - 60,480 cycles)	0.05%/min	Immediate; Drainage after cyclic	200	Yasuhara et al. 1992
Compilation of 9 Clays	13 - 320	0.1 - 1 Hz	Not available	Immediate; Drainage after cyclic	20 - 700	Yasuhara 1994
Mexico City Clay	294	Not available (100 cycles)	1%/hr	Curing (12 hours)	51 - 88.4	Diaz-Rodriguez et al. 2000
Silty and Clayey Soils from Gumusdere; Adapazari; Izmir	2 - 33	0.01 - 10 Hz (5 - 20 cycles)	0.5mm/s	Immediate	100	Erken and Ulker 2007
Wenzhou Marine Clay	35.8	0.01 - 0.1 Hz (20 - 6355 cycles)	2%/hr	Immediate	52.8	Li et al. 2011
Commercial Kaolinite (Flocculated ; Dispersed Specimens)	27; 23	0.1 Hz (5000 cycles)	0.07mm /min; 0.05mm /min	Curing (6 hours)	100 - 250	Pillai et al. 2011

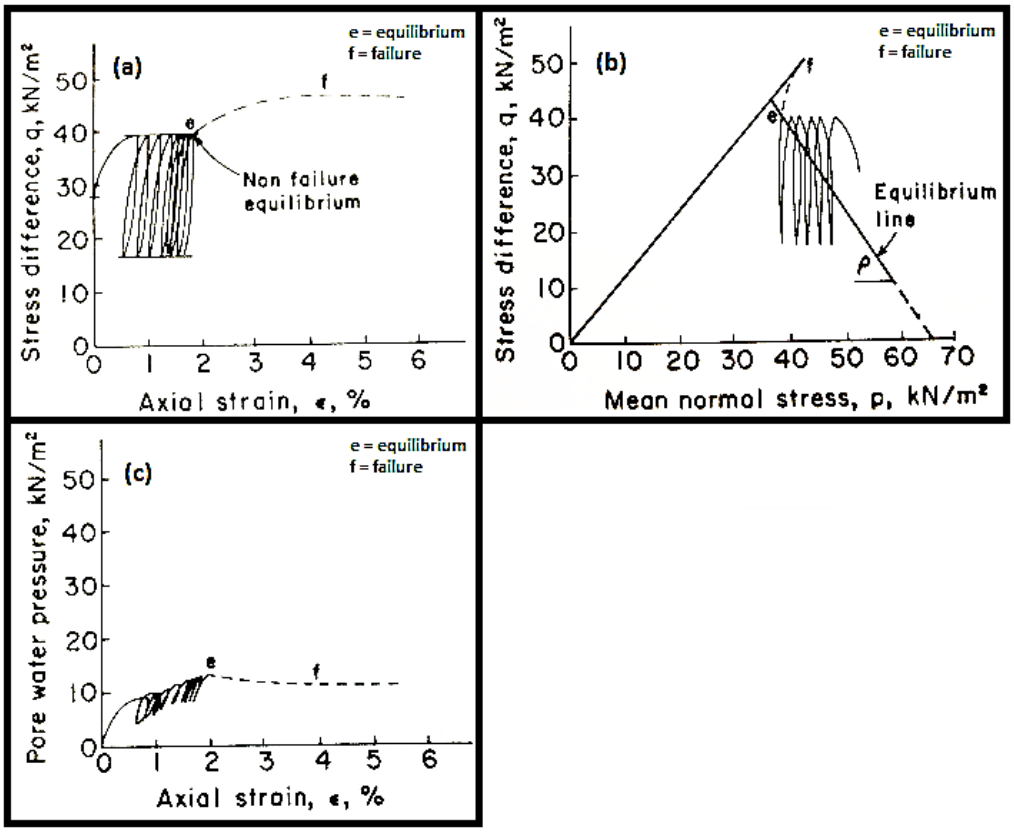

Figure 2.1 Definition of non-failure equilibrium in (a) stress-strain relationship, (b) stress path plot and (c) pore pressure variation with strain (after Sangrey and France 1980).

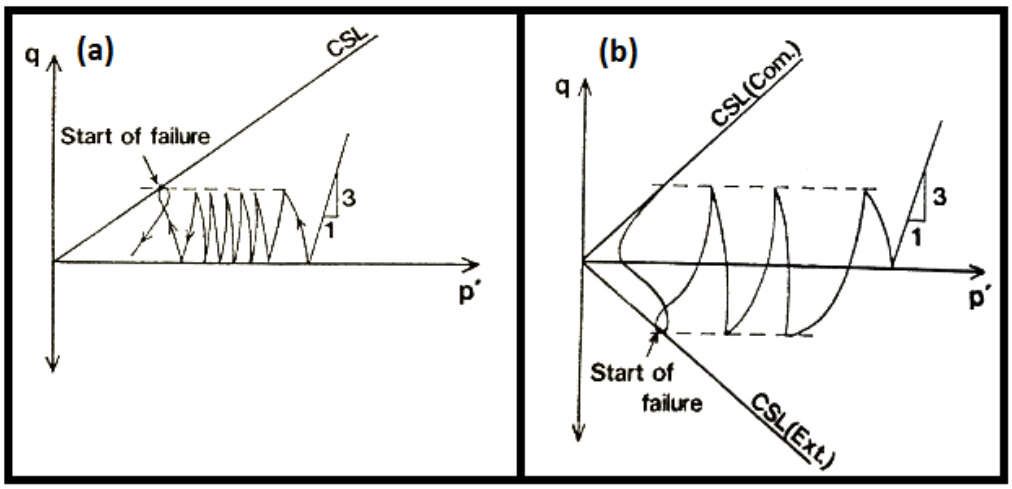

Figure 2.2 Definition of cyclic failure for (a) one-way stress-controlled and (b) two-way stress-controlled tests (Yasuhara et al. 1992).

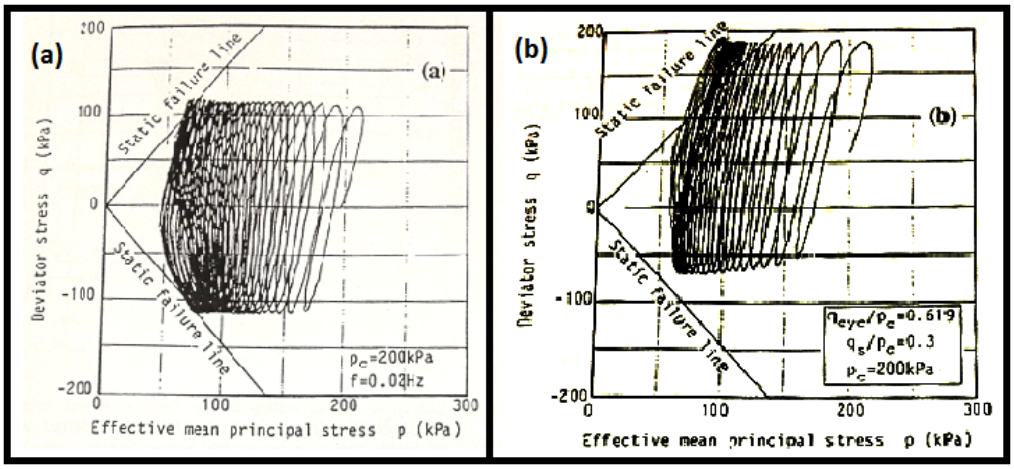

Figure 2.3 Effective stress paths of (a) an isotropic-consolidated specimen and (b) an anisotropic-consolidated specimen (Hyodo et al. 1994).

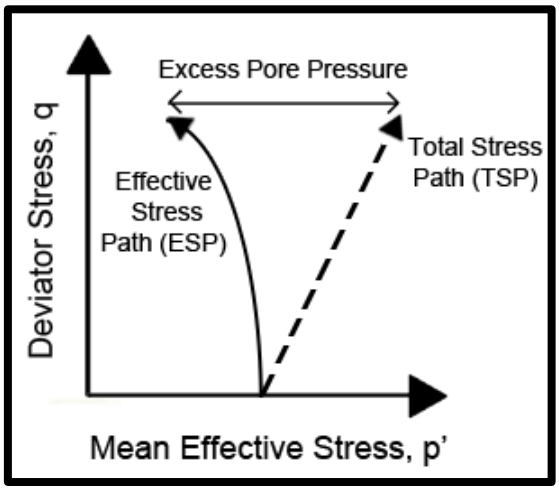

Figure 2.4 Influence of excess pore pressure on the effective stress path.

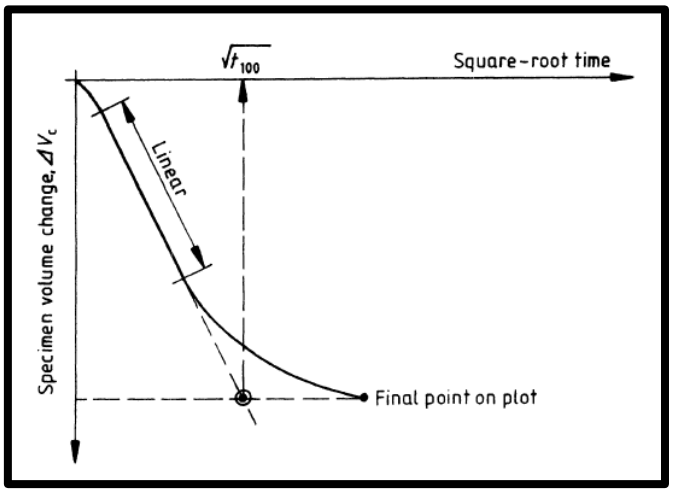

Figure 2.5 BS1377 square-root time method for t_{100} calculation (BS1377:1990).

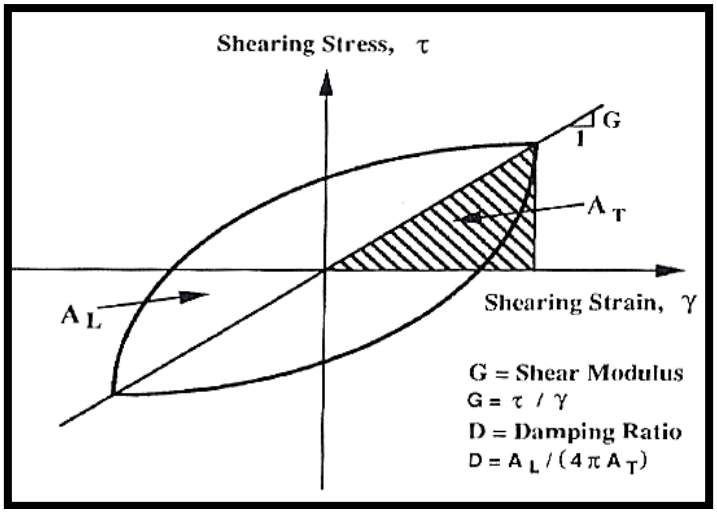

Figure 2.6 Characteristic hysteresis loop during one loading cycle for calculation of shear modulus and damping ratio (Kim et al. 1991).

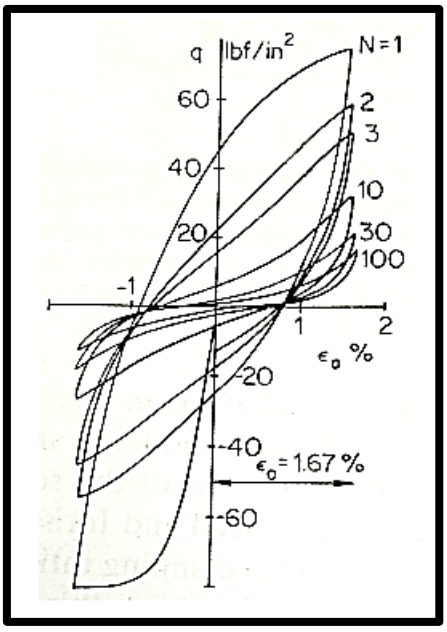

Figure 2.7 Stress-strain curve obtained in strain-controlled two-way undrained cyclic triaxial test on normally consolidated halloysite (Taylor and Bacchus 1969).

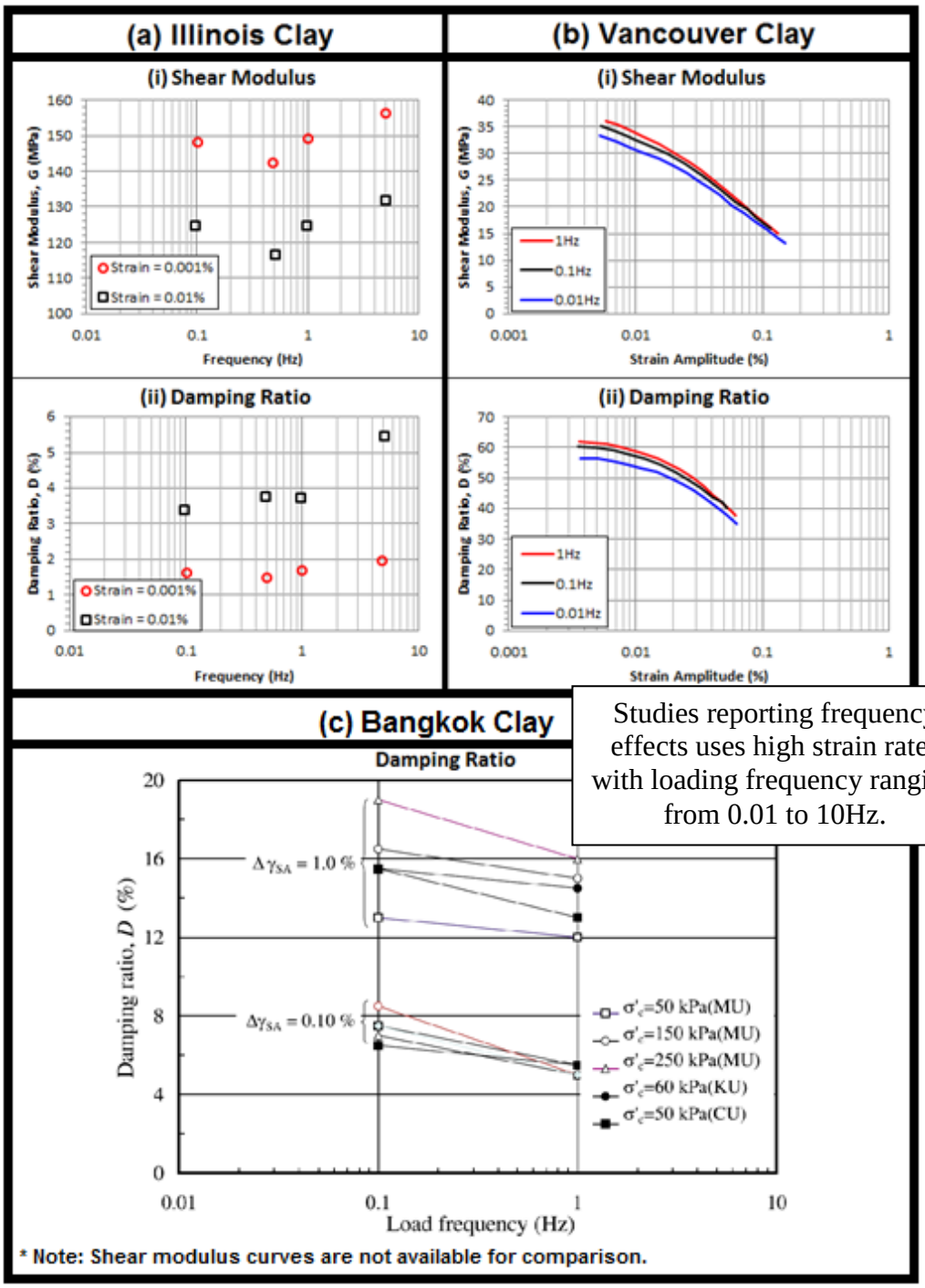

Studies reporting frequency effects uses high strain rates with loading frequency ranging from 0.01 to 10Hz.

Figure 2.8 Frequency effects on dynamic properties of (a) Illinois Clay (Edited from: Stokoe et al. 2003), (b) Vancouver Clay (Edited from: Zanvoral and Campanella 1994) and (c) Bangkok Clay (Teachavorasinskun et al. 2002).

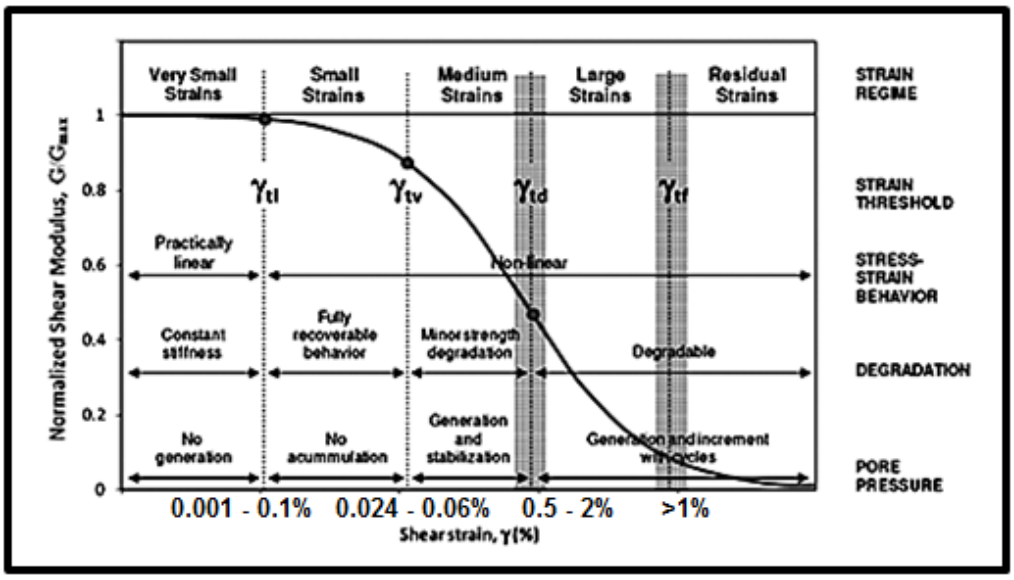

Figure 2.9 Soil behaviour between strain thresholds for saturated clayey soils (Diaz-Rodriguez and Lopez-Molina 2008).

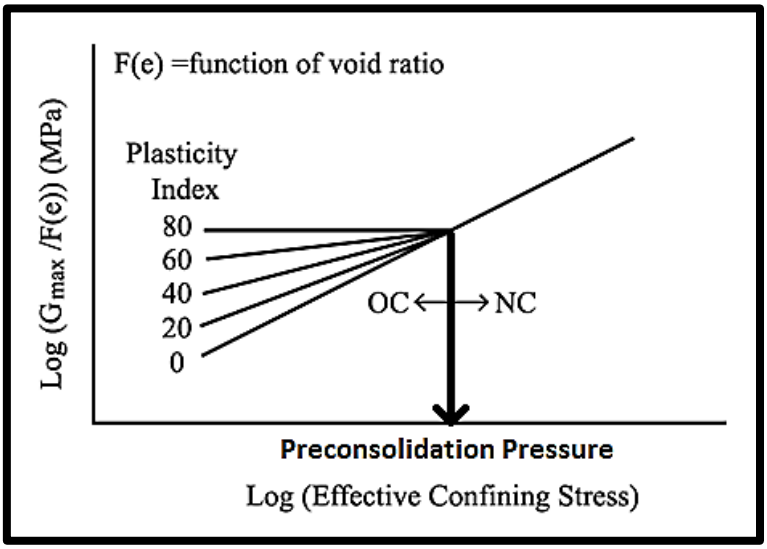

Figure 2.10 Characteristics of small-strain shear modulus as influenced by overconsolidation ratio (Edited from: Ishihara 1996).

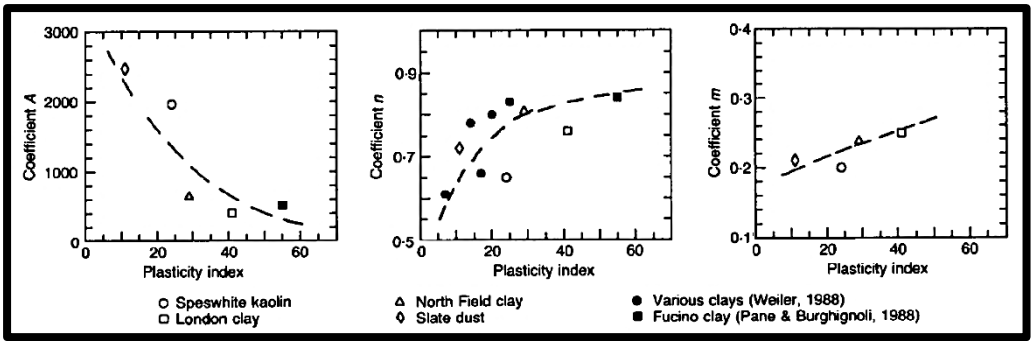

Figure 2.11 Effect of plasticity on stiffness parameters for small-strain shear modulus (Viggiani and Atkinson 1995).

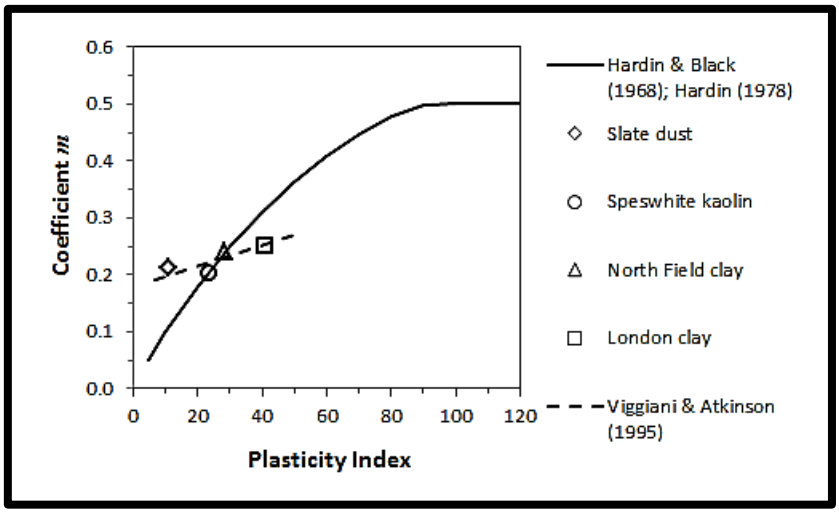

Figure 2.12 Effect of plasticity index on overconsolidation ratio exponent *m*.

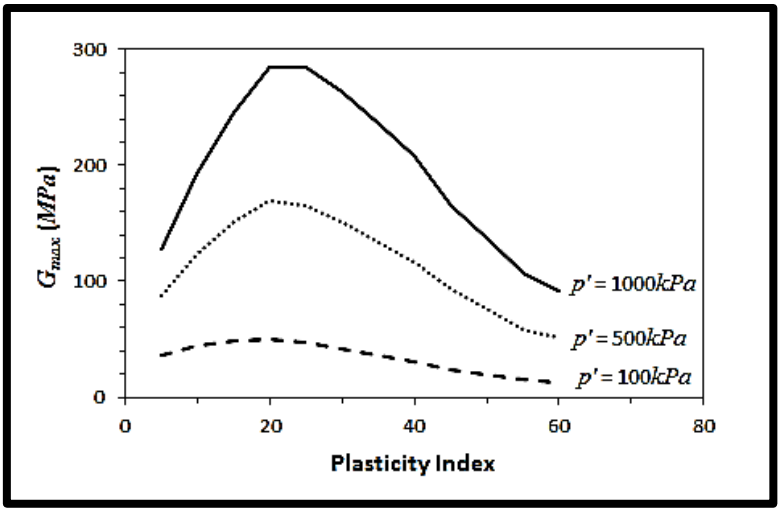

Figure 2.13 Effect of plasticity index on small-strain shear modulus for normally consolidated clays.

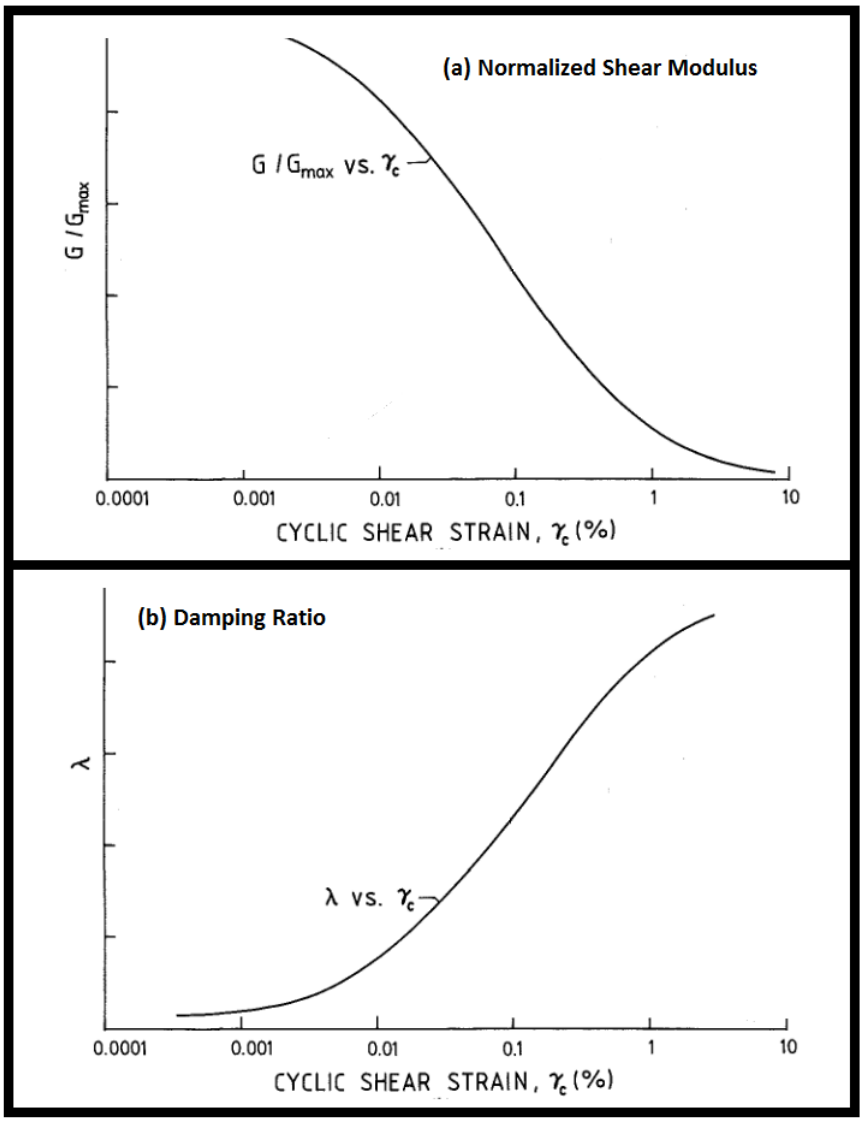

Figure 2.14 Variation of cyclic parameters with applied cyclic strain for (a) normalized shear modulus and (b) damping ratio (Edited from: Vucetic and Dobry 1991).

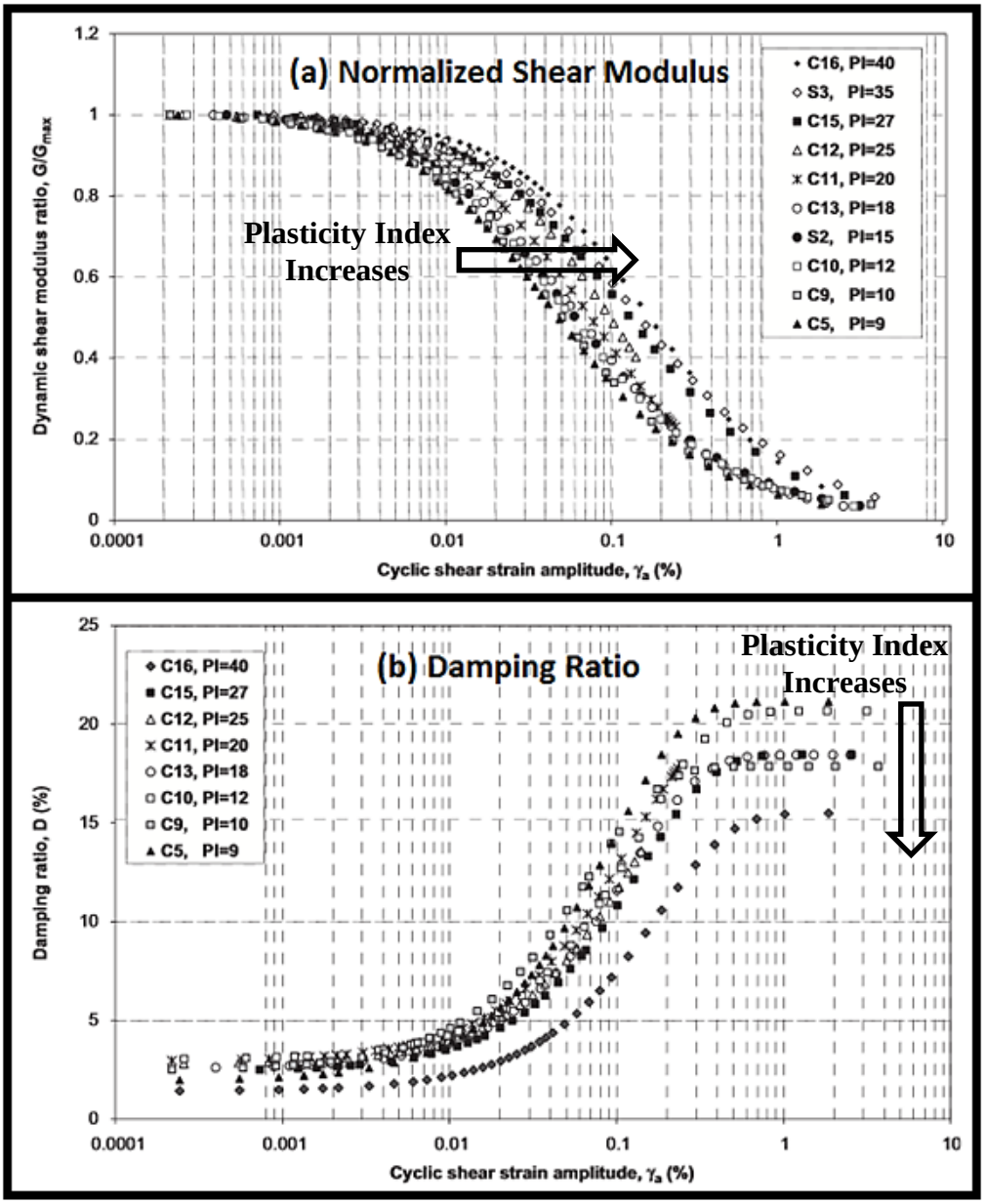

Figure 2.15 Influence of plasticity index on (a) normalized shear modulus and (b) damping ratio curves (Edited from: Okur and Ansal 2007).

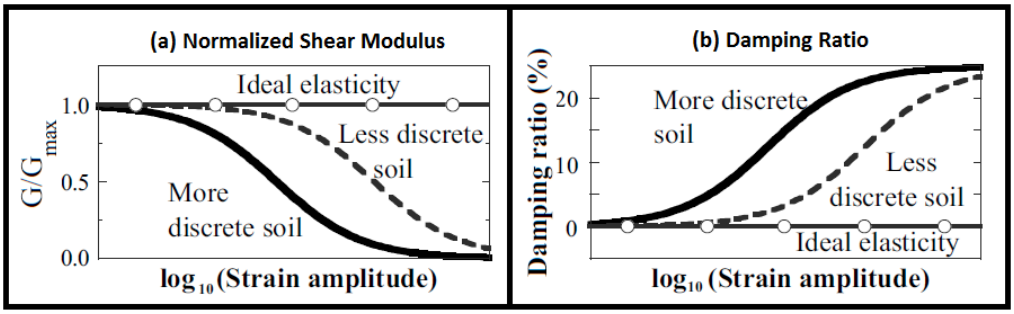

Figure 2.16 Effects of discreteness on nonlinearity in terms of (a) normalized shear modulus variation with strain and (b) damping ratio variation with strain (Towhata 2008).

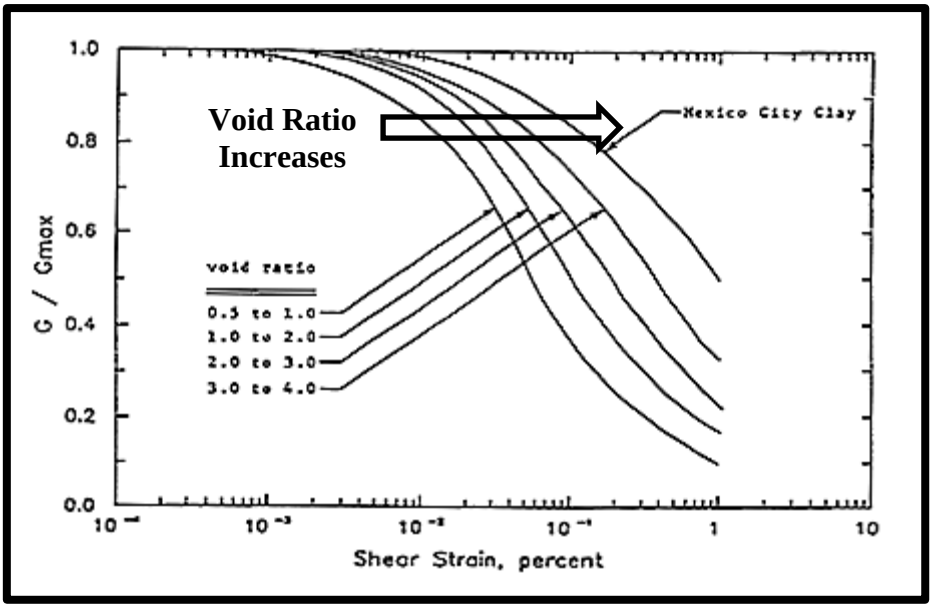

Figure 2.17 Effects of void ratio on normalized shear modulus variation with strain (Sun et al., 1988).

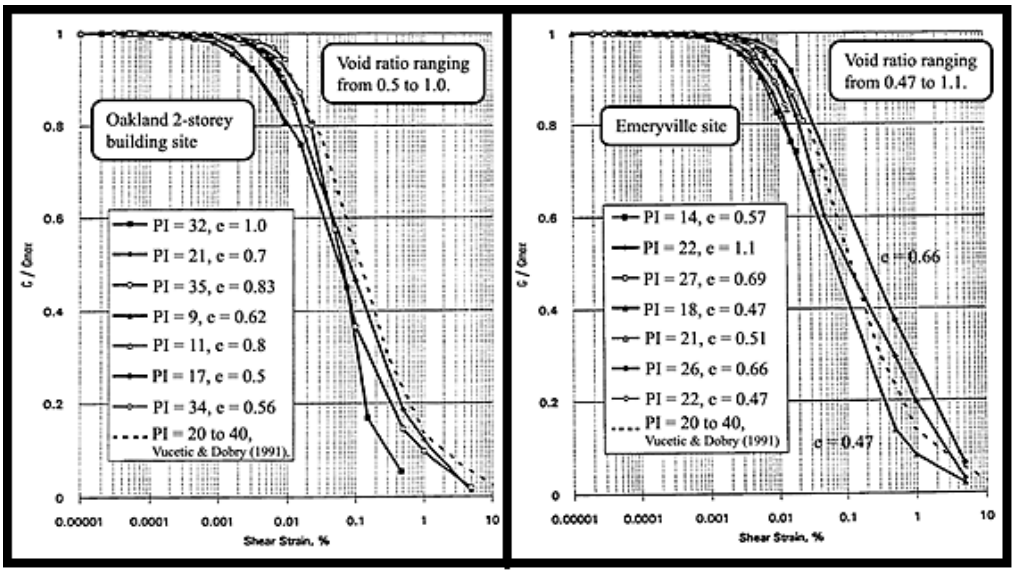

Figure 2.18 Normalized shear modulus curves for Old Bay Clay Specimens with Vucetic and Dobry (1991) curve as reference (after Guha, 1995).

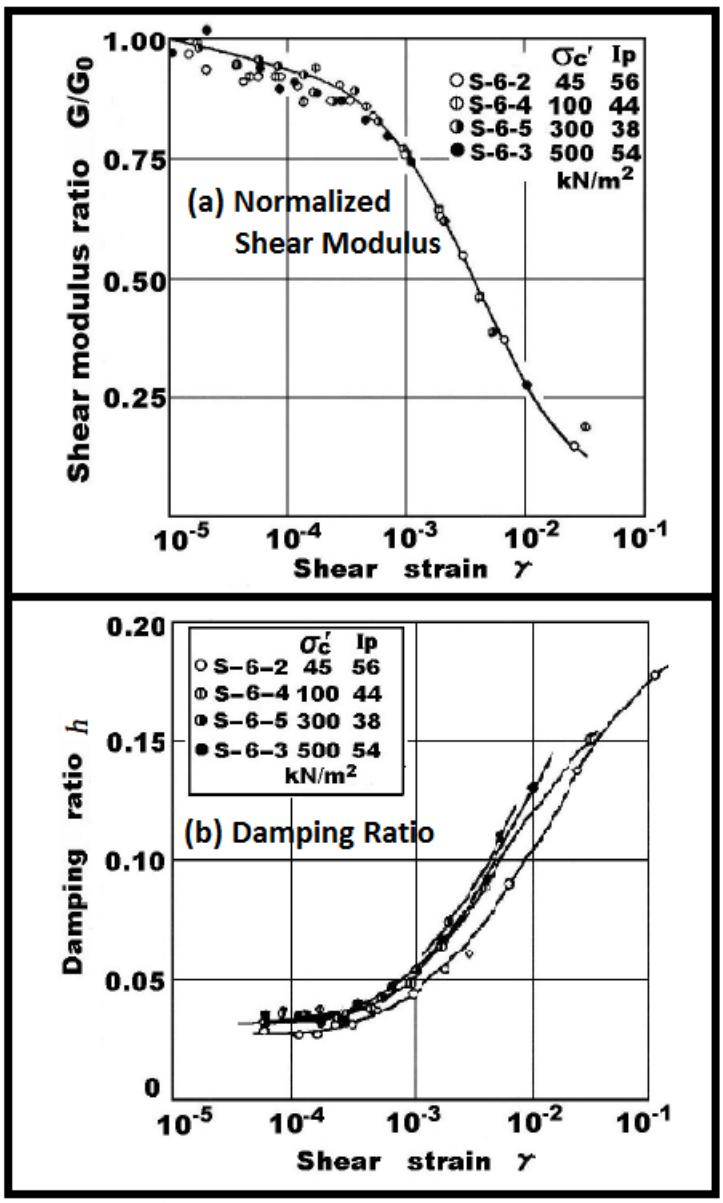

Figure 2.19 Influence of mean effective stress on (a) normalized shear modulus and (b) damping ratio curves (Edited from: Kokusho et al. 1982).

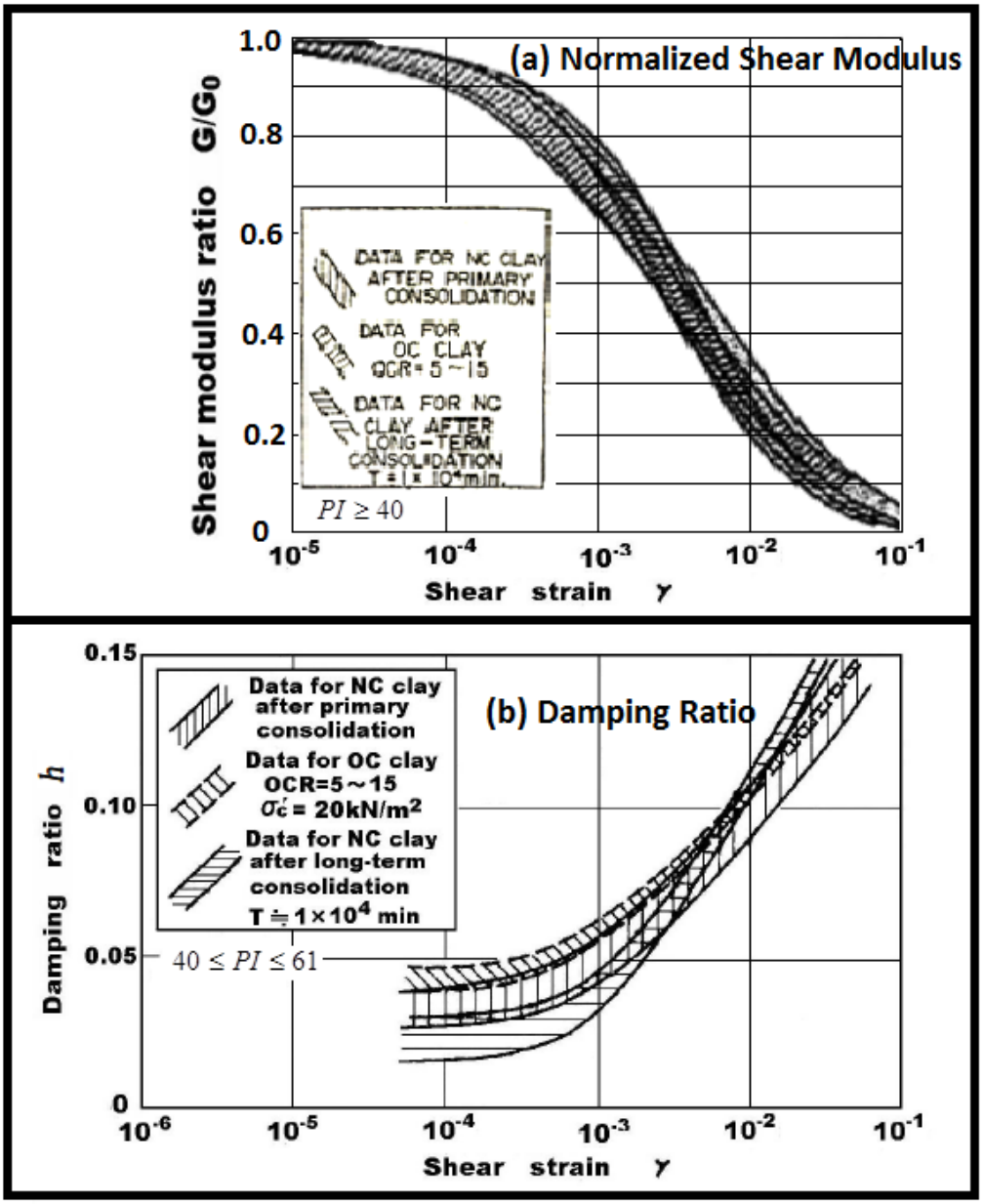

Figure 2.20 Influence of consolidation history on (a) normalized shear modulus and (b) damping ratio curves (Edited from: Kokusho et al. 1982).

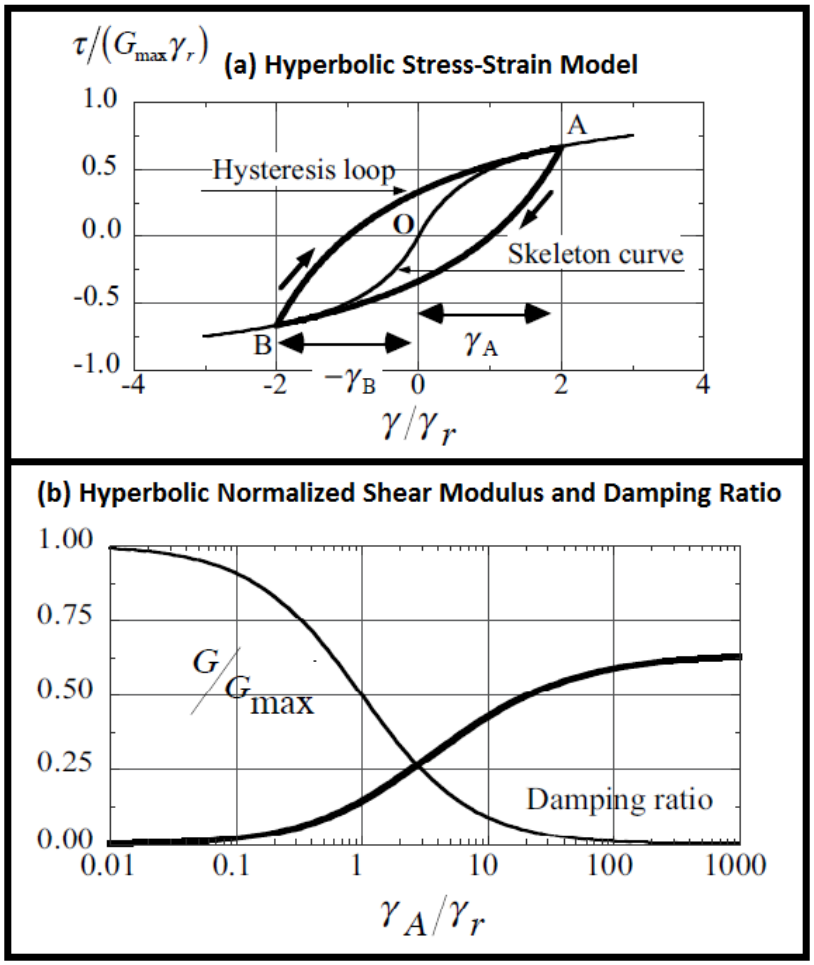

Figure 2.21 Hyperbolic model.

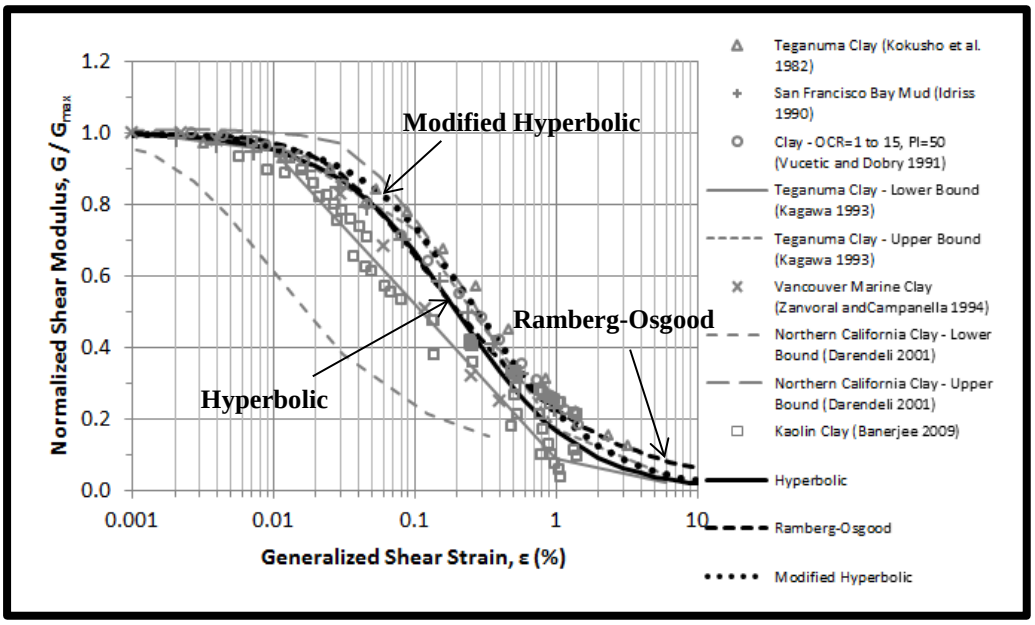

Figure 2.22 Comparison of stress-strain models against experimental data for the shear modulus degradation curves.

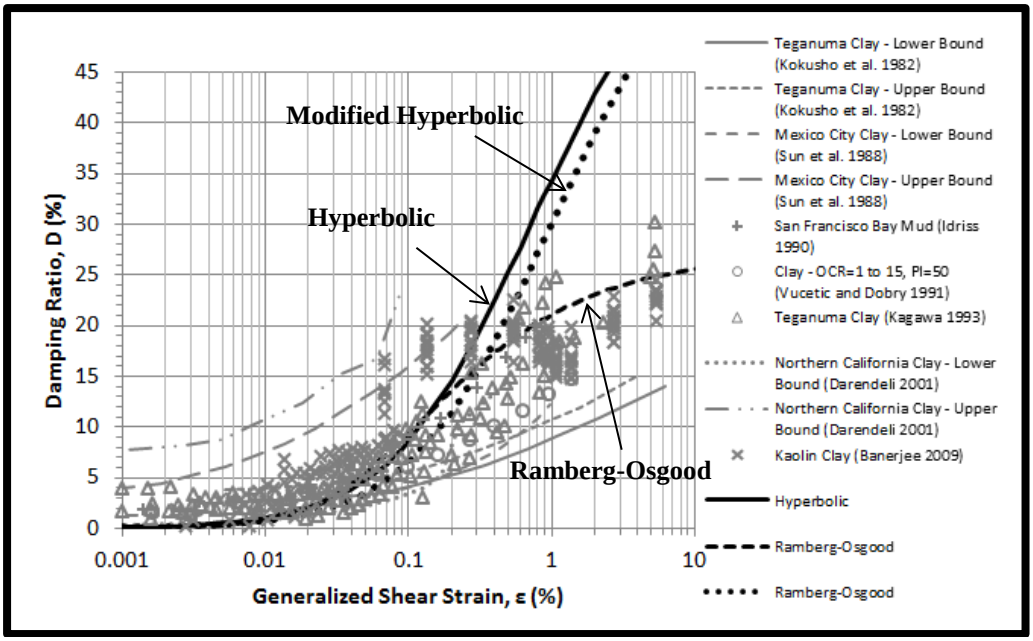

Figure 2.23 Comparison of stress-strain models against experimental data for damping ratio.

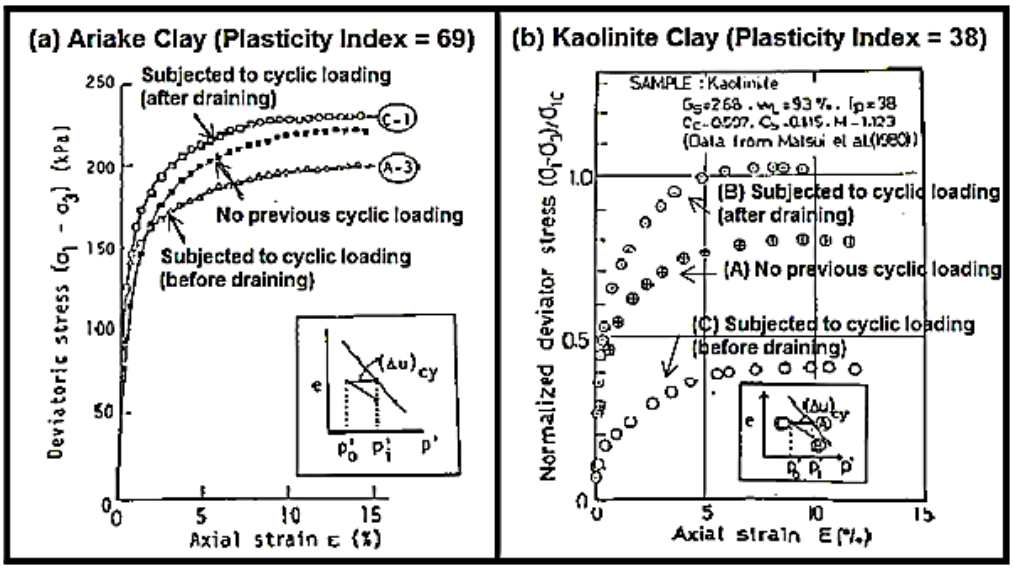

Figure 2.24 Effect of drainage on (a) highly plastic Ariake clay and (b) lowly plastic Kaolinite clay (Edited from: Yasuhara et al. 1983).

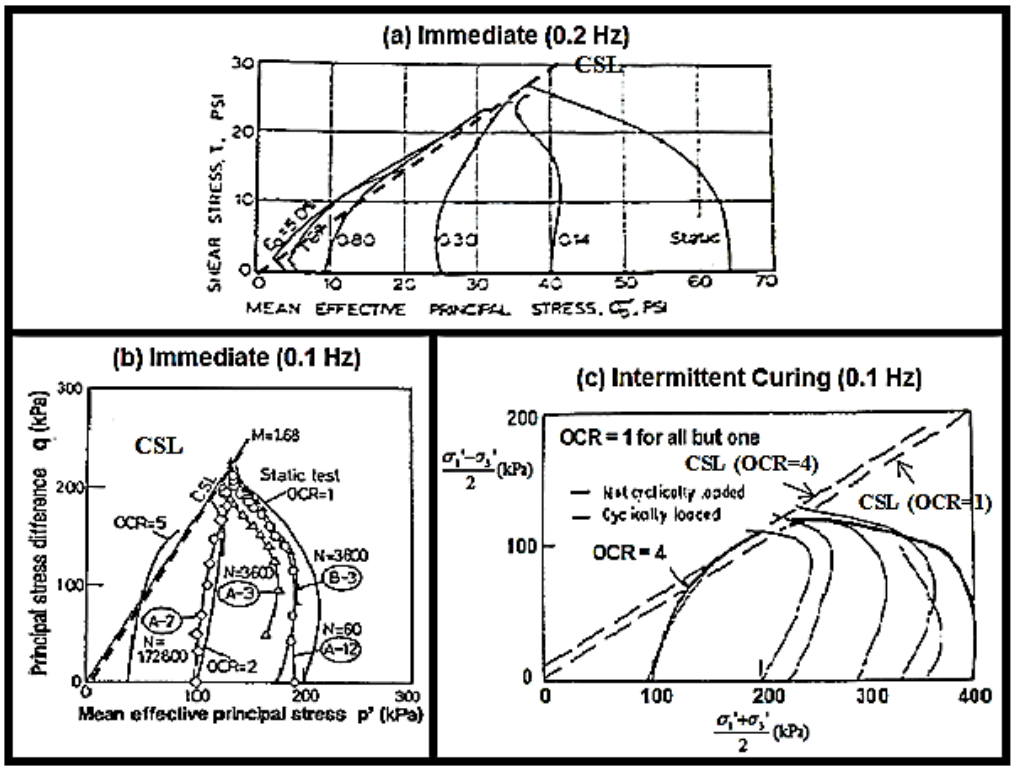

Figure 2.25 Post-cyclic undrained effective stress paths for (a) commercial Halloysite (PI = 26) and (b) Ariake clay (PI = 69) and (c) Drammen clay (PI = 27) (Edited from: Taylor and Bacchus 1969; Yasuhara et al. 1992; Andersen et al. 1980).

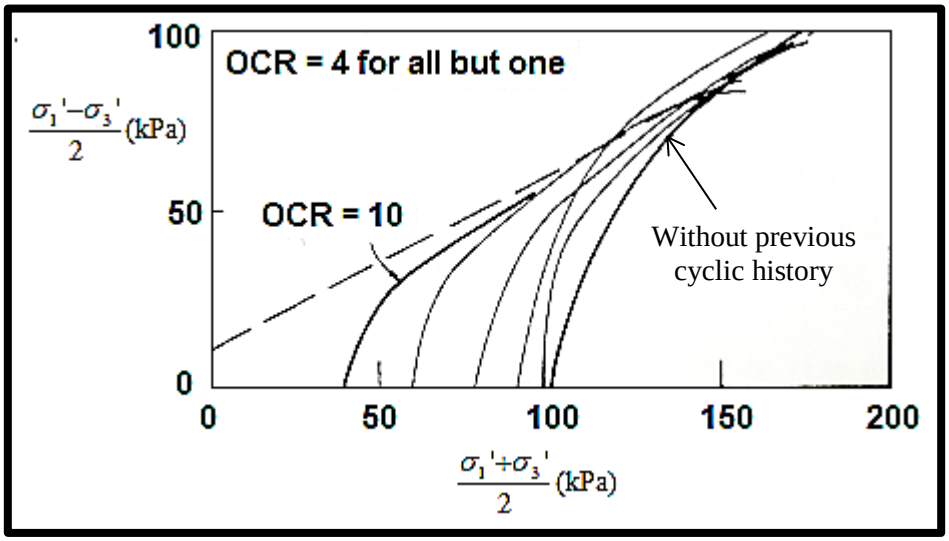

Figure 2.26 Post-cyclic undrained effective stress paths for overconsolidated Drammen clay (Andersen et al. 1980).

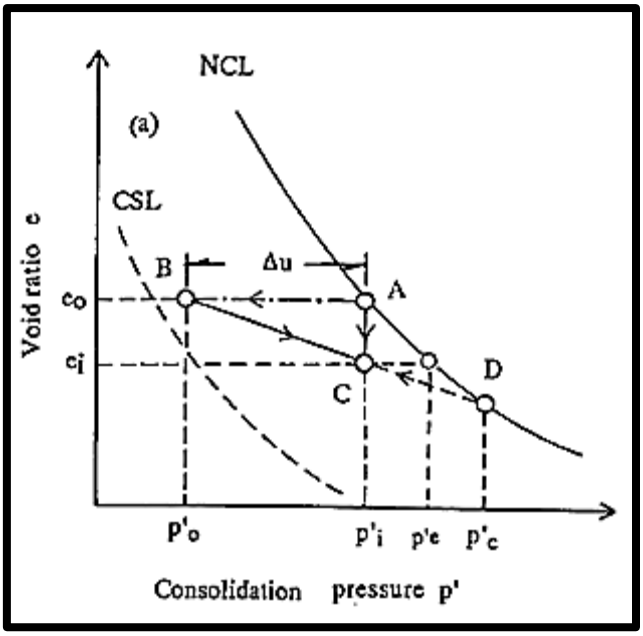

Figure 2.27 e-log p' curve for normally consolidated clays undergoing undrained cyclic loading (Yasuhara et al. 1994).

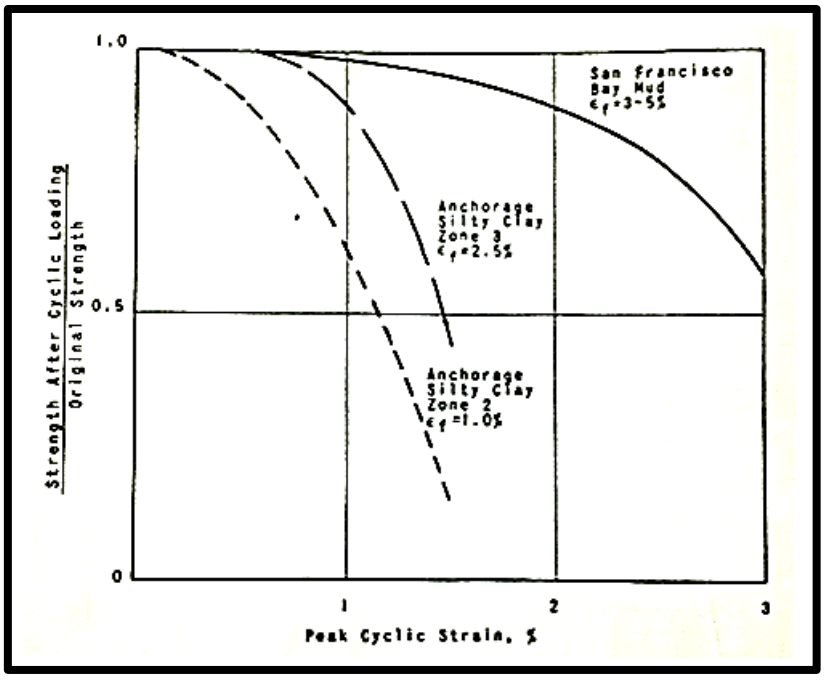

Figure 2.28 Effect of cyclic loading on post-cyclic undrained triaxial strength (frequency = 1 Hz) (Thiers and Seed 1969).

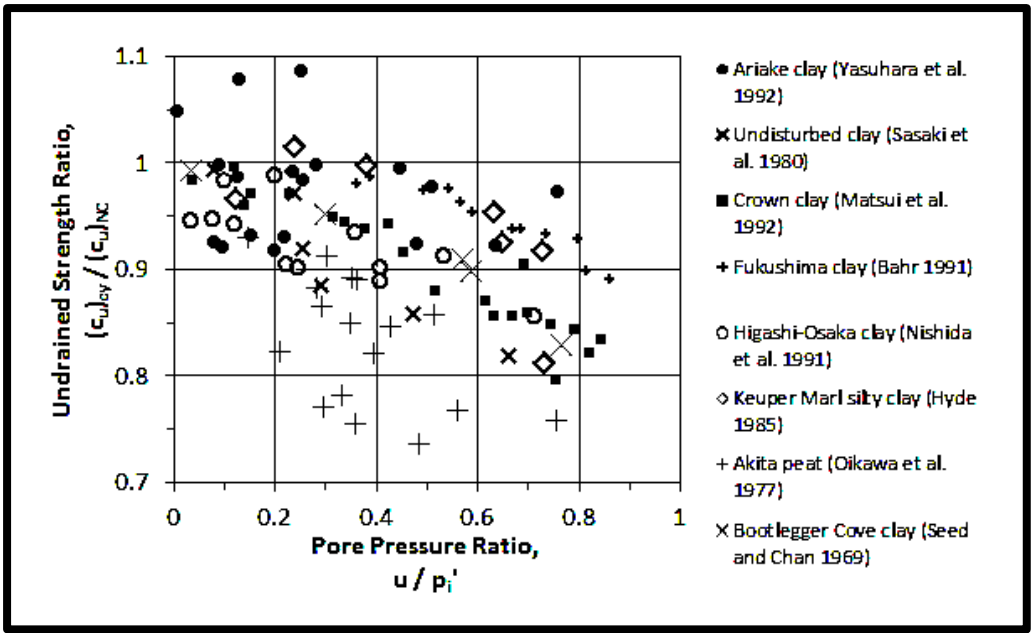

Figure 2.29 Effect of cyclic loading on post-cyclic undrained triaxial strength of 8 different cohesive soils (Edited from: Yasuhara 1994).

Chapter 3 – Experimental Methodology and Setup

3.1 Introduction

The two clays used in this study are the Kaolin Clay and Singapore Upper Marine Clay. All cyclic triaxial and resonant column tests were conducted using remoulded soil specimens prepared from commercially available kaolin powder and reconstituted Singapore Upper Marine Clay. These disturbed samples were obtained from approximately 10m depth at an excavation site along Rochor Canal Road, where the Rochor MRT station is currently being constructed. The clay obtained from the site was then manually treated to remove sand pockets as well as shell fragments. The physical properties of both clays are summarized in Tables 3.1 and 3.2. All characterization tests were conducted in accordance with Eurocode Technical Specification ISO/TS 17892.

3.2 Specimen Preparation

De-aired de-ionised water was first added to the clay to bring its water content up to 120%, which is approximately 1.5 times its liquid limits, in order to produce homogenous reconstituted specimens (Burland 1990). The remoulded Singapore Upper Marine Clay specimens were prepared from its natural wet state without pre-drying because pre-drying can lead to significant reduction in the Atterberg Limits of the clay, indicating that the activity level of the clay had been lowered through the drying and crushing process (Lee et al., 2005). Both Singapore Upper Marine Clay slurry and Kaolin Clay slurry were then separately mixed in a Hobart N50CE electric mixer using a rotational speed of 125rpm for 30 minutes (Figure 3.3).

The procedure for the specimen preparation largely follows that used by Banerjee (2009). After thorough mixing of 30 minutes, the resulting slurries were poured into pre-loading tubes of the same size (38mm diameter) as the test specimens, where they were allowed to preconsolidate one-dimensionally under an overburden pressure of 25kPa, 50kPa or 100kPa for two and four weeks for Kaolin Clay and Marine Clay respectively. This stage is critical for the specimen to gain some shear strength prior to the consolidation process in the triaxial cell. This pre-loading assembly consists of 38mm inner diameter by 240mm length stainless steel tubes, each fitted with a stand holder at its top through which loading plates can be added with minimal eccentricities (Figure 3.4). To prevent the development of side friction within these pre-loading tubes, silicone grease was used to line the inner walls of all tubes prior to

filling with clay slurries. With the reduction of side friction, the water content difference between the top and bottom for all specimens was consistently less than 2.4%. The consolidation pressure used in this stage is relatively small (i.e. approximately half) compared to the consolidation pressures applied in the triaxial cell prior to cyclic loading. For example, weights totalling up to 10kg were used to preconsolidate the slurry to an effective vertical stress of approximately 100kPa.

3.3 Equipment Used

Due to the low permeability of clays, the cyclic loading process is essentially undrained. In this study, both undrained cyclic triaxial and resonant column tests are performed on Singapore Upper Marine Clay and Kaolin Clay using the GDS Enterprise Level Dynamic (ELDyn) Triaxial Testing System and the Drnevich Long-Tor Resonant Column apparatus. This section introduces the advantages and limitations of these apparatus.

3.3.1 GDS Enterprise Level Dynamic (ELDyn) Triaxial Testing System

The GDS ELDyn Triaxial System (Figure 3.5) comprises:

(i) an axially-stiff load frame with a beam-mounted electro-mechanical actuator which has a full stoke capability of 100mm,
(ii) a load cell with a maximum axial load capability of ±5kN at 5Hz,
(iii) a triaxial cell for sample size of 38mm diameter by 76mm height,
(iv) a pneumatic cell pressure controller with a maximum pressure of 1000kPa,
(v) a hydraulic back pressure controller with a maximum pressure of 2000kPa, and
(vi) a dynamic data logger with 16 bit data acquisition.

Both pressure controllers and actuator are computer-controlled. For frequencies below 10Hz, electromechanical control provides the highest precision in contrast to hydraulic or pneumatic actuators (Figure 3.6). Below 1Hz, the electromechanical systems are much better because they are able to maintain very accurate loads and positions over extended periods of time, in addition to having good dynamic performance.

Since GDS ELDyn uses an electromechanical actuator, strain-controlled cyclic tests are recommended over stress-controlled cyclic tests. This is because the motor has a high resolution shaft encoder (8000 counts per revolution) and fixed gearing. Hence, the axial displacement can be controlled to a very high resolution that surpasses that of a displacement transducer mounted externally to the test specimen being read by a 16-bit data acquisition system (with a resolution of 1 in 64,000).

In contrast, the level of control is less precise for stress-controlled cyclic tests. With regard to load or pressure, electromechanical control relies on a load or pressure transducer in the primary control loop that is not perfectly correlated to the parameter (velocity or displacement) being controlled by the motor because it does not take into account the time lapse between the transducer reading and subsequently calculation of the corresponding velocity or displacement to be applied.

As previously highlighted in Section 2.1.2, pore pressure homogeneity within specimens is crucial under undrained triaxial conditions. Thus in this study, both mid-plane and base pore pressure transducers were used during cyclic and post-cyclic tests and pore pressure equilibration is considered achieved when both transducers produce similar excess pore pressure measurements (see Figure 3.7).

3.3.2 GDS Electromechanical Dynamic Triaxial Testing System (DYNTTS)

Due to the limited cell pressure capacity of 1000kPa for the GDS ELDyn Triaxial System, the GDS DYNTTS system (Figure 3.8) was used for cell pressures exceeding 1000kPa. This GDS DYNTTS system comprises:

(i) a cyclic actuator connected to the base of the cell which can produce cyclic platen movement of up to ±50mm,
(ii) a load cell with a maximum axial load capability of ±10kN at 5Hz,
(iii) a triaxial cell for sample size of 38mm diameter by 76mm height,
(iv) a hydraulic cell pressure controller with a maximum pressure of 2000kPa,
(v) a hydraulic back pressure controller with a maximum pressure of 2000kPa, and
(vi) a dynamic data logger with 16 bit data acquisition.

Similar to the GDS ELDyn Triaxial System, this GDS DYNTTS also utilizes an electromechanical actuator that is more suitable for strain-controlled cyclic loadings

than stress-controlled cyclic loadings. In addition, this system was also fitted with both mid-plane and base pore pressure transducers.

3.3.3 Drnevich Long-Tor Resonant Column Apparatus

A Drnevich Long-Tor resonant column was used to measure the modulus and damping characteristics of soils as functions of vibrating strain amplitude and other factors such as ambient confining stress, confinement duration and void ratio (Figure 3.9). The apparatus is capable of producing either longitudinal or torsional excitation, but only the latter will be used. This system consisted of a cylindrical specimen with platens attached to each end. The specimen is fixed at the bottom (the passive-end) and a sinusoidal torsional excitation is applied to the top (the active-end). Torsional excitation is produced by four annular permanent magnets attached to the active-end platen, passing through four fixed coils of wires (torsional coils). Sinusoidal rotational motion was induced in the active-end platen using a function generator acting through an Agilent Model 33502A power amplifier. To measure input voltage, a FLUKE Model 8010A digital multimeter was used.

An accelerometer (Columbia Research Laboratories, Inc. 200-1-H) was mounted in the active-end platen to measure the response of the active-end platen system, which consists of the active-end platen, permanent magnet and accelerometer. The accelerometer output was channelled to a Columbia Research Laboratory Model 4102 charge amplifier and displayed on a Philips Model PM3335 oscilloscope. The mass and rotational inertia of the active-end platen system was pre-determined from the calibration of the apparatus. The passive-end platen was rigidly fixed to the base of the apparatus. The active-end platen system acts as a rigid mass attached to the specimen, hence forming a one degree-of-freedom system. In order to minimize the effects of surrounding disturbances during experiments, a rubber mat of 3mm thickness was placed at the base of the resonant column to serve as a shock absorber.

As mentioned previously in Section 1.4, one of the current research objectives involves the verification of pore pressure build-up after an episode of small strain cyclic loading. To accomplish this, an additional mid-plane pore pressure transducer (Figure 3.10) was attached to the specimen for entire duration of the resonant column tests involving pore pressure measurements. This pressure transducer was connected to a separate multimeter to measure pore pressure variations during and after torsional cyclic shearing.

3.4 Equipment Setup and Experimental Procedures

3.4.1Undrained Cyclic Triaxial Tests

The GDS ELDyn and GDS DYNTTS systems (Figures 3.5 and 3.8) were used to perform strain-controlled cyclic loading tests. All tests were conducted in accordance with the ASTM D3999-91 (2003) standard. After extracting the preconsolidated test specimen from the steel tube, filter paper and porous stones were placed at both ends of the specimen. Porous stones were provided at both ends of the specimen to allow double drainage. Side filter drains were used for all Upper Marine Clay specimens to accelerate the consolidation process. In contrast, Kaolin Clay specimens do not require side filter drains due to its relatively higher permeability compared to the former (see Tables 3.1 and 3.2). The specimen was then placed in a rubber membrane to prevent air diffusion at the cylindrical surface, before being placed in the triaxial cell. A tight seal around the membrane at each end was achieved with 3 O-rings. For the mid-plane pore pressure transducer, vacuum grease was applied to prevent air ingress from the cell chamber to the soil specimen.

Since the cyclic loading involves full displacement or strain reversal, the equipment must be capable of applying tensile or extensional loading to the specimen. To facilitate the extension phase, an extension top cap and rubber sleeve attachment were fitted to the actuator and soil specimen respectively, as shown on the inset in Figure 3.5. Before the test begins, the extension top cap was lowered to fit into the rubber sleeve without compressing the specimen. The base of the extension top cap was maintained at atmospheric pressure. Hence the rubber sleeve forms a tight seal around the extension top cap due to the pressure difference. During the extension phase of the test, the suction which developed within this sleeve assembly maintained the coupling between the specimen and the actuator.

Prior to cyclic loading, all specimens were saturated and consolidated in the triaxial cell. Microscopic air pockets that might have been trapped within the specimen during preparation were dissolved into solution by the application of 500kPa back pressure. The use of de-aired water also encouraged dissolution of air pockets and enhances saturation of the specimens. During saturation, the cell pressure was set slightly higher than the back pressure so as to maintain a small positive effective stress of 5kPa in the soil specimen. The pore pressure coefficient B was calculated for every 50kPa increments of cell and back pressures, and was checked to be equal to or

greater than 0.95 for the sample to be considered saturated. For the cyclic triaxial tests performed to date, the pore pressure coefficient B fell within 0.98 ± 0.01.

When the specimen was deemed to be fully saturated, the consolidation phase was carried out with the cell and back-pressures set to the prescribed levels to achieve the desired consolidation stress. The drainage valves were then opened to permit the outflow of water from the specimen as the specimen consolidates. Upon consolidation to the desired effective stress level, the specimens were then ready for cyclic shearing. The drainage valves were closed to prevent water outflow during the cyclic shearing stage, thus ensuring undrained conditions within the specimen.

The main limitation of the cyclic triaxial test is its limited accuracy at very small strain amplitudes. The strain in the specimen was calculated based on the applied amplitude of cyclic loading defined by user. This gives an average strain value, while in reality the specimen may not compress or extend uniformly. Therefore the calculated initial shear modulus obtained in cyclic triaxial test tends to be an underestimation of the true small-strain shear modulus. Thus, for characterization of soil at strain amplitude less than 0.1%, other methods such as the resonant column test were required.

In addition to the limited accuracy of the cyclic triaxial setup at very small strain amplitudes, past researchers had highlighted potential errors in load measurements and axial displacement measurements (Baldi et al. 1988; Wood 1982). For triaxial setup that incorporates an external load cell, accuracy in load measurements can be compromised even if a low friction piston is used (Baldi et al. 1988). As both cyclic triaxial systems in the current study (i.e. ELDyn and DYNTTS) use internal load cells that are situated within the triaxial chambers, error in load measurements is minimized. In triaxial tests, specimen seating errors and misalignments between the top cap and load cell are known to lead to major errors in strain measurements (Baldi et al. 1988; Wood 1982). However, the issue of misalignment in the current triaxial setup is unlikely to occur since an extension sleeve is used for all tests to ensure that the top cap and load cell are rigidly coupled.

3.4.2 Resonant Column Tests

For the resonant column tests conducted, an air pressure controller was used to apply a constant cell pressure. Before the start of all experiments, a Hardy Portable Shaker

System Model HI-813 was used to calibrate the accelerometer together with the charge amplifier at a standard frequency of 100Hz. The same calibration was performed at the end of the test. For the charge amplifier with the accelerometer charge sensitivity, the output measured by the FLUKE Model 8010A digital multimeter is 1.218 ± 0.005 $Volts_{rms}$/g.

The clay specimens were prepared in the same way as the triaxial samples. The saturated and consolidated clay specimen was first seated on the bottom passive platen. Similar to the triaxial test setup, a rubber membrane was used to reduce air ingress into the sample. The top platen, together with a large circular magnet, was then adjusted to make contact with the upper end of the specimen. The height of the bearing shaft and spring was pre-adjusted so as to support the weight of the magnet and platen while ensuring proper contact. To ensure contact between the specimen and platens, quick dry adhesives were added to all contact surfaces during mounting of the specimen.

The procedures of obtaining the small-strain shear modulus (G_{max}) and damping ratio were based on the ASTM D4015-07 standard. The frequency of excitation is gradually increased from a low frequency of 1 Hz until resonance in the system, which comprises the specimen and the active-end platen system, is observed. The system resonant frequency is 90 degree out of phase with the torsional acceleration of the active-end platen system, as measured by the accelerometer. The system response is monitored by observing the Lissajous figure on an oscilloscope, with the response signal from the accelerometer (i.e. measured feedback acceleration of the sample) plotted against the input signal from the function generator (i.e. input sinusoidal voltage). Resonance occurs when the major axis of the elliptic figure formed is exactly vertical and the amplitude of the response signal reaches a peak. The amplitude decay method is used to obtain the damping ratio. In this method, the excitation source is cut off while the system is vibrating at its resonance frequency. The decay curve of the response signal is captured and damping ratio is calculated based on the free vibration.

The calibration procedure for this resonant column apparatus is described in Appendix A. From the ASTM D4015-07 standard, the shear modulus, torsional shear strain and damping ratio can be calculated as follows:

$$G = \rho(2\pi L)^2\left(f_T / F_T\right) \qquad [3.1]$$

Where:

G = Shear modulus,

ρ = Soil mass density,

L = Specimen length,

f_T = System resonant frequency (to be determined when testing the soil specimen),

F_T = Dimensionless frequency factor (which may be determined using the FORTRAN code provided in ASTM D4015-07).

It should be noted that the dimensionless frequency factor (F_T) is dependent on active-end inertia factor (T_T), passive-end platen inertia ratio (P), apparatus damping factor (ADF_T) and specimen damping ratio (D). Since passive-end platen is rigidly fixed, the passive-end inertia ratio, $P = \infty$. For torsional motion, the apparatus damping factor (ADF_T) is given by:

$$ADF_T = ADC_{OT} / (2\pi f_T J) = (0.0341 kgm^2 / s) / (2\pi f_T J) \qquad [3.2]$$

Where:

ADC_{OT} = Apparatus damping coefficient,

J = Rotational inertia of specimen.

The torsional shear strain (γ) is then calculated as:

$$\gamma = (RCF)(RTO)(SF)d / (2.5L) \qquad [3.3]$$

Where:

RCF = Displacement calibration factor (provided in Appendix A),

RTO = Rotational transducer output ($Volts_{rms}$),

SF = Strain factor (may be determined from FORTRAN code),

d = Specimen diameter.

Finally, the damping ratio is given by:

$$D = [\delta_S (1 + S) - S\delta_S] / (2\pi) \qquad [3.4]$$

Where:

δ_S = System logarithmic decrement from free vibration decay (Equation 3.5),

S = System energy ratio (Equation 3.6).

$$\delta_S = (1/n)\ln(A_1 / A_{n+1}) \quad [3.5]$$

Where:

n = Number of free vibration cycles (≤ 10),

A_1 = Amplitude of vibration for first cycle after power is cut off,

A_{n+1} = Amplitude of vibration for $(n+1)$th cycle of free vibration.

$$S = (J_A / J)(f_{OT} F_T / f_T)^2 \quad [3.6]$$

Where:

J_A = Rotational inertia of active-end platen system,

f_{OT} = Apparatus resonant frequency.

According to ASTM D4015-07, since the active-end platen is not restrained by a spring, the apparatus resonant frequency (f_{OT}) equals zero and consequently the system energy ratio (S) is also zero. Hence, the damping ratio is given by:

$$D = \frac{\delta_S}{2\pi} = \frac{(1/n)\ln(A_1 / A_{n+1})}{2\pi} \quad [3.7]$$

The main limitation of the resonant column is its high sensitivity to small vibrations, which had been observed to distort the Lissajous curves significantly as well as the free vibration response of the specimen during the decay stage. As an additional measure to minimize the effect of vibrations, all tests were conducted in the early mornings (between 2am to 4am) when external activities are minimal.

Table 3.1 Properties of remoulded Kaolin Clay specimens.

Properties	Sample Size	Mean Value	Standard Deviation
Compression index	3	0.236	0.012
Swelling index	3	0.040	0.009
Specific gravity	7	2.637	0.001
Atterberg Limits			
Plastic limit	20	35.3%	0.5%
Liquid Limit		76.5%	0.9%
Plasticity Index		41.2%	
Particle Size Distribution (Refer to Figure 3.1):			
Clay	3	96.9%	0.9%
Silt		3.1%	0.9%
Sand		0%	0%
Permeability			
Permeability (m/s)	**Consolidation Pressure**		
	50kPa	**100kPa**	**200kPa**
	7.16×10^{-8}	5.33×10^{-8}	1.73×10^{-8}

Table 3.2 Properties of remoulded Singapore Upper Marine Clay specimens.

Properties	Sample Size	Mean Value	Standard Deviation
Compression index	3	0.307	0.011
Swelling index	3	0.035	0.005
Specific gravity	7	2.657	0.036
Atterberg Limits			
Plastic limit	20	30.3%	1.2%
Liquid Limit		83.5%	1.5%
Plasticity Index		53.2%	
Particle Size Distribution (Refer to Figure 3.2):			
Clay	9	84.7%	2.5%
Silt		6.0%	1.7%
Sand		9.3%	2.4%
Permeability			
Permeability (m/s)	**Consolidation Pressure**		
	50kPa	**100kPa**	**200kPa**
	9.43×10^{-10}	9.68×10^{-11}	1.93×10^{-11}

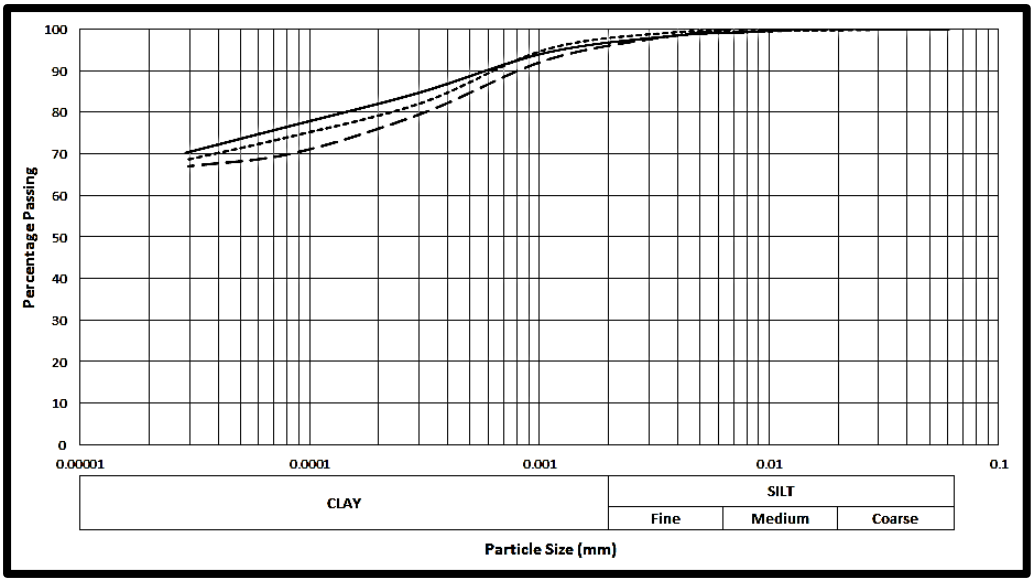

Figure 3.1 Particle size distribution curves for remoulded Kaolin Clay specimens.

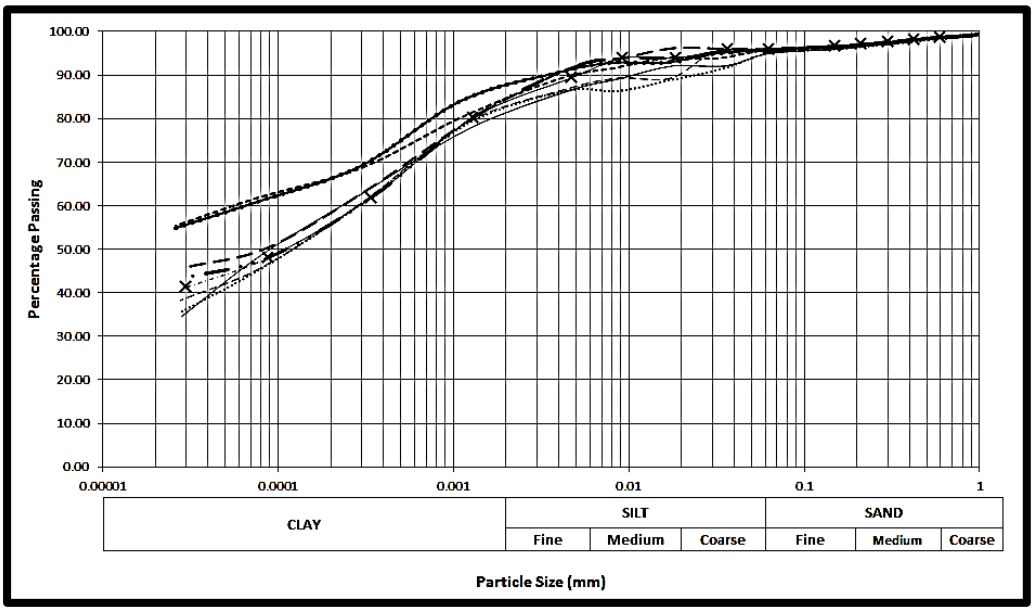

Figure 3.2 Particle size distribution curves for remoulded Singapore Upper Marine Clay specimens.

Figure 3.3 Mixing of Kaolin Clay and Upper Marine Clay slurries.

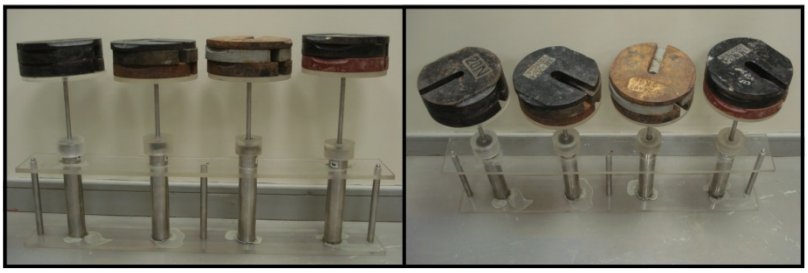

Figure 3.4 Setup for pre-loading of Kaolin Clay and Upper Marine Clay slurries.

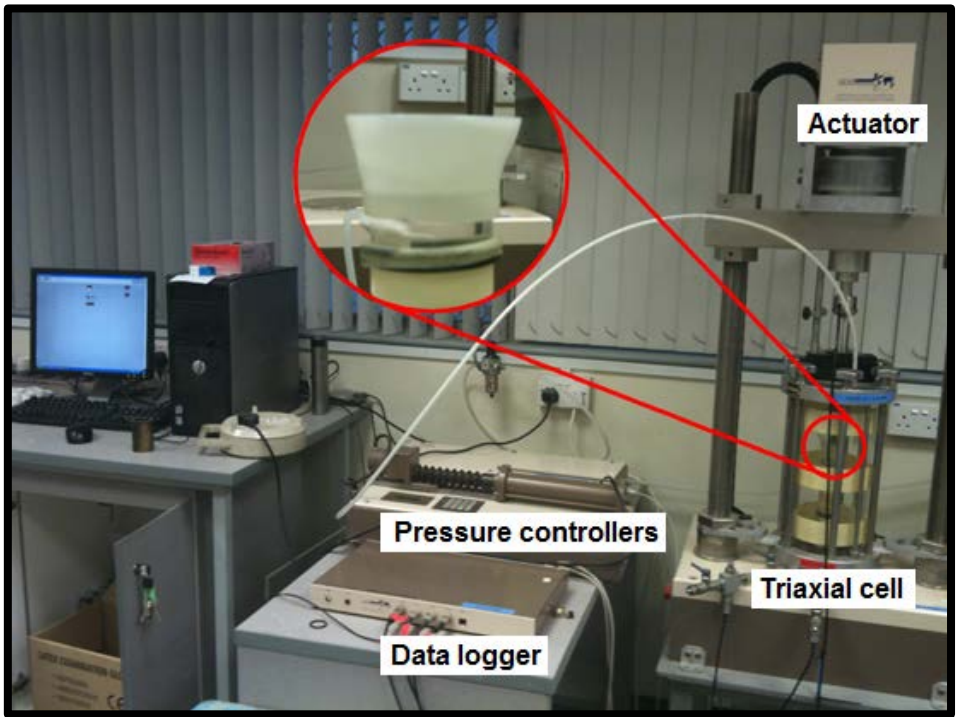

Figure 3.5 GDS ELDyn Triaxial System setup (rubber sleeve attachment for tensile loading is highlighted).

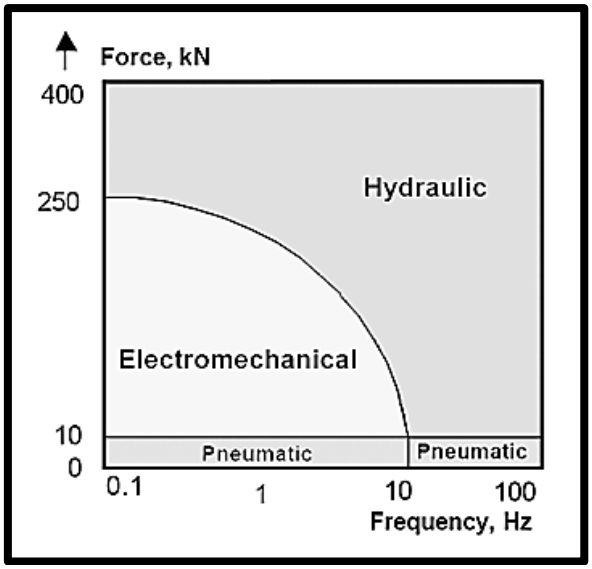

Figure 3.6 Recommended control systems overview (Edited from: Menzies et al. 2002).

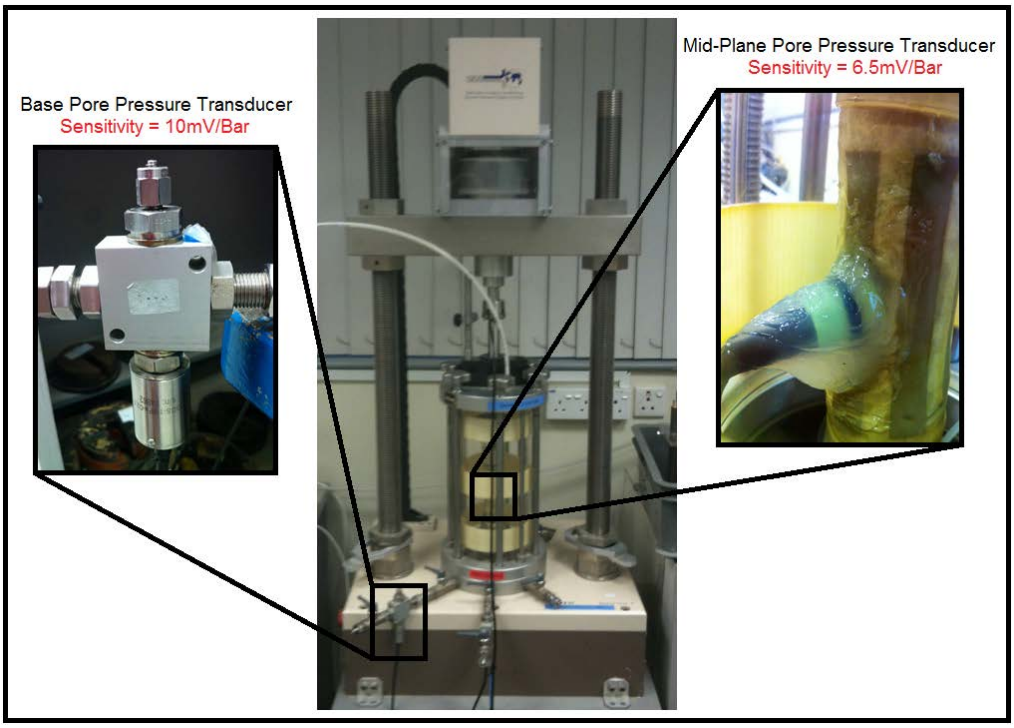

Figure 3.7 GDS mid-plane and external base pore pressure transducers used in cyclic triaxial setup.

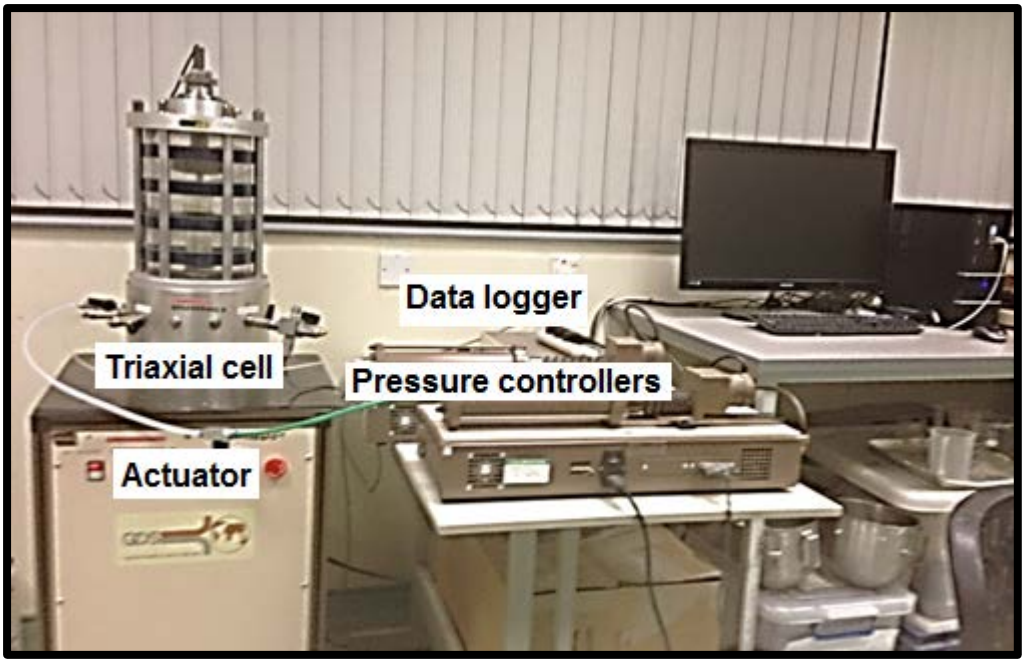

Figure 3.8 GDS DYNTTS setup.

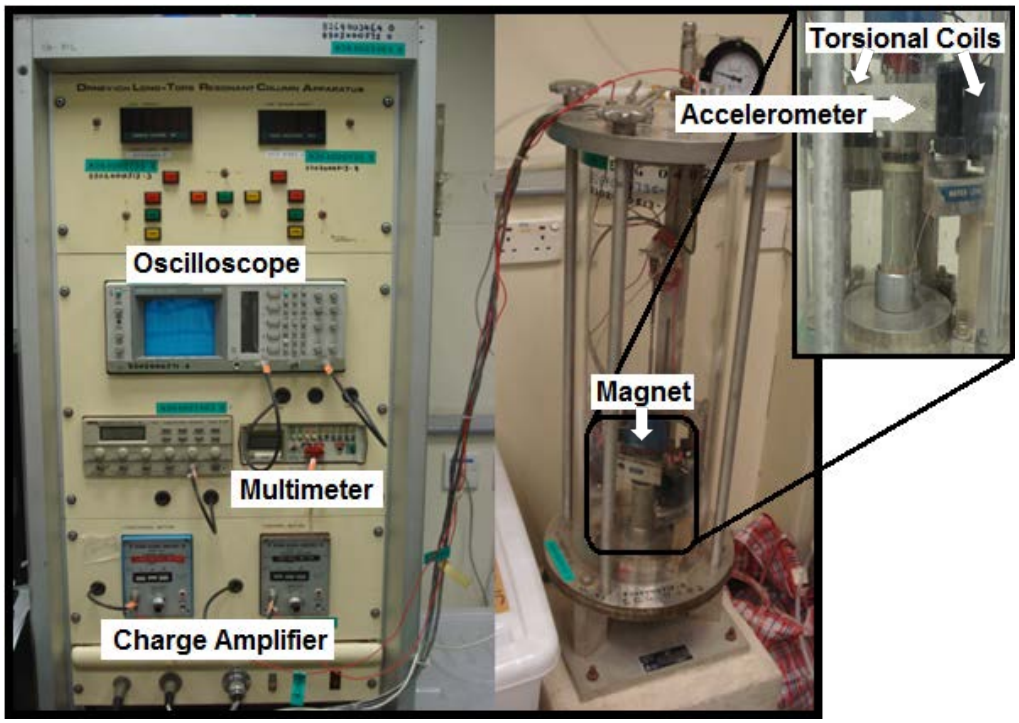

Figure 3.9 Drnevich Long-Tor resonant column setup (signal generator and signal amplifier are externally connected to the system).

Figure 3.10 Mid-plane pore pressure transducer in resonant column setup.

Chapter 4 – Effect of Cyclic Strain Rate on Pore Pressure Measurement

4.1 Introduction and Overview

The effect of cyclic strain rate on pore pressure measurement has already been highlighted in the previous chapters. The foregoing discussion shows that some of the issues surrounding pore pressure equilibration and measurement have still not been fully resolved. This chapter presents a study of this problem, leading to some recommendations on cyclic strain rate required for pore pressure equilibration.

A series of two way strain-controlled undrained cyclic triaxial tests were performed on remoulded specimens of normally consolidated kaolin and Marine Clay, 38mm diameter by 76mm height. As mentioned earlier in Section 3.4.1, both mid-plane and base pore pressure transducers (PPT) were used during cyclic tests and pore pressure equilibration was considered to be achieved when both transducers produce similar excess pore pressure measurements. Figure 4.1 shows typical plots of pore pressure measurements from both transducers for equilibrated and non-equilibrated cases. In non-equilibrated cases, the excess pore pressure measured at mid-plane is found to be consistently higher than that at the base. This agrees with several past research findings (Hirschfeld 1958; Bishop et al. 1962; Wood 1982; Germaine and Ladd 1988; Zergoun and Vaid 1994) as well as the notion that excess pore pressures are largely generated near the central segment of the specimen.

Table 4.1 presents the matrix of tests conducted to examine pore pressure equilibration. Each test was conducted on a virgin specimen. Test data were recorded in 2-second intervals. The parameters varied in the cyclic triaxial tests were the preconsolidation pressure (50, 100, 200kPa) and loading periods. All specimens were subjected to 30 cycles of sinusoidal loading with constant displacement amplitude of 1mm, which corresponds to 1.4% strain. Preliminary tests indicated that most of the excess pore pressures were generated in the initial ~20 cycles; hence 30 cycles are sufficient to capture much of the excess pore pressure generated. According to Díaz-Rodríguez and López-Molina (2008), significant pore pressure generation occurs when the applied strain exceeds their proposed degradation cyclic strain threshold of 0.5% to 1%, Figure 2.9. Hence, the applied strain amplitude of 1.4% is sufficient to ensure pore pressure generation during cyclic loadings.

In Table 4.1, the maximum and average strain rates were tabulated based on the maximum rate of sinusoidal strain applied and the weighted mean of the applied sinusoidal strain rate respectively as shown in Figure 4.2. Mathematically, the maximum and average loading rates can be expressed as follows:

$$\dot{\varepsilon}_{\max} = \frac{A}{L_C}\left(\frac{2\pi}{T}\right) \qquad [4.1]$$

$$\dot{\varepsilon}_{avg} = \frac{A}{L_C}\left(\frac{4}{T}\right) \qquad [4.2]$$

Where:

$\dot{\varepsilon}_{\max}$ = Maximum strain rate (s^{-1}),

$\dot{\varepsilon}_{avg}$ = Average strain rate (s^{-1}), obtained by dividing the strain amplitude by the quarter-period.

A = Applied displacement amplitude (mm) (as defined in Figure 4.2),

L_C = Specimen length after consolidation (mm),

T = Cyclic period (s).

4.2 Strain Rate Effects

4.2.1 Effects of Strain Rate after Achieving Pore Pressure Equilibration

Figure 4.3 presents the mid-plane excess pore pressure measurements for the various undrained cyclic triaxial tests performed on specimens consolidated to different preconsolidation pressures (p_c'). For both types of clay specimens subjected to the same preconsolidation pressure, the mid-plane pore pressure measurements are generally lower when higher strain rates (i.e. shorter cyclic periods) were used. Once the applied strain rate becomes sufficiently slow for pore pressure to equalize, the mid-plane pore pressure measurements converge. Thus, upon attaining pore pressure equilibration, strain rate effects on the amount of excess pore pressure measured become negligible. Based on Figure 4.3, the cyclic period required for pore pressure equilibration within Marine Clay specimens is consistently higher than that required for kaolin regardless of the preconsolidation pressure applied. For instance, a Marine Clay specimen consolidated to 200kPa requires 60 minutes for pore pressure equilibration while a kaolin specimen with the same stress history requires 12 minutes. One possible explanation to the significant disparity in the required cyclic periods is the difference in permeability of the two clays. The permeability of Marine Clay is at least two orders of magnitude smaller than that for kaolin (refer to Tables

3.1 and 3.2). Consequently, the required cyclic load period for pore pressure equilibration within Marine Clay specimens will be much longer than that for kaolin.

However, the disparities between the mid-plane pore pressure measurements for specimens with identical preconsolidation pressures subjected to different cyclic strain rates also implies that some time must elapse even before pore pressure within clay specimens can equilibrate radially to the mid-plane transducer. Therefore, despite previous postulations that pore pressure measurements at mid-plane are more likely to produce better quality data since the time required for pore pressure propagation to the mid-plane transducer is shorter than that for the end transducer (Yong and Townsend 1985), a minimum duration is still required to ensure radial equilibration. The mid-plane measurements for the specimens that had achieved pore pressure equilibration were then normalized by the corresponding preconsolidation pressures (Figure 4.4). Under this normalized plot, the mid-plane measurements converge and lie within the same bandwidth for both kaolin and Marine Clay specimens.

In order to investigate the inter-cycle pore pressure measurements, the residual excess pore pressure at the end of each cycle (i.e. excess pore pressure at end of cycle minus excess pore pressure at start of cycle) was tabulated for each cycle and presented in Figure 4.5. For both kaolin and Marine Clay specimens subjected to the same preconsolidation pressure, but tested under different periods, the disparity in net increment of excess pore pressure measurements only occurs in the first load cycle. This can be attributed to the phenomenon that most of the clay deformations and pore pressures are generated within the first load cycle and gradual strain-hardened behaviour can be observed once the applied strain exceeds the degradation cyclic strain threshold (Diaz-Rodriguez and Lopez-Molina 2008). This further necessitates the need for pore pressure equilibration especially at the start of cyclic loading.

Figures 4.6 to 4.8 illustrate the normalized stress plots and stress-strain relationships obtained during the cyclic tests. The deviator and mean effective stresses are normalized against the isotropic preconsolidation pressure, p_c', for ease of comparison between specimens subjected to different stress histories. For all normally consolidated kaolin specimens subjected to different preconsolidation pressure (i.e. 50kPa, 100kPa and 200kPa), upon achieving pore pressure equalization, further increase in cyclic periods (i.e. decrease in strain rate) had insignificant influence on the normalized stress paths and stress-strain plots. This implies that the

effective stress path and stress-strain behaviour of clays are largely rate-independent when pore pressures are homogenous across the specimens. This rate-independence cyclic behaviour is consistent for normally consolidated Marine Clay specimens as well.

In cases when pore pressure equalization did not occur, discrepancies in the normalized effective stress paths are evident. These erroneous stress paths deviate from those obtained from undrained monotonic triaxial compression on equivalent specimens (i.e. without cyclic loading Figure 4.6). The effect of non-uniform pore pressures on the normalized stress-strain plots is less evident. The main discrepancy lies in the first load cycle, which is consistent with the observed trend for the net increment of excess pore pressure measurements. For instance, based on Figure 4.7(a)(ii), when the applied period is 86% shorter than the required period (i.e. 14 minutes in this case) for pore pressure equilibration, a higher initial shear modulus is observed. This leads to an abrupt change in modulus, labelled Point A, within the first load cycle. In order to validate if the abrupt change can be attributed to internal migration of pore pressure within the specimen during equilibration, one additional undrained cyclic test was performed.

4.2.2 Abrupt Change in Initial Shear Modulus due to Non-homogenous Pore Pressures

An additional test was conducted on a Marine Clay specimen normally consolidated to 100kPa. Cyclic shearing (Amplitude = 1mm, Period = 2min) was applied until the normalized stress-strain curve reaches Point A (Figure 4.9), corresponding to 0.26% strain. The undrained cyclic test was then paused while keeping the cell and back pressures constant. The applied strain is kept at 0.26% without further increment. Pore pressure at mid-plane and base locations were sampled at 2-second intervals. From Figure 4.9, internal migration of pore pressure within the specimen had occurred because the base pore pressure measurement was observed to gradually increase with time until it converged with the mid-plane pore pressure measurement. Hence, the aforementioned abrupt change in initial shear modulus is due to pore pressure equilibration within non-homogenous specimens.

4.2.3 Errors Associated with Fast Cyclic Strain Rates

As highlighted previously, cyclic frequencies used in some previous studies fall in the range of 0.05Hz to 2Hz (e.g. Ansal et al. 2001; Zhou and Gong 2001; Moses et al.

2003; Matesic and Vucetic 2003; Yamada et al. 2008; Banerjee 2009). Errors may be generated as a result of the relatively high strain rates. In order to understand the error possibly associated with using such fast cyclic loading rates, two additional undrained cyclic tests were conducted on Marine Clay and kaolin specimens at a cyclic frequency of 0.05Hz. Both clay specimens were consolidated to an effective confining pressure of 200kPa. Figures 4.10 and 4.11 summarize the mid-plane pore pressure measurements, effective stress paths and stress-strain plots obtained for the two specimens. Cyclic results of specimens with the same stress history (i.e. p_c' = 200kPa) undergoing slow undrained cyclic shearing where pore pressure equilibration was achieved are included for comparison purpose.

Table 4.2 summarizes the key errors associated with using cyclic frequency of 0.05Hz on Marine Clay and kaolin specimens. When a high cyclic frequency of 0.05Hz was applied, the excess pore pressure measurements were considerably underestimated by ~75% (102kPa) and 41% (62kPa) for Marine Clay and kaolin specimens respectively. Consequently, the effective stress paths of the high frequency tests lie very closely with the corresponding total stress paths (Figures 4.10b and 4.11b) and decrease in mean effective stresses is grossly underestimated. In contrast, the percentage errors in maximum deviator stresses for the first load cycle were much less, typically ~11% for Marine Clay and ~5% for kaolin. This indicates that pore pressure non-uniformity is likely to affect the effective stress path much more significantly than the stress-strain curve. This may explains why limited or negligible frequency effects on shear modulus and damping could be observed in past experimental investigations using relatively fast cyclic loading frequencies (e.g. Zanvoral and Campanella (1994) used 0.01 to 1Hz; Shibuya et al. (1995) used 0.005Hz to 0.1Hz; Banerjee (2009) used 0.05Hz to 5Hz).

4.3 Correlations for Strain Rate

This section discusses possible modifications to the specifications stipulated in BS1377:1990 and Eurocode ISO/TS 17892:2004 for undrained monotonic triaxial compression tests to cater to cyclic loading. For ease of comparison, all strain rates are expressed in %/min in this section.

4.3.1 BS1377:1990

BS1377's specifications (Equation 2.1) can be re-written in the form,

$$\dot{\varepsilon}_{BS} = \frac{\varepsilon_f}{t_f} \times 100\% \qquad [4.3]$$

Where:

$\dot{\varepsilon}_{BS}$ = Maximum strain rate,

ε_f = Significant strain interval,

t_f = Significant testing time (min) (≥ 2 hours).

This definition of significant testing time will remain the same as follows:

$$t_f = F \times t_{100} \qquad [4.4]$$

Where:

F = Coefficient dependent on the drainage conditions and the type of compression test (i.e. undrained or drained) (refer to Table 2.2),

t_{100} = Projected time required for 100% consolidation, to be determined using square-root time method defined in BS1377 (refer to Figure 2.5).

In BS1377, significant strain interval is a user-defined parameter, depending on the strain increment over which pore pressure equilibration is required. For cyclic triaxial tests, this significant strain interval will herein be defined similarly so that it depends on the number of user-defined points per cycle required for pore pressure equilibration. For instance, if the user specified 5 points per cycle required for equilibration, the significant strain will be the strain interval between adjacent points, i.e. strain amplitude (A) as shown in Figure 4.12.

Using Equations 4.3 and 4.4, the recommended strain rates ($\dot{\varepsilon}_{BS}$) were tabulated for every clay specimen with the number of equilibration points varying from 5 to 500. A comparison between the fastest experimental average strain rates for specimens achieving pore pressure equalization and their corresponding BS1377-recommended strain rates are shown in Figure 4.13. From the current results, BS1377 maximum strain rates for pore pressure equilibration are observed to be at least one order in

magnitude slower than the acceptable maximum cyclic strain rates. This difference increases with decreasing preconsolidation pressure for both clay types. Thus, the preconsolidation pressure shall be used to correlate the experimental and BS1377 strain rates.

In order to modify BS1377 to include specifications for cyclic loading tests, the experimental strain rate is normalized against the corresponding BS1377 strain rate and plotted against the preconsolidation pressure for each specimen (Figure 4.14). As this Figure shows, a lower bound can be drawn underlying the lowest points for which pore pressure equilibration had been achieved. All the lower bounds can be fitted by an equation of the form

$$\frac{\dot{\varepsilon}_{cyclic}}{\dot{\varepsilon}_{BS}} = C_{BS}\left(\frac{p_c'}{p_r'}\right)^{-1.492} \qquad [4.5]$$

Where:

$\dot{\varepsilon}_{cyclic}$ = Experimental cyclic strain rate for pore pressure equilibration,

$\dot{\varepsilon}_{BS}$ = BS1377 strain rate tabulated from Equation 4.3,

C_{BS} = Parameter related to the number of points required for equalization (N),

p_c' = Preconsolidation pressure,

p_r' = Reference pressure for consistency in units = 1kPa.

As shown in Figure 4.15, the parameter C_{BS} can be correlated to the number of points required for equalization (N) via the relation

$$C_{BS} = 10742(N) \qquad [4.6]$$

4.3.2 Eurocode ISO/TS 17892:2004

TS17892 specifications for triaxial monotonic compression tests can also be modified in a similar way as the BS1377 specifications. From Equation 2.3, the strain rate $\dot{\varepsilon}_{ISO}$ (in %/min) can be expressed as

$$\dot{\varepsilon}_{ISO} = \frac{\varepsilon_{1f}}{F \times t_{50}} \times 100\% \qquad [4.7]$$

Where:

ε_{1f} = Significant strain interval,

F = Factor depending on type of test and drainage conditions (refer to Table 2.3),

t_{50} = Projected time required for 50% consolidation, to be determined based on the Casagrande's logarithmic time method.

Figure 4.16 shows a comparison between the fastest experimental average strain rates for specimens achieving pore pressure equalization and their corresponding TS17892-recommended strain rates. Similar to BS1377 strain rates, the recommended TS17892 strain rates are at least one order difference in magnitude from the experimental rates and this difference increases with decreasing preconsolidation pressure for both clay types. However, the magnitude of the difference is clearly less than that with the BS1377. This indicates that the BS1377 is likely to be conservative for monotonic triaxial tests. By applying the same procedure to TS17892 (Figure 4.17), the cyclic strain rate is proposed as follows:

$$\frac{\dot{\varepsilon}_{cyclic}}{\dot{\varepsilon}_{ISO}} = C_{ISO}\left(\frac{p_c'}{p_r'}\right)^{-1.199} \qquad [4.8]$$

Where:

$\dot{\varepsilon}_{cyclic}$ = Experimental cyclic strain rate for pore pressure equilibration,

$\dot{\varepsilon}_{ISO}$ = Eurocode strain rate tabulated from Equation 4.7,

C_{ISO} = Parameter related to the number of points required for equalization (N),

p_c' = Preconsolidation pressure,

p_r' = Reference pressure for consistency in units = 1kPa.

From Figure 4.18,

$$C_{ISO} = 1352(N) \qquad [4.9]$$

Comparison of Equations 4.6 and 4.9 shows that C_{ISO} is much smaller than C_{BS} indicating that the TS17892 specified rates are much closer to the observed acceptable rates than the BS1377, albeit still much lower than the observed acceptable cyclic rates.

4.4 Applicability of Proposed Correlations for Different Strain Amplitudes and Stress Histories

Based on the above Section 4.2, the proposed cyclic strain rates corresponding to BS1377 and TS17892 are:

$$\frac{\dot{\varepsilon}_{cyclic}}{\dot{\varepsilon}_{BS}} = 10742N\left(\frac{p_c'}{p_r'}\right)^{-1.492} \qquad [4.10]$$

$$\frac{\dot{\varepsilon}_{cyclic}}{\dot{\varepsilon}_{ISO}} = 1352N\left(\frac{p_c'}{p_r'}\right)^{-1.199} \qquad [4.11]$$

As a check on the applicability of Equations 4.10 and 4.11 to different strain amplitudes, additional undrained triaxial tests were performed on Marine Clay specimens with cyclic amplitudes varying from 0.5mm to 3mm (i.e. ~ 0.7% to 4.2%strain) . The selected cyclic strain rates were consistent with the fastest experimental rates that had achieved pore pressure equilibration (Table 4.1). It should be noted that the selected strain rates are slightly faster than those tabulated from Equations 4.10 and 4.11. This means that if pore pressure equilibration was achieved at the selected strain rate, pore pressure equilibration will definitely be attained at the slower recommended strain rates. In addition, the applicability of the two equations on overconsolidated specimens was verified as well. Table 4.3 provides a summary of the test conditions. The number of points required for equalization was defined as 5 points (i.e. peak-to-peak).

From Table 4.3, pore pressure equalization was achieved for all of the 7 additional tests. Typical plot of the mid-plane and base excess pore pressure measurements for normally consolidated and overconsolidated specimens with pore pressure equalization is illustrated in Figure 4.19. Although pore pressure equilibration was specified to be required at the peak compression and extension strains (i.e. N = 5 points), both mid-plane and base transducer recorded almost identical values at every 2s data interval with a maximum pressure difference of $\pm$ 0.9kPa for all specimens. This implies that pore pressure equalization can be reasonably achieved by specifying 5 points required for equalization.

In conclusion, the proposed BS1377 and TS17892 strain rate specifications are conservative when applied to undrained cyclic triaxial testing. Equations 4.10 and 4.11 are applicable for both normally consolidated and overconsolidated (up to OCR

= 2) Marine Clay and kaolin specimens with preconsolidation pressures ranging 50kPa to 200kPa and within an applied strain range of 0.7% to 4.2%. It should be noted that the above recommendations are based on 38mm diameter by 76mm height specimens and larger specimens would require slower strain rates than those proposed in this section.

Table 4.1 Experimental matrix.

Clay	Effective Preconsolidation Pressure, p_c' (kPa)	Period (min)	Pore Pressure Equalization?	Average Loading Rate, $\dot{\varepsilon}_{avg}$ (%/min)	Maximum Loading Rate, $\dot{\varepsilon}_{max}$ (%/min)	BS √Time t_{100} (min)	Log Method t_{50} (min)
Kaolin Clay	50	1	No	0.543	0.853	51.84	19.05
	50	3	Yes	0.183	0.288	50.41	18.62
	50	5	Yes	0.108	0.170	45.70	16.60
	100	5	No	0.111	0.174	43.82	16.22
	100	8	Yes	0.069	0.108	52.56	18.62
	100	10	Yes	0.055	0.087	42.90	16.22
	200	10	No	0.055	0.087	43.03	16.22
	200	12	Yes	0.047	0.074	37.95	14.13
	200	15	Yes	0.037	0.058	56.25	14.79
Singapore Marine Clay	50	2	No	0.275	0.432	138.30	38.02
	50	5	No	0.112	0.175	155.00	41.69
	50	10	Yes	0.056	0.088	153.76	41.02
	100	2	No	0.278	0.437	114.06	33.88
	100	8	No	0.070	0.110	107.54	33.11
	100	14	Yes	0.040	0.062	111.51	33.50
	100	140	Yes	0.004	0.006	114.70	34.28
	200	20	No	0.028	0.043	106.09	30.20
	200	40	No	0.014	0.022	116.64	28.51
	200	60	Yes	0.009	0.014	116.64	28.51

Table 4.2 Errors associated with the use of high strain rates.

Parameters	Singapore Upper Marine Clay				Kaolin Clay			
	T = 60min	T = 20s	Difference	% Error	T = 12min	T = 20s	Difference	% Error
Δu after 30 cycles (kPa)	135.77	33.65	-102.12	-75	150.40	88.68	-61.72	-41
p' after 30 cycles (kPa)	64.23	166.35	102.12	159	49.60	111.32	61.72	124
Max. q for Cycle 1	81.06	89.67	8.62	11	90.33	95.15	4.82	5
Max. q for Cycle 30	58.52	70.63	12.10	21	69.99	58.83	-11.16	-16

Table 4.3 Additional Tests

Clay	p_c' (kPa)	OCR	Cyclic Amplitude (mm)	$\dot{\varepsilon}_{BS}$ (%/min)	$\dot{\varepsilon}_{ISO}$ (%/min)	$\dot{\varepsilon}_{avg}$ (%/min) used	Pore Pressure Equalization ?
Upper Marine Clay	100	1	0.5	0.039	0.016	0.040	Yes
	200	1	2	0.008	0.007	0.009	Yes
	200	1	3	0.008	0.007	0.009	Yes
Kaolin Clay	100	2	1	0.064	0.068	0.069	Yes
	200	2	1	0.023	0.028	0.047	Yes
Upper Marine Clay	100	2	1	0.039	0.016	0.040	Yes
	200	2	1	0.008	0.007	0.009	Yes

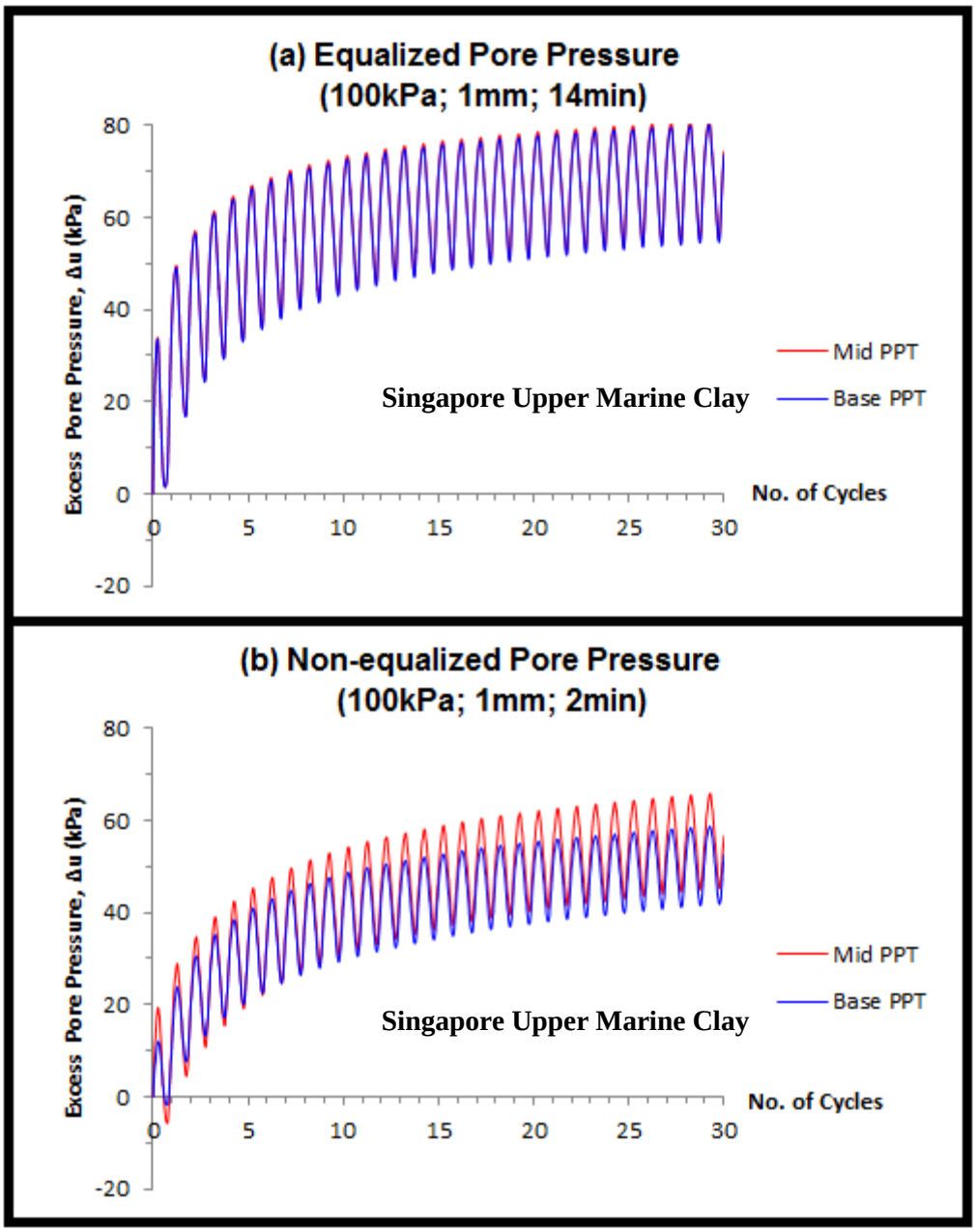

Figure 4.1 Typical plots of excess pore pressure measurements during (a) equilibration and (b) non-equilibration.

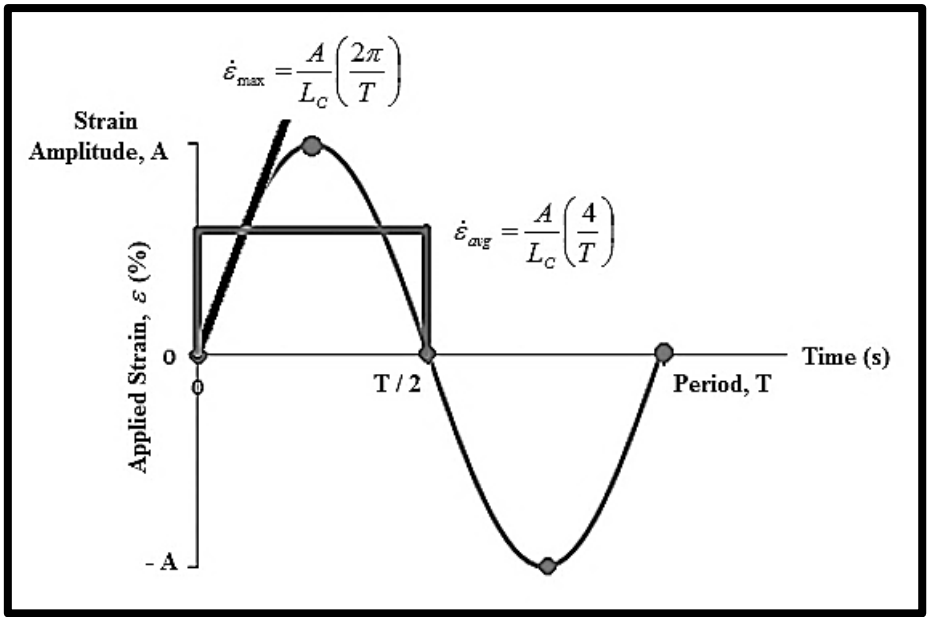

Figure 4.2 Definition of maximum and average strain rates in two-way strain-controlled tests.

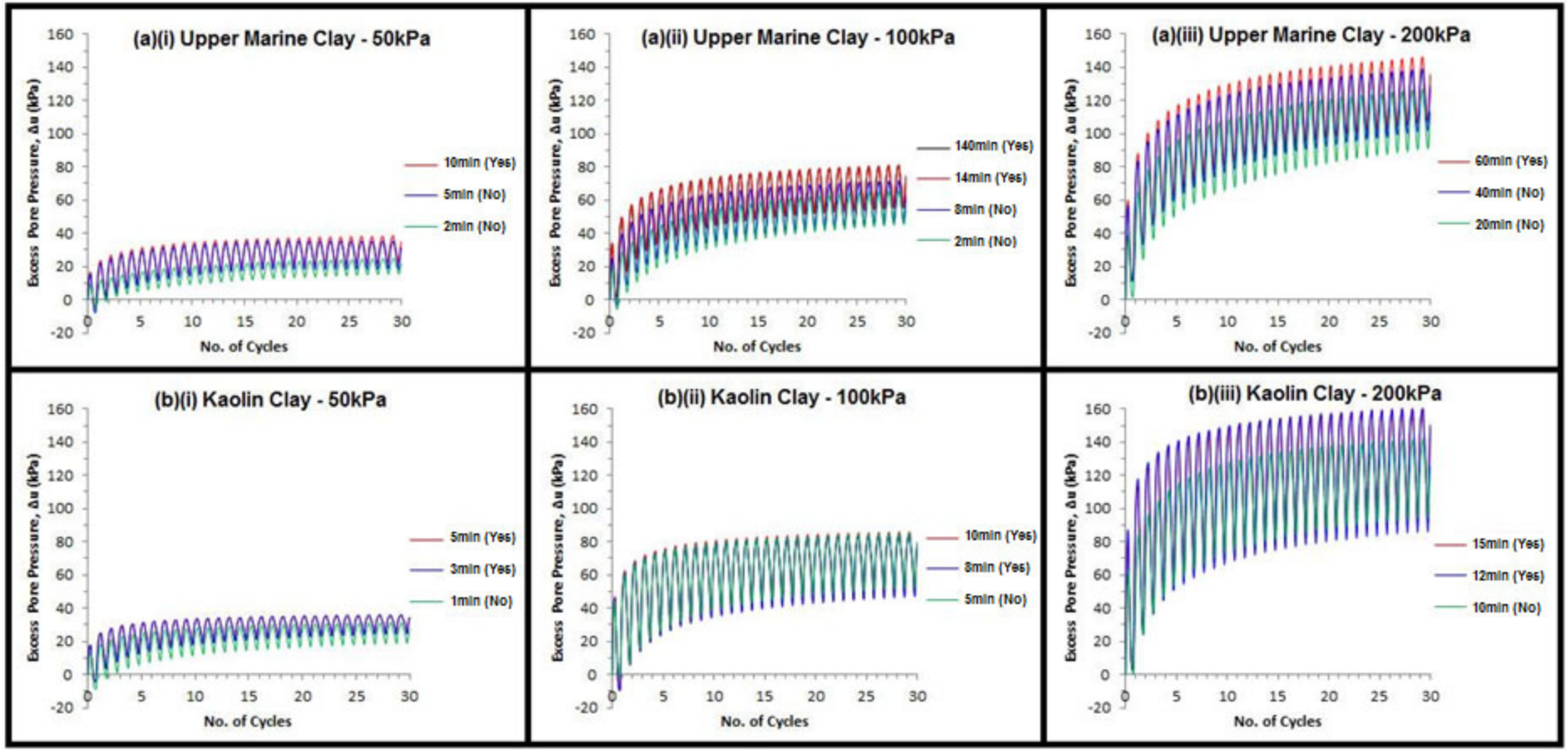

Figure 4.3 Mid-plane pore pressure measurements for (a) Singapore Upper Marine Clay and (b) Kaolin Clay.

[Yes = Pore pressure equalized; No = Pore pressure not equalized.]

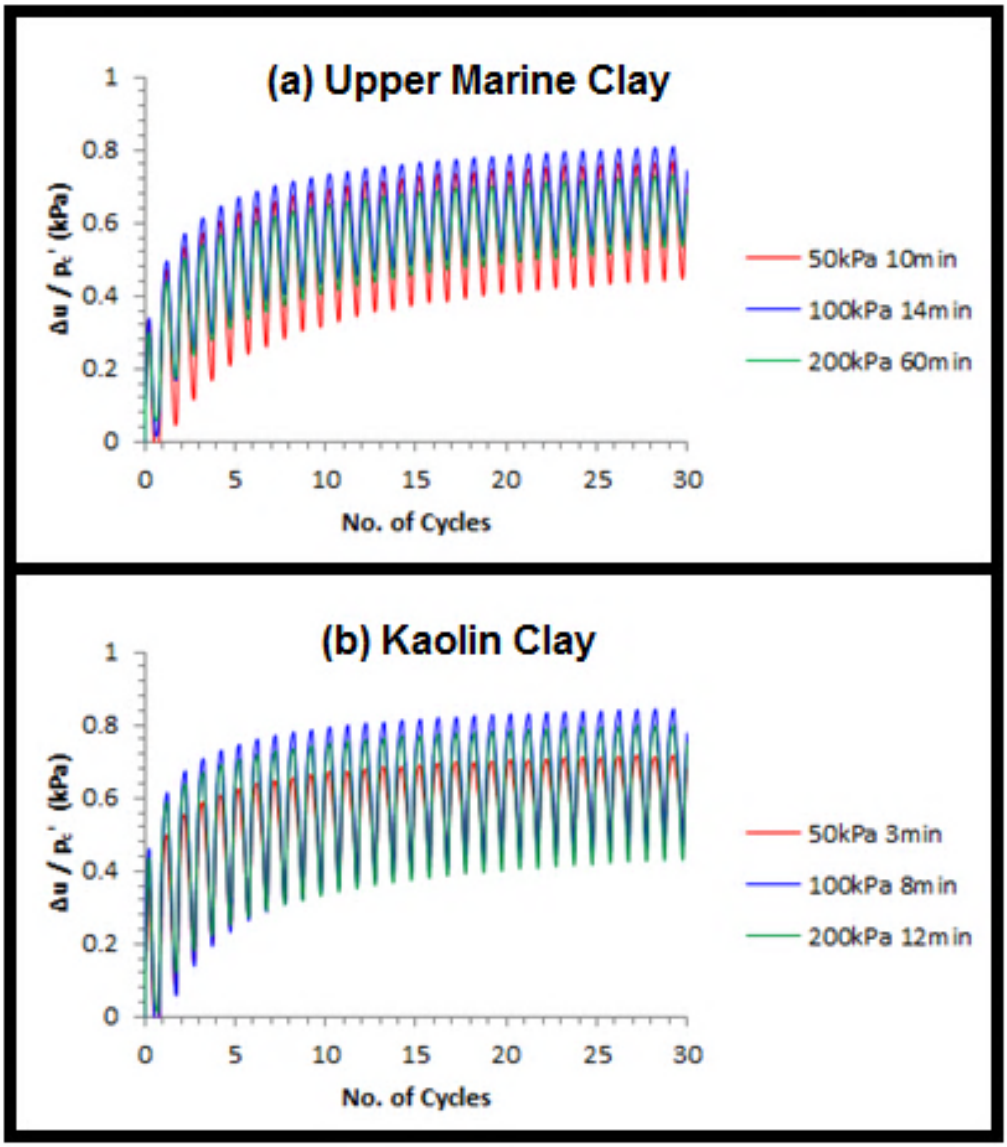

Figure 4.4 Equalized mid-plane excess pore pressure measurements for (a) Singapore Upper Marine Clay and (b) Kaolin Clay.

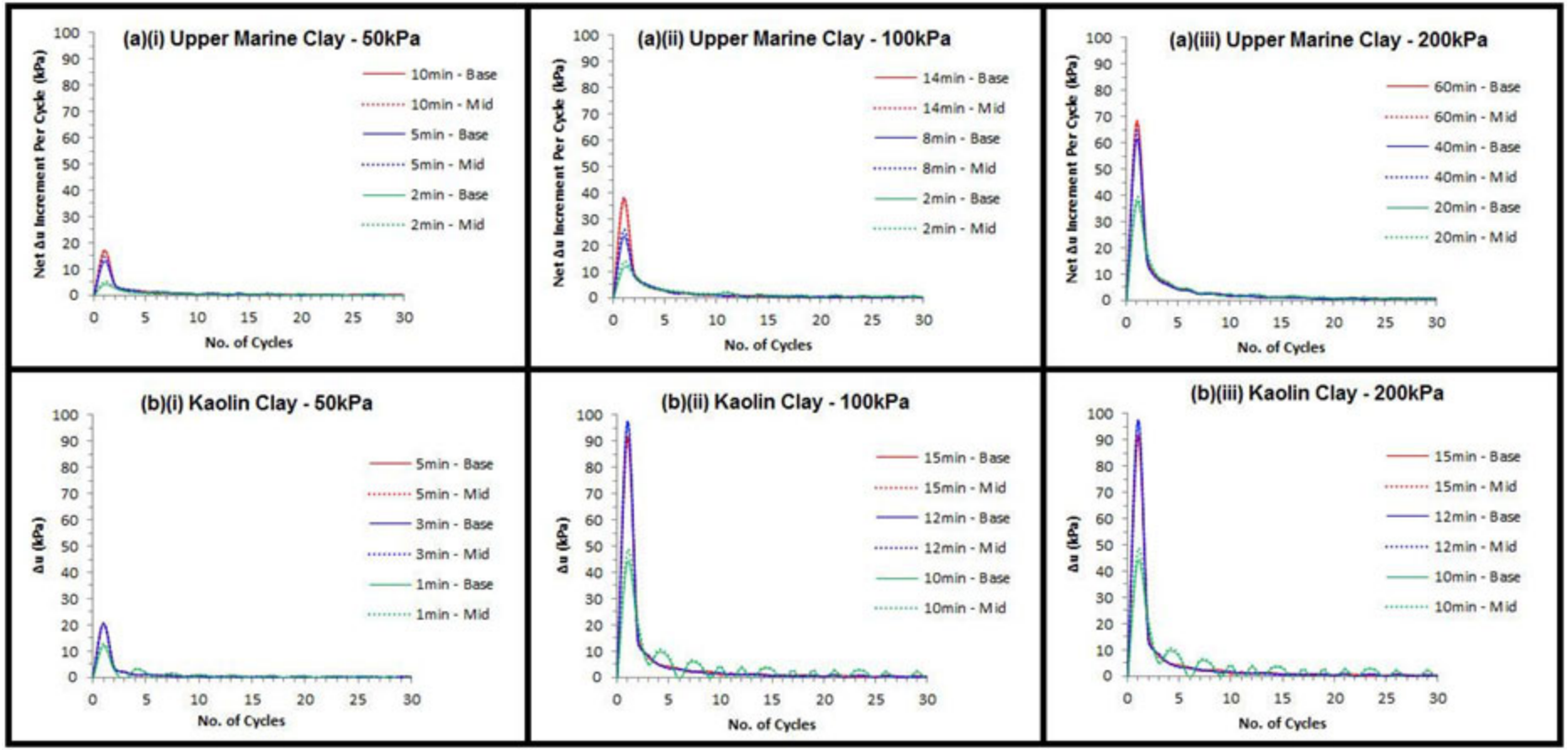

Figure 4.5 Net increment in excess pore pressure measurement per cycle for (a) Singapore Upper Marine Clay and (b) Kaolin Clay.

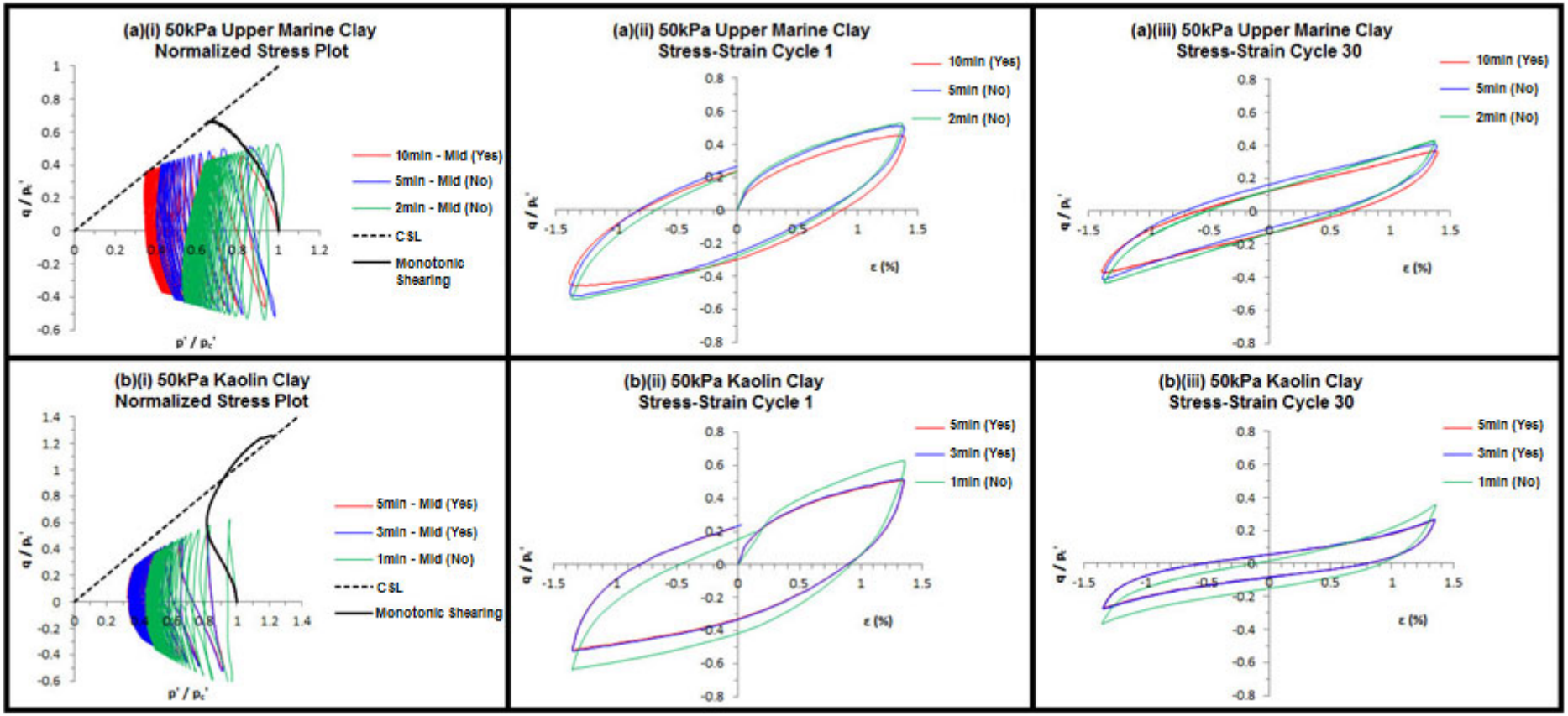

Figure 4.6 Normalized stress paths and stress-strain plots for p_c' = 50kPa specimens of (a) Singapore Upper Marine Clay and (b) Kaolin Clay.

[Yes = Pore pressure equalized; No = Pore pressure not equalized.]

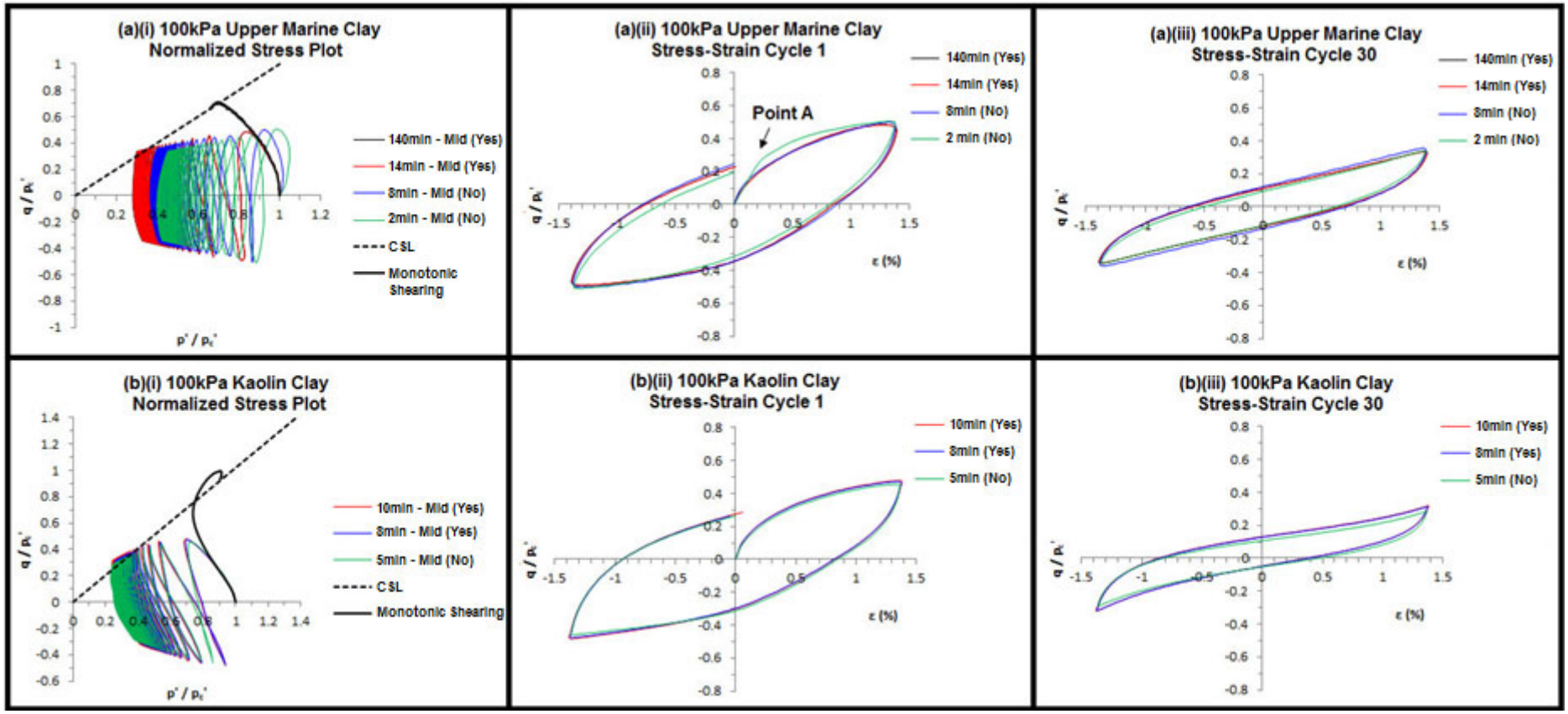

Figure 4.7 Normalized stress paths and stress-strain plots for p_c' = 100kPa specimens of (a) Singapore Upper Marine Clay and (b) Kaolin Clay.

[Yes = Pore pressure equalized; No = Pore pressure not equalized.]

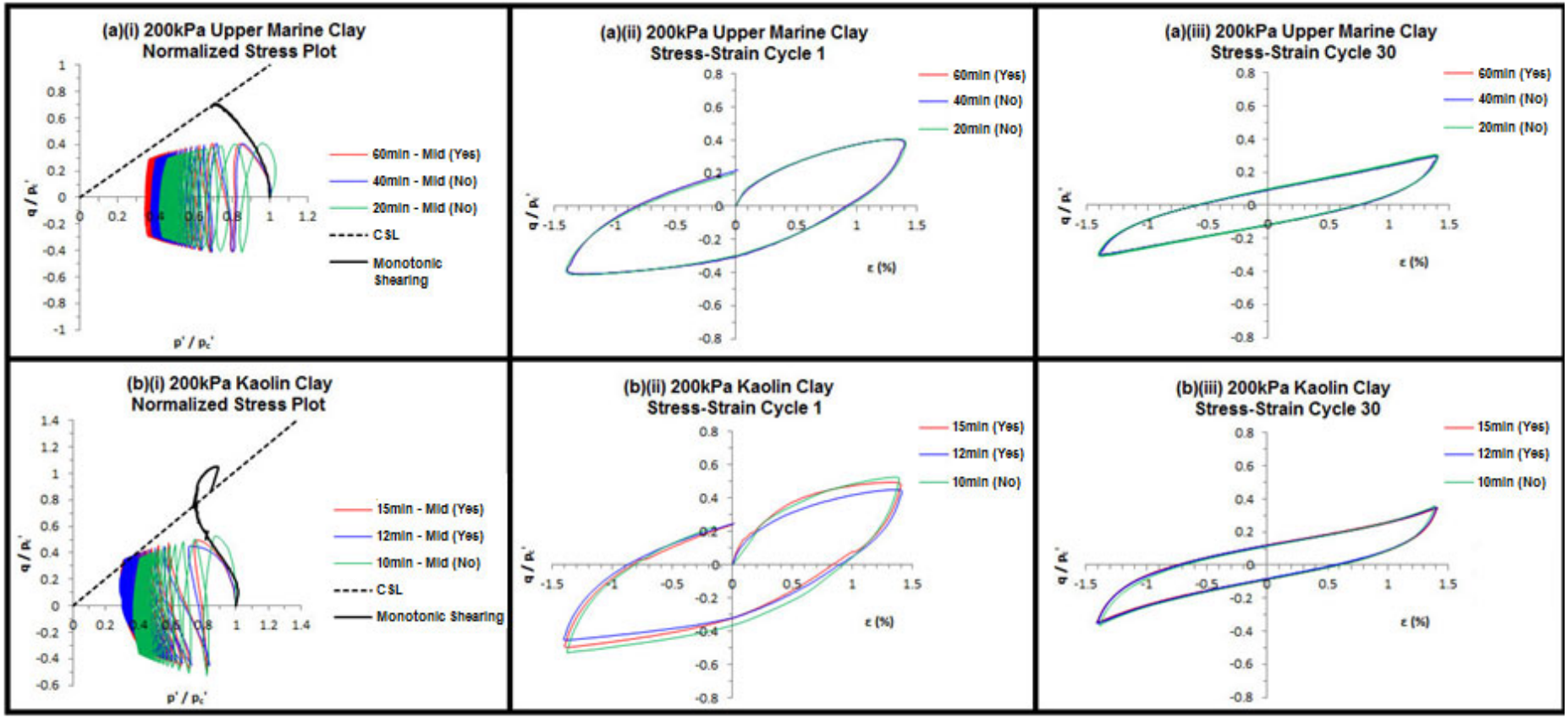

Figure 4.8 Normalized stress paths and stress-strain plots for p_c' = 200kPa specimens of (a) Singapore Upper Marine Clay and (b) Kaolin Clay.

[Yes = Pore pressure equalized; No = Pore pressure not equalized.]

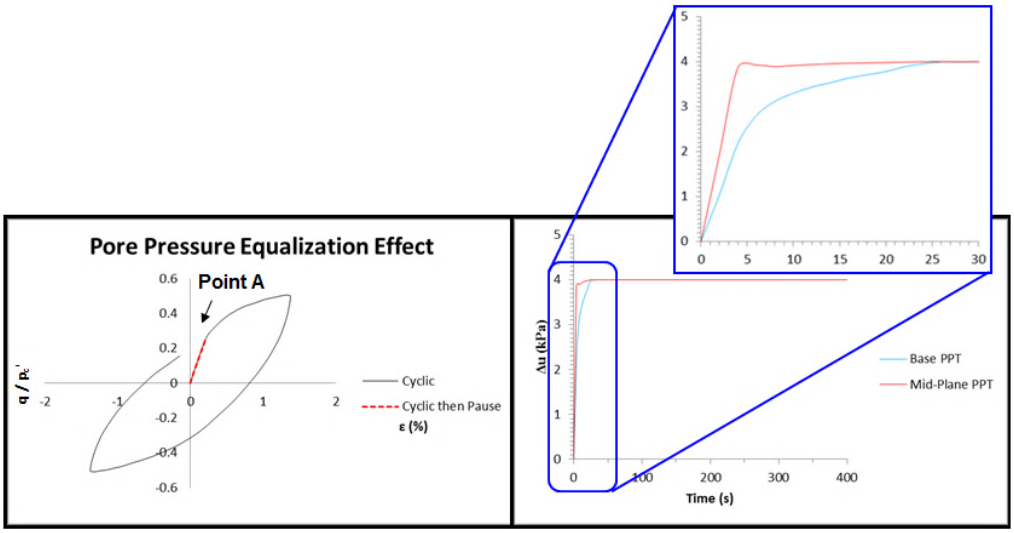

Figure 4.9 Investigation into the abrupt change in initial shear modulus.

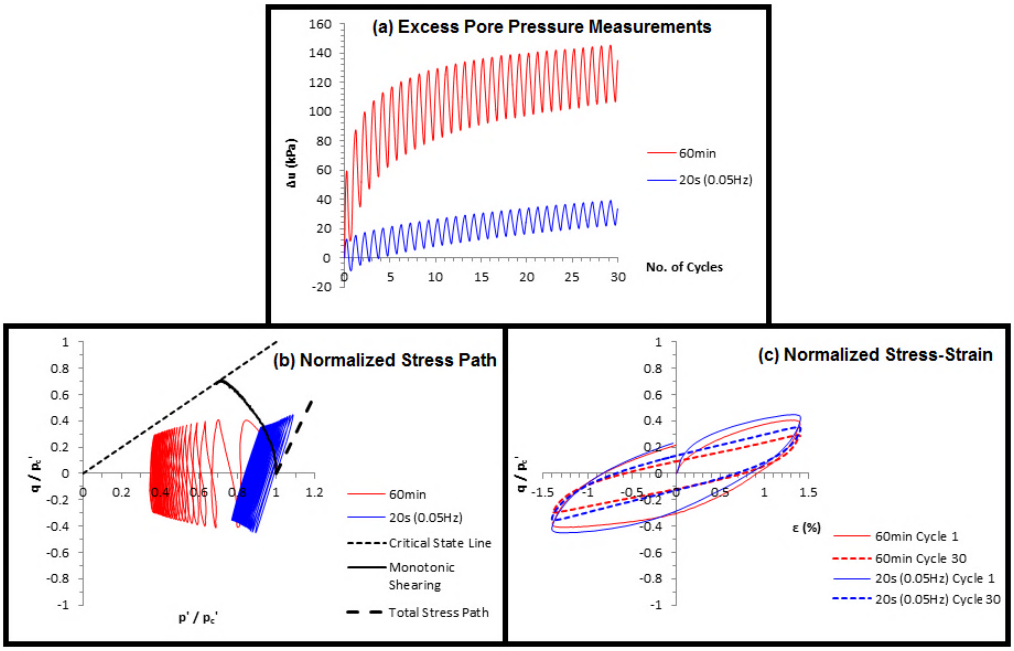

Figure 4.10 Experimental results for Singapore Upper Marine Clay specimens tested at 0.05Hz.

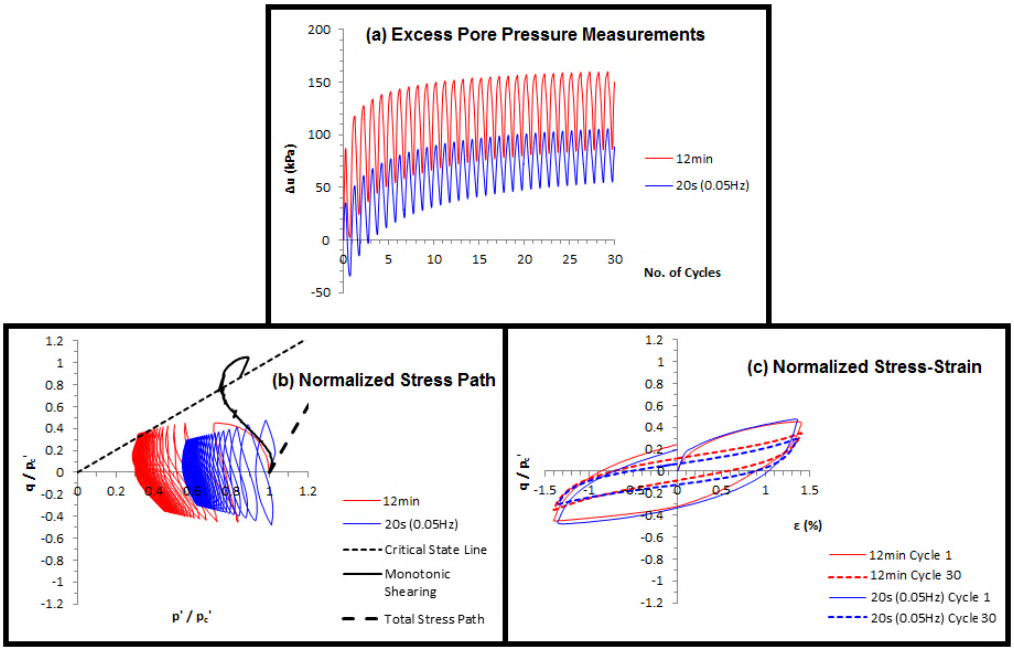

Figure 4.11 Experimental results for Kaolin Clay specimens tested at 0.05Hz.

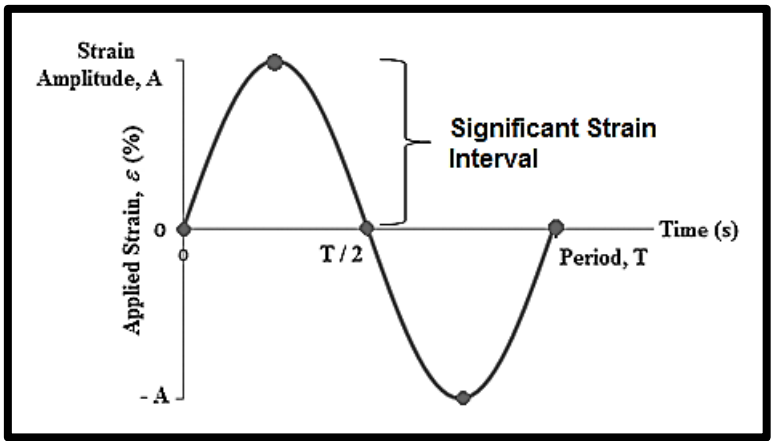

Figure 4.12 Definition of significant strain interval for cyclic tests.

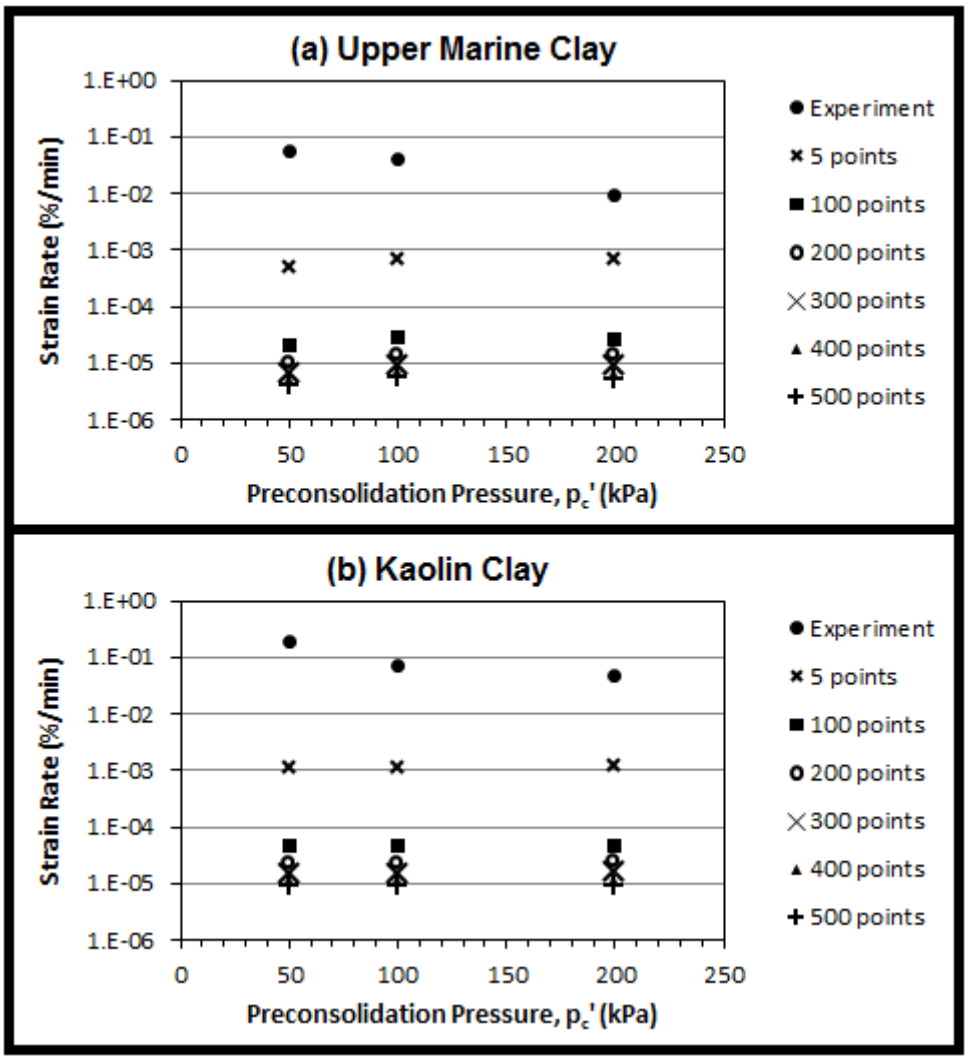

Figure 4.13 Comparison of BS1377 and fastest experimental average strain rates for (a) Singapore Upper Marine Clay and (b) Kaolin Clay.

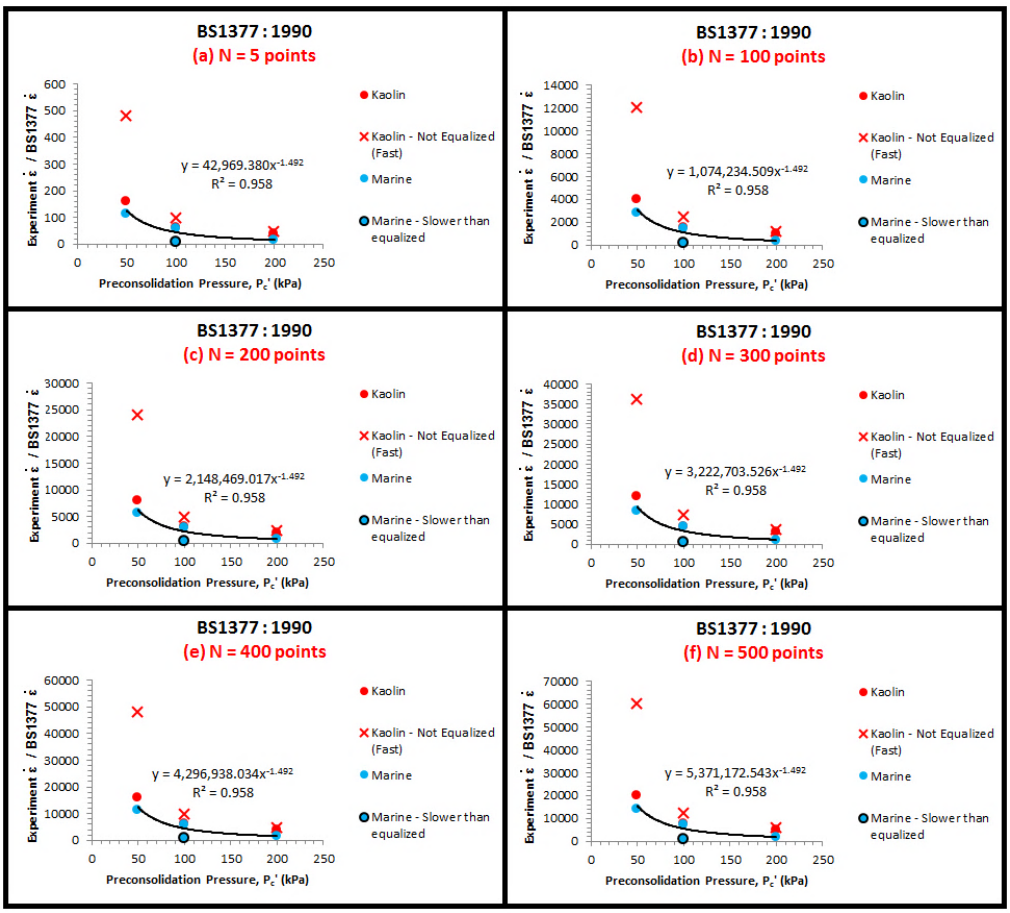

Figure 4.14 Fitted power trendlines for BS1377.

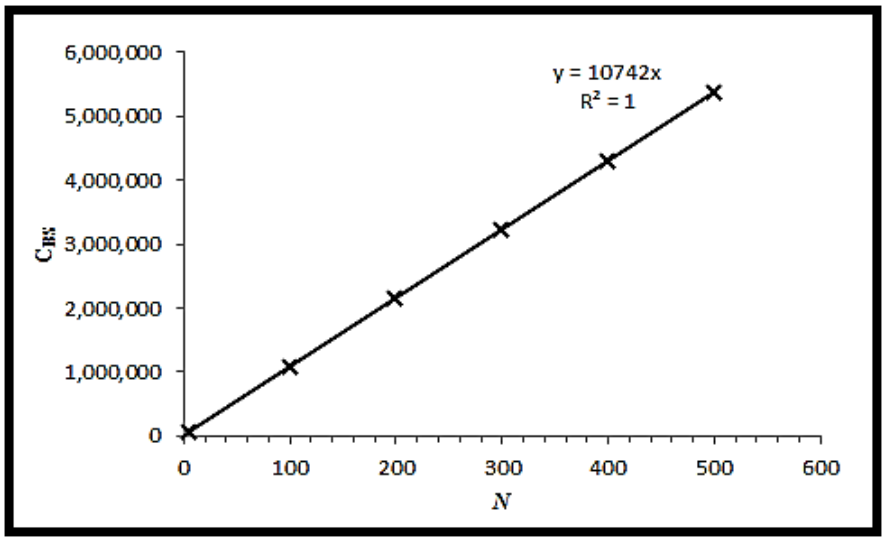

Figure 4.15 Parameter C_{BS} .

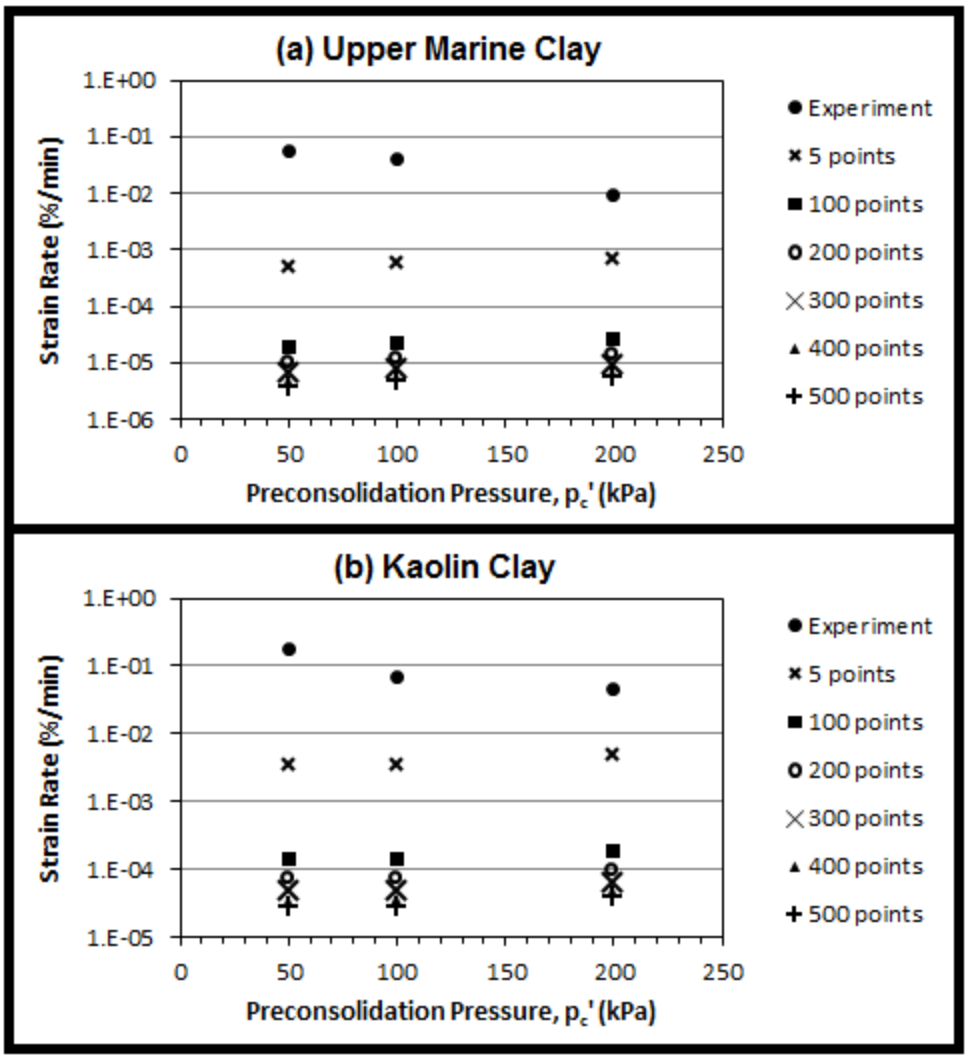

Figure 4.16 Comparison of Eurocode and fastest experimental average strain rates for (a) Singapore Upper Marine Clay and (b) Kaolin Clay.

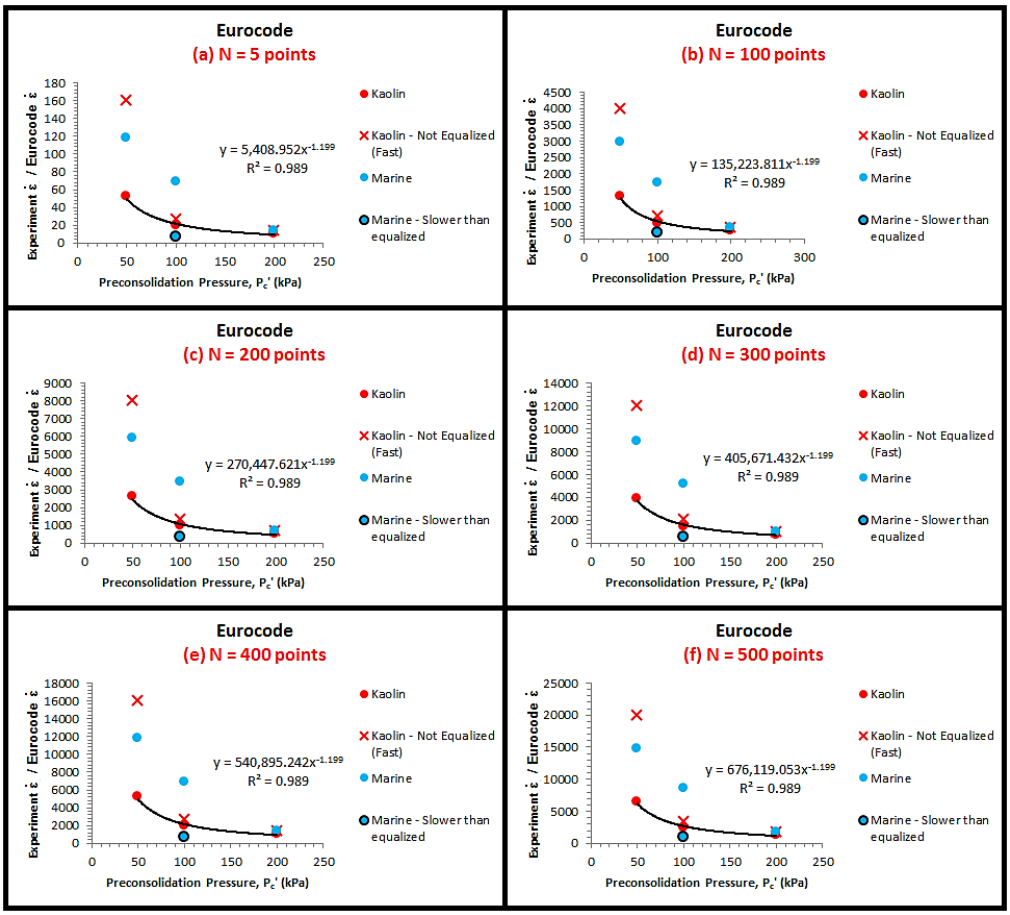

Figure 4.17 Fitted power trendlines for Eurocode TS17892.

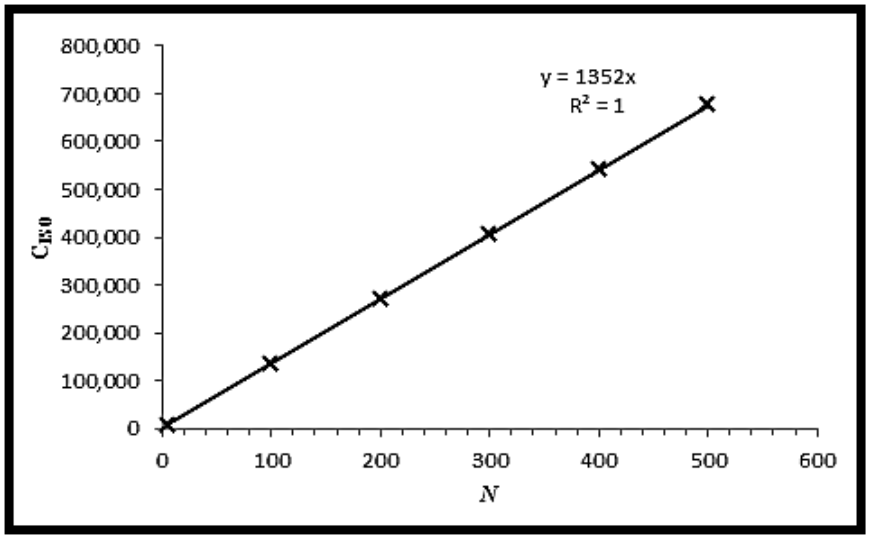

Figure 4.18 Parameter C_{ISO} .

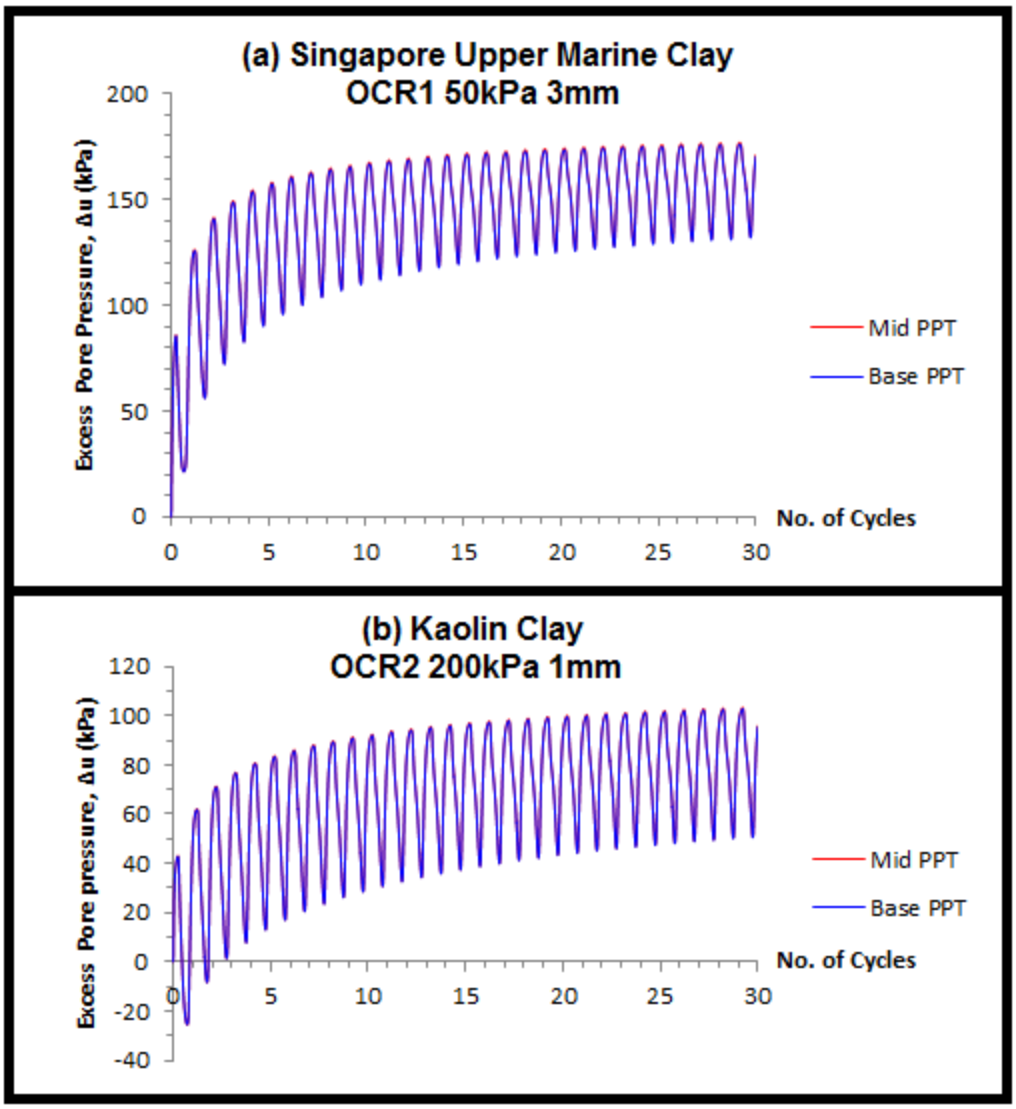

Figure 4.19 Typical plots showing pore pressure equalization for (a) normally consolidated Singapore Upper Marine Clay and (b) overconsolidated Kaolin Clay.

Chapter 5 – Shear Modulus and Damping Ratio

5.1 Overview

In this section, the shear modulus and damping ratio of Marine Clay and kaolin are discussed. Tables 5.1 and 5.2 summarize the resonant column and cyclic triaxial tests that were conducted on the two clay types. The parameters varied in the tests are the preconsolidation pressure (50, 100, 200kPa), overconsolidation ratio (OCR = 1, 1.5, 2) and applied strain amplitude. There is also a series of resonant column tests conducted with mid-plane pore pressure measurements, in which the specimens were subjected to 100,000 torsional cycles at different strain levels.

5.1.1 Some Issues Relating to the Interpretation of Resonant Column Test Results

5.1.1.1 Pore Pressure Equilibration in Resonant Column Specimens

Pore pressure equilibration in cyclic triaxial tests has been discussed in the previous chapter. The input frequency for the resonant column tests were varied according to the resonant frequency of the specimens, and are generally much higher than that required for pore pressure equilibration in cyclic triaxial tests. The high frequency in the resonant column tests means that there will be insufficient time for pore pressure equilibration, should there by non-uniformity. However, this is unlikely to affect the results of the study in a significant way, for the following reasons:

(i) The torsional shear strain in a resonant column test varies from zero to a maximum at the periphery of the specimen. The maximum torsional shear strain amplitude (γ) reached in the resonant column tests is approximately 0.3%; this being equivalent to about 0.17% in terms of generalized shear strain. As will be shown in the results discussed below, for such strain amplitudes, no significant excess pore pressure was detected even when the specimen was left to "cure" for about 12 hours with a mid-plane pore pressure transducer attached. Hence, pore pressure generation is not a significant issue in the resonant column tests.

(ii) Pore pressure measurements were not made for most of the resonant column tests and effective stress paths were not plotted for these tests. The resonant column tests were used mainly to provide information on the changes in the shear modulus and damping ratio in the small strain regime. As mentioned

earlier, pore pressure non-uniformity affect stress-strain behaviour to a much lesser extent than effective stress path.

5.1.1.2 Shear Strains from Resonant Column Tests

Unlike the cyclic triaxial setup that applies longitudinal cyclic shear strains, the resonant column produces rotational excitations that translate to torsional shear loadings. Since the resonant column tests were conducted in accordance to the ASTM D4015-07 standard, the tabulated torsional shear strain is defined as the strain at 0.8 times the specimen radius from the centre of the specimen. This definition was based on Chen and Stokoe's (1979) equivalent radius approach to account for the effects of nonlinear stress-strain behaviour occurring over the radius of soil specimens loaded in torsion. Thus, in order to plot the resonant column and cyclic triaxial results on the same shear strain axis, the torsional shear strain in the resonant column is converted to a generalized shear strain value (i.e. engineering strain), which corresponds to the axial strain in the triaxial setup, using the following Equation 5.1:

$$\varepsilon = \frac{\gamma}{\sqrt{3}} \qquad [5.1]$$

Where:

ε = Generalized shear strain,

γ = Torsional shear strain measured in the resonant column.

For ease of comparison, all strain values presented in this section are the generalized shear strain values.

5.1.1.3 Frequency Effect on Shear Modulus and Damping Ratio

As discussed in the literature review, most previous studies treat the modulus as a frequency-independent but strain-dependent property (Towhata 2008). Many studies have also shown that cyclic stress-strain behaviour of clays is only rate-dependent to a very limited extent (Brown et al. 1975; Vucetic and Dobry 1991; Zanvoral and Campanella 1994; Ishihara 1996; Shibuya et al. 1995; Teachavorasinskun et al. 2002; Matesic and Vucetic 2003; Towhata 2008). Hence the use of the resonant frequency to determine the shear modulus and damping is unlikely to cause significant errors.

5.1.1.4 Back-Electromotive Force (EMF) in Damping Ratio Measurements

As discussed in Section 3.3.3, torsional excitation in the resonant column used herein is produced by four annular permanent magnets passing through four fixed coils of wires. According to several researchers (e.g. Kim 1991; Hwang 1997; Cascante et al. 2003; Wang et al. 2003), such magnet-coil driving system induces a back-electromotive force (EMF) that counters the torsional motion. Although this induced back-EMF has negligible effect on the measured resonant frequency (Wang et al. 2003), it dissipates the energy within the system in addition to the energy losses experienced by the test specimen (Meng and Rix 2003). With this additional equipment-induced damping that can be as high as 4% (Meng and Rix 2003), the measured damping ratio increases significantly (Wang et al. 2003). However, Wang et al. (2003) had demonstrated that back-EMF can be eliminated with the coils in open circuit or removed during free vibration decay tests. In the current study, the output circuit to the excitation coils are open during the free vibration decay tests, so there is no back-EMF generated. The damping ratio presented herein represents the true material response of the test specimens.

5.1.2 Some Issues Relating to the Interpretation of Cyclic Triaxial Test Results

One possible issue in the cyclic triaxial tests is the absence of internal strain measurements (e.g. Hall effect transducer, submersible LVDT). This means that very small strain measurements are likely to be susceptible to errors. In Jastrzebska's (2010) study on Tulowice Clay, the shear modulus was underestimated by up to 5 times when an external displacement measurement is used compared to an internal transducer within an applied cyclic strain range of 0.001% to 0.1%. However, such disparity vanishes at the upper bound of the strain range (Jastrzebska 2010). Furthermore, according to Jardine et al. (1984) and Burland (1989), external strain measurements underestimate the soil stiffness only for strains less than 0.01%. In the current study, the applied strain levels are higher than 0.7% which renders the use of an internal strain measurement unnecessary. In addition, based on Goto et al. (1991) and Tatsuoka and Shibuya's (1992) findings, Tatsuoka et al. (1994) concluded that although internal strain measurements on the lateral surface of specimen is needed for most soils, it is not required for soft clays. Therefore, internal strain measurements are not performed in the current cyclic triaxial tests.

5.2 Small-strain Shear Modulus, G_{max}

Figure 5.1 shows the shear modulus against generalized shear strain obtained from the resonant column and cyclic triaxial tests on remoulded specimens of Marine Clay and kaolin. The values of the small-strain shear modulus ($G_{\max}$) were determined from Figure 5.1 and summarized in Table 5.3.

As suggested by Viggiani and Atkinson (1995):

$$\frac{G_{\max}}{p_r} = A\left(\frac{p'}{p_r}\right)^n (OCR)^m \qquad [5.2]$$

Where:

A = Empirically derived constant,

p_r = Reference pressure required to make Equation 5.2 dimensionally consistent,

n = Exponential factor of effective mean principle stress (p'),

m = Exponential factor of overconsolidation ratio (OCR).

Note that $G_{\max}$ and p' are expressed in kPa.

For OCR = 1 and p_r = 1kPa,

$$G_{\max} = A(p')^n \qquad [5.3]$$

Or

$$\log G_{\max} = n\log(p') + \log A \qquad [5.4]$$

The values of n and $\log A$ are evaluated using linear regression of variables $\log G_{\max}$ and $\log p'$ as shown in Figure 5.2. Using Figure 5.2, the correlations for Singapore Marine Clay and Kaolin Clay can be expressed as:

Singapore Marine Clay:

$$\log G_{\max} = 0.855\log(p') + 2.669 \qquad [5.5]$$

So $n = 0.855$ and $A = 467$.

Kaolin Clay:

$$\log G_{\max} = 0.850\log(p') + 2.841 \qquad [5.6]$$

So $n = 0.850$ and $A = 693$.

Hence, by applying Equation 5.2 and assuming p_r = 1kPa and p' = 50kPa, 100kPa and 200kPa respectively, we have:

Singapore Marine Clay:

p' = 50kPa $\log G_{\max} = 4.122 + m \log OCR$ [5.7]

p' = 100kPa $\log G_{\max} = 4.379 + m \log OCR$ [5.8]

p' = 200kPa $\log G_{\max} = 4.637 + m \log OCR$ [5.9]

Kaolin Clay:

p' = 50kPa $\log G_{\max} = 4.285 + m \log OCR$ [5.10]

p' = 100kPa $\log G_{\max} = 4.541 + m \log OCR$ [5.11]

p' = 200kPa $\log G_{\max} = 4.797 + m \log OCR$ [5.12]

Similarly, the values of m are derived using linear regression of variables $\log G_{\max}$ and $\log OCR$ as shown in Figure 5.3. From Figure 5.3, the average values of m are 0.4037 ± 0.0021 and 0.2547 ± 0.0006 for Marine Clay and kaolin respectively.

Thus, the small-strain shear modulus for Singapore Marine Clay and Kaolin Clay can be mathematically expressed as:

Singapore Marine Clay: $$\frac{G_{\max}}{p_r} = 467\left(\frac{p'}{p_r}\right)^{0.855}(OCR)^{0.4037} \quad [5.13]$$

Kaolin Clay: $$\frac{G_{\max}}{p_r} = 693\left(\frac{p'}{p_r}\right)^{0.850}(OCR)^{0.2547} \quad [5.14]$$

The parameters A, n and m in Equations 5.13 and 5.14 are compared against the design chart (Figure 2.11) proposed by Viggiani and Atkinson (1995). Based on the plasticity indices of 53.2% and 41.2% for Singapore Upper Marine Clay and Kaolin Clay respectively, the design values of A, n and m are interpolated. As Table 5.4 shows, the fitted parameters agree reasonably well with those interpolated from Viggiani and Atkinson's design chart.

5.3 Normalized Shear Modulus and Damping Curves

Figures 5.4 and 5.5 show the normalized shear modulus and damping ratio against shear strain. Results from undrained cyclic triaxial tests were also included to provide experimental data for generalized shear strains exceeding 0.3% (refer to Tables 4.1 and 4.3). As can be seen, a smooth and continuous trend is observed for all specimens

across the entire range of strain, indicating consistency between the resonant column and cyclic triaxial results. The normalized shear modulus and damping curves respectively follow the typical inverse S-shape and S-shape profiles reported by various past researchers (Vucetic and Dobry 1991; Kagawa 1992; Hardin and Drnevich 1972a and 1972b; Ishibashi and Zhang 1993; Kokusho et al., 1982). As the plasticity index of Marine Clay (PI = 53.2%) is higher than kaolin (PI = 41.2%), it demonstrates a slower rate of attenuation with increasing shear strain whereas its damping ratio versus strain curves tend to locate lower than those for kaolin. This observation is consistent with findings from previous studies (e.g. Kokusho et al. 1982; Vucetic and Dobry 1991; Okur and Ansal 2007; Towhata 2008).

The results show that, over the range of 50 to 200kPa, the mean effective stress has negligible influence on the normalized modulus degradation and damping curves for both clay types. Similarly, as Figures 5.4 and 5.5 show, overconsolidation ratio also has insignificant effect on the positions of the normalized shear modulus and damping curves. This is consistent with findings reported by previous studies (e.g. Kokusho et al. 1982; Vucetic and Dobry 1991; Ishihara 1996 etc.).

In Figures 5.6 and 5.7, the data from published literature is appended to the normalized shear modulus values and damping ratios obtained from the present resonant column and cyclic triaxial tests. All of the current normalized shear modulus data fall within a well-defined band together with the published data. As reviewed in Section 2.2.1, clay behaviour within a very small strain regime is essentially elastic and its shear modulus reaches a nearly constant limiting value. Available empirical data indicates that this strain regime is smaller than a threshold value ranging from 0.001% to 0.01% (e.g. Hardin and Black 1968; Anderson and Richart 1976; Stokoe and Lodde 1978; Kokusho et al. 1982; Georgiannou et al. 1991; Viggiani and Atkinson 1995; Diaz-Rodriguez and Lopez-Molina 2008). As Figure 5.6 shows, the threshold values for Marine Clay and kaolin are 0.007% and 0.005% respectively; which safely fall within the reported range of 0.001% to 0.01%.

As shown in Figure 5.7, the damping ratio from resonant column test results correlates well with values from published literature. The damping ratio from the first cycle of the triaxial test also appears to correlate well. However, significant degradation is observed with successive cycles; this trend being consistent for both clay types. For instance, for a normally consolidated kaolin specimen, the average decrement in damping ratio over the first 30 load cycles is approximately 15% for

strain amplitude of 1.4%. This is consistent with the findings of Hardin and Drnevich (1972a) and Guha (1995) that the damping ratio of clays decreases with increasing number of load cycles. Kim et al. (1991) also showed that the effect of load cycles is only negligible for applied strains below 0.1%. On the other hand, Banerjee's (2009) study on remoulded kaolin specimen with the same stress history shows a decrement in damping ratio of approximately 7% over 60 cycles, for shear strain from 0.1% to 1.37%. This difference may be attributed to the use of slower cyclic loading rates to allow for pore pressure equilibration and the use of virgin specimens for every triaxial test in this study. Banerjee (2009) used much higher loading frequencies of between 0.05Hz to 1.5Hz on the same specimen subjected to increasing strain levels. If this is true, then the non-uniformity in pore pressure is likely to have a significant effect on the cyclic degradation behaviour of soil, even though the stress-strain behaviour in the initial cycle may not be significant.

5.4 Pore Pressure Variations During and After Small-strain Cyclic Loading

As previously shown in Table 5.1, 12 additional tests are conducted to investigate pore pressure variations in clay specimens during and after small-strain cyclic loading in the resonant column. In this series of tests, a small constant value of torsional strain is applied while increasing the input frequency until resonance is achieved. Once resonance is reached, the specimen was subjected to 100,000 load cycles under its resonant frequency; this maximises the strain amplitude which the resonant column can actuate. During this loading stage, mid-plane pore pressure measurements are taken at 5 minutes intervals. After the application of 100,000 load cycles, the input excitation voltage is paused and pore pressure measurements are continuously recorded at fixed intervals of 2 hours until no further change in pore pressure is detected (at least 12 hours of monitoring). After pore pressure stabilization is achieved, the same steps are repeated on the same specimen for higher strain levels.

The mid-plane excess pore pressure measurements recorded are summarized in Figure 5.8. For each specimen, these pore pressure data represent cumulative pore pressure from the start of the torsional shear at low strain amplitude (0.003%) until the test was terminated at the highest strain level (0.15%). From the current results, the maximum excess pore pressure measured was only 1.35kPa for all specimens subjected to increasing strain levels regardless of its clay type and stress history. This

pore pressure reading corresponds to a pore pressure transducer output of 0.01V which lies within the error range of the multimeter (±0.01V); hence it is an insignificant value. Based on this, one can conclude that no pore pressure accumulation occurred during and after cyclic loading at shear strain amplitudes up to 0.15%. This observation agrees with the findings of Matasovic and Vucetic (1995) and Diaz-Rodríguez and Lopez-Molina (2008).

5.5 Degradation Cyclic Strain Threshold

According to Diaz-Rodriguez and Lopez-Molina (2008), the degradation cyclic strain threshold defines the onset of significant de-structuring of saturated clays where excess pore pressure generation becomes apparent (refer to Figure 2.9). As this threshold strain marks the transition in the clay's cyclic behaviour from hysteretic equilibrium to substantive effective stress degradation (Diaz-Rodriguez and Lopez-Molina, 2008), the determination of this threshold value becomes essential.

In this test series, cyclic triaxial specimens were subjected to 30 slow load cycles that allows pore pressure equilibration, followed by another 1000 cycles applied at a frequency of 5Hz, after which the test is paused at the current stress state to allow for pore pressure equalization. The same procedure is then repeated on the same specimen for higher strain levels (0.05%, 0.1%, 0.15% and 0.2%). As demonstrated by Yasuhara et al. (1982), excess pore pressure accumulations within clay specimens is not influenced by the loading method (repeated or sustained) regardless of the applied shear strain level. Since the loading method has no impact on pore pressure generation, the above test procedures were adopted due to time constraints.

Figure 5.9 shows the excess pore pressure measurements for Marine Clay and kaolin specimens. Since the test procedure allows time for pore pressure equalization, the excess pore pressure is plotted against time in Figure 5.10 to show its variation during this "curing" period as well. In both Figures 5.9 and 5.10, increase in excess pore pressures was observed when the applied shear strain approached ~0.2% and ~0.17% for Marine Clay and kaolin specimens respectively. Prior to these threshold strains, the pore pressure variation during the "curing" period was negligible. Once the threshold strain is applied, the excess pore pressure build-up during the subsequent "curing" period increases significantly. Furthermore, these threshold strains appear to apply to all specimens regardless of preconsolidation pressure and overconsolidation ratio. As Figure 5.11 shows, these degradation cyclic strain thresholds correspond to

a normalized shear modulus of 0.5, similar to that reported by Diaz-Rodriguez and Lopez-Molina (2008). However, these measured strain thresholds are lower than the typical range of 0.5% to 2% (Houston and Herrmann, 1980; Lefevbre et al. 1989; Diaz-Rodriguez and Santamarina, 2001). Nonetheless, Diaz-Rodriguez and Lopez-Molina (2008) noted that the threshold value may be affected by various factors such as soil composition, plasticity index, void ratio and stress history.

5.6 Comparison with Some Empirical Stress-Strain Models

In this section, the applicability of some empirical stress-strain models, previously discussed in Section 2.2.3, are examined. A summary of the model parameters used is provided in Table 5.5. For the Hyperbolic and Ramberg-Osgood models, the reference shear strain (γ_r) at which G/G_{max} = 0.5 had been established as 0.2% and 0.17% for Marine Clay and kaolin specimens respectively (see Section 5.5). Using the nonlinear curve fit function in OriginPro 9.0 software, the remaining material parameters (i.e. α, C_1, r and R) for the Ramberg-Osgood and Modified Hyperbolic models were adjusted to achieve the best fit (corresponding to the highest R^2 values) for the shear modulus attenuation relationships with strain that were experimentally derived for Marine Clay and kaolin specimens.

Differences in these models are shown in the graphs of normalized shear modulus and damping ratio plotted against shear strain (Figures 5.12 and 5.13). As can be seen, while the variation in normalized shear modulus with strain is fairly well modelled by all three models ($R^2 \geq 0.829$), none of them were able to model the damping ratio of both clay types. For strain level exceeding 0.4%, the Hyperbolic and Modified Hyperbolic models over-predict the damping ratio while the Ramberg-Osgood model under-predicts the damping characteristics of Marine Clay. Similar conclusions with regards to the Ramberg-Osgood and Hyperbolic models had been drawn by Ray and Richart (1988), Saada and Macky (1985) and Kagawa (1993). The differences between the model results and empirical data, however, were more prominent for kaolin specimens ($R^2 \leq 0.339$). The Ramberg-Osgood model consistently under-predicts the damping ratio by a significant margin. The other two models under-predict the damping ratio at strain levels up to about 0.3%. At higher strain levels, they appear to over-predict the damping ratio. This contradicts Banerjee's (2009) observation that the Modified Hyperbolic Model can reasonably capture the strain-dependent damping characteristics of Kaolin Clay for strains up to 1%. As Figure 5.14 shows, at an applied strain of 1.4%, the areas enclosed by the stress-strain loops

for both Hyperbolic and Modified Hyperbolic are larger than that for the experimental data. Although the Ramberg-Osgood model simulates a flatter stress-strain loop, the response is the closest to the experimental data. This can be attributed to the complexity in the Ramberg-Osgood model as it requires 4 input parameters. Nonetheless, all three models are unable to predict the damping ratio variation over the entire range of strain. It should also be noted that none of these models predict pore pressure generation; all of them are total stress models.

Table 5.1 Experimental matrix for resonant column tests.

Resonant Column Test - Without Pore Pressure Measurements			**Resonant Column Test - With Pore Pressure Measurements**		
Clay	**OCR**	**p_c' (kPa)**	**Clay**	**OCR**	**p_c' (kPa)**
Upper Marine Clay	1	50	**Upper Marine Clay**	1	50
		100			100
		200			200
	1.5	50		2	50
		100			100
		200			200
	2	50	**Kaolin Clay**	1	50
		100			100
		200			200
Kaolin Clay	1	50		2	50
		100			100
		200			200
	1.5	50			
		100			
		200			
	2	50			
		100			
		200			

Table 5.2 Experimental matrix for cyclic triaxial tests.

Clay	**OCR**	**p_c' (kPa)**	**Frequency (Hz)**	**No. of Load Cycles**
Upper Marine Clay	1	50	For 30 cycles, the cyclic frequency depends on the applied strain level (0.05 - 0.2%). For 1000 cycles, frequency = 5Hz.	30 and 1000
		100		
		200		
	2	50		
		100		
		200		
Kaolin Clay	1	50		
		100		
		200		
	2	50		
		100		
		200		

Table 5.3 Small-strain shear modulus (G_{max}).

OCR	p_c' (kPa)	G_{max} (MPa)	
		Upper Marine Clay	Kaolin Clay
1	50	13.22	19.25
	100	23.97	34.70
	200	43.25	62.55
1.5	50	15.32	21.35
	100	28.01	38.46
	200	51.18	69.34
2	50	17.50	22.96
	100	31.71	41.42
	200	57.29	74.65

Table 5.4 Comparison of experimentally-derived parameters *A*, *n* and *m* against design chart.

Parameters	Upper Marine Clay			Kaolin Clay		
	Equation 5.8	Design Value	% Difference	Equation 5.9	Design Value	% Difference
A	467	430	8.60	693	640	8.28
n	0.855	0.84	1.79	0.850	0.83	2.41
m	0.4037	0.38	6.24	0.2547	0.26	-2.04

Table 5.5 Material parameters used for the available stress-strain models.

Model	Parameters	Upper Marine Clay	Kaolin Clay
Hyperbolic	γ_r	0.2	0.17
Ramberg-Osgood	γ_r	0.2	0.17
	α	6.50	8.37
	C_1	1.00	0.75
	r	2.92	2.81
Modified Hyperbolic	R	165.54	193.40

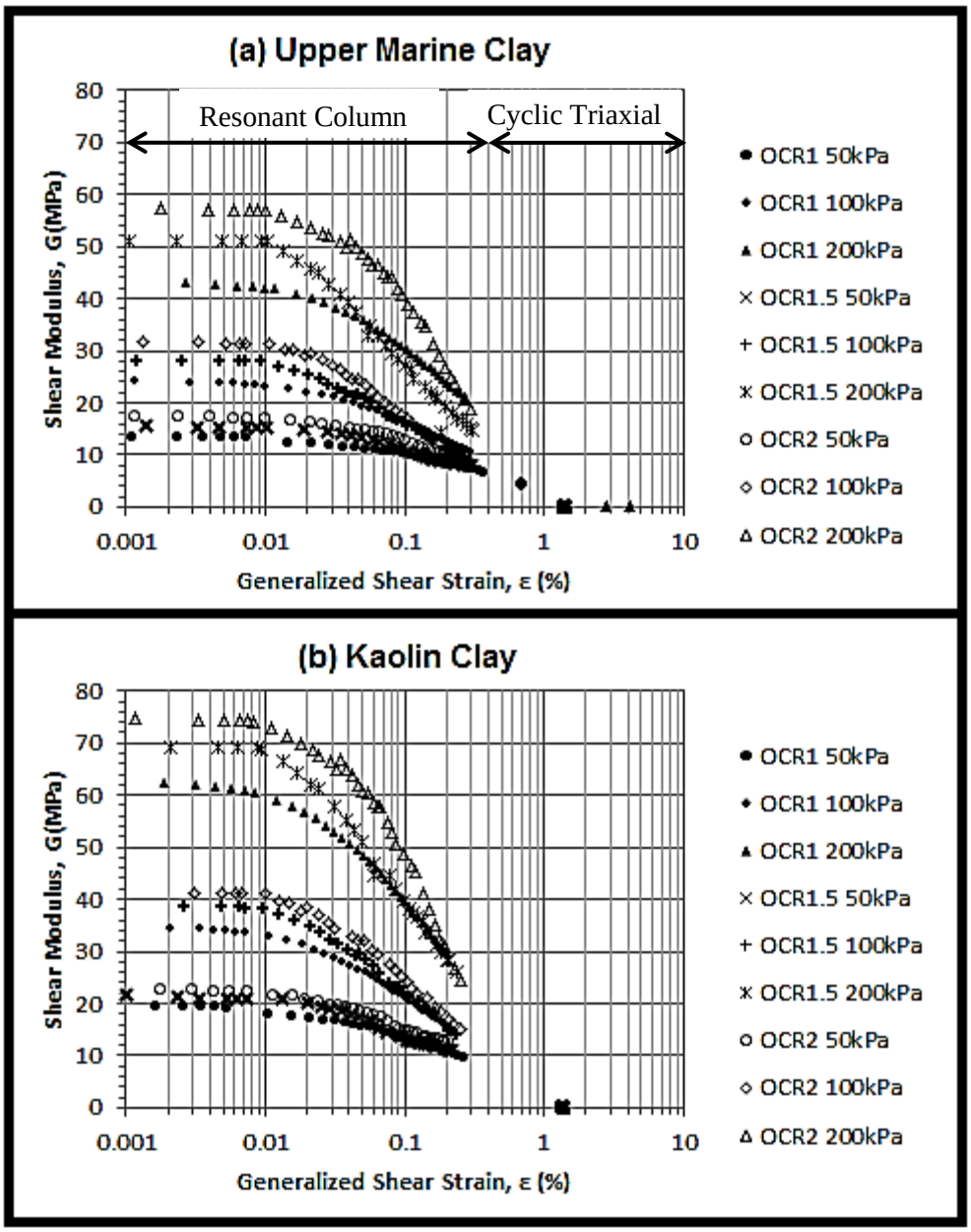

Figure 5.1 Shear modulus attenuation curves for (a) Singapore Upper Marine Clay and (b) Kaolin Clay.

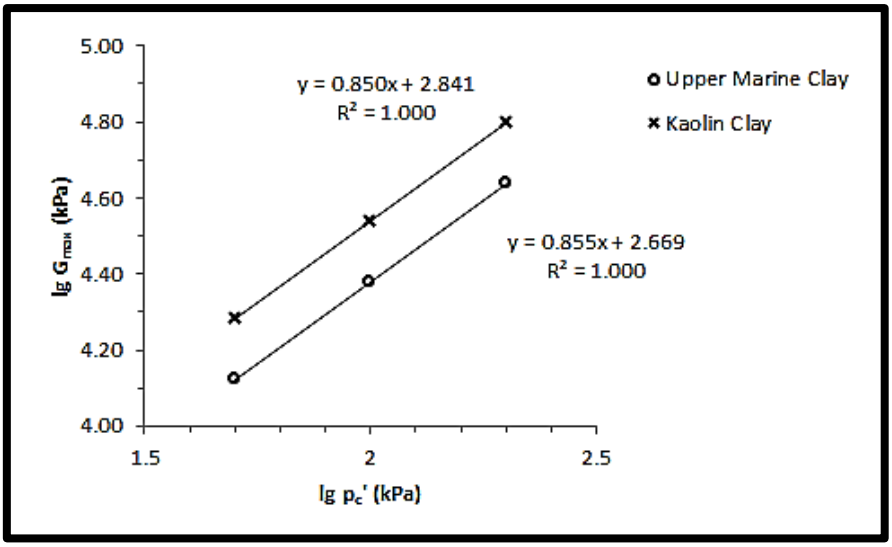

Figure 5.2 Coefficients *n* and *A*.

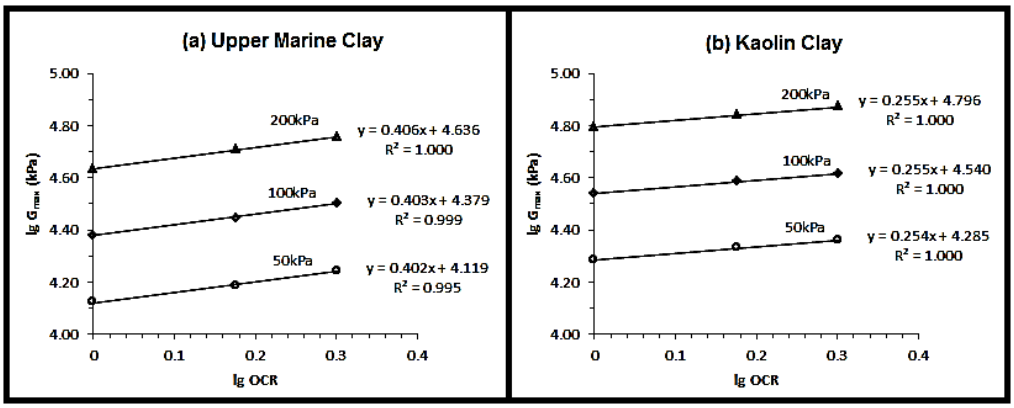

Figure 5.3 Coefficient *m*.

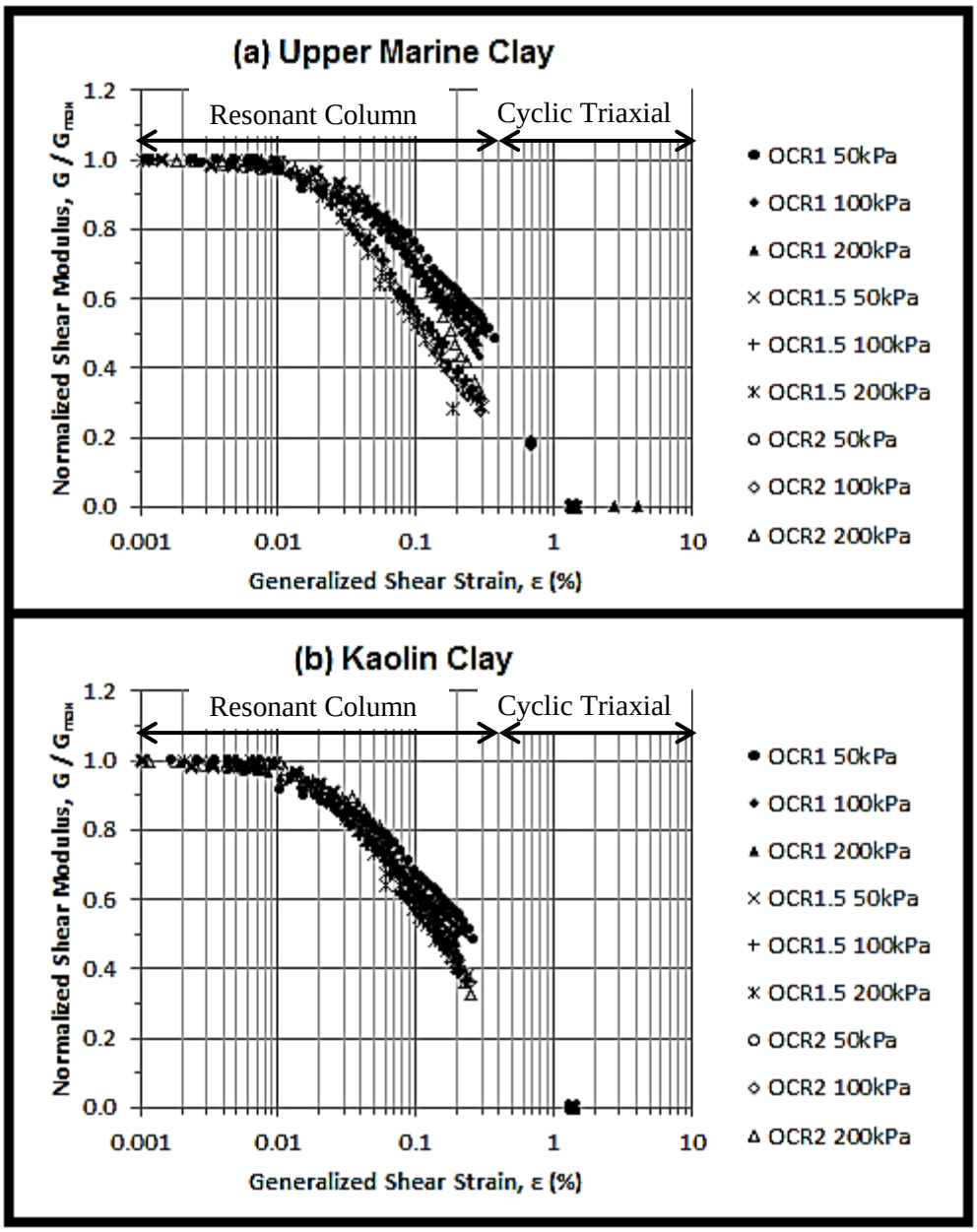

Figure 5.4 Normalized shear modulus attenuation curves for (a) Singapore Upper Marine Clay and (b) Kaolin Clay.

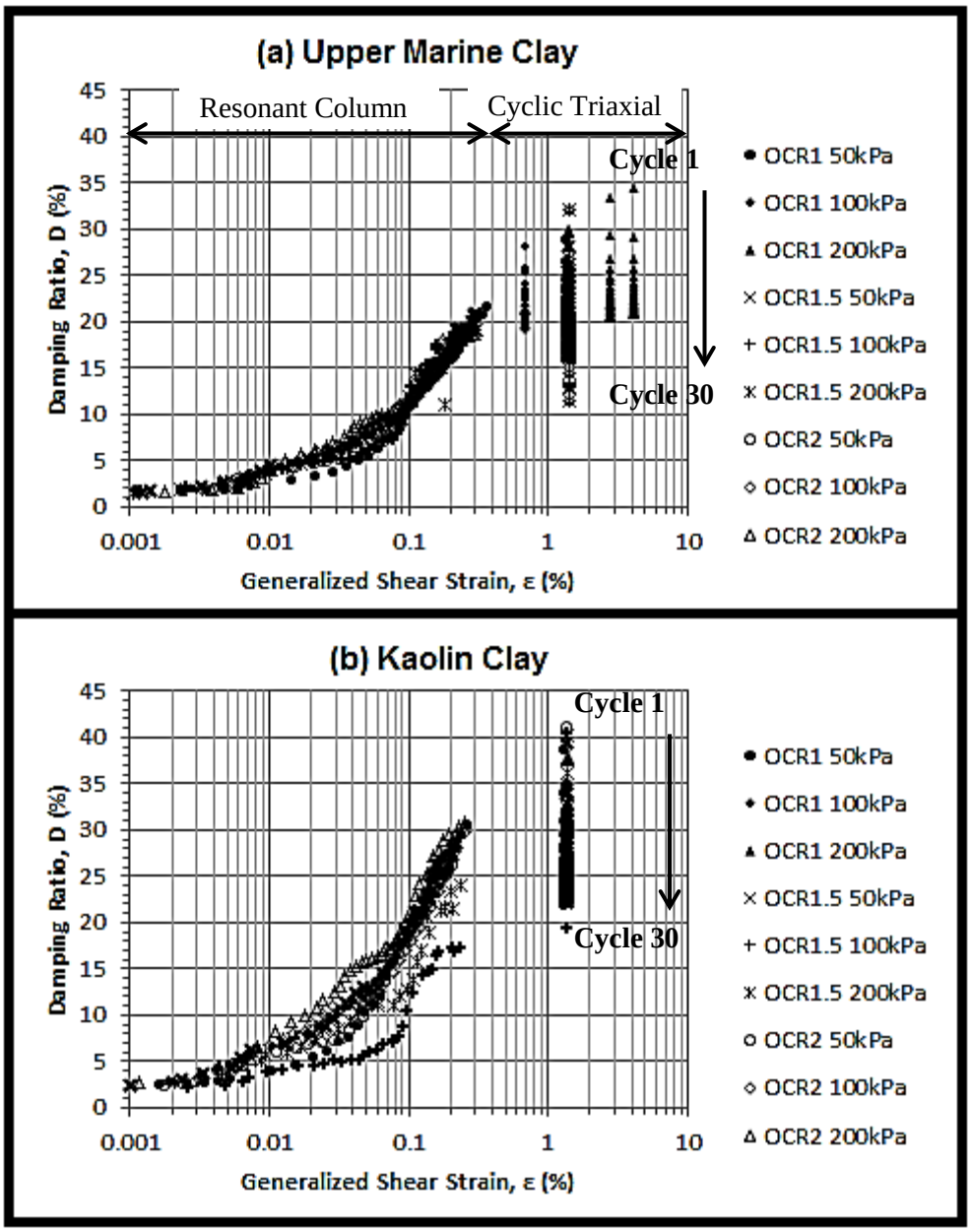

Figure 5.5 Damping ratio curves for (a) Singapore Upper Marine Clay and (b) Kaolin Clay.

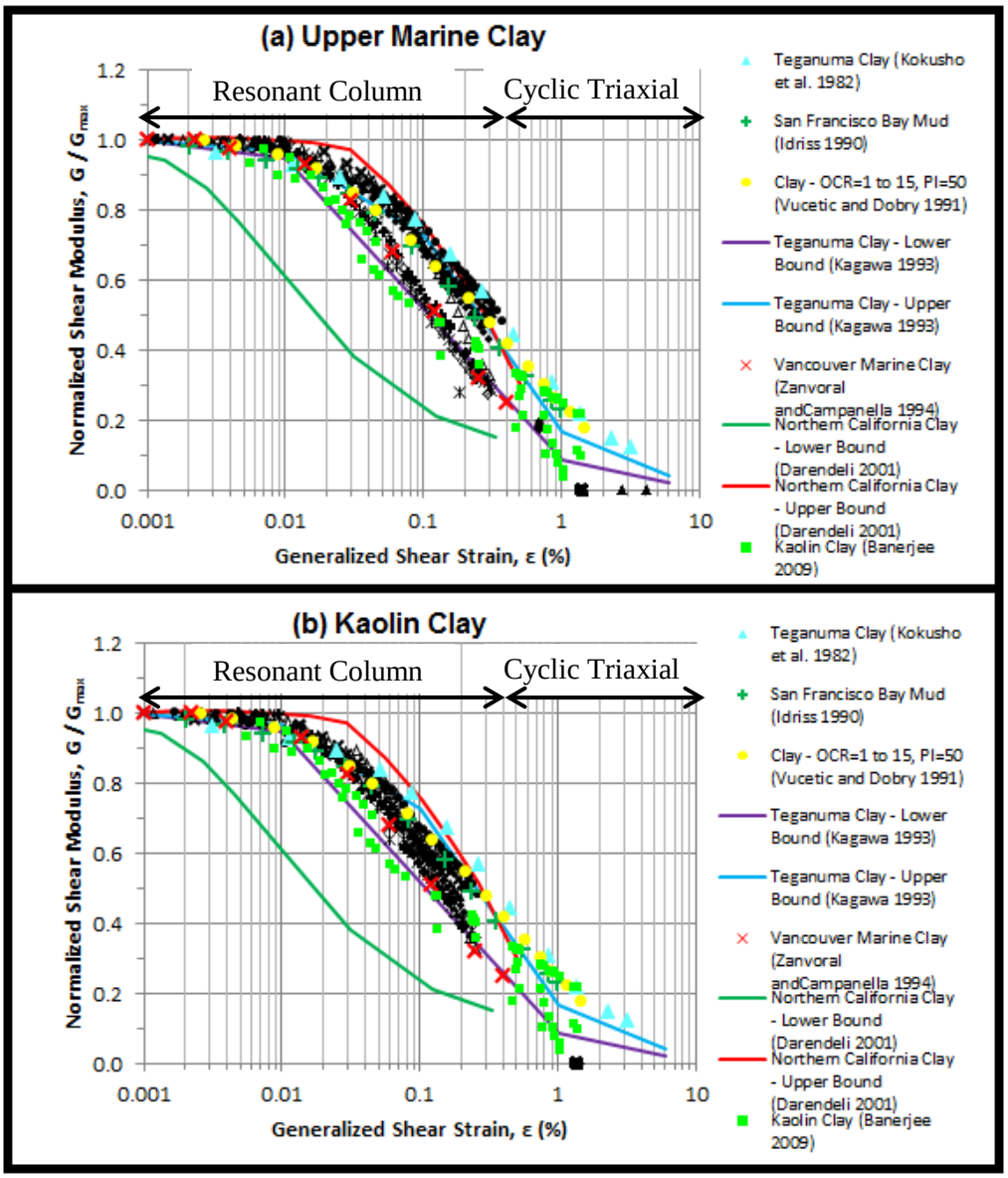

Figure 5.6 Comparison of the normalized shear modulus curves against published literature data for (a) Singapore Upper Marine Clay and (b) Kaolin Clay.

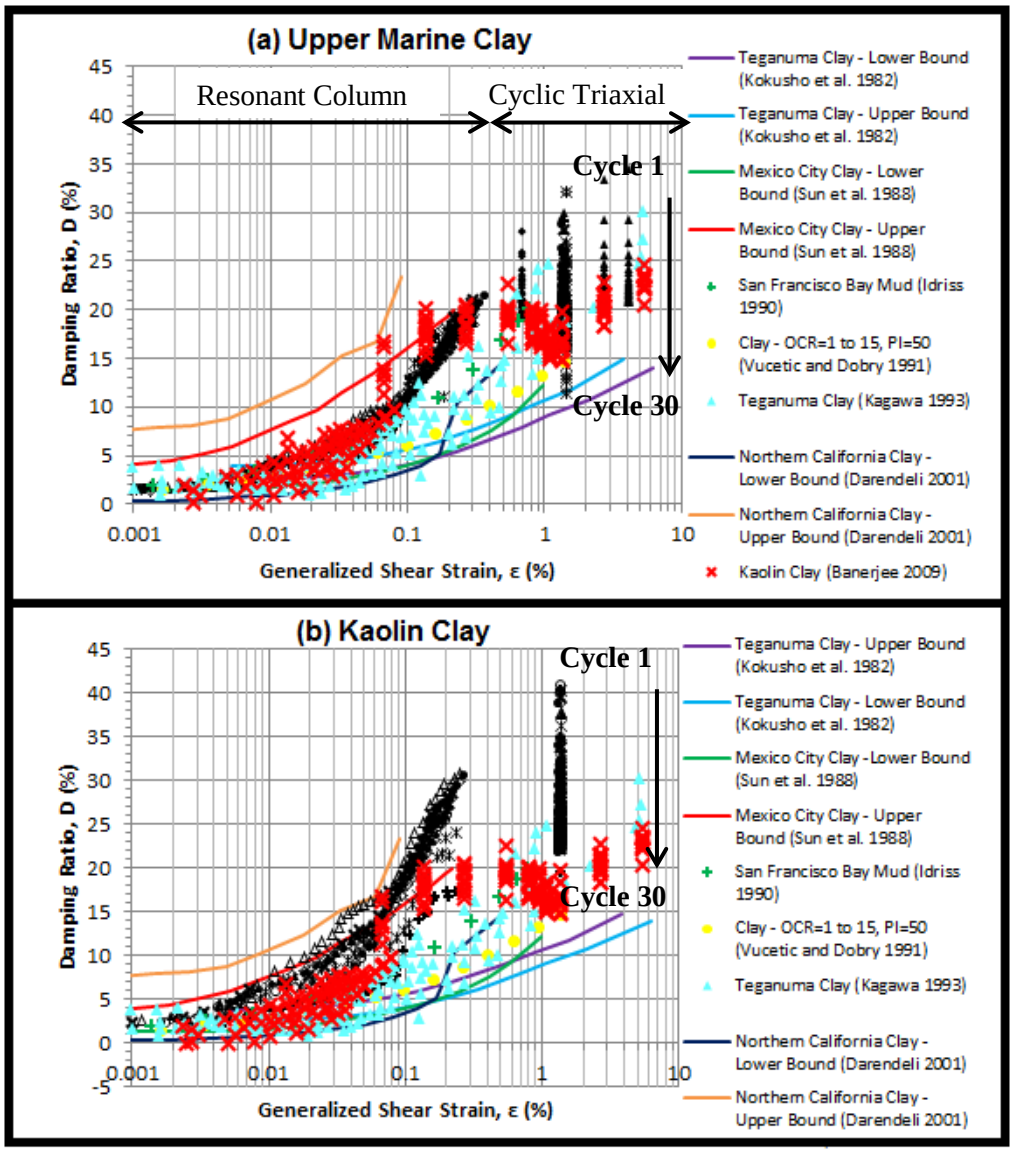

Figure 5.7 Comparison of the damping ratio curves against published literature data for (a) Singapore Upper Marine Clay and (b) Kaolin Clay.

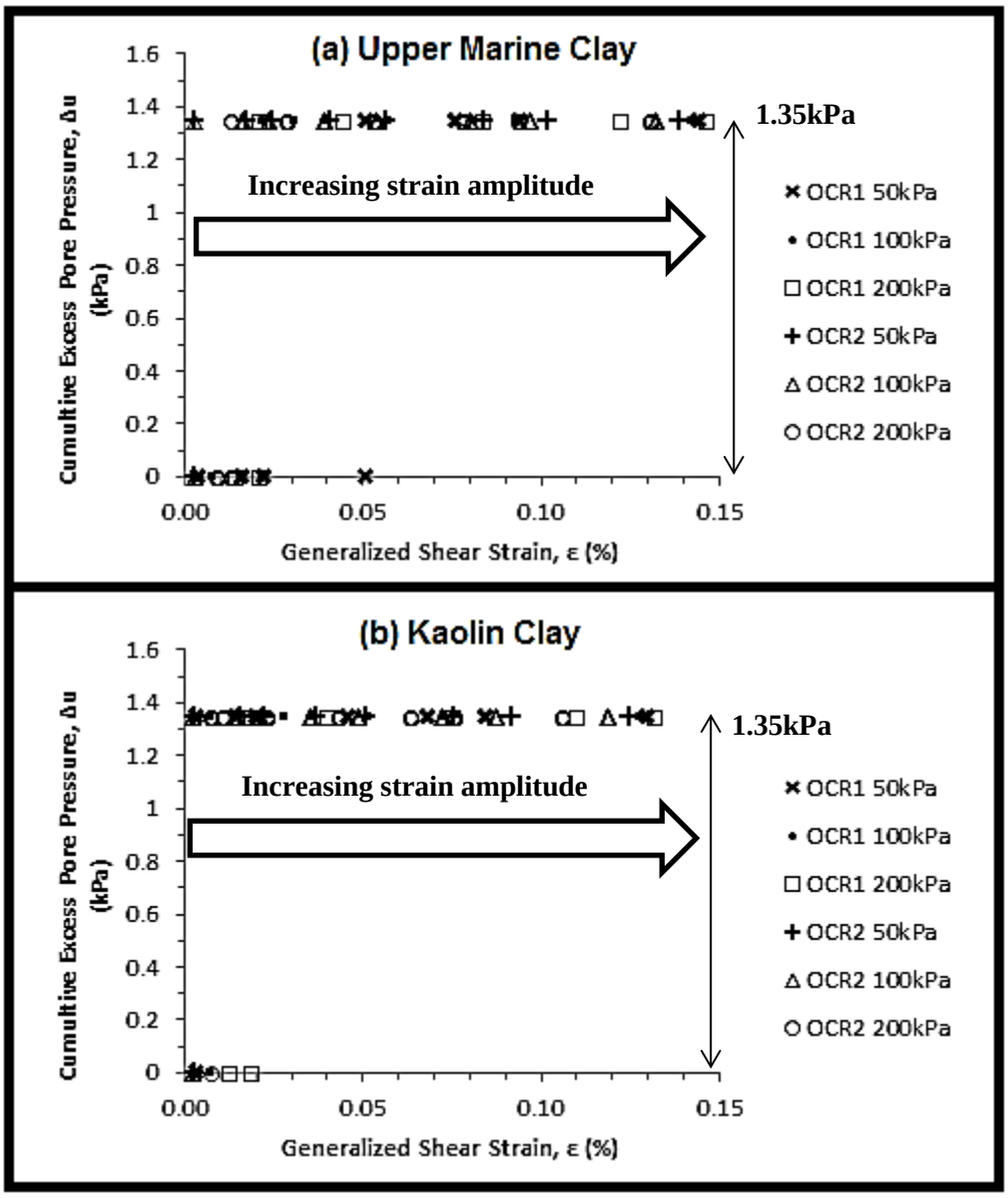

Figure 5.8 Excess pore pressure measurements during and after small-strain cyclic loadings for (a) Singapore Upper Marine Clay and (b) Kaolin Clay.

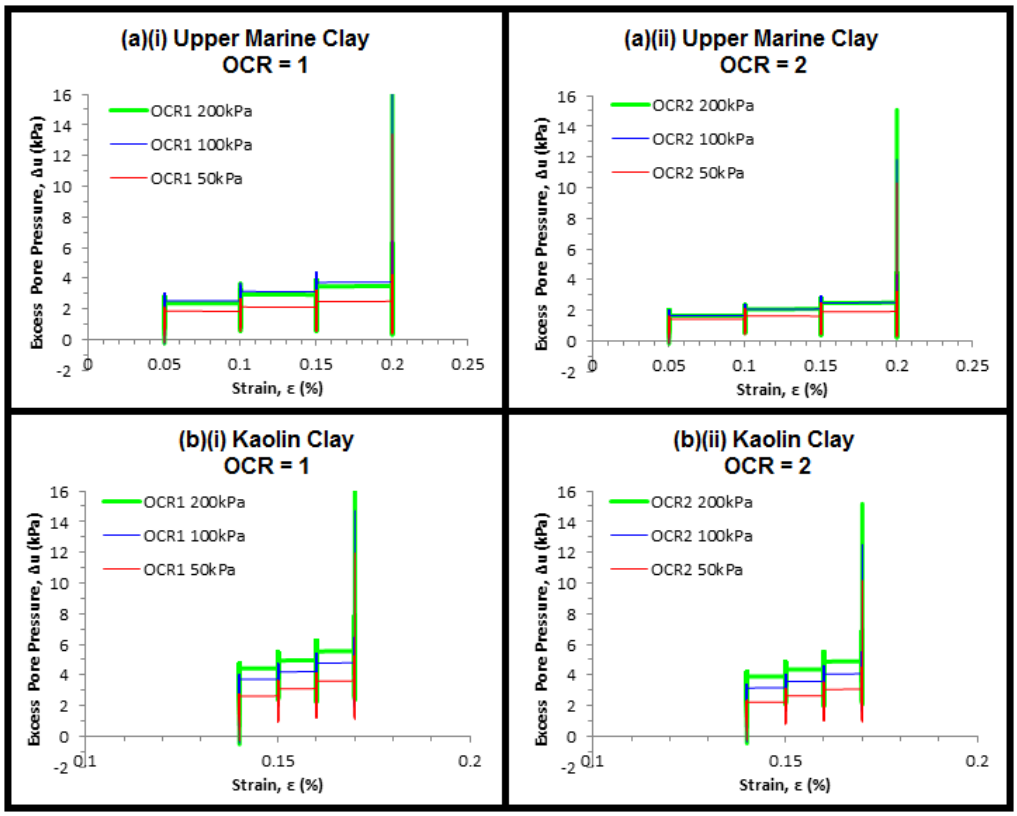

Figure 5.9 Plot of excess pore pressure against strain obtained from undrained cyclic triaxial tests on (a) Singapore Upper Marine Clay and (b) Kaolin Clay.

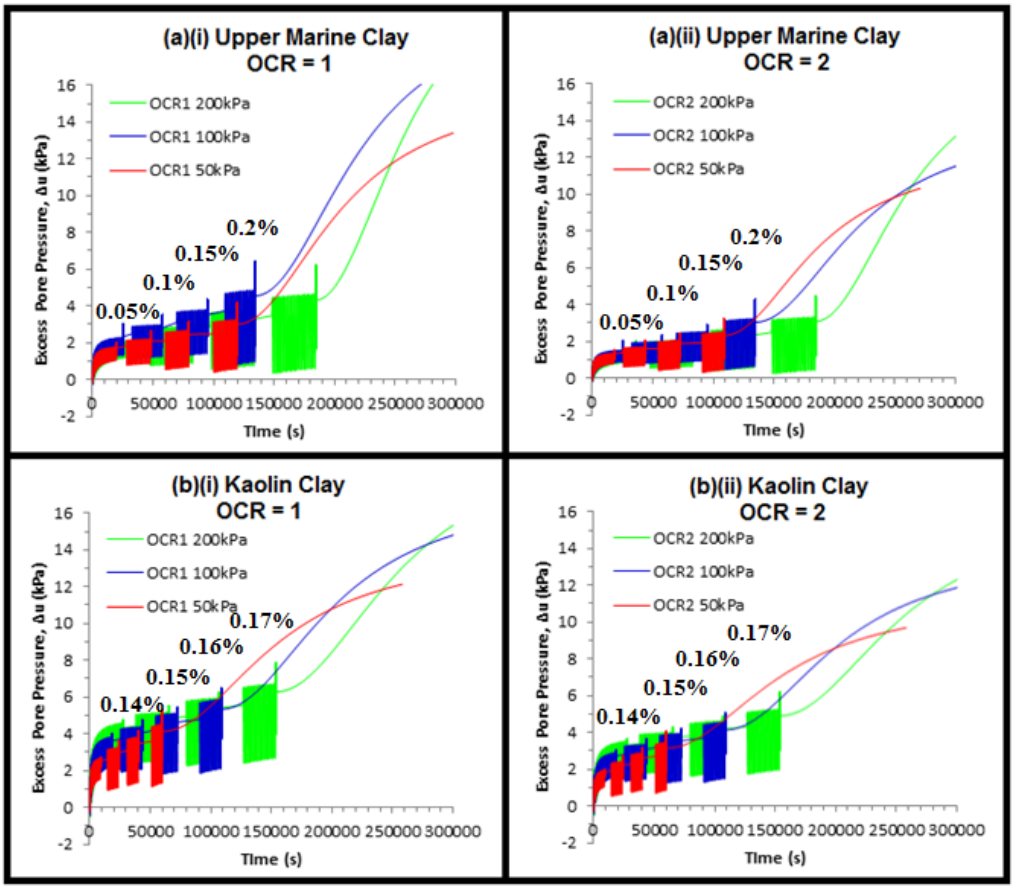

Figure 5.10 Plot of excess pore pressure against time obtained from undrained cyclic triaxial tests on (a) Singapore Upper Marine Clay and (b) Kaolin Clay.

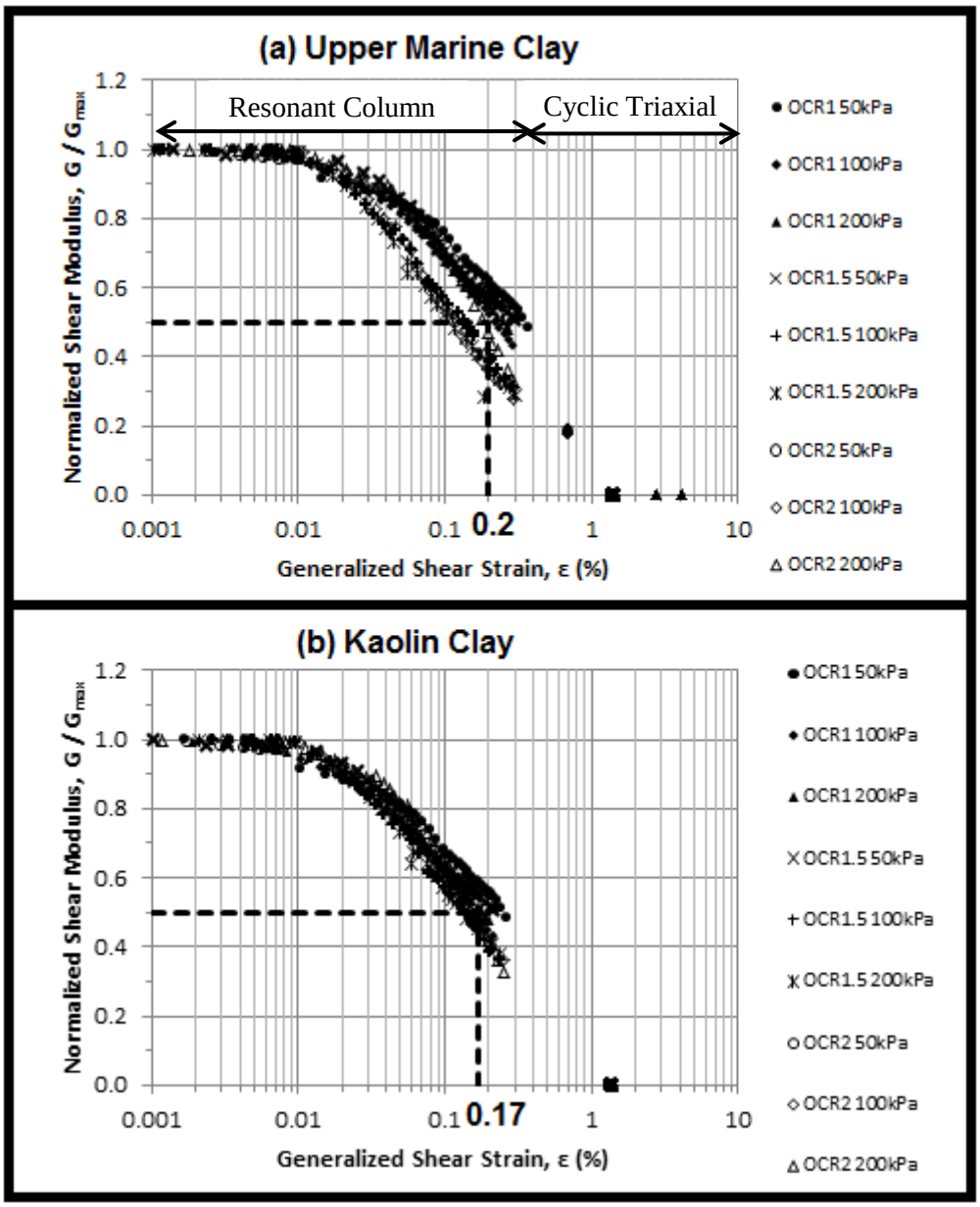

Figure 5.11 Degradation strain threshold from strain-dependent normalized shear modulus curves for (a) Singapore Upper Marine Clay and (b) Kaolin Clay.

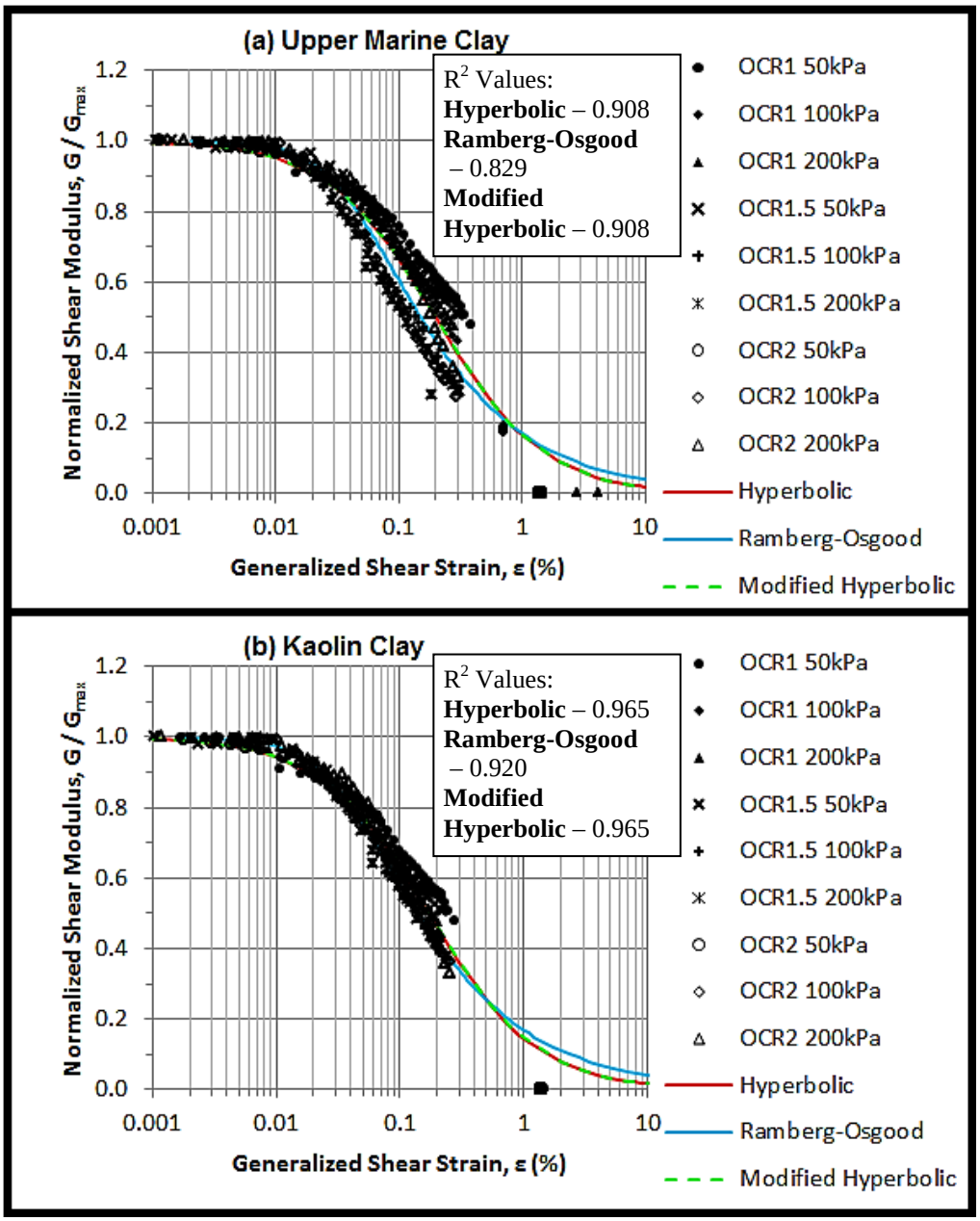

Figure 5.12 Comparison of the normalized shear modulus curves against available stress-strain models for (a) Singapore Upper Marine Clay and (b) Kaolin Clay.

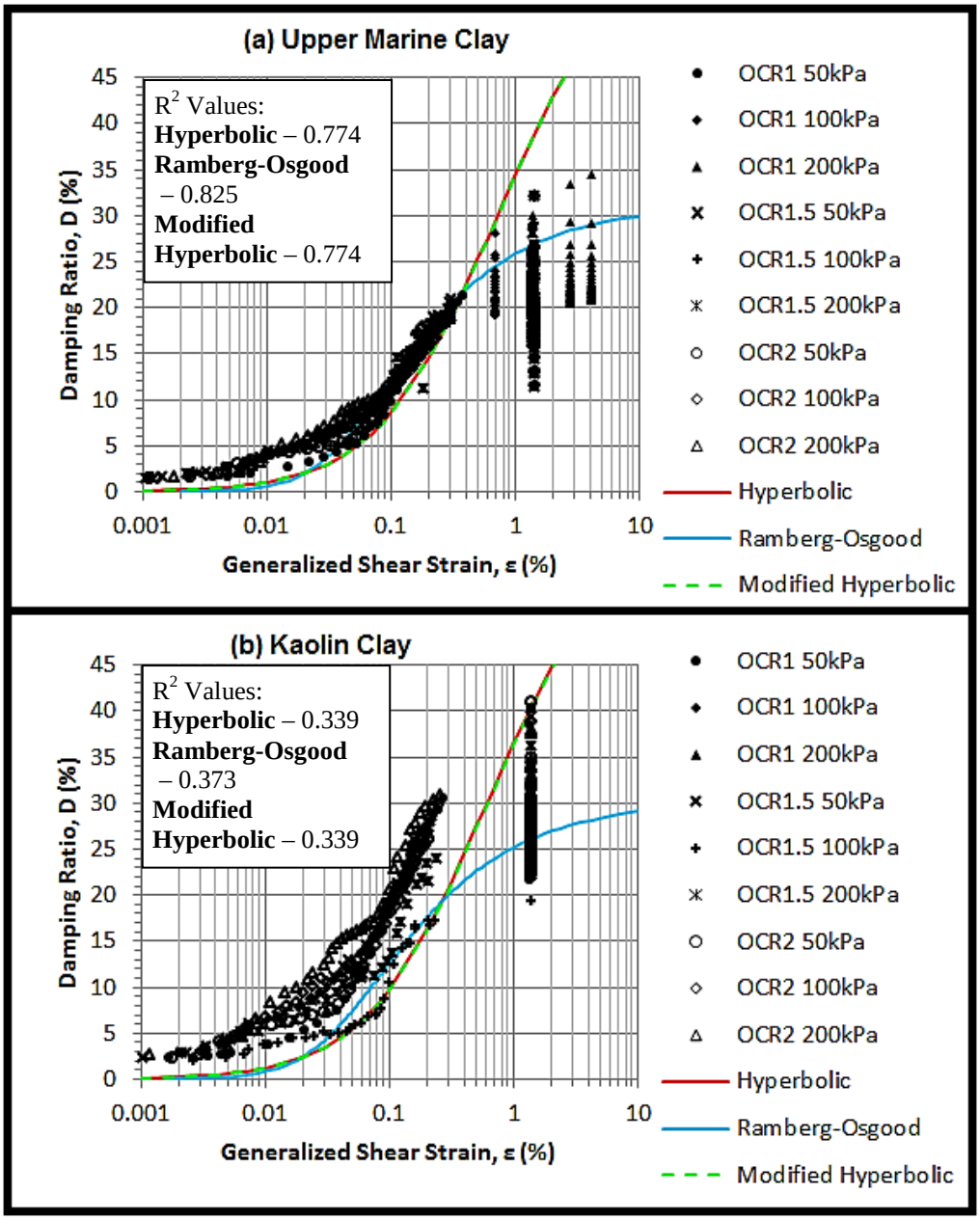

Figure 5.13 Comparison of the damping ratio curves against available stress-strain models for (a) Singapore Upper Marine Clay and (b) Kaolin Clay.

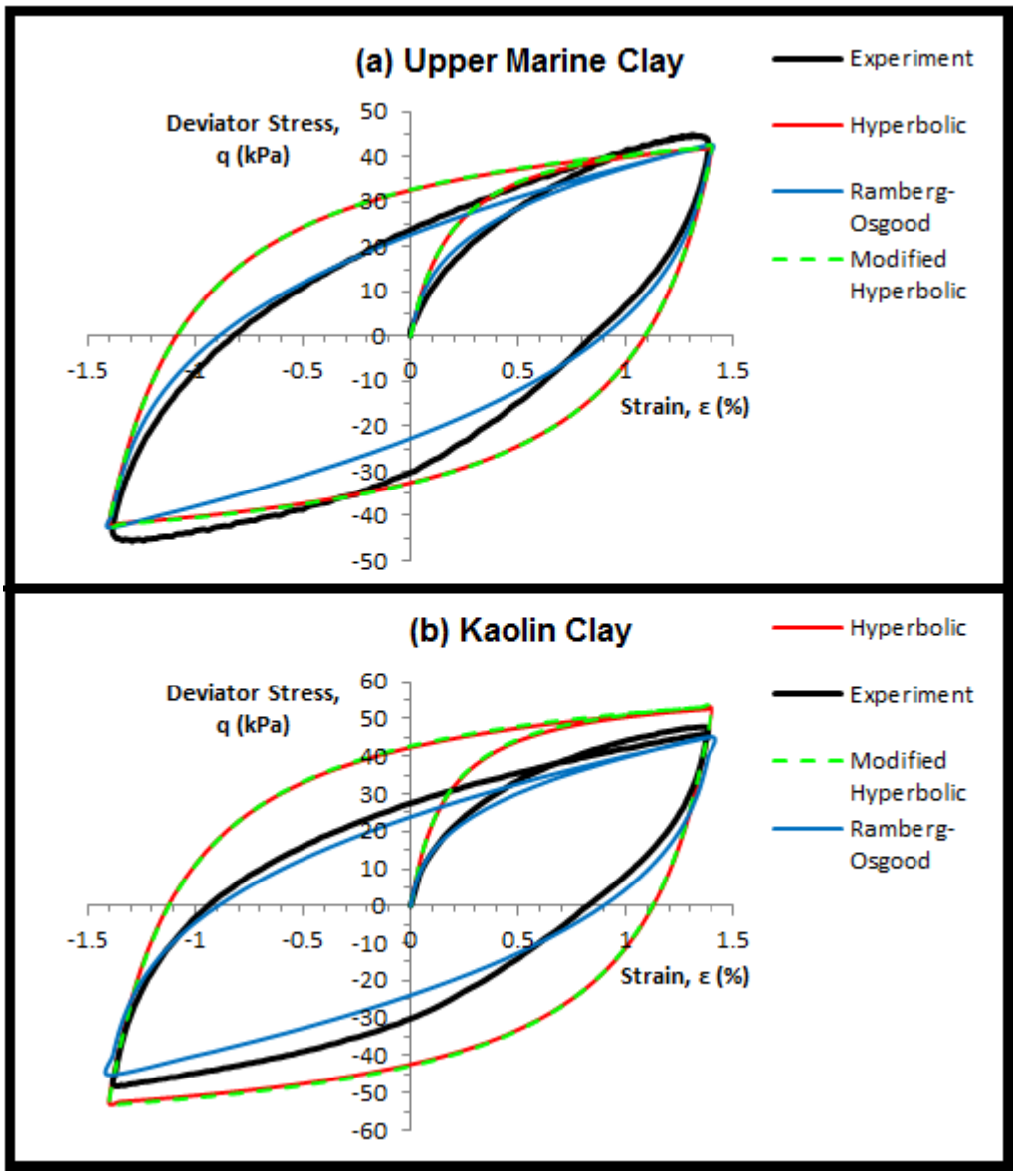

Figure 5.14 Comparison of the 1st load cycle of the experimental stress-strain curve (OCR = 1, p_c' = 100) against available stress-strain models for (a) Upper Marine Clay and (b) Kaolin Clay.

Chapter 6 – Cyclic and Post-Cyclic Behaviour

6.1 Overview

This chapter summarizes the cyclic and post-cyclic experimental results obtained in this study. Two-way strain-controlled undrained cyclic triaxial tests were performed on remoulded specimens (38mm diameter by 76mm height) of Marine Clay and kaolin, the standard properties of which had been reported previously in Section 3.1. Two-way (i.e. compression-extension) cyclic loadings were conducted. Two-way cyclic loading is often considered to be more "damaging" than one-way cyclic loading (Diaz-Rodriguez at al. 2000). Furthermore, in extreme cases of earthquake loading, complete stress reversals often occur when the earthquake-induced shear waves propagate upwards through a horizontal clay layer from the base rock (Thiers and Seed 1969). In the local context, local site amplification of earthquake bedrock motion through the soft Singapore Marine Clay strata is an important issue (Pan et al. 2006 and 2007), hence performing two-way cyclic tests on Singapore Marine Clay is important.

In Section 4.1.1, it was shown that intrinsic strain rate effects on pore pressure measurements, effective stress paths and stress-strain relationships are negligible when undrained cyclic triaxial tests on clays are conducted at a sufficiently slow rate for pore pressure equilibration. Since the focus of this section is not on strain rate effects, all tests were conducted at slow rates evaluated from Equations 4.10 and 4.11.

Tables 6.1 and 6.2 present the matrices of the tests for Marine Clay and kaolin specimens, respectively. Each test was conducted on a virgin (i.e. newly prepared) specimen. Test data were recorded in 2-second intervals. The parameters varied in the cyclic triaxial tests were the overconsolidation ratio (OCR = 1, 1.5, 2), effective confining pressure (p_c' = 50, 100, 200kPa), applied cyclic strain amplitude, loading period, and number of load cycles. All post-cyclic compression loading tests were conducted immediately after cyclic loading at the same strain rate (i.e. equivalent to the average cyclic strain rate) to avoid discontinuities between cyclic and post-cyclic effective stress paths such as those obtained by Andersen et al. 1980, Diaz-Rodriguez et al. (2000), Pillai et al. (2011) etc. This is to enable a direct comparison between the cyclic and post-cyclic behaviour of clays. The use of the average cyclic strain rate as the post-cyclic compression loading rate was verified to be sufficiently slow as the

mid-plane and base excess pore pressure measurements were observed to agree for all post-cyclic compression tests.

6.2 Cyclic Loading

Figure 6.1 shows typical excess pore pressure measurements, stress plots and stress-strain relationships obtained during the undrained cyclic tests on the two clay types. Post-cyclic effective stress paths are included in this figure as well. The critical state lines (CSL) are also plotted based on the critical state friction angles of 25.4 degrees and 24.9 degrees for Marine Clay and kaolin, respectively, measured in monotonic triaxial compression tests. The equivalent friction coefficients at critical state for the two clays are 1.0 and 0.98. The initial yield locus is plotted based on the isotropic preconsolidation pressure (p_c'). It is assumed to be elliptic as this is a commonly assumed shape of the yield locus for soft clays (e.g. Roscoe and Burland 1968; Zienkiewicz et al. 1985; Whittle and Kavvadas, 1994; Crouch and Wolf 1994). A final yield locus, also elliptical, is also drawn based on the maximum deviator stress reached in the monotonic undrained test. As Figure 6.1 shows, the post-cyclic stress paths are also asymptotic to this final yield locus. This indicates that the final yield locus applies to both monotonic and cyclic loading. Comparison of the initial and final yield loci shows that hardening has occurred; this being consistent with the expected volumetric hardening of the soft clay under undrained loading. For specimens of the same clay type subjected to the same effective confining pressure, the excess pore pressure measurements, effective stress paths and stress-strain relationships shown on Figure 6.1 for different number of applied cycles are similar, reflecting a remarkable degree of consistency amongst the specimens.

For all specimens, the mean effective stress decreases progressively with successive cycles, especially during the compression loading phase. This indicates generation of positive excess pore pressure, which is consistent with the contractive tendency of the soil. However, after the initial phase of the cyclic loading, the rate of decrease in effective stress (p') moderates when the deviator stress exceeds a certain level, in the compression phase (points B to C in Figure 6.2), leading finally to a partial recovery of the effective stress. In Figure 6.2, this is represented by a local increase in the gradient of the stress path, causing the latter to trend toward the vertical and then to the right. In the normally consolidated Marine Clay and kaolin specimens tested herein, the transition (point B) can be seen after the 4th cycle. This transition marks a change in the behaviour of the clay, from contractive (point A to point B in Figure 6.2)

to dilative (point B to point C in Figure 6.2) and will hereafter be referred to as phase transformation. This observed phase transformation behaviour is typical of the other test results obtained in this study. All phase transformation points plotted in the effective stress space (denoted by crosses in Figure 6.2) correspond to the lowest mean effective stress value (p') during the compression loading phase. This means that the rate of change in mean effective stress becomes instantaneously zero at the phase transformation points, which further implies that the rate of excess pore pressure variation is also zero at these points. As illustrated in Figures 6.3b and 6.4b, the phase transformation points corresponds to almost zero rate of change in excess pore pressure with a maximum deviation of 0.08kPa/s and 0.06kPa/s for Marine Clay and kaolin respectively. This indicates that the error arising from identifying the phase transformation point by visual inspection is acceptably small.

The phase transformation point defined herein is similar to that defined by Ishihara et al. (1975) for sand, who also defined a phase transformation line joining the points (Ishihara et al. 1975). Luong (1982) also defined a "characteristic state" line for sand, based on the criterion of zero volumetric strain increment. Lade and Ibsen (1997) showed that the two lines are essentially identical and actually slightly curved for sands; the gradient increasing with effective confining stress (σ_3'). However, their data also showed that the angle of the phase transformation line (ϕ_{PT}') varies by only about 5^o and trend seems to change with different types of sand. Furthermore, at sufficient high confining stress, the angle of phase transformation ϕ_{PT}' reaches a constant value.

During unloading, dilative behaviour is generally observed. The dilation continues into the extension loading phase (point D to point E in Figure 6.2). Upon unloading in the extension phase, the response becomes contractive again (point E to point F in Figure 6.2). This suggests that there is a significant amount of plastic volumetric strains occurring during unloading. After numerous cycles, the behaviour of the specimens reaches a steady state consisting of alternate phases of dilation and contraction, with dilation occurring at large deviator stress during loading and contraction occurring during unloading and possibly during loading at low deviator stress. As Figure 6.2 shows, the stress path adopts this distinctive profile after about 100 cycles.

These profiles are similar to the "butterfly" stress paths which are commonly observed in saturated dense sands, Figure 6.5, (Wood 1982; Lee and Schofield 1988; Lee and Foo 1991; Parra-Colmenares 1996; Elgamal et al. 2002; Yang and Sze 2011). Lee and Schofield (1988) associated this phenomenon with cyclic mobility of dense sand arising from cyclic oscillations in effective stress and shear stiffness of the sand.

Similar cyclic oscillations in the moduli are also evident in the stress-strain curves in Figure 6.1, although they are not as pronounced as those in Figure 6.5. The occurrence of phase transformation in specimens under cyclic loading has a direct influence on the stress-strain behaviour. As shown in Figures 6.6 and 6.7, in both Marine and kaolin clays, the occurrence of phase transformation and the recovery of mean effective stress leads to an increase of clay stiffness during the compression loading phase. The converse may be observed during the unloading phase that is attributed to the tendency to densify. Consequently, the stress-strain relationship is characterized by alternate hardening and softening phases and the hysteresis loops collapse in size to form S-shaped loops. These loops have been observed in past studies on clays (refer to Figure 2.7). Hence, from a qualitative viewpoint the stress-strain behaviour in both clay types is analogous to that observed in dense sands under cyclic loadings (Figure 6.5).

Although the occurrence of "cyclic mobility" in cohesive soils under cyclic loadings as observed in the current results have been reported in previous literature, only limited data are available (see Figure 6.8), and indeed much less so than for sand. Furthermore, the cyclic mobility features observed in Figure 6.8 were obtained in slow cyclic tests. For example, Sangrey et al. (1969) used 10 hours per cycle while Cekerevac and Laloui (2010) used 1 hour per cycle. Faster cyclic tests do not appear to exhibit such phenomenon (see Figure 6.9). Zergoun and Vaid (1994) noted that the stress-strain behaviour of Cloverdale Clay (see Figure 6.10) is similar to dense sands under cyclic loadings but no further investigation was carried out. Since effective stress results from slow cyclic tests provide a more reliable guide to the cyclic clay behaviour (as emphasized in Section 2.1.2), the cyclic mobility observed in the current results should not be overlooked.

6.2.1 Phase Transformation Line

Figure 6.11 shows the locations of the phase transformation points in the effective stress space for normally consolidated specimens of Marine Clay and kaolin

subjected to different effective preconsolidation pressures (p_c'). In this figure, the deviator stress (q) and mean effective stress (p') are normalized by the preconsolidation pressure (p_c') for easy comparison between specimens subjected to different stress histories. Linear regression trend lines have also been fitted through the phase transformation points. As shown in Table 6.3, linear regression lines provide the best fit with the highest R^2 values as compared to other regression types. As discussed earlier, Lade and Ibsen (1997) noted that the phase transformation lines for sand is curved. The observations from the current tests on clay shows that the straight line provides as good a fit as curves and also has the advantage of simplicity. For this reason, a straight line of phase transformation is assumed instead. This means that the dilation of the clay structure occurs when the stress ratio reaches a specific value, corresponding to the gradient of the phase transformation line, during the loading phase. Such stress-induced dilatancy is analogous to that reported for dense sands (Lade and Ibsen 1997; Lee and Foo 1991; Wan and Guo 2001).

Based on the fitted trendlines in Figure 6.11, the phase transformation lines correspond to a stress ratio of 0.598 for Marine Clay and 0.587 for kaolin. This is equivalent to a phase transformation angle (ϕ_{PT}') of 15.8º and 15.5º for Marine clay and kaolin, respectively. The preconsolidation pressure (p_c') does not have significant influence on the phase transformation stress ratio for both clay types. In a general form, the equation of the phase transformation line within the effective stress space can be expressed as:

$$\frac{q}{p_c'} = \eta_{PT}\left(\frac{p'}{p_c'}\right) \qquad [6.1]$$

Where:

q = Deviator stress,

p_c' = Preconsolidation pressure,

p' = Mean effective principal stress,

η_{PT} = Stress ratio of the phase transformation line.

For both clays, the stress ratios of the phase transformation lines (η_{PT}) is well approximated by

$$\eta_{PT} = 0.6M \qquad [6.2]$$

6.2.1.1 Effect of Overconsolidation Ratio (OCR)

In Figures 6.12 and 6.13, the effect of over-consolidation ratio on the location of the phase transformation line for kaolin was examined in two ways:

(i) Phase transformation points for specimens isotropically consolidated to different preconsolidation pressures (p_c') and then swelled to the same effective confining pressure (p_0') were plotted within the same normalized stress space to determine the stress ratio of the phase transformation line (Figure 6.12).

(ii) Phase transformation points for specimens isotropically consolidated to the same preconsolidation pressure (p_c') and then swelled to different effective confining pressures (p_0') were plotted within the same normalized stress space to determine the stress ratio of the phase transformation line (Figure 6.13).

For overconsolidated kaolin specimens subjected to the same effective confining pressure (p_0'), the overconsolidation ratio does not significantly influence the position of the phase transformation line within the normalized stress space (Figure 6.12). The derived stress ratios of 0.5956 (p_0' = 100kPa) and 0.598 (p_0' = 200kPa) have a nominal difference of approximately 2% from that reported for normally consolidated kaolin. The same observation applies for overconsolidated kaolin specimens subjected to the same effective preconsolidation pressure (p_c') where the derived stress ratios is approximately 3% higher than that for normally consolidated specimens (Figure 6.13). Equation 6.2 is thus applicable for both normally consolidated and overconsolidated (up to OCR = 2) kaolin specimens with preconsolidation pressures ranging 50kPa to 400kPa.

The overconsolidation ratio of Marine Clay, however, affects the manifestation of phase transformation. Unlike kaolin, the effective stress paths for all overconsolidated Marine Clay specimens do not exhibit phase transformation as illustrated in Figure 6.14. One intrinsic difference between Marine Clay and kaolin is that the former has a higher plasticity index of 53.2% compared to the latter's 41.2%. The absence of phase transformation in the effective stress paths of overconsolidated Marine Clay specimens may be attributed to the dilative tendency of overconsolidated clays. As shown in Figure 6.14, overconsolidated Marine Clay exhibits initial dilative behaviour during the compression loading phase of the first load cycle. Consequently, the effective stress paths of overconsolidated Marine Clay do not show initial

contractive followed by dilative behaviour (i.e. phase transformation), in contrast to the normally consolidated Marine Clay specimens that have a tendency to densify.

6.2.1.2 Effect of Cyclic Strain Amplitude

The deduced Equations 6.1 and 6.2 representing the phase transformation line were based on a fixed applied cyclic strain of approximately 1.4%. In order to verify their applicability to a range of cyclic strain amplitudes, the phase transformation points of cyclic triaxial results of normally consolidated Marine Clay specimens subjected to different strain amplitudes were compared in Figure 6.15. Based on the current results, the cyclic strain amplitude applied does not significantly influence the stress ratio of the phase transformation line. Equation 6.2 holds for a range of cyclic strain amplitude varying from 0.7% to 4.2%.

6.2.2 Influence of Various Parameters

Figures 6.16 to 6.18 examine the effects of (i) preconsolidation pressure, (ii) overconsolidation ratio and (iii) cyclic strain amplitude on the normalized effective stress paths and stress-strain loops of Marine Clay and kaolin. In all these figures, the comparison is made for stress path and stress-strain curve segments at the same normalized mean effective stress (p'/p_c'). In Figure 6.16, the phase transformation points for preconsolidation pressure of 100kPa and 200kPa (denoted by crosses) appended to these figures lie reasonably close to the phase transformation line defined by Equation 6.2 (i.e. dashed lines within the normalized stress spaces in Figures 6.16 to 6.18). The same can be said for overconsolidation ratio and cyclic strain amplitude (Figures 6.17 and 6.18).

Although the above parameters do not appear to influence the phase transformation stress ratio, increasing overconsolidation ratio and applied cyclic strain amplitude generally allow the specimens to reach a lower normalized mean effective stress for a given number of cycles (Figures 6.19 and 6.20). For instance, in Figure 6.19, for the normally consolidated Marine Clay specimen, the normalized mean effective stress after 100cycles is about 0.24. For a specimen of the same clay starting at over-consolidation ratio of 2, i.e. normally mean effective stress of 0.5, the normalized mean effective stress after 100 cycles is 0.10. Thus, less load cycles are required for overconsolidated specimens or specimens subjected to higher cyclic strain amplitude (4.2%) to degrade to the same value of normalized mean effective stress. This

explains the different load cycle numbers used in the comparison in Figures 6.17 and 6.18.

Based on Figures 6.16 to 6.18, the effects of preconsolidation pressure, overconsolidation ratio and applied strain amplitude can be summarized as follows:

(i) For the same overconsolidation ratio and cyclic strain amplitude, the fraction of mean effective stress lost over a given number of cycles is largely independent of the effective preconsolidation pressure (Figure 6.16). The corresponding normalized stiffness is also largely unaffected. The normalized shear modulus appears to be slightly lower for 200kPa preconsolidation pressure, but the difference is less than 0.038 (Figure 6.21) and unlikely to be significant.

(ii) As Figure 6.17 shows, specimens consolidated to different overconsolidation require different number of cycles to reach the same normalized mean effective stress during cyclic loading. For Marine Clay specimens, at a given normalized mean effective stress, the stress paths and stress-strain curves are fairly similar between specimens with different overconsolidation ratio except for the compressive unloading phase (point C to point D in Figure 6.17). For kaolin specimens, the difference between stress paths at the same normalized mean effective stress, of specimens consolidated to different overconsolidation ratio, appears to be larger. However, the stress-strain curves remain fairly similar. This suggests that the normalized mean effective stress has a significant influence on the stress-strain curve. It should also be highlighted that overconsolidated Marine Clay specimens do not exhibit phase transformation, and therefore phase transformation cannot be defined; this is an important difference.

(iii) The effect of the cyclic strain amplitude on the stress path does not appear to be very significant (see Figure 6.18). However, it has a much larger influence on the stress-strain curve, with the higher strain amplitude resulting in a “gentler” stress-strain curve with lower shear modulus (Figure 6.22). This is not unreasonable as larger strain amplitude is known to result in a lower shear modulus and greater degradation (e.g. Kokusho et al., 1982; Vucetic and Dobry 1991; Kagawa 1992; Banerjee 2009). For kaolin, the effect of cyclic strain amplitude was not investigated. However, Banerjee (2009) showed that the trend is similar.

6.3 Post-Cyclic Loading

As highlighted in Section 2.3.2, many past studies had concluded that, during undrained compression tests, the effective stress path of a normally consolidated clay after cyclic loading evolves into one similar to that of an overconsolidated clay. As Figure 6.23 shows, the post-cyclic effective stress paths of normally consolidated Marine Clay and kaolin specimens show dilative behaviour with the mean effective stresses recovering as the specimen heads towards the critical state analogous to that of heavily overconsolidated clays under monotonic shearing. This is quite typical of overconsolidated clay and may also be viewed as a part of the phase transformation behaviour of the soil. The post-cyclic stress-strain curves typically show an initial increase in deviator stress up to a peak value (when the stress state reaches the state boundary surface), followed by a decrease in stress to its critical value (see Figure 6.23). This suggests that the decrease in effective stress during cyclic loading has induced a highly overconsolidated state in the soil, causing it to dilate upon loading to failure. As shown in Figures 6.1 and 6.23, the assumed elliptical yield loci (corresponding to the state boundary and critical state boundary surfaces) appear to provide a good envelope to the post-cyclic effective stress paths for Marine Clay and kaolin.

6.3.1 Effect of Phase Transformation on Post-Cyclic Effective Stress Path

In order to clarify the relationship between the phase transformation line and the subsequent post-cyclic monotonic behaviour, post-cyclic compression tests were conducted immediately after prescribed numbers of load cycles. Figure 6.24 shows the stress paths and stress-strain plots of normally consolidated Marine Clay under undrained post-cyclic monotonic compression. The monotonic stress path, i.e. obtained without prior cyclic loading, is designated by N=0. Phase transformation points are also highlighted.

For Marine Clay specimens, there are three general forms which the stress paths can take, based on the range of normalized mean effective stress at the start of the post-cyclic monotonic loading. At high normalized mean effective stress, effective stress decreases throughout the loading phase of the cycle, indicating contractive tendency. This is similar to the behaviour of remoulded normally consolidated or lightly overconsolidated clays under monotonic loading. However, the magnitude of the decrease in mean effective stress observed in post-cyclic specimens is generally smaller than that in monotonically loaded specimens without prior cyclic loading. As

the mean effective stress decreases, transformation between contractive and dilative phases are manifested, separated by the phase transformation line. Phase transformation generally initiates when the normalized mean effective stress decreases to about 0.5 (see Figure 6.24a). The post-cyclic effective stress path also shows a similar change around this point. When the normalized mean effective stress decreases to between 0.5 and 0.6, the post-cyclic effective stress path becomes approximately vertical, indicating no pore pressure generation. This may be considered as a transition zone between contractive and dilative post-cyclic behaviour. The congruency of these two phenomena suggests that initiation of phase transformation in cyclic loading also marks the onset of dilative post-cyclic behaviour. As the normalized mean effective stress decreased below ~0.5, the post-cyclic stress path of Marine Clay shows significant dilative tendency, similar to that of overconsolidated clays (e.g. Andersen et al. 1980, Hyde and Ward 1985, Matsui et al. 1992, Yasuhara et al. 1992). As Figures 6.25 and 6.26 show, these behavioural changes are consistent regardless of the effective preconsolidation pressure and applied strain amplitude.

The behaviour of kaolin is different. As Figure 6.27 shows, normally consolidated kaolin specimen shows phase transformation under monotonic loading, without prior cyclic loading, that is N=0. For the cyclic loading specimens, phase transformation is also observed at normalized mean effective stress as high as 0.7. This motivates the postulation that phase transformation occurs throughout the entire range of possible normalized mean effective stress (p'/p_c'), from 0 to 1. For the monotonically loaded specimen, the phase transformation stress ratio is ~0.65. As Figure 6.27 shows, this lies reasonably close to the cyclic phase transformation stress ratio defined by Equation 6.2.

Similar behaviour in remoulded kaolin specimens subjected to static tests had been previously reported by Pillai et al. (2011). In their study, reconstituted kaolin specimens, prepared by mixing kaolin with distilled water and sheared at a strain rate 0.092%/min also produces effective stress paths with phase transformation. They attributed the phase transformation behaviour to the flocculated microstructure of the reconstituted specimens as phase transformation was not observed for kaolin specimens mixed with sodium oxalate to form a dispersed structure (see Figure 6.28).

6.3.2 Post-Cyclic Undrained Shear Strength

As discussed in Section 2.3.2, the undrained shear strength of normally consolidated or lightly overconsolidated clays have been observed to decrease after cyclic loading. The amount of strength reduction was reported to be related to the ratio of peak cyclic stress/strain to the monotonic failure stress/strain (e.g. Thiers and Seed 1969; Koutsoftas1978; Sangrey and France 1980; Yasuhara 1994; Diaz-Rodriguez et al. 2000) or the cumulative plastic strain and cyclic-induced excess pore pressure (e.g. Yasuhara et al. 1992; Li et al. 2011). As Figure 6.20 shows, the above two factors are related since the peak cyclic strain also affects the amount of excess pore pressure accumulated.

As observed in Figures 6.24 to 6.26, undrained strain-controlled cyclic loading resulted in some residual deviator stresses in both Marine Clay and kaolin at the end of cyclic loading. Figure 6.29 shows the cyclic-induced residual deviator stresses at the start of post-cyclic loading summarized from tests using different number of load cycles. The maximum residual deviator stresses recorded are ~38kPa and ~35kPa for Marine Clay and kaolin respectively. This is ~18% and ~19% of the post-cyclic undrained strength of the corresponding specimens. The residual deviator stresses generally decreases with decreasing normalized mean effective stresses. This suggests that the residual deviator stresses are influenced by the stress reversals experienced during two-way cyclic loadings in a similar way as the maximum cyclic deviator stresses decrease with increasing load cycles (corresponding to decreasing normalized mean effective stresses). Such behaviour had been attributed to the Bauschinger effect in which cyclic-induced plastic deformations cause directional anisotropy in soils; i.e. the plastic deformation produced in one direction of loading reduces the soil resistance in the subsequent opposite direction of loading (Chen and Baladi 1985).

Figure 6.30 presents the post-cyclic undrained shear strength, which is defined herein as half of the peak deviator stress measured in post-cyclic tests. The monotonic undrained shear strengths without prior cyclic loading are also included in this figure. As can be seen, the post-cyclic undrained shear strength is almost always lower than the monotonic undrained shear strength. As shown in Figure 6.30, for normally consolidated specimens, the undrained strength is largely independent of its cyclic stress history except for specimens consolidated under 200kPa effective confining pressure, which shows a post-cyclic strength decrease of about 24%. For these specimens, the undrained strength degrades approximately linearly with respect to

decreasing normalized mean effective stress. This relation was observed to be independent of the cyclic strain amplitude (see Figure 6.30c(i)). Strength degradation becomes more apparent at lower confining pressure as over-consolidation ratio increases. For over-consolidation ratio of 2, strength degradation was evident even at 50kPa confining pressure. In all cases, the undrained shear strength decreases linearly with normalized mean effective stress.

The observed cyclic-induced degradation in undrained shear strength of normally consolidated clay contradicts the notion that cyclic-induced overconsolidation is same as unloading-induced overconsolidation (e.g. Taylor and Bacchus 1969; Andersen et al. 1980; Yasuhara et al. 1992). For instance, as Figure 6.31 shows, in the idealized critical state framework (Schofield and Wroth 1968), an isotropic normally consolidated specimen without a prior cyclic history will follow the effective stress path AB, from an initial isotropic state at A to ultimate failure at B. Likewise, specimens starting from initial states C and D will also reach ultimate failure at B and will therefore have the same undrained shear strength at critical state as A. In undrained loading, the critical state is only dependent upon the void ratio or specific volume. If the critical state framework is adhered to by cyclically loaded clay specimens in undrained condition, then the void ratio (or specific volume) ought to remain unchanged. Therefore the undrained shear strength at ultimate failure should also remain unchanged, regardless of whether its post-cyclic state is at C or D. Hence, real clay evidently does not behave exactly in the manner prescribed by the critical state framework.

Andersen et al. (1980) reported that a normally consolidated Drammen clay specimen which has a post-cyclic mean effective stress of 95kPa, has a post-cyclic stress path which is almost identical to the stress path for standard static testing on an overconsolidated specimen with overconsolidation ratio of 4 (see Figure 2.25c). Atkinson and Richardson (1987) also reported that the effective stress paths of overconsolidated clays (by unloading) that lie on the dry side of critical can reach a peak deviator stress at point P in Figure 6.32a and subsequently terminate at a lower deviator stress at point T without approaching point F corresponding to the critical failure that is reached for normally consolidated specimens. They attributed this to the development of shear zones within overconsolidated specimens during undrained loading that had resulted in localized drainage which translates to small specific volume changes although the overall volume of the specimen was constant. Consequently, the undrained strength of overconsolidated clay may be lower than that

of normally consolidated clay subjected to the same preconsolidation pressure. In view of this, the observed cyclic-induced undrained shear strength reduction in normally consolidated clays could have occurred due to the same phenomenon (see Figure 6.33). Similarly, the cyclic-induced degradation in undrained shear strength of overconsolidated clay may be attributed to the development of shear zones. Visual inspection of post-test specimens shows that the development of shear zones was more extensive in overconsolidated clays that had undergone cyclic loading compared to overconsolidated clays that did not undergo cyclic loading (see Figure 6.34). Consequently, it is likely that cyclic loading facilitates the formation of shear zones in overconsolidated clays during post-cyclic monotonic loading such that undrained strength degradation was observed.

Yasuhara et al. (1983) also indicated that the cyclic-induced undrained shear strength reduction in normally consolidated clays could not be adequately explained through available theoretical frameworks. In order to verify if the post-cyclic effective stress path of a cyclically-induced overconsolidated clay is to the same as that overconsolidated by real unloading such that both correspond to the same value of undrained shear strength, additional tests were conducted on Marine Clay and kaolin specimens overconsolidated by real unloading.

6.3.3 Cyclic-Induced Apparent Overconsolidation

Table 6.4 summarized the triaxial compression tests conducted on overconsolidated Marine Clay and kaolin specimens. For this test series, the confining pressure (p_0') corresponds to the confining pressure of the normally consolidated clay at the start of the post-cyclic monotonic test (i.e. Point O in Figure 6.35). The preconsolidation pressures (p_c') are back-calculated using the compression and swelling indices derived from isotropic triaxial compression tests (refer to Figure 6.35).

Figures 6.36 and 6.37 compare the monotonic (overconsolidated) and post-cyclic undrained stress paths and stress-strain curves. Figure 6.35 shows the scheme for calculating the equivalent overconsolidation ratio. For a specimen cyclically loaded undrained from A to O, the equivalent preconsolidation pressure (p_c') was obtained by constructing the swelling line through O and then projecting it to point C. The monotonic specimen was prepared by isotropically consolidating it to p_c' and then allow it to swell back to p_0'. In Figures 6.36 and 6.37, the comparison was conducted for specimens prepared using three preconsolidation pressures (p_c'). As shown in both

figures, the post-cyclic stress paths and stress-strain curves lie close to those of specimens with the equivalent unloading-induced overconsolidation ratio. In addition to the shape of the effective stress path, similarities are also detected in the maximum deviator stress achieved. All effective stress paths are observed to converge on the critical state line as well. Furthermore, a comparison of the post-cyclic Marine Clay specimens that were subjected to varying cyclic strain amplitudes (0.7 to 4.2%) with the respective overconsolidated specimens (Figure 6.38) showed that the above observations are independent of the applied cyclic strain amplitude.

The foregoing comparison shows that the apparent overconsolidation effect induced by the undrained cyclic loading is similar to that induced by swelling from an equivalent preconsolidation pressure p_c'. Hence, the apparent overconsolidation ratio present in the cyclically loaded specimen may be taken to be equal or close to that of the overconsolidated specimens in Table 6.4 (i.e. p_c'/p_0'). As shown in Table 6.5, the difference in the undrained strengths of cyclically loaded specimens and their respective overconsolidated specimens is less than 8%. Therefore, the results and discussion in this section shows that the post-cyclic effective stress paths of clays with apparent overconsolidation induced by cyclic loading are similar to those of clays overconsolidated by real unloading. The similarities in the maximum deviator stress achieved indicate that the undrained strength of a cyclically loaded specimen may be predicted based on the apparent overconsolidation ratio induced by the end of the cyclic loading phase.

Table 6.1 Experimental matrix for Singapore Marine Clay specimens.

SINGAPORE MARINE CLAY EXPERIMENTAL MATRIX							
No.	**OCR**	**Mean Effective Pressure (kPa)**		**Applied Cyclic Strain**		**Period (min)**	**No. of Load Cycles**
		Confining, p_0'	**Preconsolidation, p_c'**	**Amplitude (mm)**	**Strain (%)**		
1	1	50	50	-	-	-	0
2	1	50	50	1	1.32	10	5
3	1	50	50	1	1.42	10	10
4	1	50	50	1	1.35	10	15
5	1	50	50	1	1.35	10	20
6	1	50	50	1	1.38	10	100
7	1	100	100	-	-	-	0
8	1	100	100	0.5	0.70	14	10
9	1	100	100	0.5	0.69	14	15
10	1	100	100	0.5	0.70	14	20
11	1	100	100	0.5	0.70	14	110
12	1	100	100	1	1.39	14	2
13	1	100	100	1	1.39	14	3
14	1	100	100	1	1.32	14	4
15	1	100	100	1	1.39	14	5
16	1	100	100	1	1.39	14	6
17	1	100	100	1	1.39	14	20
18	1	100	100	1	1.39	14	30
19	1	100	100	1	1.38	14	100
20	1	200	200	-	-	-	0
21	1	200	200	1	1.42	60	2
22	1	200	200	1	1.42	60	3
23	1	200	200	1	1.44	60	4
24	1	200	200	1	1.42	60	5
25	1	200	200	1	1.42	60	6
26	1	200	200	1	1.40	60	10
27	1	200	200	1	1.40	60	30
28	1	200	200	1	1.40	60	100
29	1	200	200	2	2.83	120	3
30	1	200	200	2	2.82	120	10
31	1	200	200	2	2.80	120	30
32	1	200	200	2	2.80	120	100
33	1	200	200	3	4.19	180	3
34	1	200	200	3	4.20	180	10
35	1	200	200	3	4.18	180	30
36	1	200	200	3	4.19	180	100
37	1.5	50	75	-	-	-	0
38	1.5	50	75	1	1.36	12	7

39	1.5	50	75	1	1.41	12	100
40	1.5	100	150	-	-	-	0
41	1.5	100	150	1	1.39	45	7
42	1.5	100	150	1	1.41	45	100
43	1.5	200	300	-	-	-	0
44	1.5	200	300	1	1.40	75	7
45	1.5	200	300	1	1.43	75	100
46	2	50	100	-	-	-	0
47	2	50	100	1	1.38	14	10
48	2	50	100	1	1.40	14	100
49	2	100	200	-	-	-	0
50	2	100	200	1	1.40	60	10
51	2	100	200	1	1.43	60	100
52	2	200	400	-	-	-	0
53	2	200	400	1	1.47	90	7
54	2	200	400	1	1.40	90	100

Table 6.2 Experimental matrix for Kaolin Clay specimens.

KAOLIN CLAY EXPERIMENTAL MATRIX							
No.	**OCR**	**Mean Effective Pressure (kPa)**		**Applied Cyclic Strain**		**Period (min)**	**No. of Load Cycles**
		Confining, p_0'	**Preconsolidation, p_c'**	**Amplitude (mm)**	**Strain (%)**		
1	1	50	50	-	-	-	0
2	1	50	50	1	1.39	5	2
3	1	50	50	1	1.35	5	100
4	1	100	100	-	-	-	0
5	1	100	100	1	1.38	10	1
6	1	100	100	1	1.38	10	6
7	1	100	100	1	1.38	10	30
8	1	100	100	1	1.38	10	100
9	1	200	200	-	-	-	0
10	1	200	200	1	1.40	15	4
11	1	200	200	1	1.41	15	100
12	1.5	50	75	-	-	-	0
13	1.5	50	75	1	1.36	10	2
14	1.5	50	75	1	1.38	10	100
15	1.5	100	150	-	-	-	0
16	1.5	100	150	1	1.39	15	3
17	1.5	100	150	1	1.39	15	100
18	1.5	200	300	-	-	-	0
19	1.5	200	300	1	1.40	30	3
20	1.5	200	300	1	1.39	30	100
21	2	50	100	-	-	-	0
22	2	50	100	1	1.37	10	3
23	2	50	100	1	1.38	10	100
24	2	100	200	-	-	-	0
25	2	100	200	1	1.38	15	2
26	2	100	200	1	1.40	15	100
27	2	200	400	-	-	-	0
28	2	200	400	1	1.38	30	2
29	2	200	400	1	1.39	30	100

Table 6.3 Comparison of different regression types.

Regression Type	R^2 Values	
	Singapore Upper Marine Clay	kaolin
Linear	0.8734	0.7166
Quadratic	0.8652	0.7046
Power	0.8469	0.6290

Table 6.4 Additional triaxial compression tests.

Clay	Mean Effective Pressure (kPa)		OCR	Post-cyclic test to compare against			
	Confining, p_0'	Preconsolidation, p_c'		OCR	p_c' (kPa)	Cyclic Amplitude (mm)	No. of Cycles
Singapore Upper Marine Clay	28	56	2.0	1	50	1 (≈ 1.4%)	5
	15	63	4.2	1	50	1 (≈ 1.4%)	100
	67	108	1.6	1	100	0.5 (≈ 0.7%)	15
	45	117	2.6	1	100	0.5 (≈ 0.7%)	110
	70	107	1.5	1	100	1 (≈ 1.4%)	2
	24	132	5.5	1	100	1 (≈ 1.4%)	100
	122	220	1.8	1	200	1 (≈ 1.4%)	3
	73	244	3.3	1	200	1 (≈ 1.4%)	30
	114	223	2.0	1	200	2 (≈ 2.8%)	3
	52	260	5.0	1	200	2 (≈ 2.8%)	30
	79	239	3.0	1	200	3 (≈ 4.2%)	3
	29	291	10.0	1	200	3 (≈ 4.2%)	100
kaolin	29	60	2.1	1	50	1 (≈ 1.4%)	2
	10	88	8.8	1	50	1 (≈ 1.4%)	100
	70	114	1.6	1	100	1 (≈1.4%)	1
	31	150	4.8	1	100	1 (≈ 1.4%)	30
	102	253	2.5	1	200	1 (≈ 1.4%)	4
	53	317	6.0	1	200	1 (≈ 1.4%)	100

Table 6.5 Comparison of post-cyclic undrained shear strength against the undrained shear strength from monotonic compression of equivalent swelling-induced overconsolidated specimens.

Clay	Post-cyclic Shearing of Specimens					Undrained Shearing of Equivalent Swelling-Induced OCR Specimens		
	OCR	p_c' (kPa)	Cyclic Amplitude (mm)	No. of Cycles	Undrained Strength (kPa)	AOCR	Undrained Strength (kPa)	% difference in strength
Singapore Upper Marine Clay	1	50	1 (≈ 1.4%)	5	16.2	2.0	16.2	0.0
				100	17.5	4.2	17.1	-1.9
	1	100	0.5 (≈ 0.7%)	15	35.0	1.6	32.8	-6.1
				110	34.6	2.6	32.9	-4.9
			1 (≈ 1.4%)	2	33.6	1.5	31.7	-5.6
				100	33.9	5.5	33.5	-1.0
	1	200	1 (≈ 1.4%)	3	61.7	1.8	58.3	-5.4
				30	63.5	3.3	62.9	-1.0
			2 (≈ 2.8%)	3	58.9	2.0	56.0	-4.9
				30	48.7	5.0	50.1	2.8
			3 (≈ 4.2%)	3	54.4	3.0	53.4	-1.8
				30	37.6	10.0	37.0	-1.6
Kaolin Clay	1	50	1 (≈ 1.4%)	2	33.8	2.1	33.6	-0.5
				100	31.8	8.8	31.8	-0.2
	1	100	1 (≈1.4%)	1	51.4	1.6	49.2	-4.4
				30	59.2	4.8	56.6	-4.3
	1	200	1 (≈ 1.4%)	4	91.4	2.5	84.1	-7.9
				100	76.1	6.0	73.7	-3.0

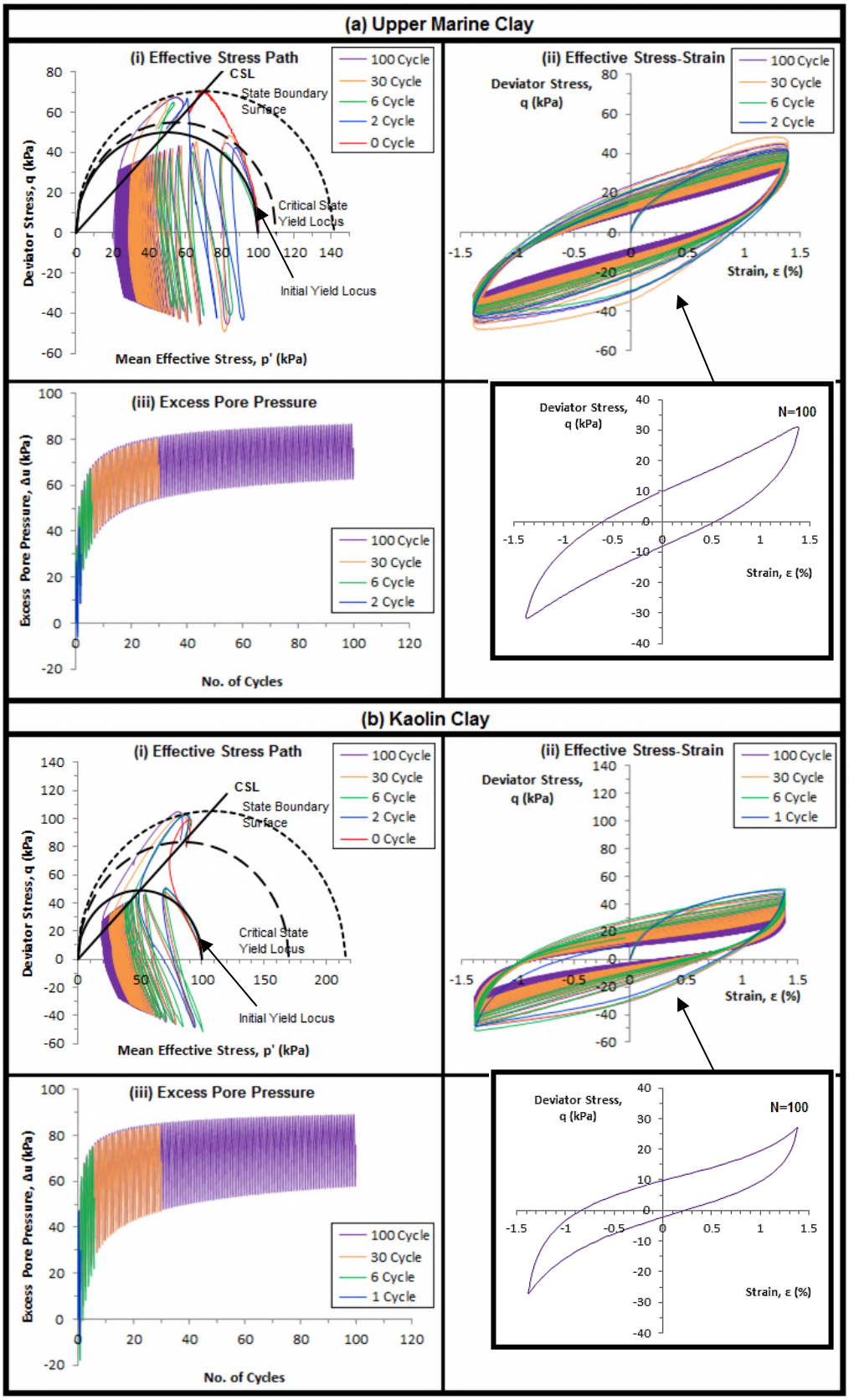

Figure 6.1 Cyclic behaviour of normally consolidated specimens (p_c' = 100kPa) of (a) Singapore Marine Clay and (b) Kaolin Clay.

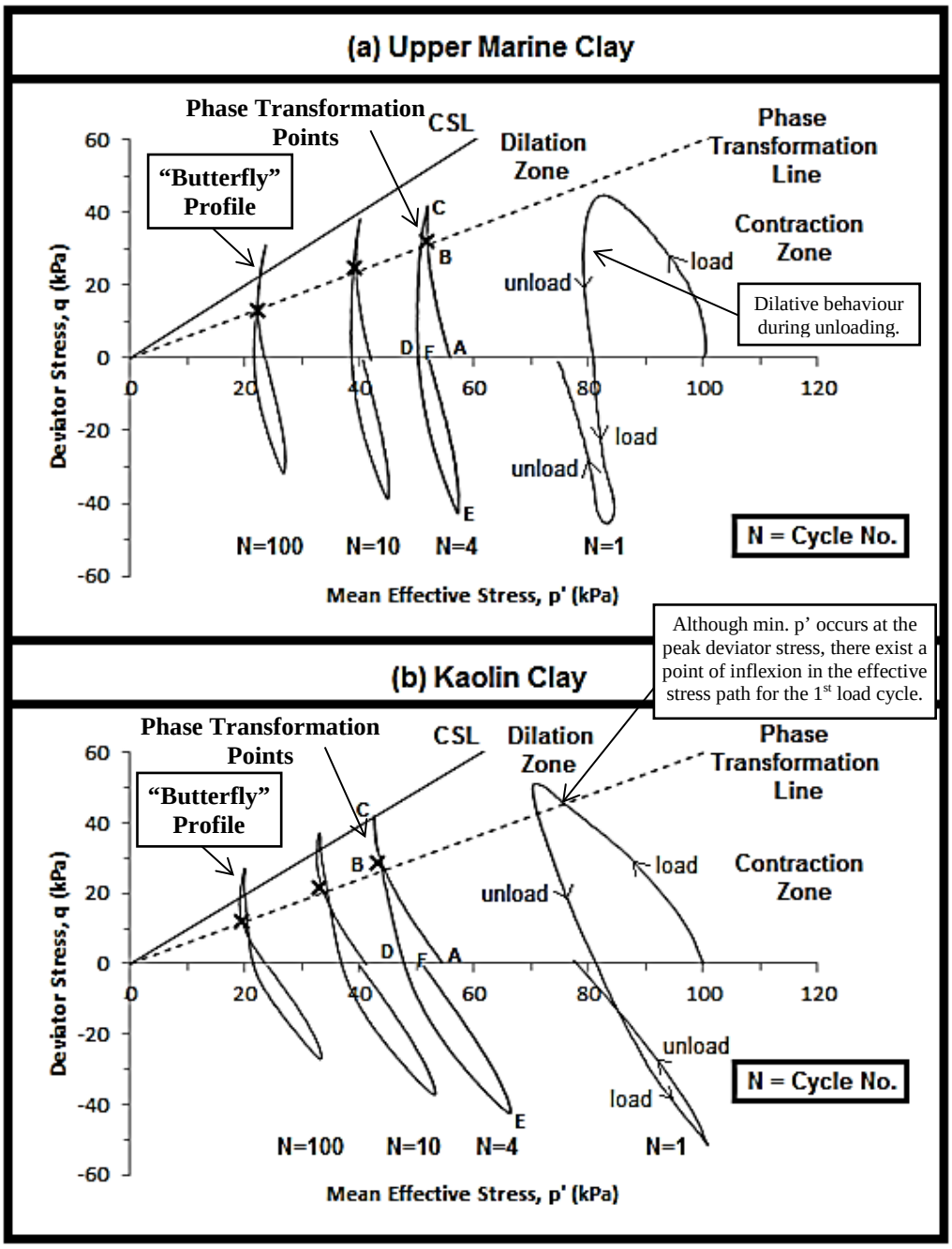

Figure 6.2 Typical phase transformation from contractive to dilative behaviour observed in normally consolidated specimens (p_c' = 100kPa) of (a) Singapore Upper Marine Clay and (b) Kaolin Clay.

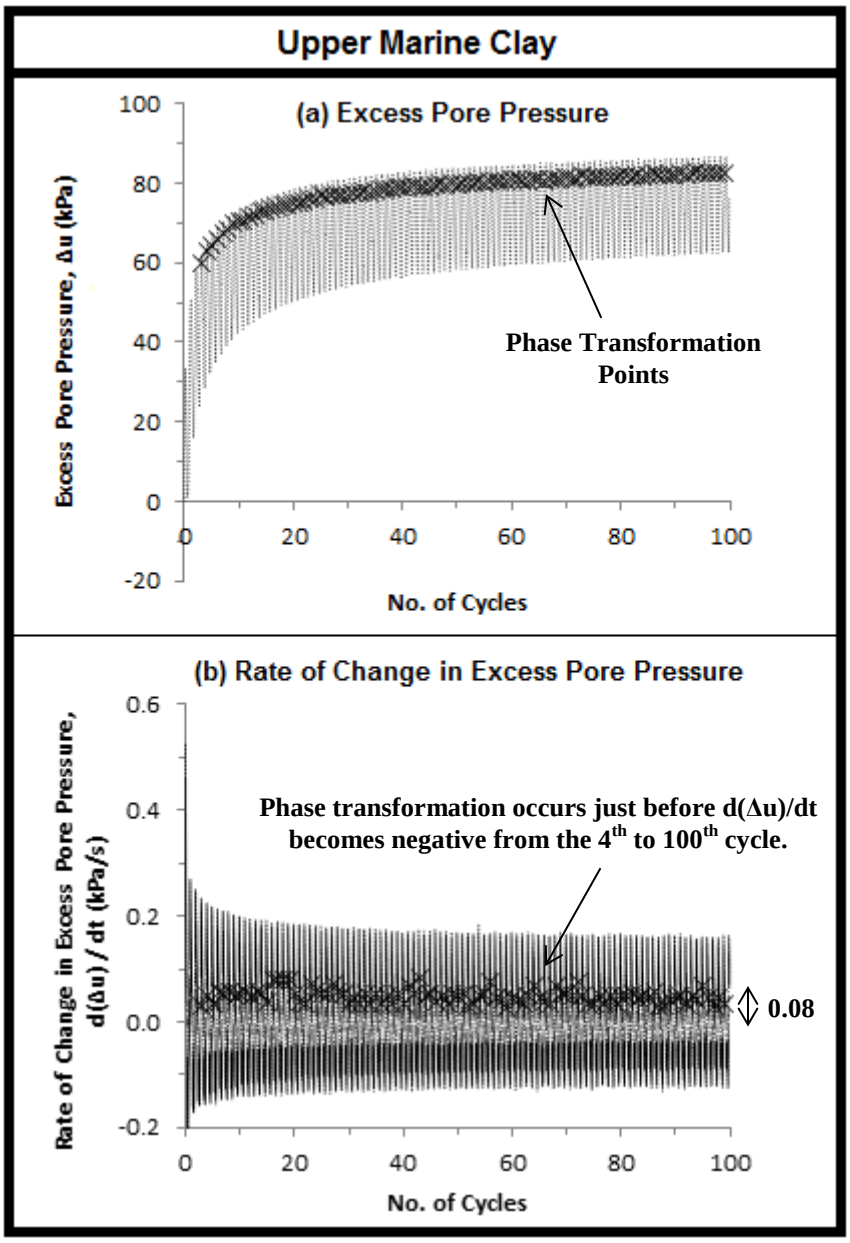

Figure 6.3 Excess pore pressure measurements for normally consolidated Singapore Upper Marine Clay (p_c' = 100kPa).

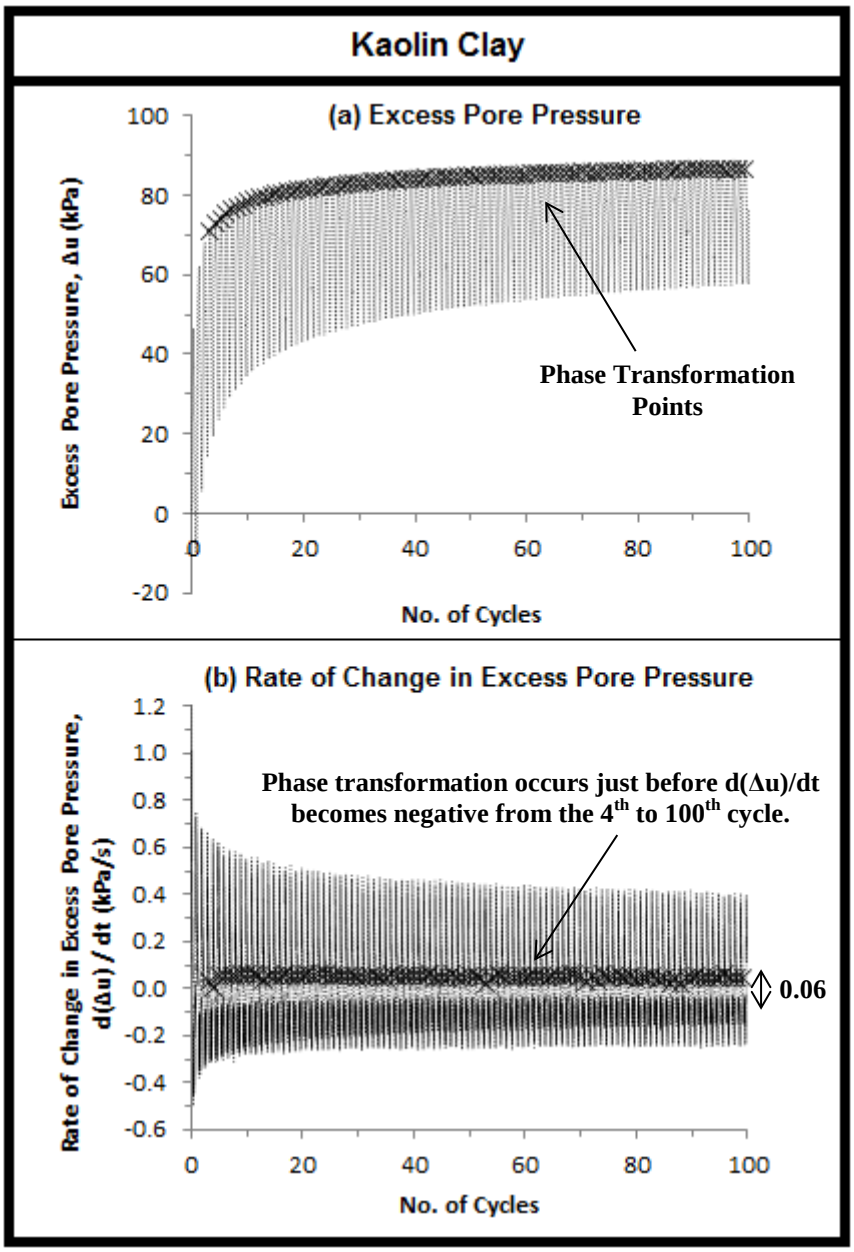

Figure 6.4 Excess pore pressure measurements for normally consolidated Kaolin Clay (p_c' = 100kPa).

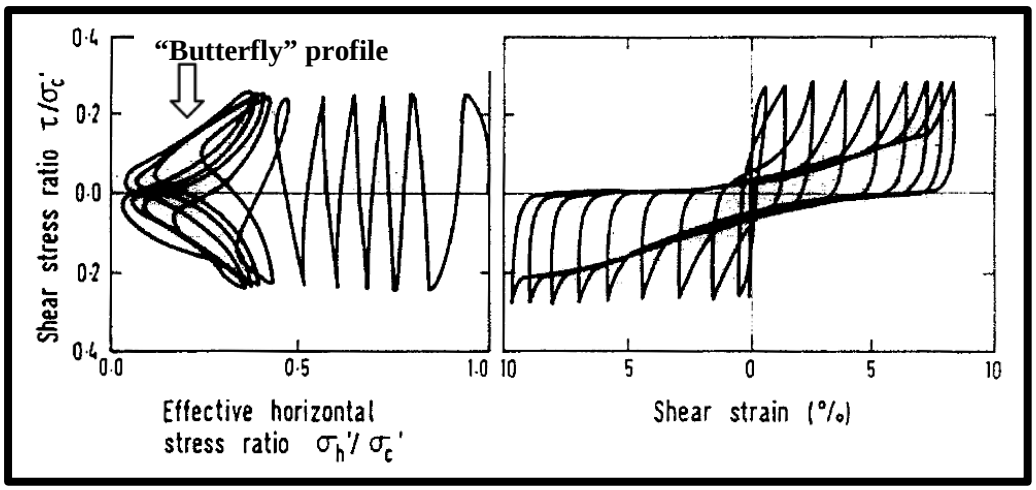

Figure 6.5 Effective stress path and stress-strain of Toyoura sand (relative density = 77%) subjected to torsional simple shear test (Tatsuoka et al. 1982).

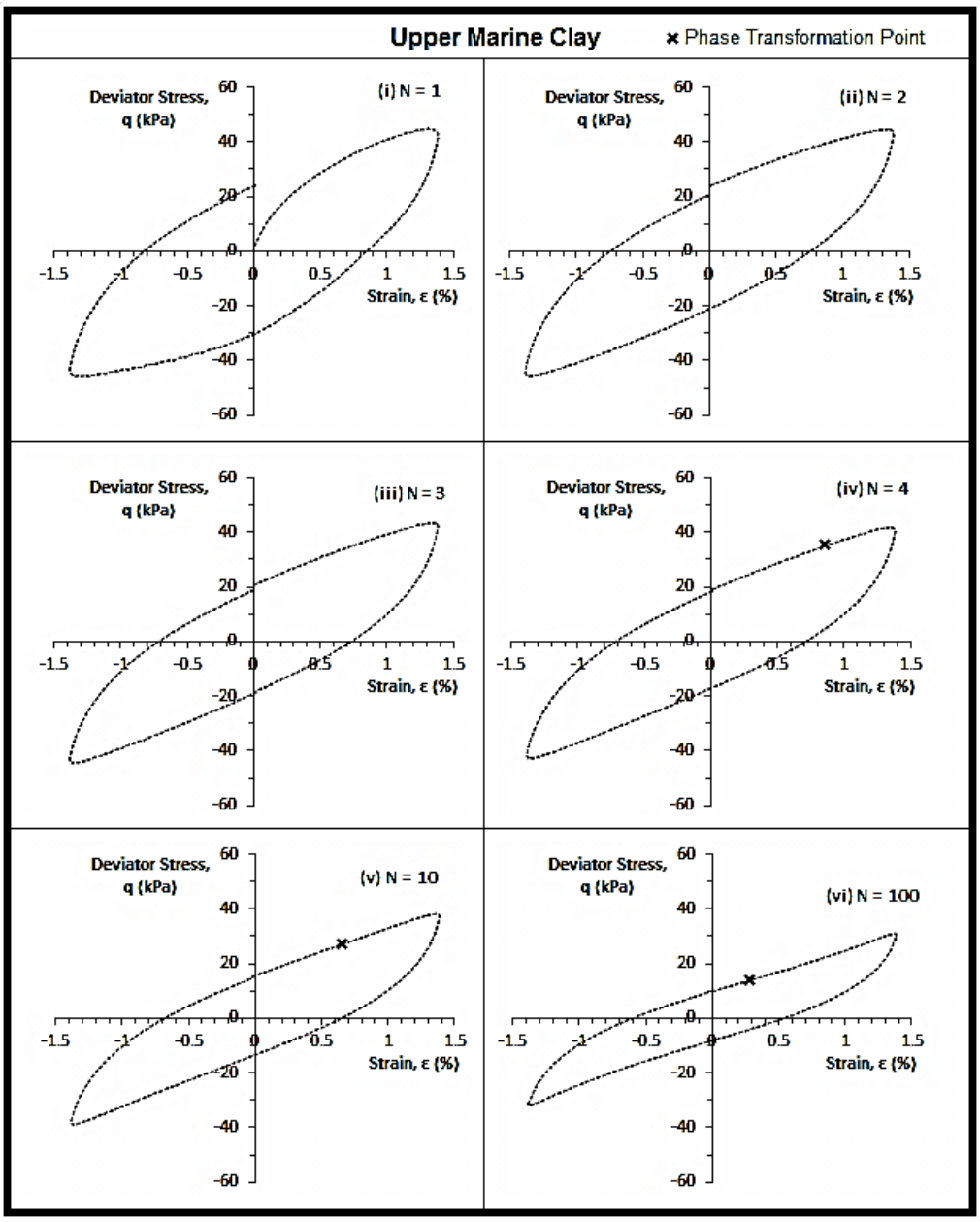

Figure 6.6 Effect of phase transformation on effective stress-strain relationship for Singapore Upper Marine Clay (OCR = 1, p_c' = 100kPa, ε = 1.4%).

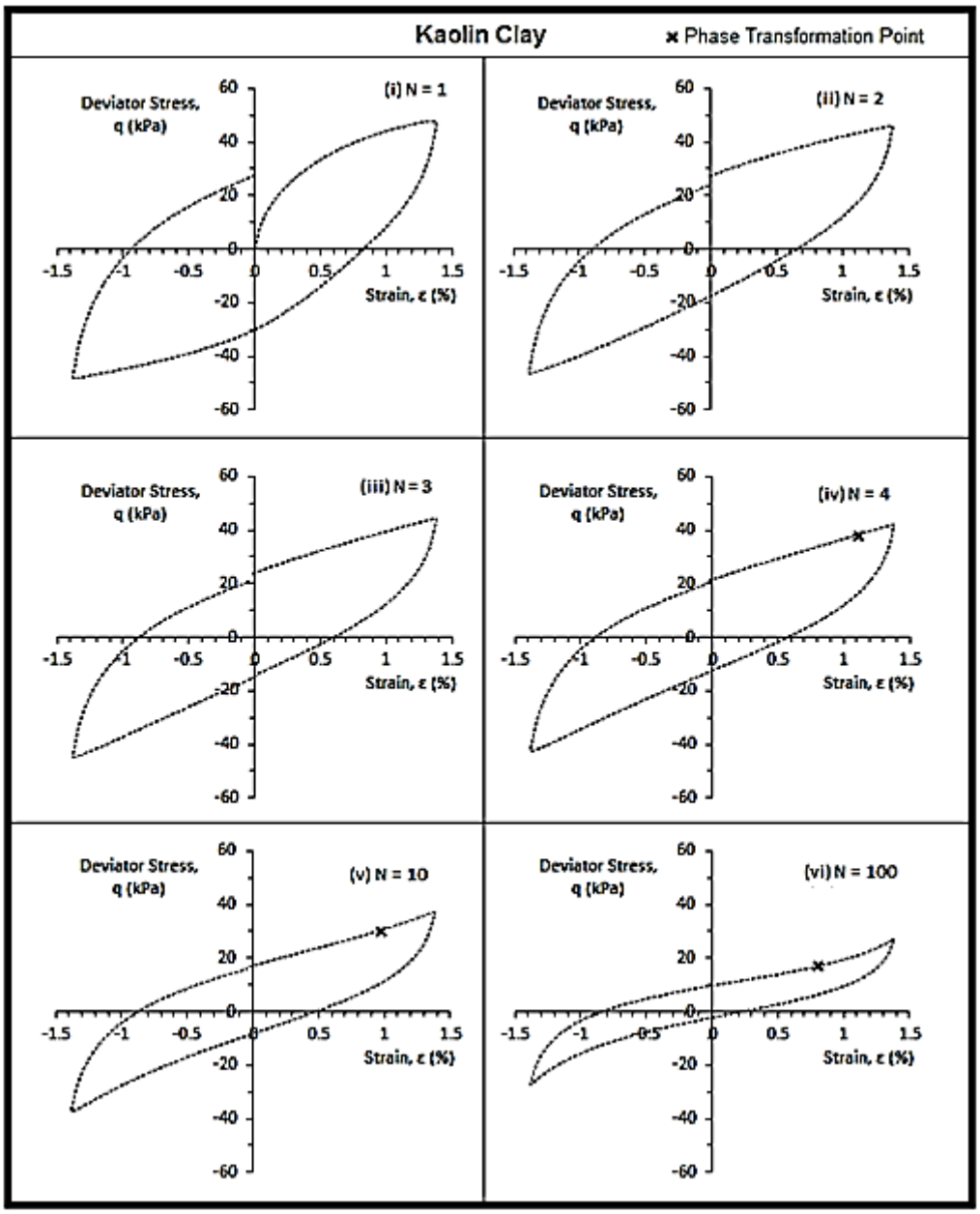

Figure 6.7 Effect of phase transformation on effective stress-strain relationship for Kaolin Clay (OCR = 1, p_c' = 100kPa, ε = 1.4%).

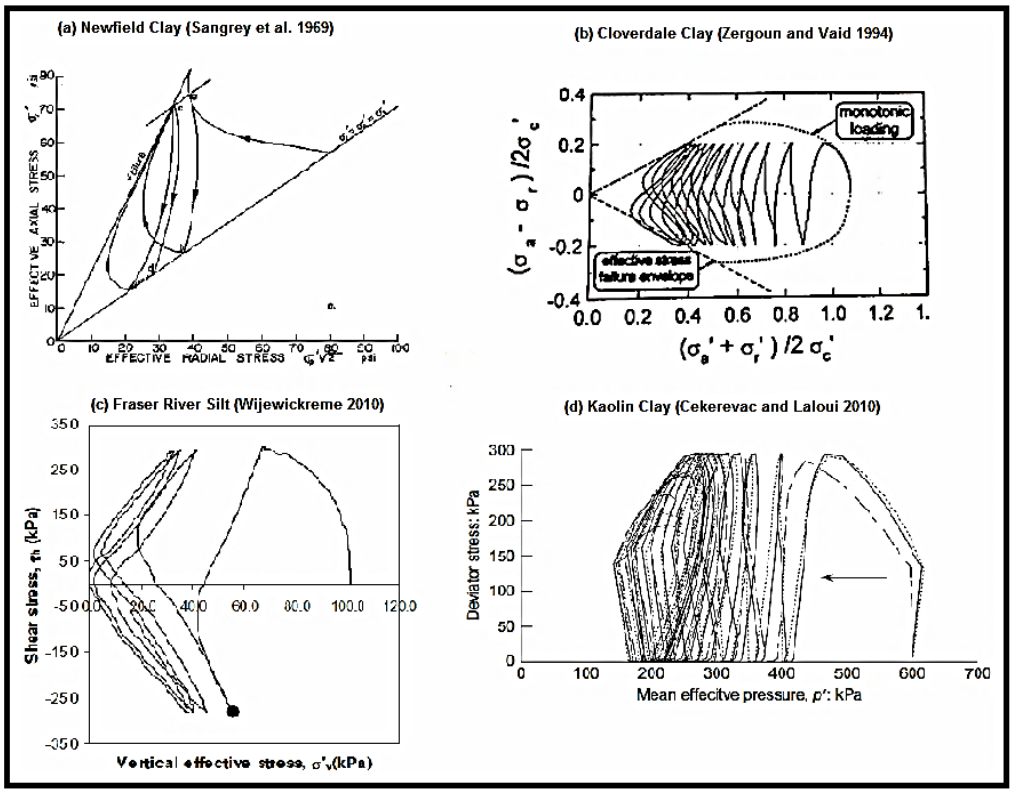

Figure 6.8 Cyclic mobility in cohesive soils (Edited from: Sangrey et al. 1969; Zergoun and Vaid 1994; Cekerevac and Laloui 2010; Wijewickreme 2010).

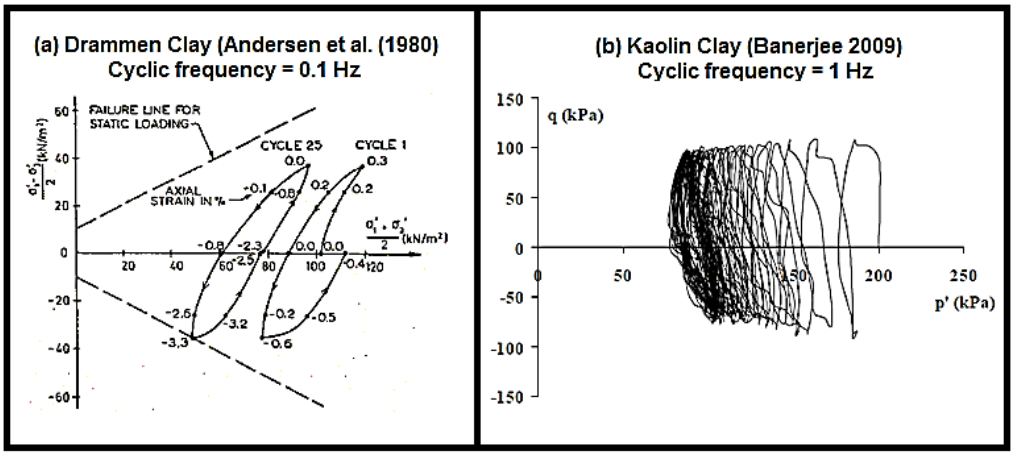

Figure 6.9 Effective stress paths of clays under relatively fast cyclic loadings (Edited from: Andersen et al. 1980; Banerjee 2009).

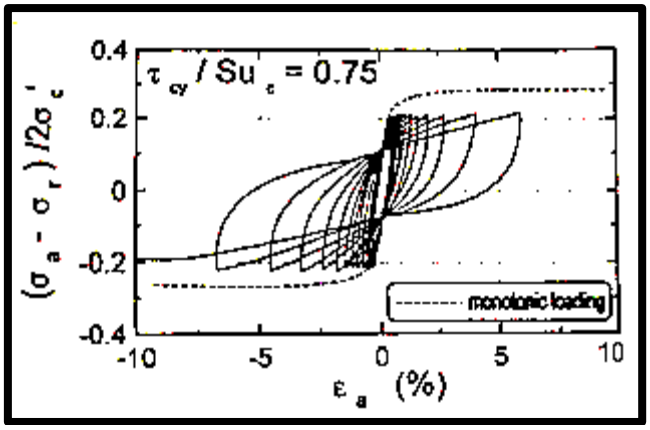

Figure 6.10 Effective stress-strain relationship for Cloverdale Clay under two-way undrained cyclic loading (Zergoun and Vaid 1994).

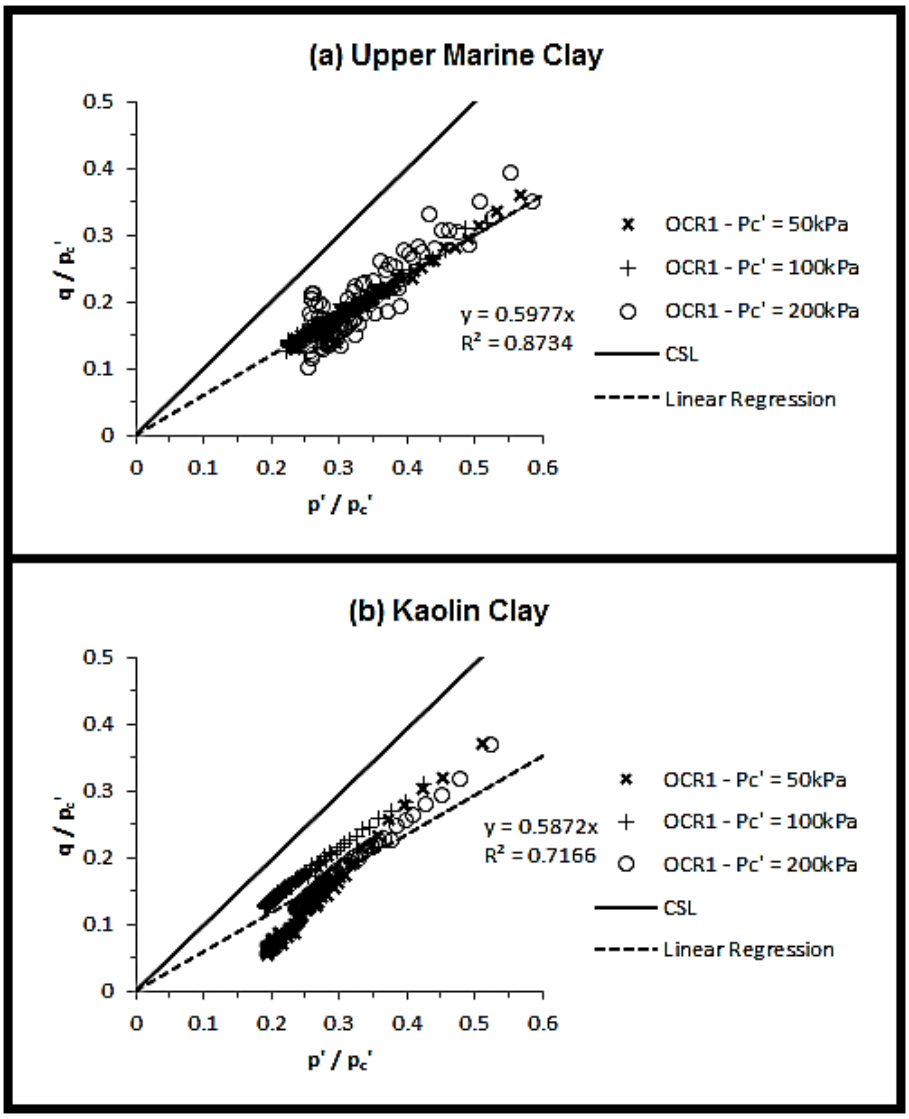

Figure 6.11 Phase transformation points for normally consolidated specimens of (a) Singapore Upper Marine Clay and (b) Kaolin Clay.

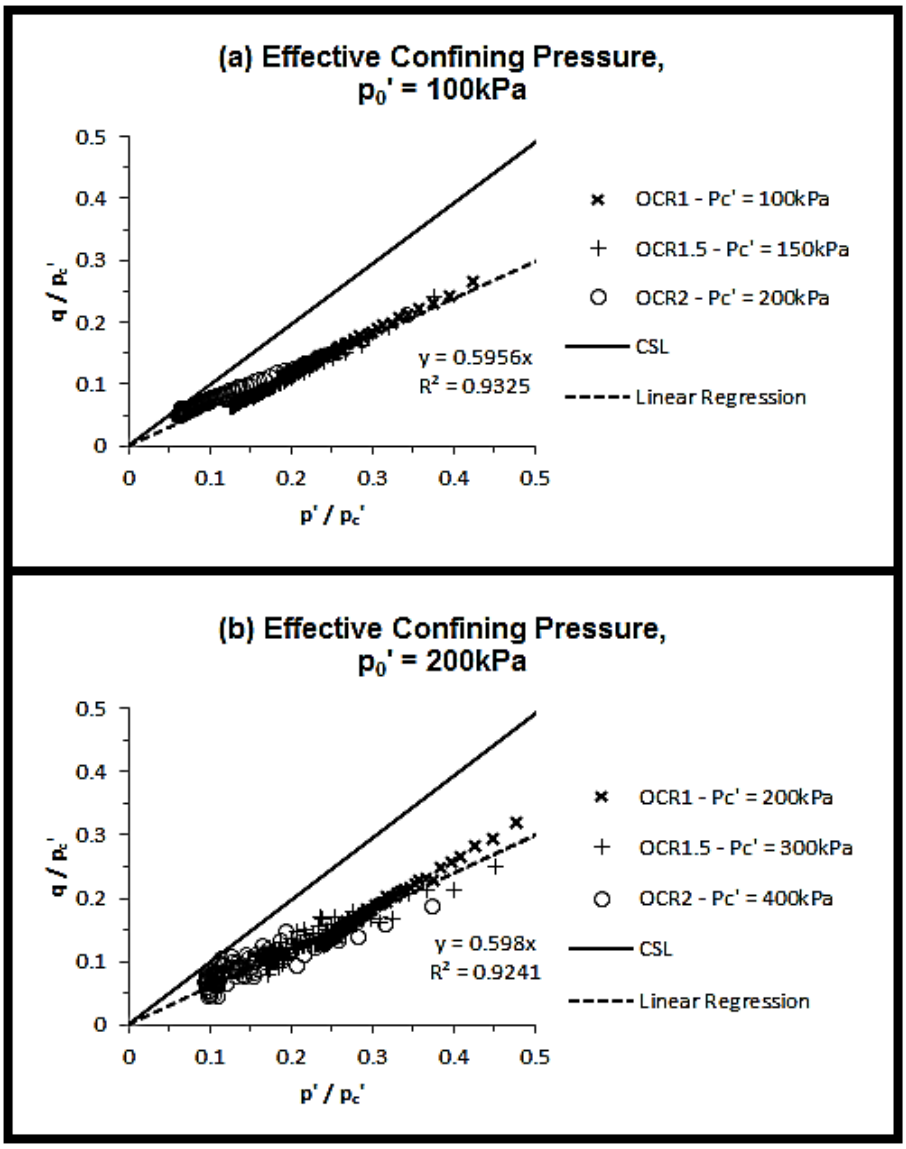

Figure 6.12 Phase transformation points for overconsolidated specimens of Kaolin Clay subjected to effective confining pressures of (a) 100kPa and (b) 200kPa.

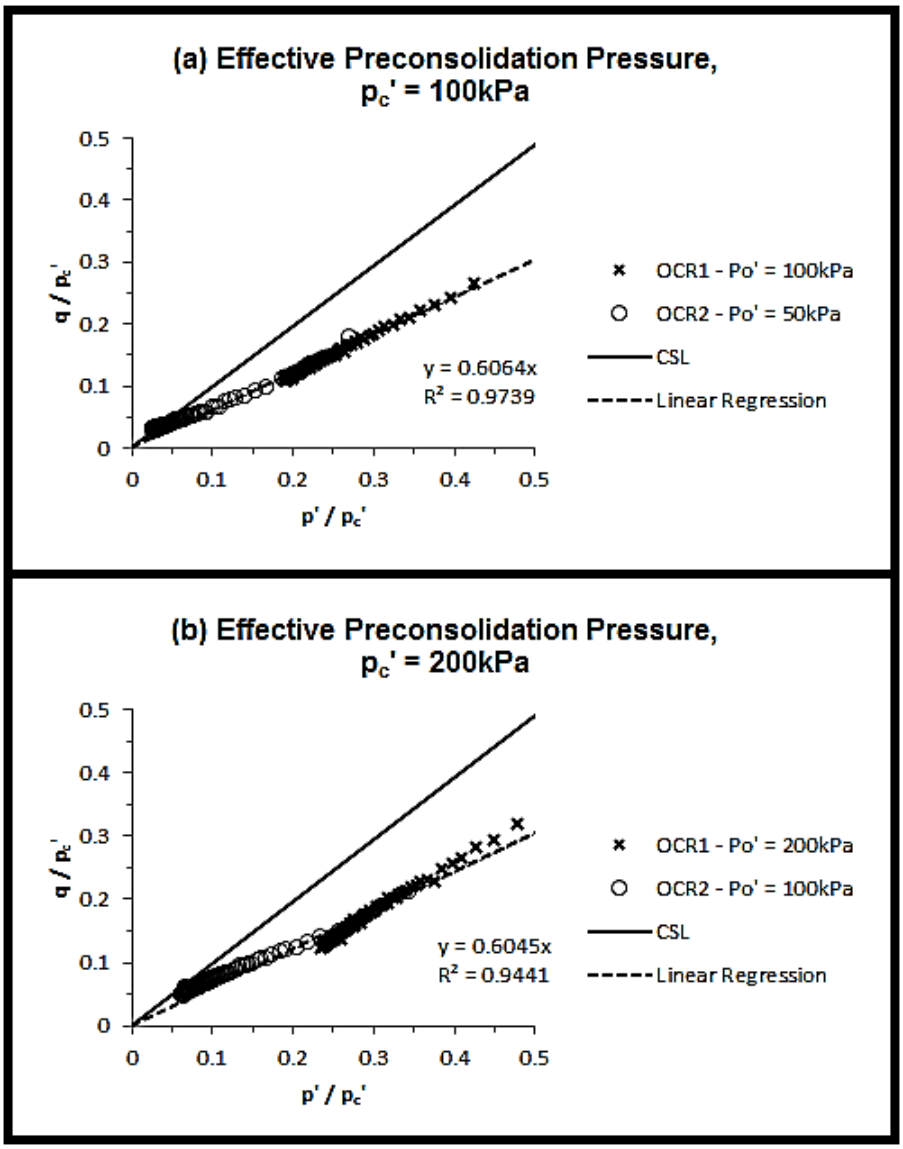

Figure 6.13 Phase transformation points for overconsolidated specimens of Kaolin Clay subjected to preconsolidation pressures of (a) 100kPa and (b) 200kPa.

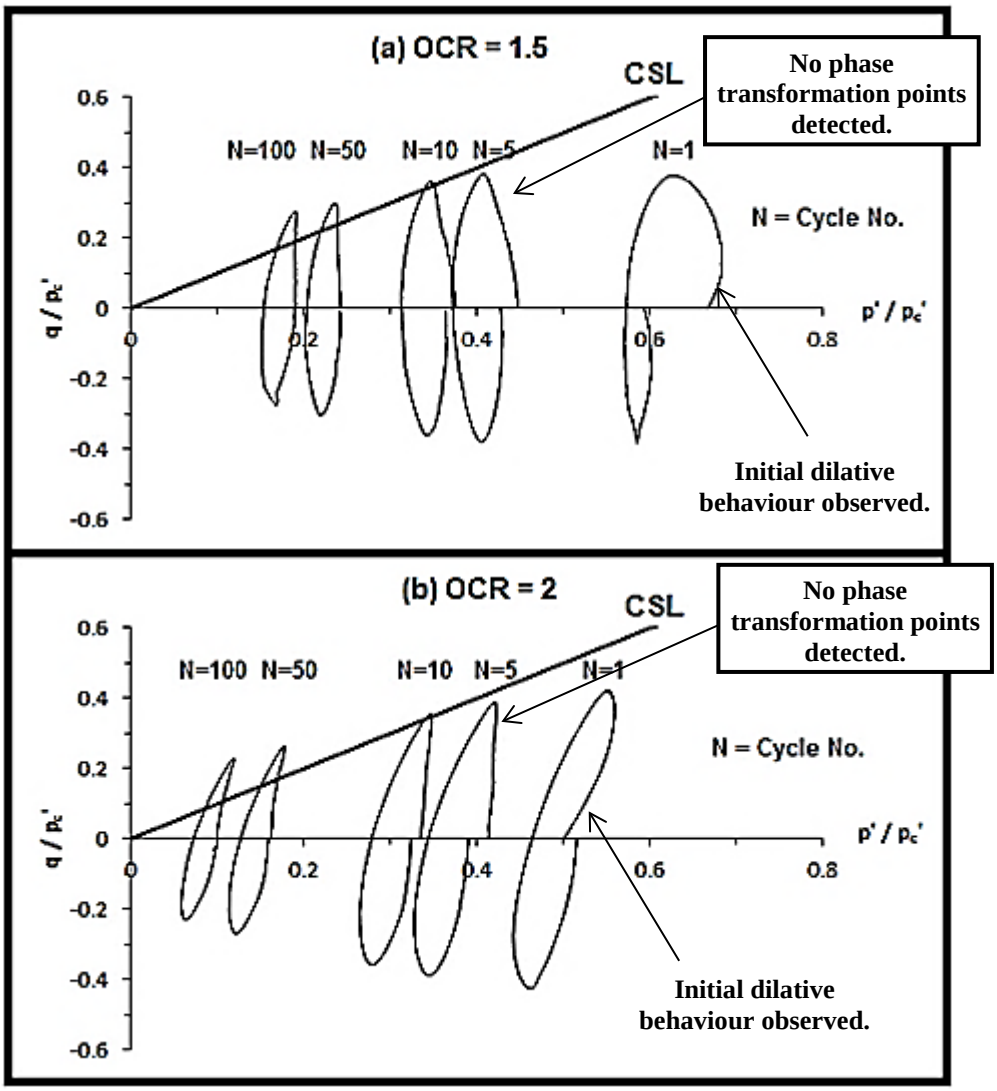

Figure 6.14 Typical normalized effective stress path of overconsolidated Singapore Upper Marine Clay specimens (p_c' = 100kPa, ε = 1.4%).

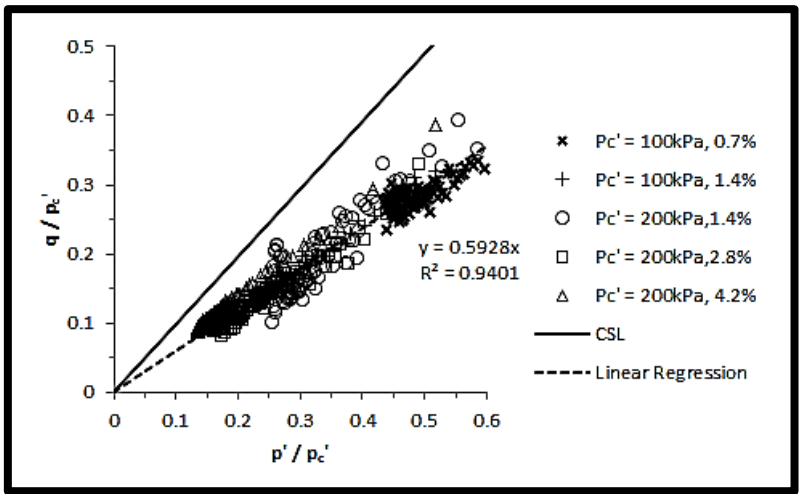

Figure 6.15 Effect of cyclic strain amplitude on phase transformation points.

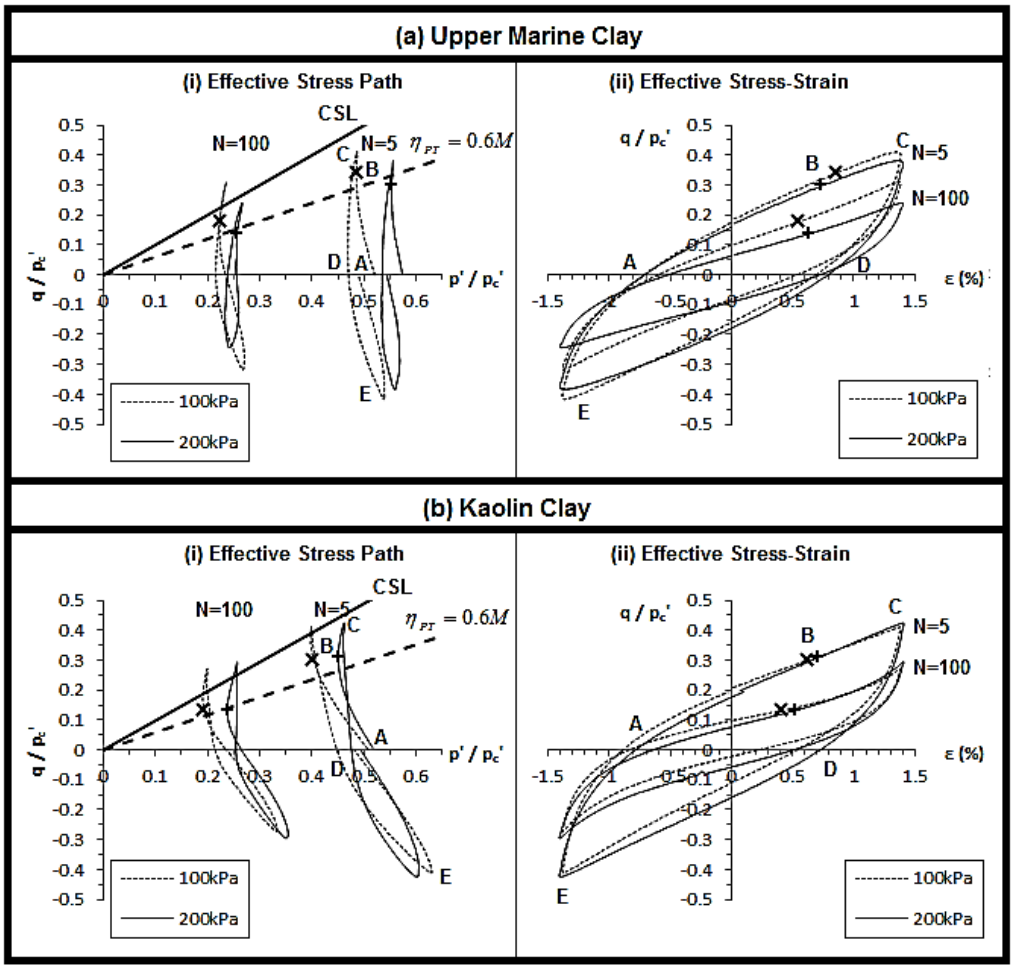

Figure 6.16 Effect of effective preconsolidation pressure on the normalized effective stress path and stress-strain plots for (a) Singapore Upper Marine Clay and (b) Kaolin Clay.

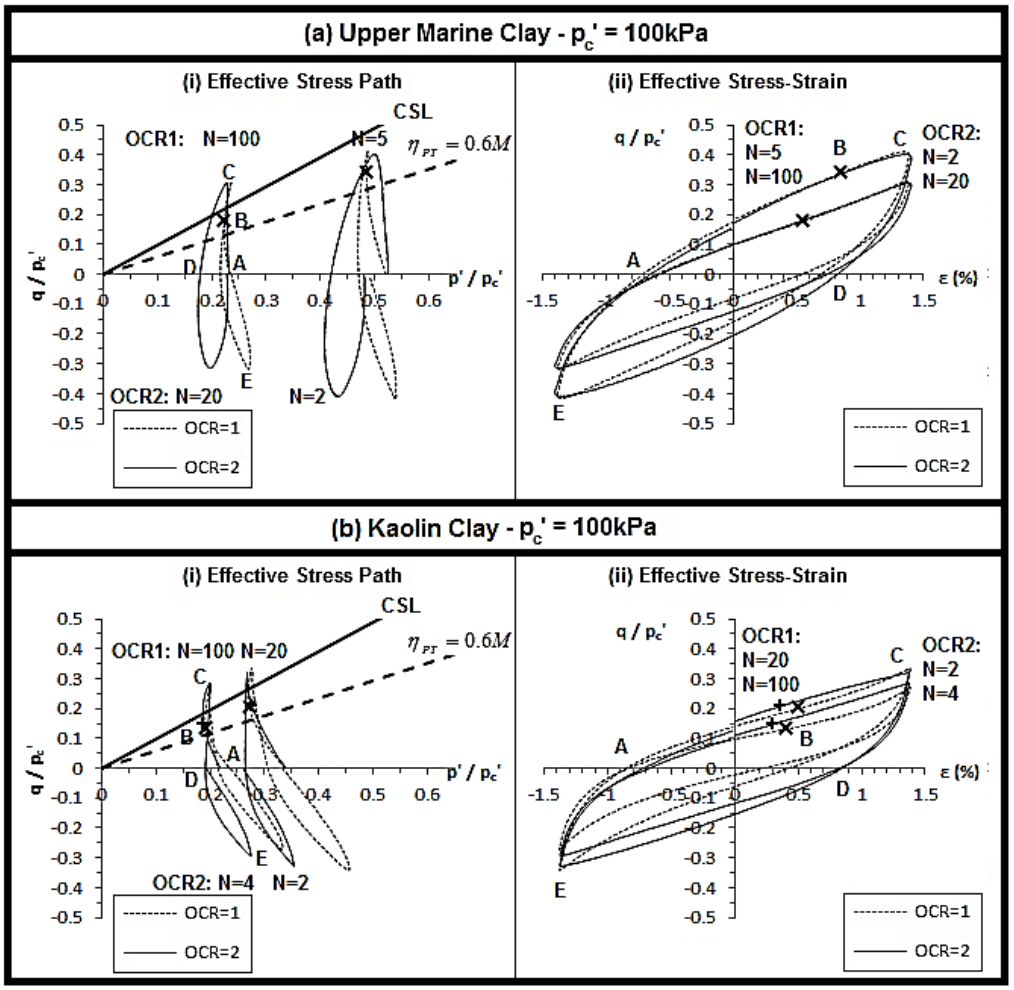

Figure 6.17 Effect of overconsolidation ratio on the normalized effective stress path and stress-strain plots for (a) Singapore Upper Marine Clay and (b) Kaolin Clay.

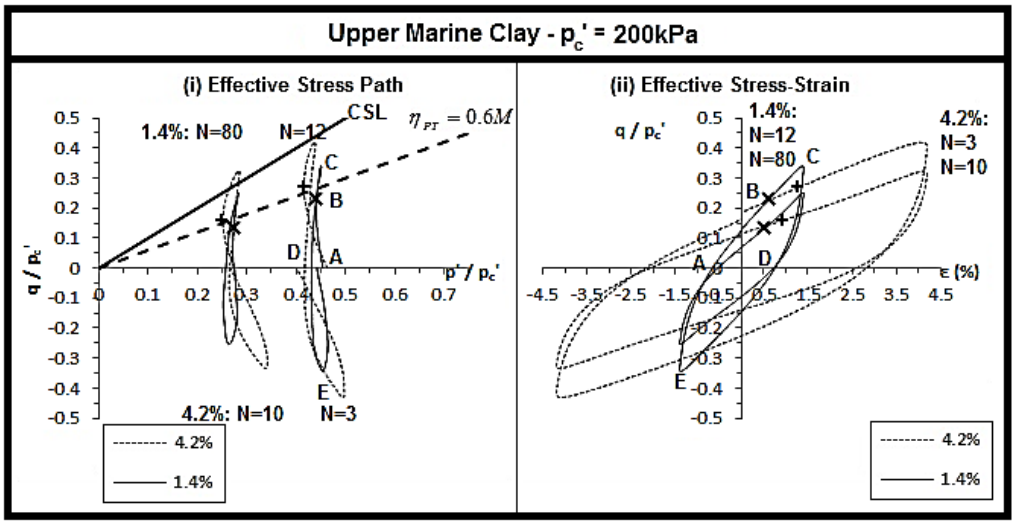

Figure 6.18 Effect of cyclic strain amplitude on the normalized effective stress path and stress-strain plots for Singapore Upper Marine Clay.

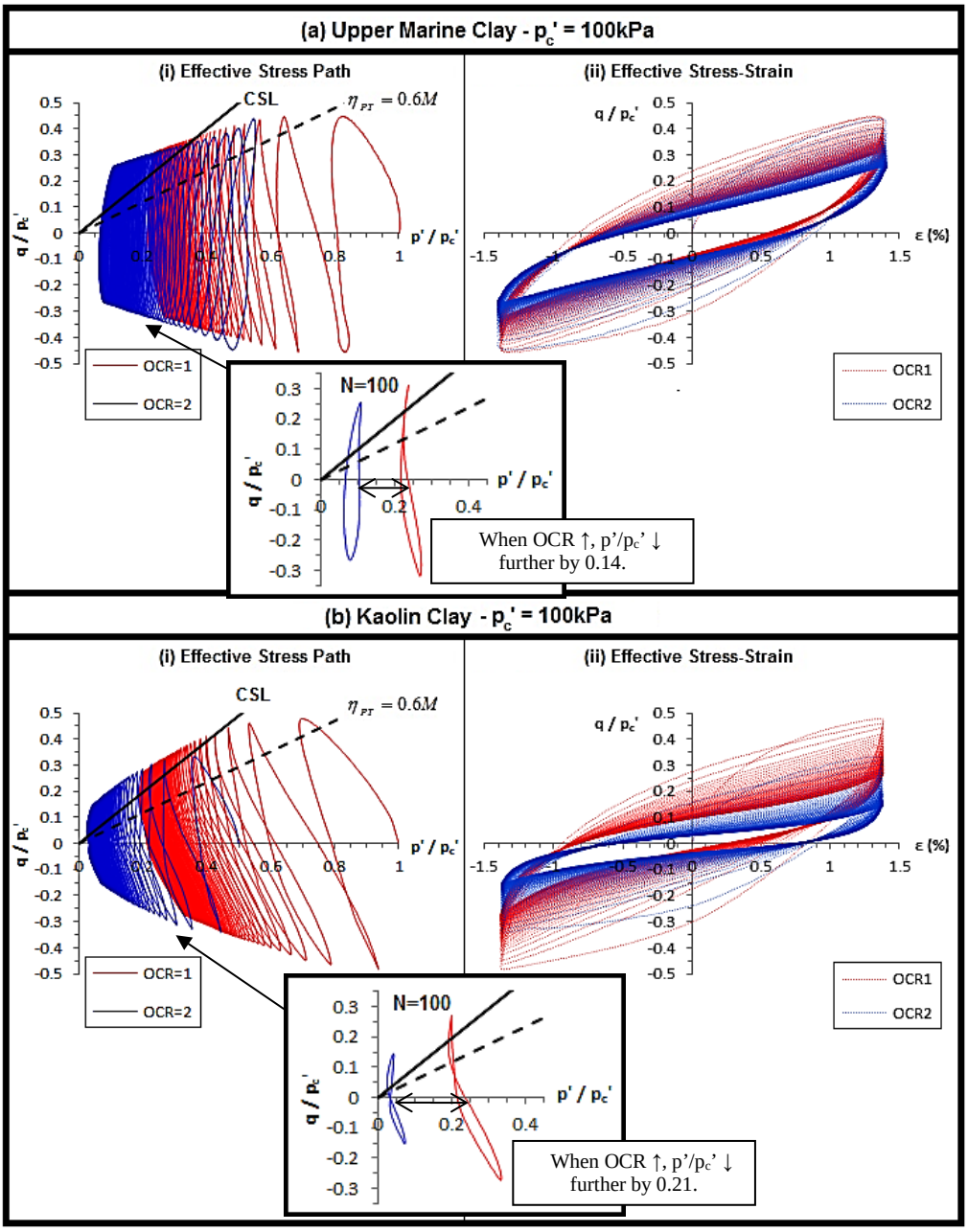

Figure 6.19 Effect of overconsolidation ratio on the normalized effective stress path and stress-strain plots for (a) Singapore Upper Marine Clay and (b) Kaolin Clay.

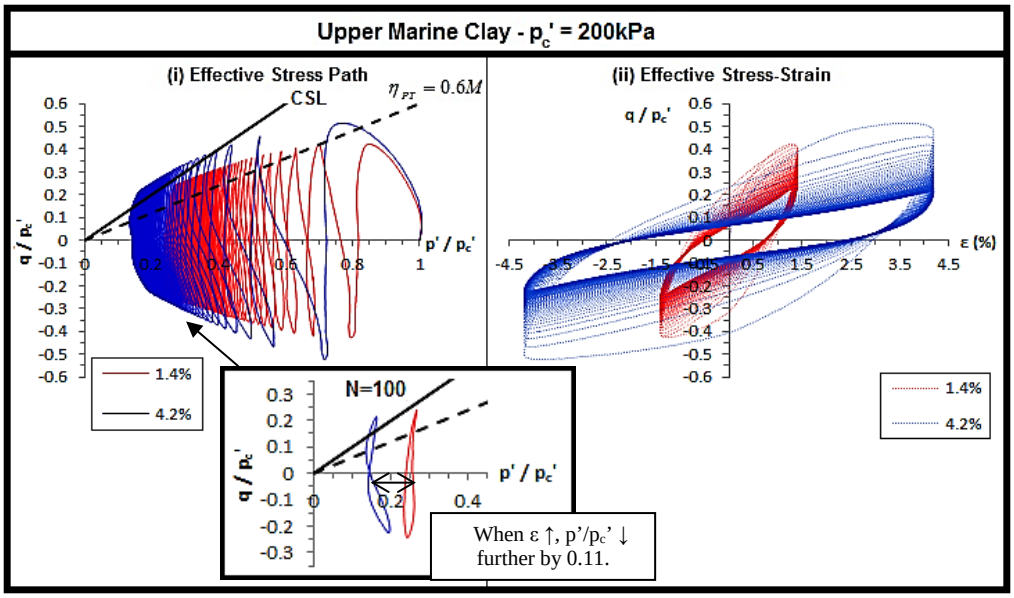

Figure 6.20 Effect of cyclic strain amplitude on the normalized effective stress path and stress-strain plots for Singapore Upper Marine Clay.

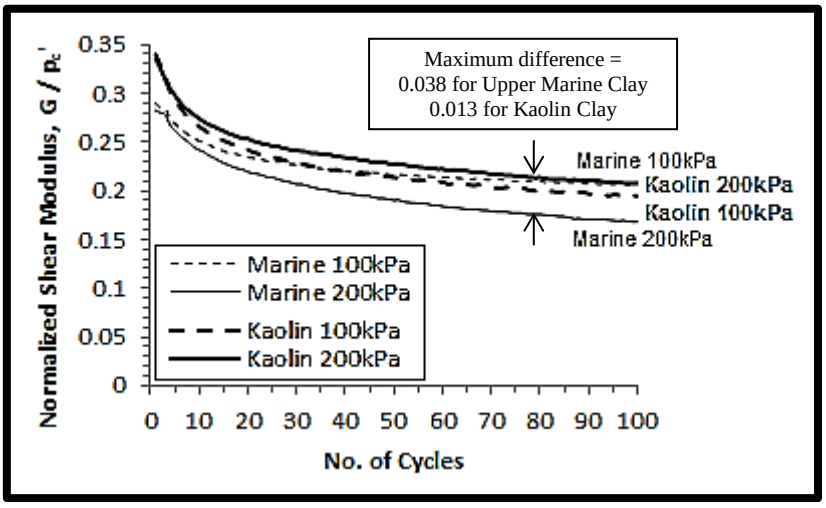

Figure 6.21 Degradation in normalized secant shear modulus with load cycles for specimens normally consolidated to 100kPa and 200kPa.

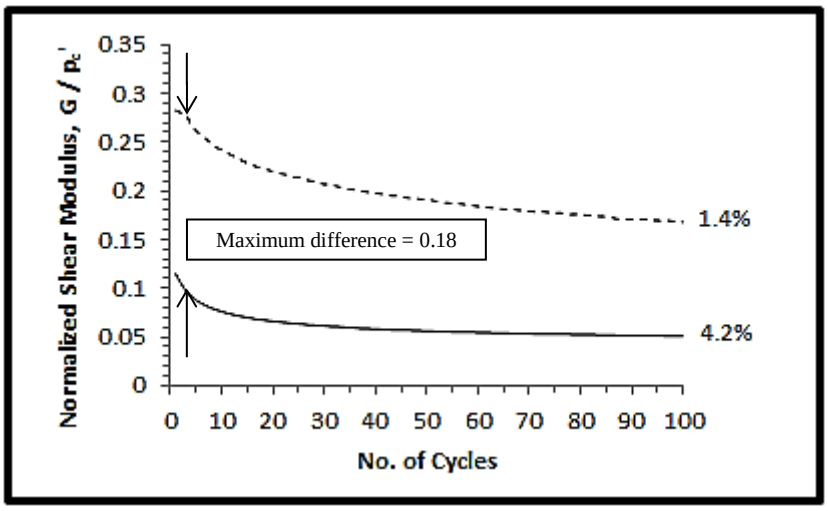

Figure 6.22 Degradation in normalized secant shear modulus with load cycles for specimens subjected to 1.4% and 4.2% strain amplitude.

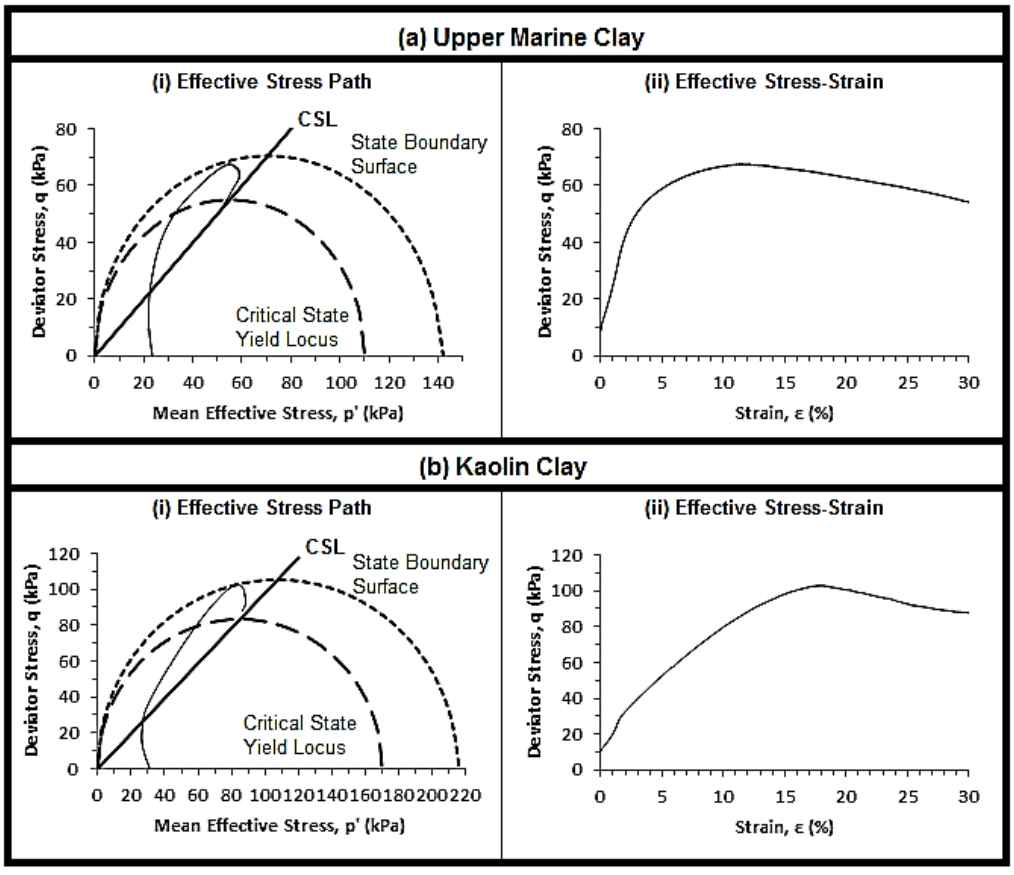

Figure 6.23 Post-cyclic behaviour of normally consolidated specimens (p_c' = 100kPa) of (a) Singapore Upper Marine Clay and (b) Kaolin Clay.

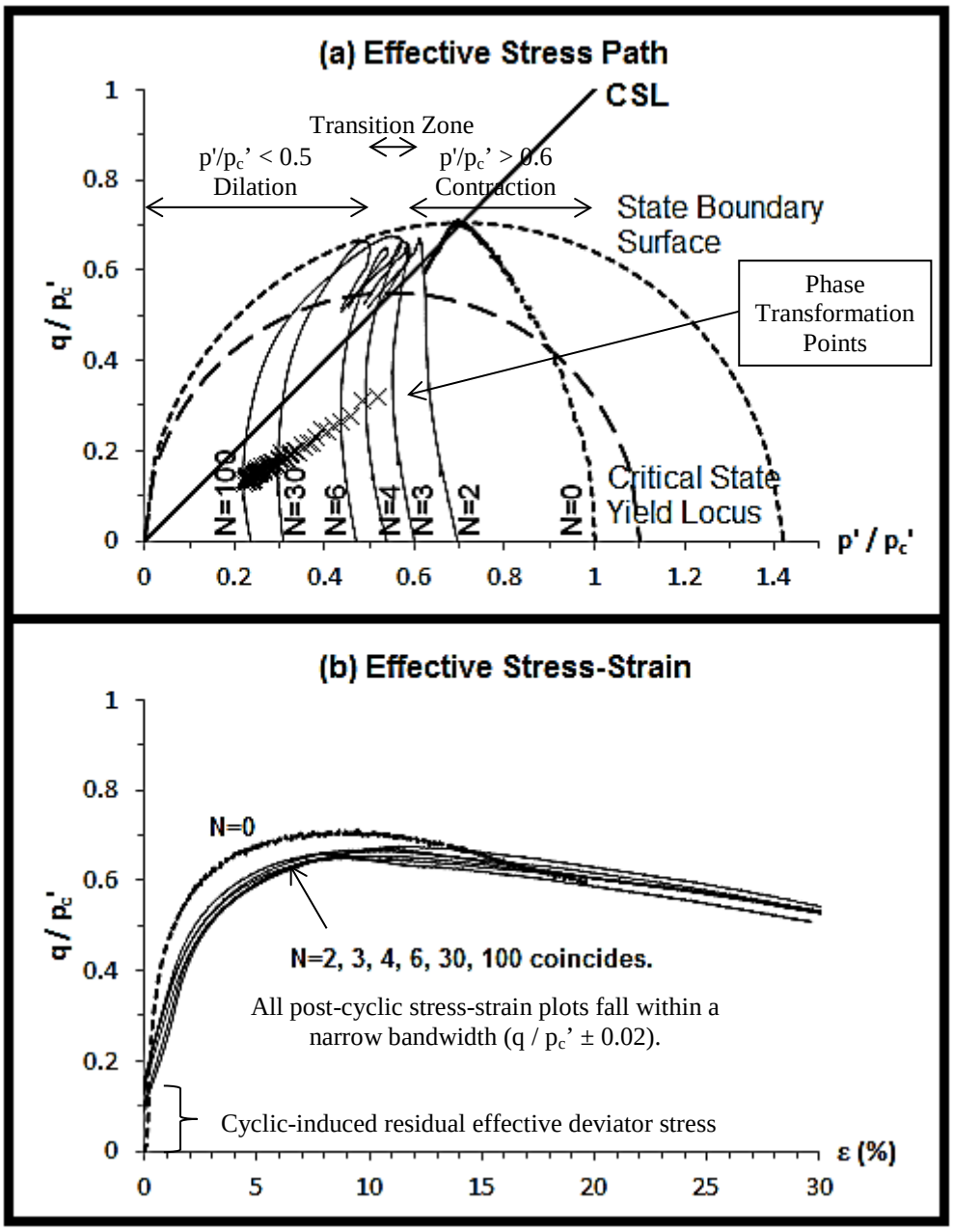

Figure 6.24 Typical post-cyclic behaviour for normally consolidated Singapore Upper Marine Clay (p_c' = 100kPa; ε = 1.4%).

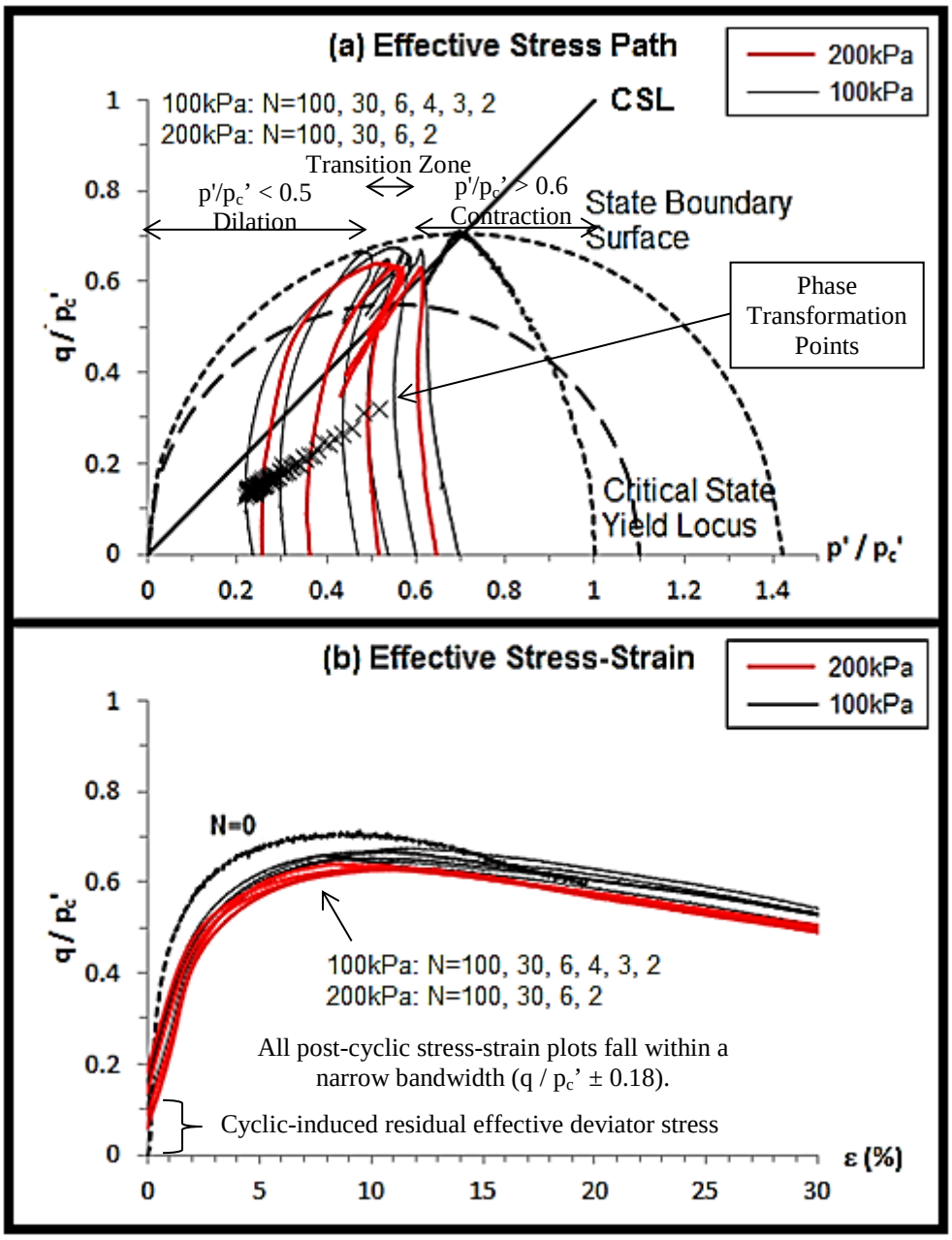

Figure 6.25 Effect of effective preconsolidation pressure on the post-cyclic behaviour of normally consolidated Singapore Upper Marine Clay.

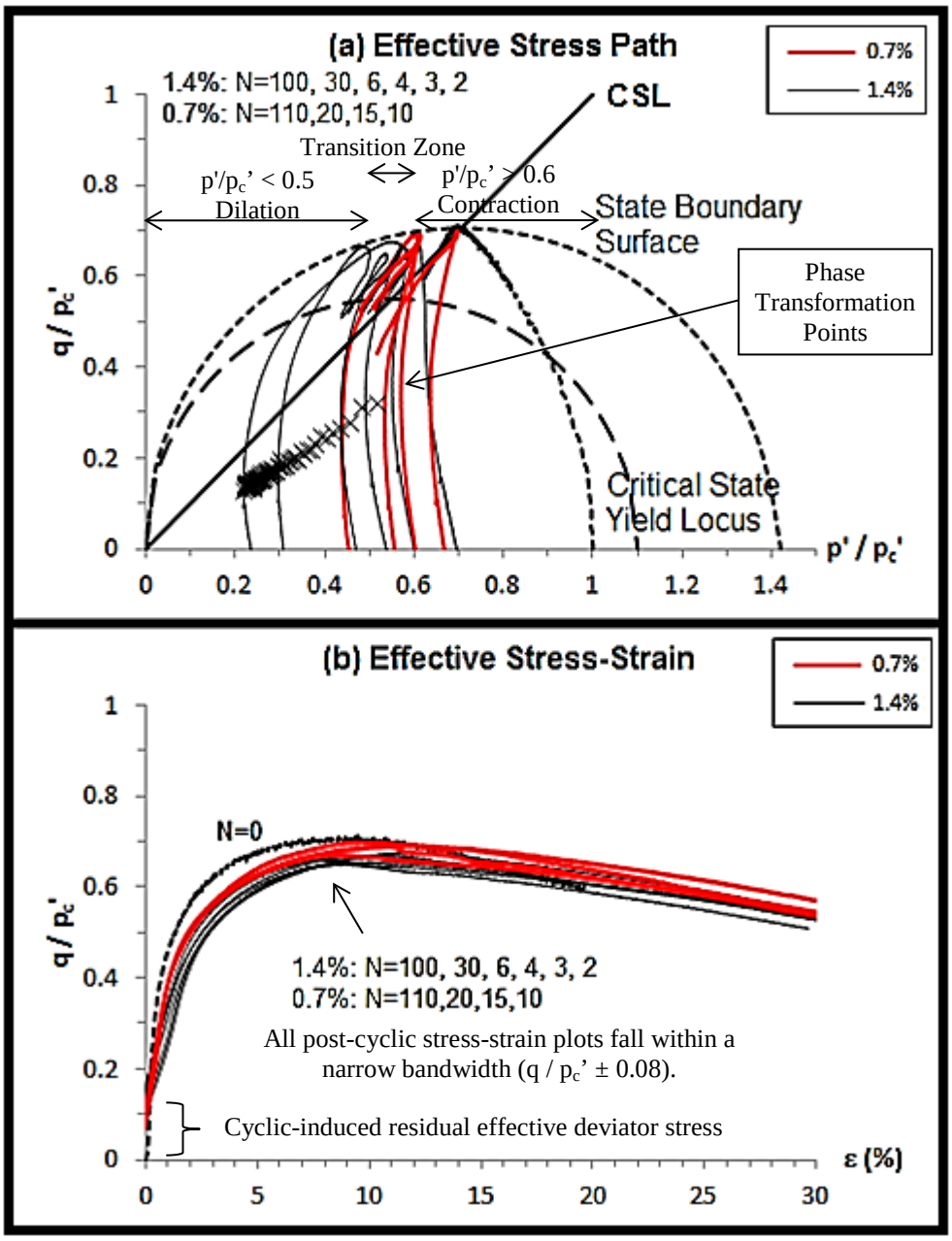

Figure 6.26 Effect of cyclic strain amplitude on the post-cyclic behaviour of normally consolidated Singapore Upper Marine Clay.

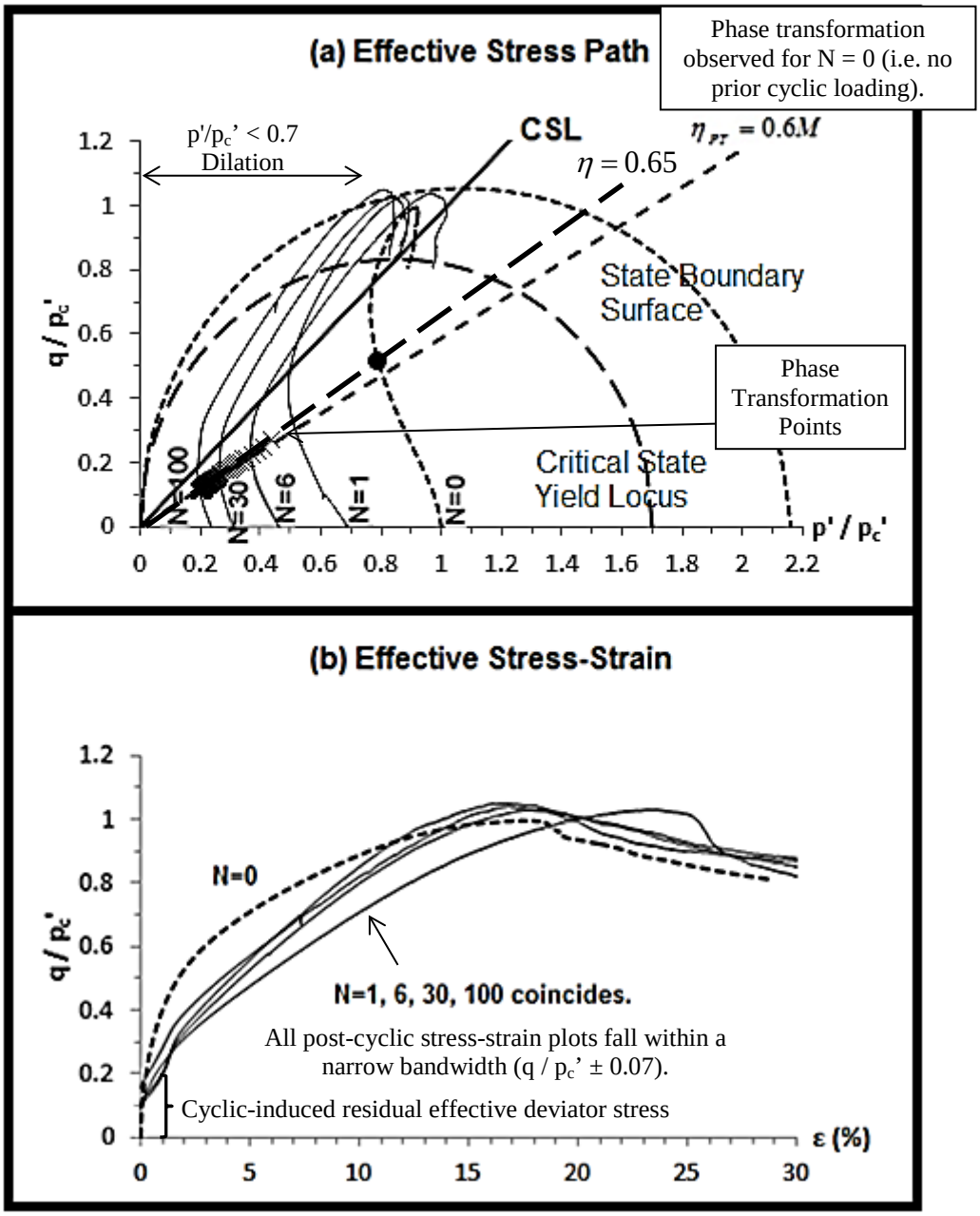

Figure 6.27 Typical post-cyclic behaviour for normally consolidated Kaolin Clay (p_c' = 100kPa).

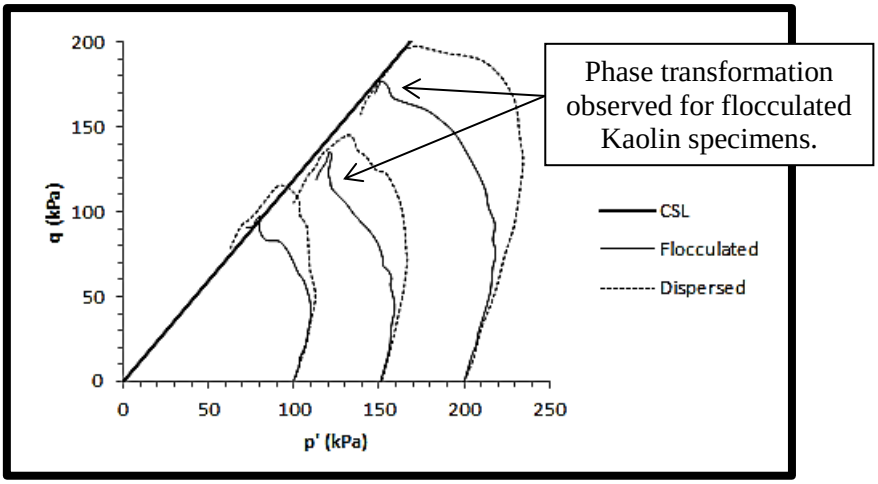

Figure 6.28 Effective stress paths of flocculated and dispersed Kaolin Clay specimens subjected to undrained triaxial compression tests (after Pillai et al. 2011).

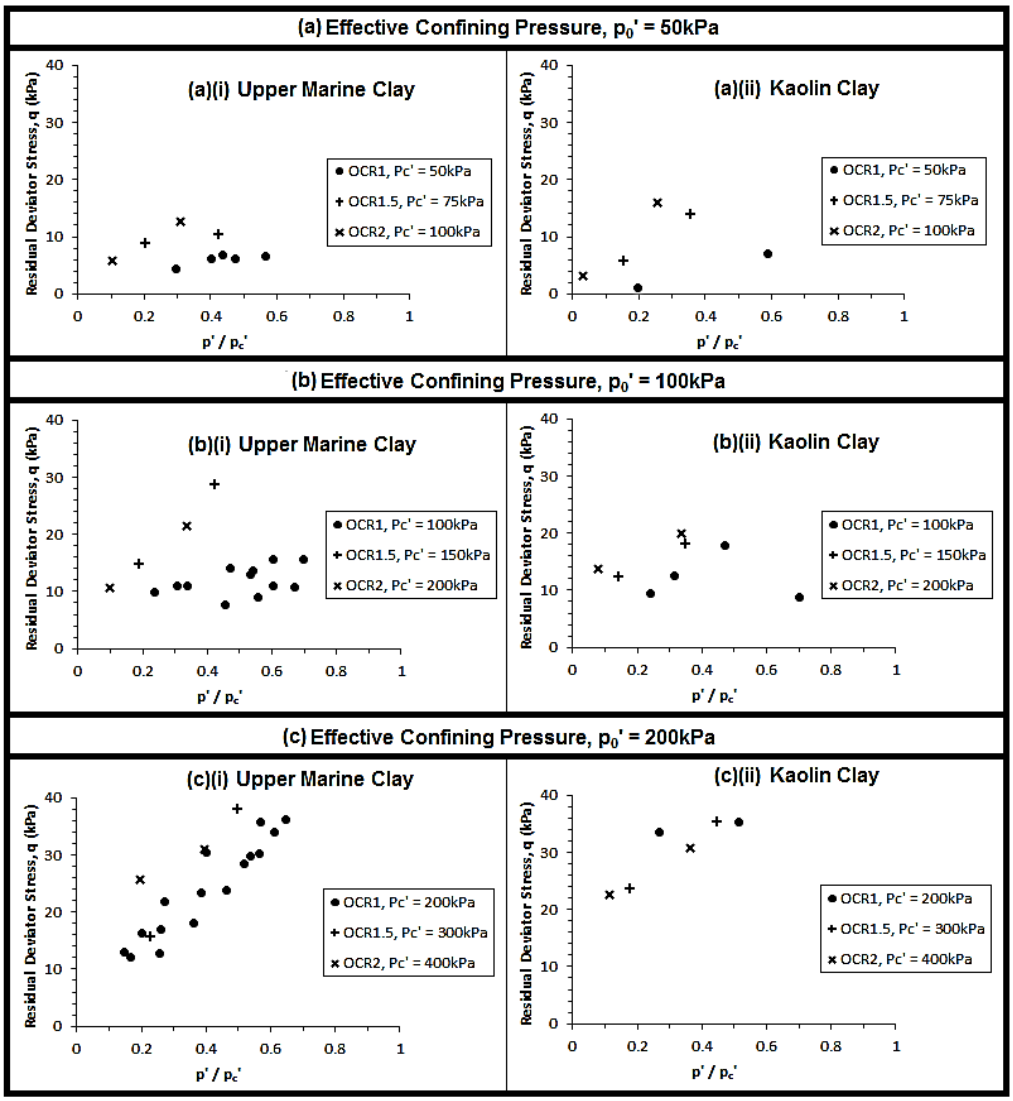

Figure 6.29 Cyclic-induced residual deviator stresses at start of post-cyclic compression tests.

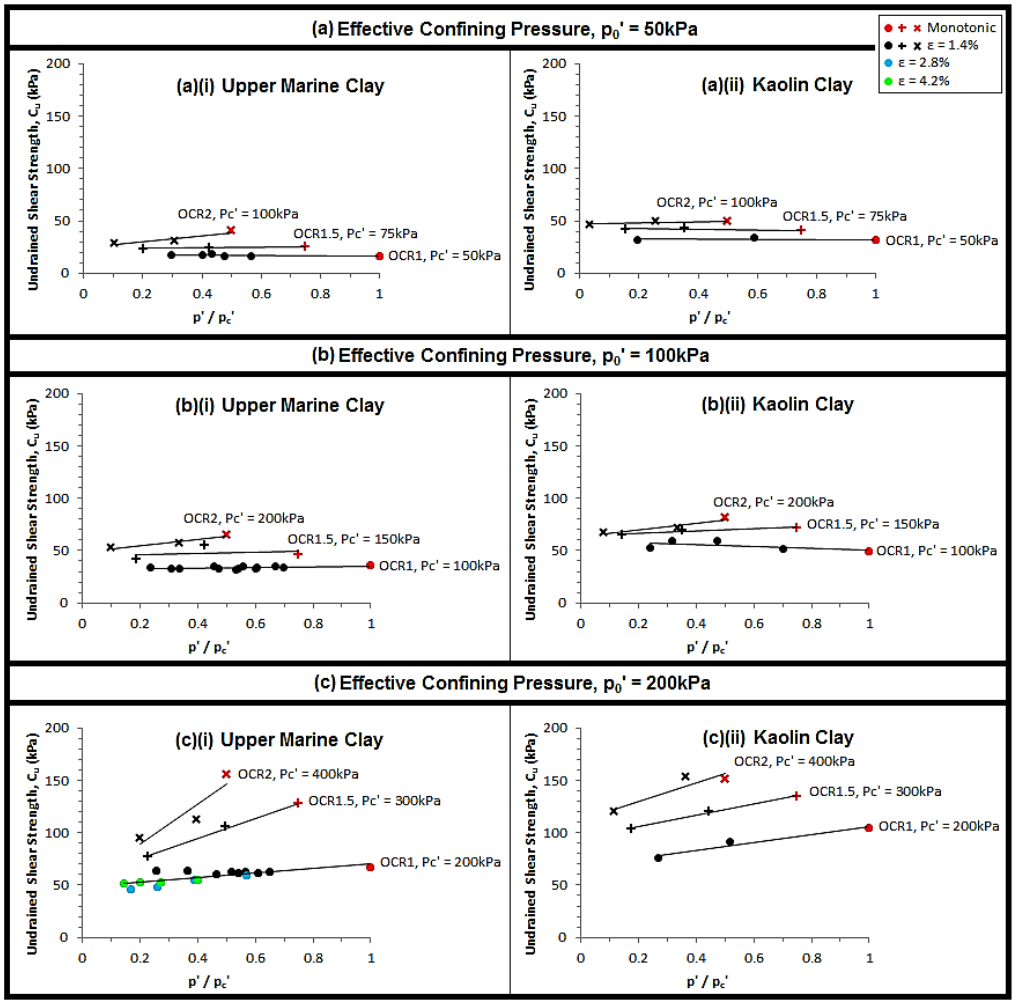

Figure 6.30 Post-cyclic undrained shear strengths.

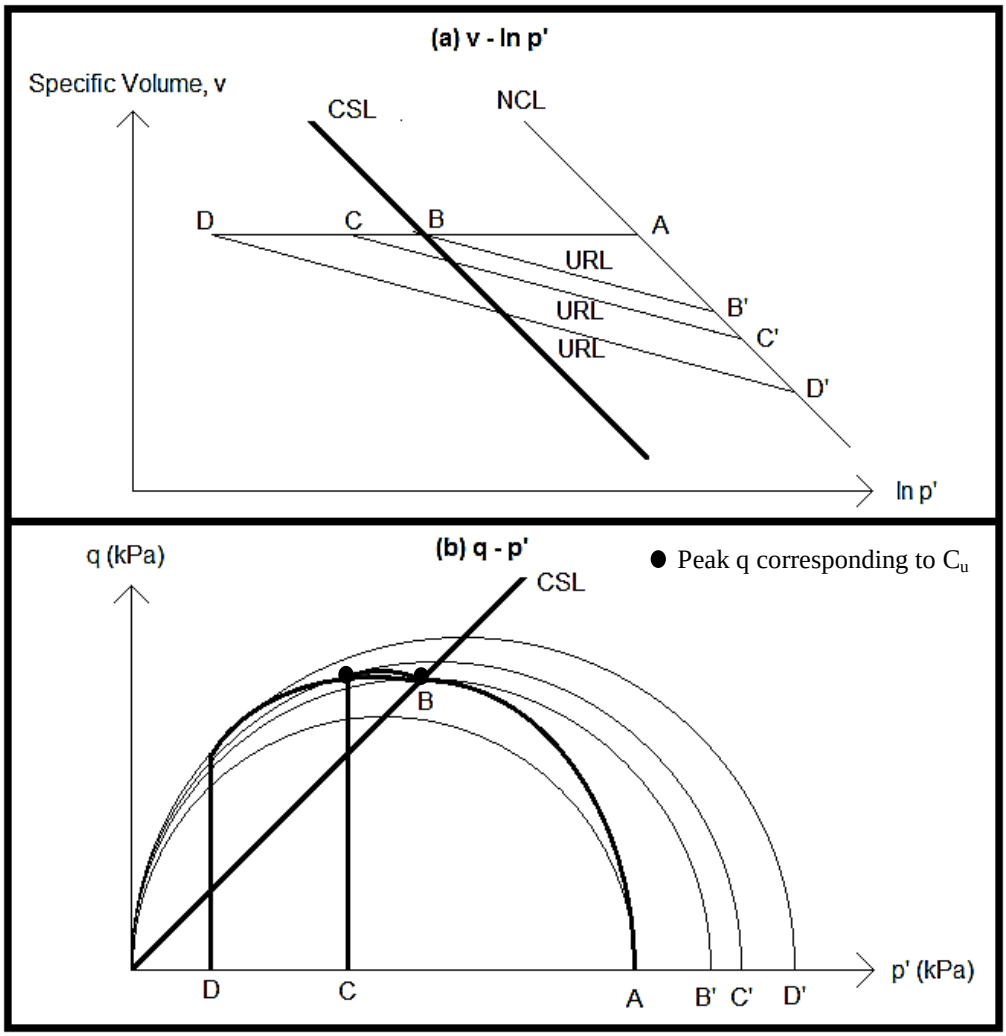

Figure 6.31 Idealized post-cyclic clay behaviour.

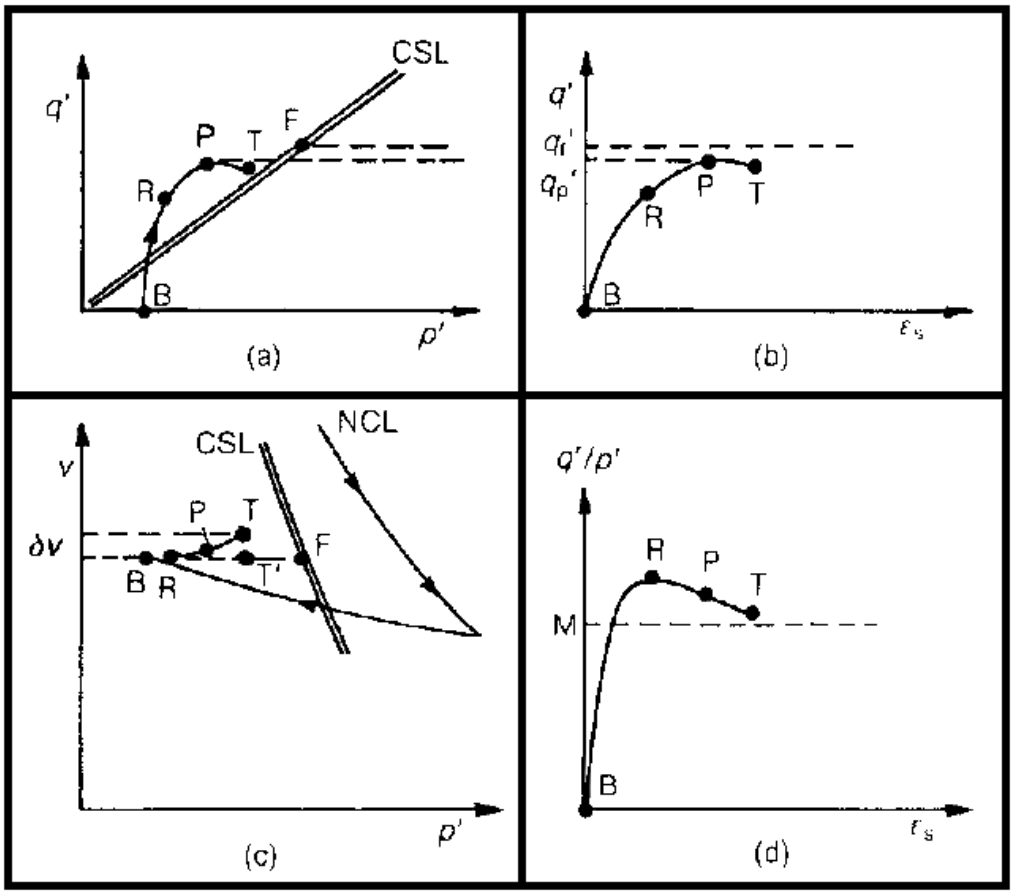

Figure 6.32 Idealized undrained behaviour of overconsolidated clay with localized drainage due to development of shear zones under undrained compression loading (Edited from: Atkinson and Richardson 1987).

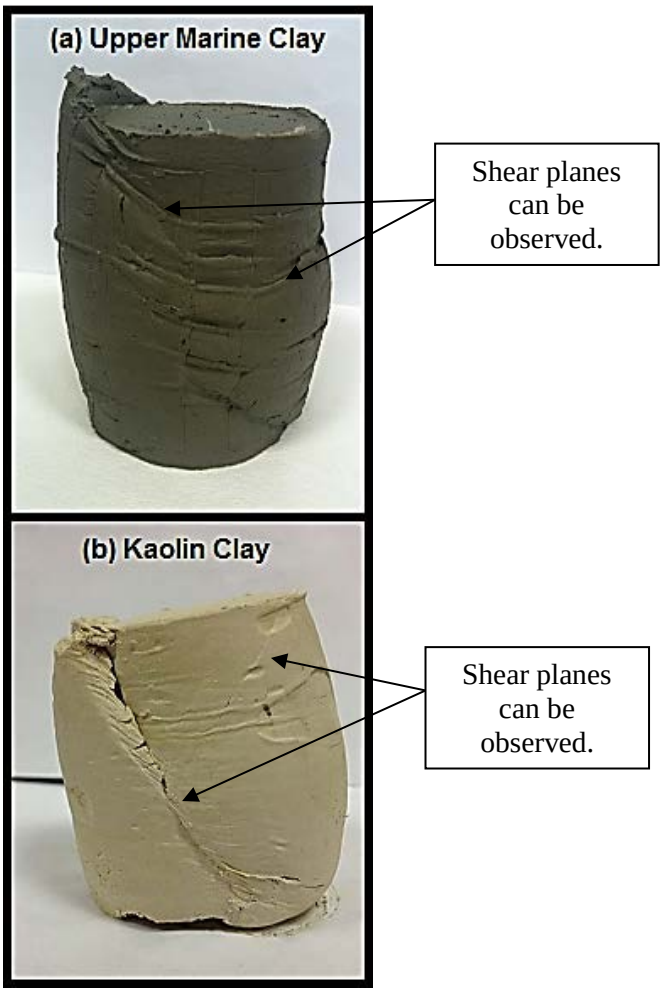

Figure 6.33 Shear planes observed in normally consolidated specimens after post-cyclic compression tests (Cyclic loading conditions: p_c' = 200kPa, ε = 1.4%, N = 100).

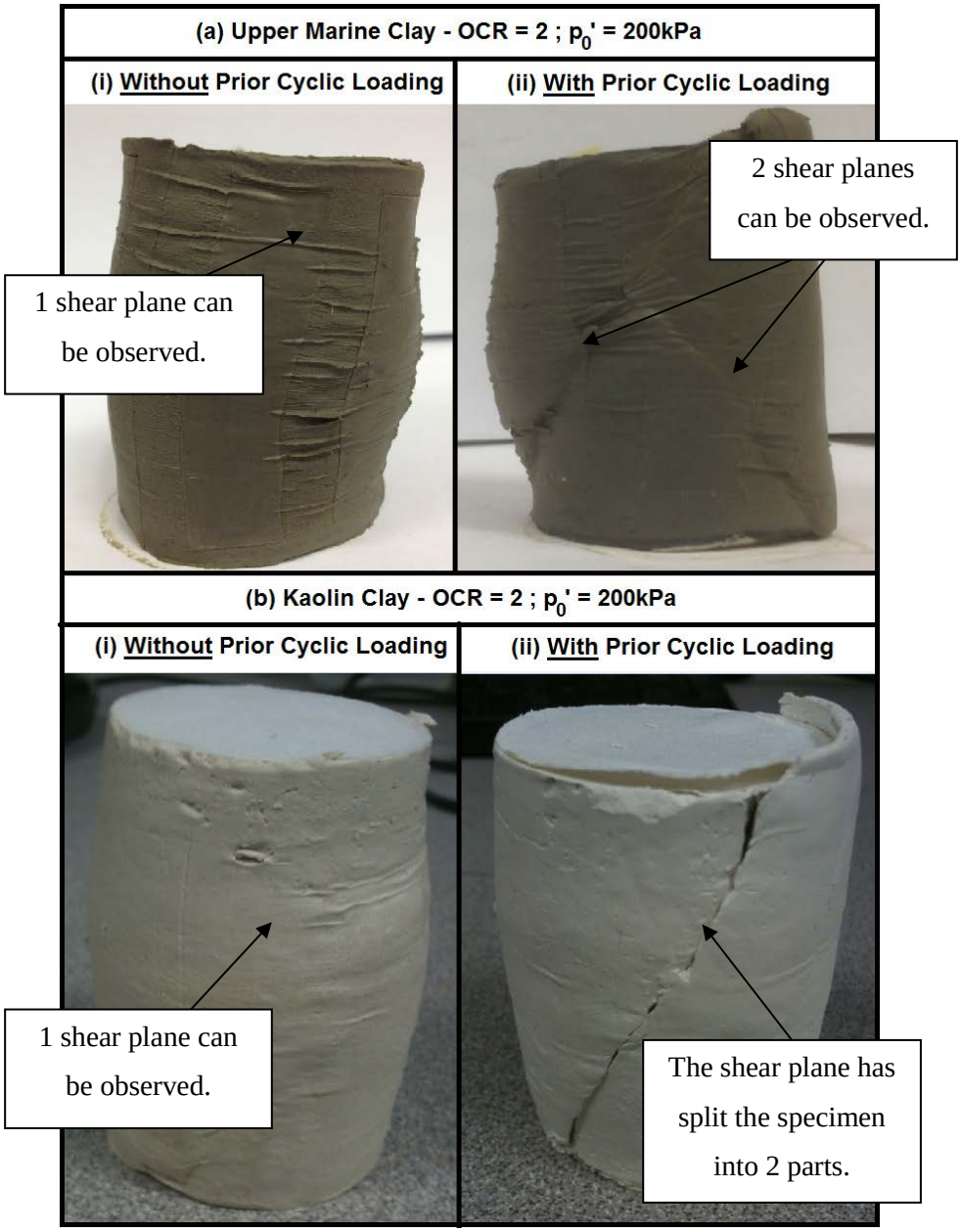

Figure 6.34 Comparison of shear planes observed in overconsolidated specimens subjected to monotonic compression tests and post-cyclic compression tests (Cyclic loading conditions: p_0' = 200kPa, ε = 1.4%, N = 100).

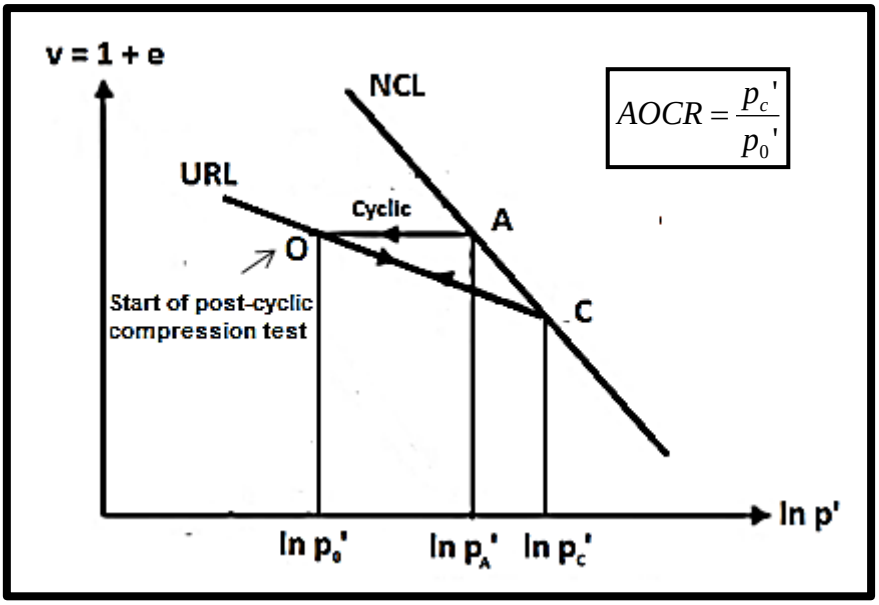

Figure 6.35 v – ln p’ curve.

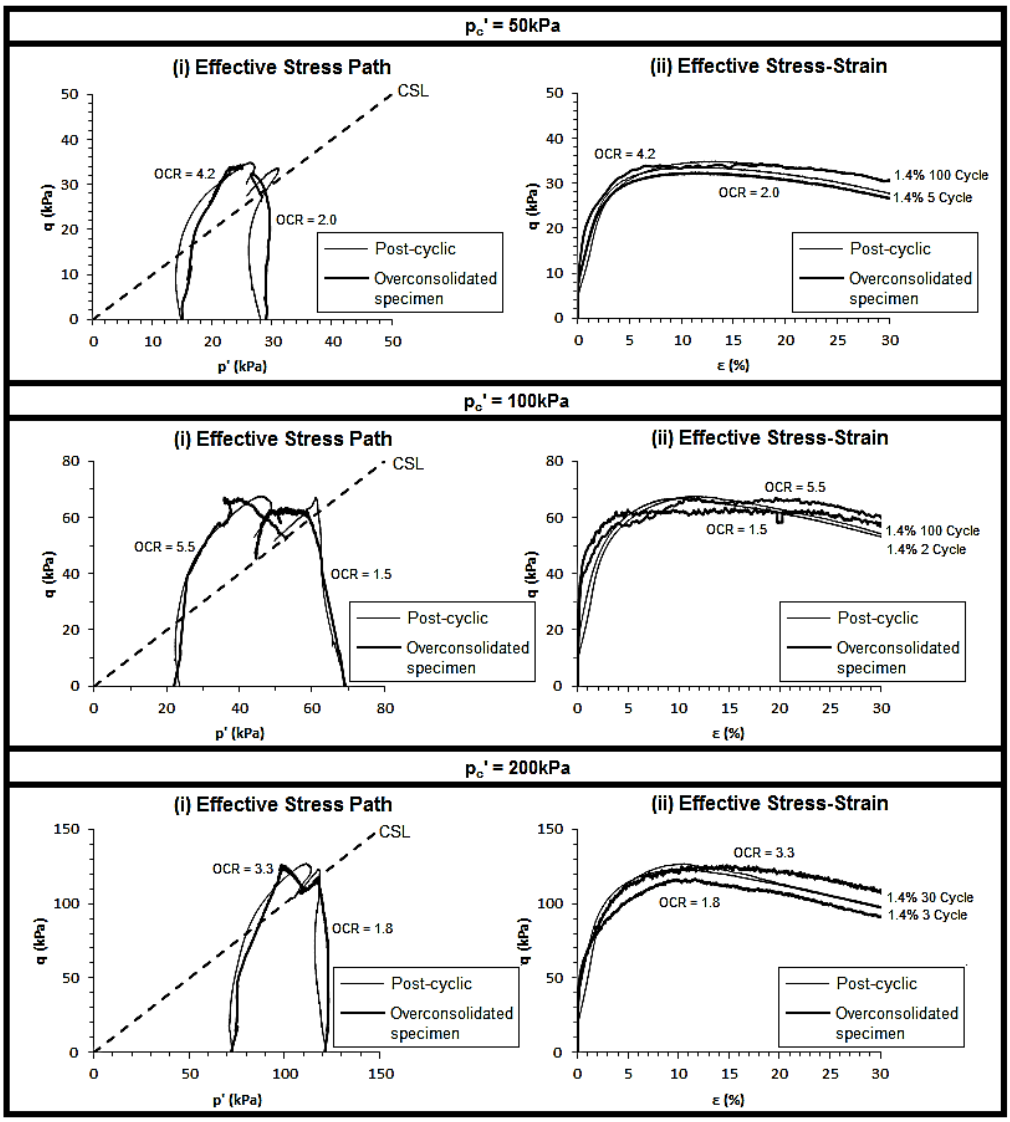

Figure 6.36 Comparison of undrained monotonic shearing response for normally consolidated specimens loaded undrained cyclically with overconsolidated specimens of Singapore Upper Marine Clay.

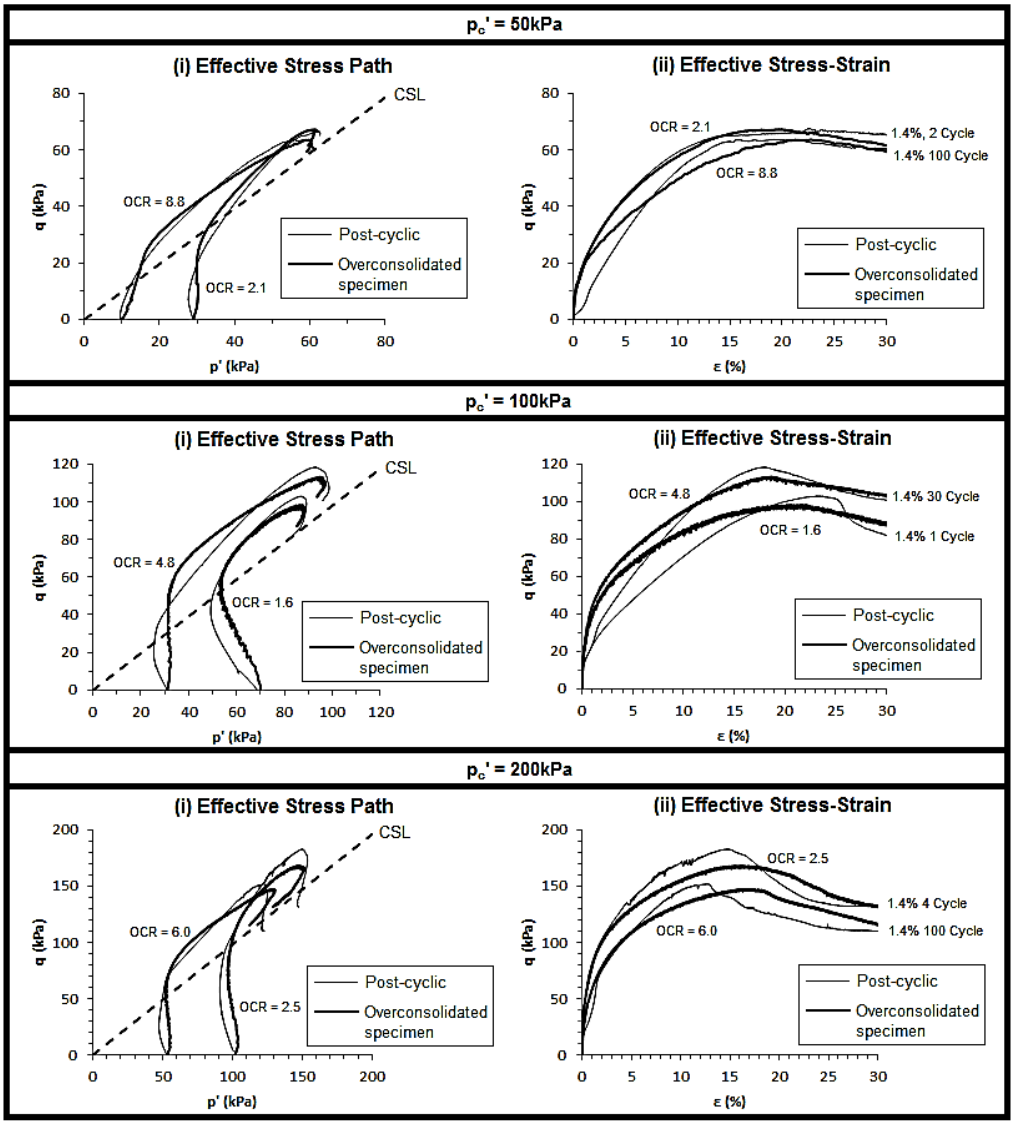

Figure 6.37 Comparison of undrained monotonic shearing response for normally consolidated specimens loaded undrained cyclically with overconsolidated specimens of Kaolin Clay.

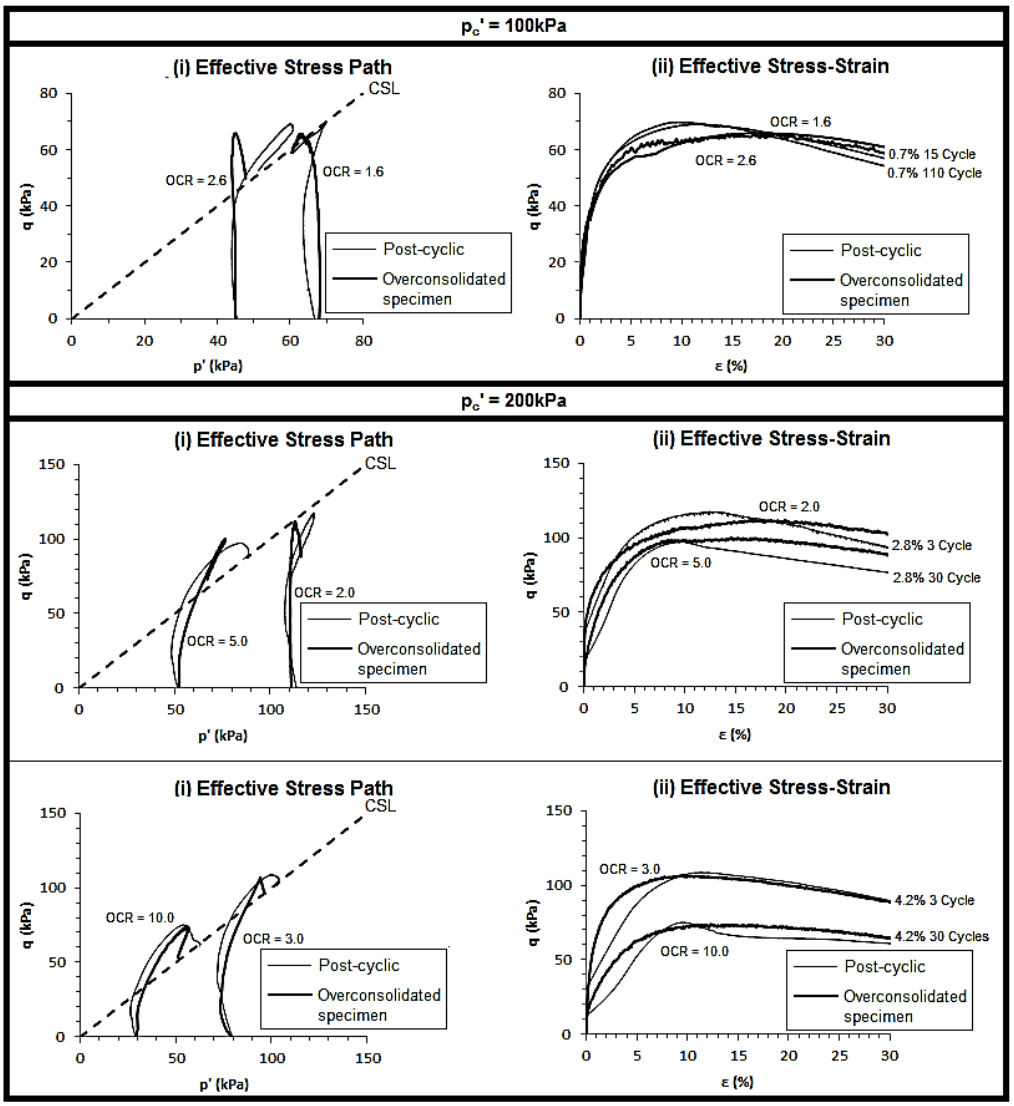

Figure 6.38 Comparison of undrained monotonic shearing response for normally consolidated specimens loaded undrained cyclically with varying cyclic strain amplitudes against overconsolidated specimens of Singapore Upper Marine Clay.

Chapter 7 – Constitutive Model for Cyclic Loading

7.1 Available Constitutive Models

Numerous constitutive models based on elasto-plastic theory have been proposed to describe clay behaviour under monotonic loading. Examples include the Drucker-Prager cap model proposed by Drucker and Prager (1952), the Modified Cam Clay model by Roscoe and Burland (1968), the Brick model by Simpson et al. (1979) as well as many other latter, more sophisticated models. However, the performance of many of these models are often less satisfactory when dealing with repeated loading-unloading situations (Prevost 1977; Carter et al. 1982; Zienkiewicz et al. 1985). Many of these models are unable to capture the observed hysteresis and permanent strain accumulation for drained cyclic loading and excess pore pressure build-up for undrained cyclic loading, especially when the stress path remains within the yield surface. This is due partly to the assumptions of elastic unloading as well as elastic behaviour beneath the yield locus, which precludes plastic behaviour until yielding occurs (Dafalias and Herrmann 1982; Zienkiewicz et al. 1985; Whittle and Kavvadas, 1994).

Numerous models have also been developed to model cyclic loading of clay. The first line of approach involves extensions of the original critical state model for clays and applying volumetric strain hardening plasticity theory with an associated flow rule (Crouch and Wolf 1994). An alternative class of model based on viscoelastic-plastic theories were also developed (e.g. Bazant et al. 1982; Valanis and Read 1982; Oka at al. 2004) but this class of model has a significant drawback compared to the former approach, in terms of their inability to model the monotonic soil response well (Zienkiewicz et al. 1985).

Many of the available cyclic loading models based on extensions of the classic elastoplastic framework are very complex and requires a large number of material parameters to use (Zienkiewicz et al. 1985; Whittle and Kavvadas, 1994). For example, the anisotropic two-surface and multi-surface models (e.g. Mroz et al. 1978; Prevost 1978; Mroz and Pietruszczak 1984) suffer from geometric complexities due to the inclusion of kinematic hardening which incorporates both volumetric and deviatoric strain hardening concepts (Whittle and Kavvadas 1994). In addition, unified models for sand and clay (e.g. Crouch and Wolf 1994; Pestama and Whittle 1999) also require a large number of material parameters. Crouch and Wolf's (1994)

unified 3D critical state bounding-surface plasticity model, in particular, require 25 parameters to use. The general trend which has been observed to date is that constitutive models which give good fits to experimental data generally require a large number of material parameters and are therefore not practical for wider engineering use.

In contrast, the bounding surface formulation of soil plasticity that employs the critical state framework (e.g. Dafalias and Popov 1977; Dafalias and Herrmann 1982; Zienkiewicz et al. 1985) is able to include plastic strains within the yield surface while retaining the benefit of using few material parameters. For instance, the bounding surface models proposed by Dafalias and Herrmann (1982) and Zienkiewicz et al. (1985) respectively require only 3 parameters and 1 parameter additional to those needed for a standard critical state model. Whittle and Kavvadas (1994) extended the bounding surface model by incorporating small strain nonlinearity to simulate perfectly hysteretic behaviour. This MIT-E3 model, though versatile (Whittle 1993; Whittle et al. 1994), also requires 15 material parameters.

Since the simple bounding surface models developed by Dafalias and Herrmann (1982) and Zienkiewicz et al. (1985) are able to preserve the accurate modelling of clay response under monotonic loading conditions compared to endochronic viscoplasticity models (Zienkiewicz et al. 1985) while retaining the basic simplicity requirement, an evaluation of their applicability to the experimental results presented in Chapter 6 is performed.

7.2 Applicability of Bounding Surface Models to the Cyclic Behaviour of Singapore Upper Marine Clay and Kaolin Clay

A schematic illustration of the bounding surface concept is provided in Figure 7.1. The essential feature of the bounding surface formulation is its ability to include plastic strains within the yield surface. For a typical stress state P’ (Figure 7.1) that lies within the yield surface (i.e. bounding surface), unloading is usually assumed to remain elastic (e.g. Dafalias and Herrmann 1982; Zienkiewicz et al. 1985), but reloading from P’ (Figure 7.1) result in irrecoverable plastic strains that are linked explicitly to the behaviour of its projected “image” point P (Figure 7.1) that falls on the normally consolidated surface through the use of simple mapping or interpolation

rules (e.g. Dafalias and Herrmann 1982; Zienkiewicz et al. 1985; Whittle and Kavvadas 1994).

The main differences between the available constitutive models based on bounding surface formulations lies in the use of different yield surfaces and mapping or interpolation rules. For example, Dafalias and Herrmann (1982) employed the radial rule that assumes interpolations from a fixed origin O (Figure 7.2) that always lies within a convex yield surface. The form of the yield surface in stress–invariant space, as illustrated in Figure 7.3, is rather complicated, comprising 2 different ellipses and 1 hyperbola. They further proposed a mathematical expression for the shape hardening function in the triaxial space as follows:

$$H^* = hp_a\left(1+\left|\frac{M}{\eta}\right|^m\right) \qquad [7.1]$$

Where:

H^* = Hardening function in triaxial space,

h and m = Dimensionless material constants,

p_a = Atmospheric pressure,

M = Slope of the critical state line,

η = Stress ratio.

Dafalias and Hermann recommended that the constant m in Equation 7.1 should have a small value of 0.2 to reduce the influence of $|M/\eta|$ for most clays while h is the most critical parameter that controls the response for stress states within the yield surface because it directly limits the amount of plastic deformations within the yield surface. Apart from these two user-defined constants, this model requires another parameter which controls the shape of the hyperbolic part of the yield surface for heavily overconsolidated states (Constant "A" in Figure 7.3). Thus, Dafalias and Herrmann's (1982) model needs a total of 3 parameters additional to those required for a standard critical state model. For static loading conditions of lightly and heavily overconsolidated clays, Dafalias and Herrmann (1982) had demonstrated, through comparison with existing empirical data (see Figures 7.4 and 7.5), that the model is able to perform satisfactorily.

Figure 7.6 presents the model simulations for the cyclic effective stress paths of clays subjected to different cyclic compression stress amplitudes. The corresponding cyclic

stress-strain curves are not available for comparison. Based on Figure 7.6, this model exhibits the same phase transformation behaviour that was discussed in Chapter 6. By joining the observed phase transformation points in Figure 7.6, the resultant phase transformation line obtained corresponds to an approximate stress ratio of 0.87*M* (Figure 7.6). This stress ratio is slightly higher than the proposed value of 0.6*M* (refer to Equation 6.2) for both Marine Clay and kaolin. Similar to the current experimental observation, the phase transformation line identified in this model is a unique line in the stress space. Cyclic loading of smaller stress amplitudes (i.e. $q / p_0' = 0.25$) produces effective stress paths that do not exhibit phase transformation as long as it lies below the phase transformation line.

However, upon reaching the dry side of critical, that is when the overconsolidation ratio becomes sufficiently high, excess pore pressure ceases to accumulate, even under high cyclic stress amplitude (i.e. $q / p_0' = 0.42$). This is manifested in the stress path by a cessation in the drift of the effective stress path. Hence, a potential drawback of this model lies in the inability of the effective stress paths to migrate to the dry side of critical; which is at odds with the experimental observations. As shown in Figures 6.1, 6.2, 6.21 and 6.22, the effective stress paths obtained for Marine Clay and kaolin did progress to the dry side of critical in the stress space if the number of load cycles is sufficient. This is observed to occur for cyclic strain amplitude ranging from 0.7% to 4.2%.

One may surmise that this shortcoming may be due to the assumption of purely elastic unloading. As Section 6.1.3 shows, significant contractive behaviour is observed during unloading of both clay types. This suggests that plastic strains may be induced even during unloading. As both types of clay specimens tend to dilate after sufficient number of load cycles (i.e. start of phase transformation), plastic deformations during unloading is necessary if the effective stress path is to migrate to the dry side of critical. Hence, Dafalias and Herrmann's (1982) bounding surface model will grossly underestimate the amount of degradation in mean effective stress (p') for clays that are subjected to a large number of load cycles. Consequently, the "cyclic mobility" observed in Marine Clay and kaolin could not be reproduced by this model.

In an attempt to provide an even simpler constitutive model, Zienkiewicz et al. (1985) introduced a "generalized plasticity" model incorporating the bounding surface formulation. This "generalized plasticity" model only requires 1 parameter in addition

to those needed for a standard critical state model. The shape of the yield surface is assumed to be elliptical. With reference to Figure 7.1, the interpolation rule for the "generalized plasticity" model proposed is:

$$H_L = H_L^{CS}\left[\frac{\delta_0}{\delta}\right]^{\gamma} \qquad [7.2]$$

Where:

H_L = Loading plastic modulus for stress states within yield surface (Point P'),

H_L^{CS} = Loading plastic modulus for corresponding 'image' (Point P) on yield surface,

δ_0 and δ = Distances from the origin of the stress space as defined in Figure 7.1,

γ = Hardening rule dimensionless material constant.

From Equation 7.2, material constant γ is the governing factor for the amount of plastic deformations occurring within the yield surface. A larger value of γ corresponds to a higher plastic modulus and this translates to reduced degradation in the mean effective stress under undrained cyclic conditions. Similar to the bounding surface model by Dafalias and Herrmann (1982), this "generalized plasticity" model was able to capture the undrained behaviour of slightly overconsolidated clay under monotonic triaxial loadings (Figure 7.7). However, its performance for heavily overconsolidated clays (OCR =10) under undrained compression is less satisfactory (Figure 7.8) with an underestimation of undrained strength. This is because H_L^{CS} and thus H_L in Equation 7.2 vanish when the stress path hits the critical state line. Hence, the dilation that is typically observed in overconsolidated clays cannot be modelled and undrained strength bounded by the critical state line. In a similar fashion, the cyclic effective stress path for undrained strain-controlled test is constricted by the critical state line as shown in Figure 7.9. This contradicts the observed behaviour of Marine Clay and kaolin as shown in Figure 6.1, the stress paths of which are not bounded by the critical state line. In addition, this "generalized plasticity" model is unable to simulate the phase transformation behaviour found in Marine Clay and kaolin.

Figure 7.10 illustrates a typical plot of the cyclic stress-strain produced by the "generalized plasticity" model for predicting the behaviour of kaolin under two-way

strain-controlled undrained cyclic triaxial test. By the 25th load cycle, the model predicts perfectly plastic behaviour during loading for both compression and extension phases. From Figure 6.7, the kaolin used in this study clearly does not exhibit perfectly plastic behaviour throughout the 100 load cycles applied despite using higher cyclic strain amplitude of 1.4% whereby more plasticity is expected. Likewise, the stress-strain curves for Marine Clay also do not show any perfectly plastic regime (Figure 6.6). Instead, as cyclic loading progresses, the hysteretic stress-strain loops for both clay types transform to S-shapes loops, which indicate an increase in shear modulus towards the end of each loading phase. This clearly differs from the behaviour prescribed by the "generalized plasticity" model.

Based on the above discussion on the bounding surface models, one distinct weakness in the above models lie in their inability to provide accurate modelling of undrained cyclic clay behaviour on the dry side of critical. Nevertheless, the simplicity in these models, especially the "generalized plasticity" model, makes them a good basis for the development of a new constitutive model that can reproduce the cyclic behaviour of Marine Clay and kaolin in the present study. Since the "generalized plasticity" model by Zienkiewicz et al. (1985) utilizes fewer parameters compared to the bounding surface model by Dafalias and Herrmann (1982) and it assumes an elliptical yield surface that can be reasonably fitted to the current data (refer to Figures 6.1 and 6.23), it is used herein as a basis for the development of a proposed model.

7.3 Proposed Model

Based on the work of Zienkiewicz et al. (1985), the "generalized plasticity" model was extended to include the phase transformation and subsequent cyclic mobility observed in the current experimental results. Figure 7.11 shows a schematic of the bounding surfaces used in the proposed model. Due to the presence of phase transformation, two different bounding surfaces were introduced for the cyclic loading phases in this framework. One is the Modified Cam Clay, with elliptical yield locus passing through the origin of the general stress space (i.e. q – p') and the second involves the Mohr Coulomb yield criterion, defined as a straight line passing through the origin of the stress axes. For cyclic unloading phases, the non-hardening unloading yield locus postulated by Lee and Foo (1991), based on the combination of Taylor's energy equation with an associated flow rule together with the assumption of unloading-induced plasticity, is used as the unloading bounding surface. Prior to yielding, the clay behaviour is mainly controlled by the distance of the current stress

state from its projections on the bounding surfaces though the use of radial interpolation rule. As Figure 7.11 shows, the model assumes that the phase transformation line divides the stress space into contractive and dilative regimes similar to that observed in current experimental results (e.g. Figure 6.2).

7.3.1 Contractive Regime below Phase Transformation Line

The proposed model herein is based on the Modified Cam Clay model by Roscoe and Burland (1968) that had been previously proven to reasonably predict the behaviour of reconstituted, isotropically consolidated specimens of Singapore Marine Clay (Chua 1990). The Modified Cam Clay energy equation that allows energy to be dissipated by both volumetric and shear strain increments is given by:

$$p' d\varepsilon_v^p + q d\varepsilon_s^p = \sqrt{M^2 p'^2 \, d\varepsilon_s^{p2} + p'^2 \, d\varepsilon_v^{p2}} \qquad [7.3]$$

Where:

p' = Mean effective principal stress,

q = Deviator stress,

M = Critical state friction coefficient,

$d\varepsilon_v^p$ = Plastic volumetric strain increment,

$d\varepsilon_s^p$ = Plastic shear strain increment.

For strain-hardening clays on the wet side of critical, the assumption of associated plastic flow was found to be reasonably realistic (e.g. Atkinson and Richardson 1985; Wood 1990). By assuming an associated flow rule, the Modified Cam Clay yield function ($F_1(p', q)$) under triaxial conditions is derived as:

$$F_1(p', q) = q^2 + M^2 p'^2 - M^2 p_c' \, p' = 0 \qquad [7.4]$$

Where:

p_c' = Preconsolidation pressure.

and the plastic potential ($G_1(p', q)$) is

$$G_1(p', q) = F_1(p', q) = 0 \qquad [7.5]$$

Within the yield surface, ideal isotropic elasticity is assumed so the bulk modulus is dependent on the mean effective stress:

$$K' = \frac{1 + e_0}{\kappa} p' \qquad [7.6]$$

Where:

K' = Effective bulk modulus,

e_0 = Initial void ratio of the specimen (corresponds to the start of cyclic loading),

κ = Slope of the elastic unloading-reloading line.

Accordingly, assuming a constant value of Poisson's ratio, the shear modulus is also proportional to the stress state:

$$G' = \frac{3K'(1-2\upsilon')}{2(1+\upsilon')} \qquad [7.7]$$

Where:

G' = Effective shear modulus,

υ' = Effective Poisson's ratio.

Using the generalized Hooke's Law, the elastic matrix $[D_e']$ under triaxial conditions is formulated:

$$D_e' = \begin{bmatrix} K' & 0 \\ 0 & 3G' \end{bmatrix} \qquad [7.8]$$

In the loading direction, the normal vectors to the plastic potential and yield surface are defined as $\underline{a_1}$ and $\underline{b_1}$ respectively:

$$\underline{a_1} = \begin{Bmatrix} \frac{\partial G_1}{\partial p'} \\ \frac{\partial G_1}{\partial q} \end{Bmatrix} = \begin{Bmatrix} 2M^2 p' - M^2 p_c' \\ 2q \end{Bmatrix} \qquad [7.9]$$

and

$$\underline{b_1} = \begin{Bmatrix} \frac{\partial F_1}{\partial p'} \\ \frac{\partial F_1}{\partial q} \end{Bmatrix} = \begin{Bmatrix} 2M^2 p' - M^2 p_c' \\ 2q \end{Bmatrix} \qquad [7.10]$$

For the Modified Cam Clay model, the hardening parameter is the preconsolidation pressure (p_c'), which defines the size of the yield locus. The hardening law is given by:

$$\underline{h} = H d\varepsilon^p \qquad [7.11]$$

Where:

$\underline{h}$ = Vector of hardening parameters used in the yield surface,

$d\varepsilon^p$ = Plastic strain increment vector,

H = [1 0].

As the Modified Cam Clay model only allows for isotropic hardening, $\underline{h}$ is related to only the plastic volumetric strain increment ($d\varepsilon_v^p$). Therefore, under triaxial conditions,

$$\underline{h} = \begin{bmatrix} 1 & 0 \end{bmatrix} \begin{bmatrix} d\varepsilon_v^p \\ d\varepsilon_s^p \end{bmatrix} = d\varepsilon_v^p \qquad [7.12]$$

Since $\underline{h}$ contains only one element, the gradient of the yield function with respect to $\underline{h}$ is a scalar. Thus,

$$\underline{c}^T = \frac{\partial F}{\partial h} = \frac{-M^2 v_0 p' p_c'}{\lambda - \kappa} \qquad [7.13]$$

The work-hardening elasto-plastic matrix for Modified Cam Clay under triaxial conditions is then given by:

$$\left[D_{ep}\right] = \left[D_e'\right]\left(\underline{I} - \frac{\underline{a_1}\,\underline{b_1}^T \left[D_e'\right]}{\underline{b_1}^T \left[D_e'\right]\underline{a_1} - \underline{c}^T H\, \underline{a_1}} \right) \qquad [7.14]$$

Where: $\underline{I}$ is the identity matrix.

In the "generalized plasticity" model, the interpolation rule proposed (Equation 7.2) depends on distances δ_0 and δ as defined in Figure 7.1. In a similar way, the proposed model assumes that the actual stress state (p', q) corresponds to an elliptical sub-yield surface (defined by Equation 7.4) with preconsolidation pressure labelled as "Sub-yield p_c'" in Figure 7.12b. Its projected "image" stress state (p_{yield}', q_{yield}) that falls on the Modified Cam Clay bounding surface (also defined by Equation 7.4) will correspond to a preconsolidation pressure "Yield p_c'" in Figure 7.12b.

From the Modified Cam Clay yield function (Equation 7.2),

$$Sub-yield \;\; p_c' = p' + \frac{q^2}{M^2 p'} \qquad [7.15]$$

Using the v-ln p' space (Figure 7.12a),

$$Yield\ \ p_c' = e^{\frac{v_\lambda - v_\kappa}{\lambda - \kappa}} \qquad [7.16]$$

Where:

v_λ and v_κ = Specific volume axis intercepts for normal consolidation line and elastic unloading-reloading line respectively. (Note that v_κ is a variable),

λ = Slope of the normal consolidation line.

The irrecoverable plastic strains are then included within the Modified Cam Clay yield surface through the use of radial interpolation rule:

$$\partial \varepsilon^p = \left[\frac{Sub - yield\ \ p_c'}{Yield\ \ p_c'} \right]^\alpha \frac{\underline{a_1}\underline{b_1}^T [D_e']}{\underline{b_1}^T [D_e'] \underline{a_1} - \underline{c}^T H \underline{a_1}} \partial \varepsilon \qquad [7.17]$$

Where:

α = Dimensionless material constant for plastic strain interpolation from Modified Cam Clay yield surface.

Consequently, under triaxial conditions, the work-hardening elasto-plastic matrix for the contractive regime is derived as:

$$[D_{ep}^{CON}] = [D_e'] \left(\underline{I} - \left(\frac{Sub - yield\ \ p_c'}{Yield\ \ p_c'} \right)^\alpha \frac{\underline{a_1}\underline{b_1}^T [D_e']}{\underline{b_1}^T [D_e'] \underline{a_1} - \underline{c}^T H \underline{a_1}} \right) \qquad [7.18]$$

7.3.2 Dilative Regime above Phase Transformation Line

In Section 6.1.1, the stress ratio defining the phase transformation line in the effective stress space is given by:

$$\eta_{PT} = 0.6M \qquad [7.19]$$

When the stress path crosses the phase transformation line upon compression loading or reloading, soil behaviour changes from contractive to dilative. In an undrained specimen, this is manifested through a recovery in mean effective stress. To model this dilative behaviour, the Mohr Coulomb yield criterion that predicts continuous dilative behaviour was incorporated as a second bounding surface. Under triaxial conditions, the Mohr Coulomb yield function ($F_2(p', q)$) is:

$$F_2(p',q) = q - M_{peak}\, p' = 0 \qquad [7.20]$$

Where:

M_{peak} = Friction coefficient corresponding to the peak angle of friction (or maximum deviator stress).

and the plastic potential ($G_2(p',q)$) is

$$G_2(p',q) = q - Np' = 0 \qquad [7.21]$$

Where:

$$N = \frac{6\sin\psi}{3-\sin\psi} \qquad [7.22]$$

ψ = Angle of dilation.

The normal vectors to the plastic potential and yield surface are defined as $\underline{a_2}$ and $\underline{b_2}$ respectively:

$$\underline{a_2} = \begin{Bmatrix} \frac{\partial G_2}{\partial p'} \\ \frac{\partial G_2}{\partial q} \end{Bmatrix} = \begin{Bmatrix} -N \\ 1 \end{Bmatrix} \qquad [7.23]$$

and

$$\underline{b_2} = \begin{Bmatrix} \frac{\partial F_2}{\partial p'} \\ \frac{\partial F_2}{\partial q} \end{Bmatrix} = \begin{Bmatrix} -M_{peak} \\ 1 \end{Bmatrix} \qquad [7.24]$$

Under triaxial conditions, the elasto-plastic matrix for Mohr-Coulomb is thus given by:

$$[D_{ep}] = [D_e'] \left(\underline{I} - \frac{\underline{a_2}\,\underline{b_2}^T [D_e']}{\underline{b_2}^T [D_e'] \underline{a_2}} \right) \qquad [7.25]$$

The interpolation rule used to include plastic strains from the Mohr Coulomb yield surface is then dependent on 3 stress ratios – the actual stress state (η), the phase transformation line (η_{PT}), and the Mohr-Coulomb yield surface (M_{peak}).

$$\partial\varepsilon^{p} = \left[\frac{\eta - \eta_{PT}}{M_{peak} - \eta_{PT}}\right]^{1-p'/p_c'} \frac{\underline{a_2}\underline{b_2}^{T}[D_e']}{\underline{b_2}^{T}[D_e']\underline{a_2}}\partial\varepsilon \qquad [7.26]$$

As discussed in Section 6.1, the effective stress paths adopt a more distinctive "butterfly" profile after numerous load cycles, indicating progressively larger plastic strains especially on unloading. To model this behaviour, the plastic strain is assumed to vary with the interpolation term $\left[\frac{\eta - \eta_{PT}}{M_{peak} - \eta_{PT}}\right]$ to the power of (1- p'/p_c'). Since the entire range of possible normalized mean effective stress (p'/p_c') is from 0 to 1 and p'/p_c' reduces during cyclic loading, $\left[\frac{\eta - \eta_{PT}}{M_{peak} - \eta_{PT}}\right]^{1-p'/p_c'}$ will increase as cyclic loading progresses. Consequently, the plastic strain increment increases with increasing load cycles to model the "butterfly" stress paths after numerous load cycles.

Although the angle of dilation (ψ) can control the amount of recovery in mean effective stress, this parameter alone is unable to replicate the onset of dilative behaviour during cyclic loading. The Mohr Coulomb bounding surface will predict dilative behaviour throughout the entire range of possible normalized mean effective stress (p'/p_c'), from 0 to 1, as long as the stress state lies above the phase transformation line. This agrees with experimentally observed kaolin behaviour. However, Marine Clay shows dilative tendency only when the normalized mean effective stress decreases to about 0.5. Thus, for stress states within the dilative regime above the phase transformation line, plastic strains are linked to both Modified Cam Clay and Mohr Coulomb bounding surfaces as follows:

$$\partial\varepsilon^{p} = \left\{\frac{p'}{p_c'}\left[\frac{Sub-yield\ p_c'}{Yield\ p_c'}\right]^{\alpha} \frac{\underline{a_1}\underline{b_1}^{T}[D_e']}{\underline{b_1}^{T}[D_e']\underline{a_1} - \underline{c}^{T}H\underline{a_1}} + \left(1 - \frac{p'}{p_c'}\right)\left[\frac{\eta - \eta_{PT}}{M_{peak} - \eta_{PT}}\right]^{1-p'/p_c'} \frac{\underline{a_2}\underline{b_2}^{T}[D_e']}{\underline{b_2}^{T}[D_e']\underline{a_2}}\right\}\partial\varepsilon$$

[7.27]

This interpolation rule uses the normalized mean effective stress (p'/p_c') as the parameter governing the onset of dilative behaviour. With decreasing normalized mean effective stress as cyclic loading progresses, the Modified Cam Clay term in

Equation 7.27 diminishes while the Mohr Coulomb term has an increasing effect on the plastic strains. This assumption is also applicable to kaolin because the degradation in normalized mean effective stress (p'/p_c') for the first load cycle is more pronounced as compared to Marine Clay (see Figure 6.2). Thus, the onset of dilative behaviour will occur earlier for kaolin under cyclic loading.

Consequently, under triaxial conditions, the work-hardening elasto-plastic matrix for the dilative regime is derived as:

$$\left[D_{ep}^{DIL}\right]=\left[D_e'\right]\left(\underline{I}-\frac{p'}{p_c'}\left[\frac{Sub-yield\ p_c'}{Yield\ p_c'}\right]^{\alpha}\frac{\underline{a_1}\,\underline{b_1}^{T}\left[D_e'\right]}{\underline{b_1}^{T}\left[D_e'\right]\underline{a_1}-\underline{c}^{T}H\,\underline{a_1}}-\left(1-\frac{p'}{p_c'}\right)\left[\frac{\eta-\eta_{PT}}{M_{peak}-\eta_{PT}}\right]^{1-p'/p_c'}\frac{\underline{a_2}\,\underline{b_2}^{T}\left[D_e'\right]}{\underline{b_2}^{T}\left[D_e'\right]\underline{a_2}}\right) \qquad [7.28]$$

7.3.3 Unloading

The other component of the proposed model is the tendency of the clay to densify during unloading, which is translated into a decrease in mean effective stress under undrained conditions. Based on the Taylor's energy equation, assuming associated flow rule and unloading-induced plasticity, Lee and Foo (1991) derived a non-hardening unloading yield locus ($F_U(p',q)$) as:

$$F_U(p',q)=\eta_r\,p'+Mp'\ln p'-Mp'\ln p_r'-q \qquad [7.29]$$

Where:

η_r = Reversal stress ratio (defined at the stress reversal point), from which unloading occurs rather than the current value, see Figure 7.13),

p_r' = Mean effective stress corresponding to the stress reversal point.

and the plastic potential ($G_U(p',q)$) is

$$G_U(p',q)=F_U(p',q)=0 \qquad [7.30]$$

In the unloading direction, the normal vectors to the plastic potential and yield surface are defined as $\underline{a_U}$ and $\underline{b_U}$ respectively:

$$\underline{a_U}=\begin{Bmatrix}\frac{\partial G_U}{\partial p'}\\ \frac{\partial G_U}{\partial q}\end{Bmatrix}=\begin{Bmatrix}\eta_r+M+M\ln p'-M\ln p_r'\\ -1\end{Bmatrix} \qquad [7.31]$$

and $$\underline{b_U} = \begin{Bmatrix} \dfrac{\partial F_U}{\partial p'} \\ \dfrac{\partial F_U}{\partial q} \end{Bmatrix} = \begin{Bmatrix} \eta_r + M + M \ln p' - M \ln p_r' \\ -1 \end{Bmatrix} \qquad [7.32]$$

Under triaxial conditions, the elasto-plastic matrix for the unloading yield surface is then defined as:

$$[D_{ep}] = [D_e'] \left(\underline{I} - \frac{\underline{a_U}\,\underline{b_U}^T [D_e']}{\underline{b_U}^T [D_e'] \underline{a_U}} \right) \qquad [7.33]$$

Using the non-hardening unloading yield surface, the radial interpolation rule used for stress states prior to yielding is taken as:

$$\partial \varepsilon^p = \beta \left[\frac{\eta_r}{M} \right]^{\mu} \frac{\underline{a_U}\,\underline{b_U}^T [D_e']}{\underline{b_U}^T [D_e'] \underline{a_U}} \partial \varepsilon \qquad \text{for } \left| \frac{\eta_r}{M} \right| < 1$$

$$\partial \varepsilon^p = \beta \frac{\underline{a_U}\,\underline{b_U}^T [D_e']}{\underline{b_U}^T [D_e'] \underline{a_U}} \partial \varepsilon \qquad \text{for } \left| \frac{\eta_r}{M} \right| \geq 1 \qquad [7.34]$$

Where:

μ = Dimensionless material constant for plastic strain interpolation from unloading yield surface,

β = Dimensionless material constant for the unloading phase.

The unloading interpolation rule proposed here is similar to the unloading relation used in the modified "generalized plasticity" model by Pastor et al. (1985). Their unloading relation assumes that the degradation in mean effective stress (or excess pore pressure increase) during unloading is more pronounced as the stress reversal point approaches the critical state line. Likewise, in the current study, the unloading phase of the first load cycle is almost elastic but the subsequent cycles show more degradation in mean effective stress (e.g. Figure 7.13). From a conceptual viewpoint, Lee and Foo's (1991) has a theoretical basis since it is derived from energy consideration assuming the large-scale particulate sliding does occur during unloading, that is, under conditions of negative shear strain increments. In contrast, Pastor et al. (1985) gave no reason for their relation and one would have to assume that it is essentially an empirically fitted relation.

Under triaxial conditions, the work-hardening elasto-plastic matrix for the unloading phase is then derived as:

$$\left[D_{ep}^{U}\right]=\left[D_e'\right]\left(\underline{I}-\beta\left[\frac{\eta_r}{M}\right]^{\mu}\frac{\underline{a_U}\,\underline{b_U}^{T}\left[D_e'\right]}{\underline{b_U}^{T}\left[D_e'\right]\underline{a_U}}\right) \qquad \text{for } \left|\frac{\eta_r}{M}\right|<1$$

$$\left[D_{ep}^{U}\right]=\left[D_e'\right]\left(\underline{I}-\beta\frac{\underline{a_U}\,\underline{b_U}^{T}\left[D_e'\right]}{\underline{b_U}^{T}\left[D_e'\right]\underline{a_U}}\right) \qquad \text{for } \left|\frac{\eta_r}{M}\right|\geq 1 \qquad [7.35]$$

7.4 Evaluation of Model Input Parameters

The proposed model herein comprises three bounding surfaces, each of which contributes material parameters in the overall formulation as shown above. In order to clarify the presentation, the required parameters are summarized as follows:

Modified Cam Clay

- M the critical state friction coefficient. M is related to ϕ_{crit}', the critical state friction angle obtained in triaxial compression tests, by

$$M=\frac{6\sin\phi_{crit}'}{3-\sin\phi_{crit}'} \qquad [7.36]$$

- λ the slope of the normal consolidation line in $v-\ln p'$ space, which can be determined directly from a standard oedometer test.
- κ the slope of the elastic unloading-reloading line in $v-\ln p'$ space, which can also be determined directly from a standard oedometer test.
- e_0 the initial void ratio of the specimen.
- υ' the effective Poisson's ratio.

Mohr-Coulomb

- M_{peak} the friction coefficient. M_{peak} is related to ϕ_{peak}', the peak friction angle friction obtained in triaxial compression tests, by

$$M_{peak}=\frac{6\sin\phi_{peak}'}{3-\sin\phi_{peak}'} \qquad [7.37]$$

Based on monotonic triaxial compression tests on overconsolidated Marine Clay and kaolin, their peak friction angles (ϕ_{peak}') measured are 31.1 degrees and 29.5 degrees, respectively (see Figure 7.14). Their equivalent

peak friction coefficients (M_{peak}) are 1.25 and 1.18. Figure 7.15 shows that the peak friction coefficients obtained compare well with the post-cyclic effective stress paths.

According to Atkinson (2007), a linear Mohr Coulomb failure criterion over-predicts the peak strength of overconsolidated clays confined at relatively small mean effective stresses (p' < 50kPa). In his study on 7 different clays, the peak strength envelope becomes highly non-linear once the overconsolidation ratio exceeds 4 (i.e. $p'/p_c' \leq 0.25$). Figure 7.16 compares his kaolin data against those obtained in the current study. Both data sets correlate reasonably well. The dashed lines OA and AC represent the no-tension cut-off and the Horslev surface respectively (Atkinson 2007). When the normalized mean effective stresses fall below 0.25, the peak state points lie well below line AC and fall closely to the curve OC proposed by Atkinson (2007). However, the linear Mohr Coulomb criterion adopted in the current model assumes no cohesion such that the peak strength becomes underestimated in this region (see Figure 7.16). Apart from conservative purpose, the use of a linear Mohr Coulomb criterion (instead of the curve proposed by Atkinson (2007)) as the bounding surface has the advantage of simplicity in the interpolation rule proposed (Equation 7.26).

- ψ the angle of dilation.

Unloading

The parameters used for defining the unloading yield surface are the same as those specified for the Modified Cam Clay above.

Bounding Surface Parameters

- α the dimensionless material constant for plastic strain interpolation from Modified Cam Clay yield surface.
- μ the dimensionless material constant for plastic strain interpolation from the unloading yield surface.
- β the dimensionless material constant for the unloading phase.

The total number of parameters is 10, of which 7 are parameters related to the Cam Clay and Mohr-Coulomb models and 3 are bounding surface parameters. In the

present formulation, the bounding surface parameters α and β govern the degradation in the deviator and mean effective stresses. In order to demonstrate the individual effects of both parameters, α and β were varied in Figures 7.17 and 7.18 respectively. From Figure 7.17, an increase in α from 2 to 10 leads to less degradation in the mean effective stress by 4kPa after 10 load cycles. For the loading phase of the first load cycle, the model produces the same effective stress paths and stress-strain profiles because the ratio $\left[\frac{Sub-yield\ \ p_c'}{Yield\ \ p_c'}\right]$ equals 1 such that the interpolation term $\left[\frac{Sub-yield\ \ p_c'}{Yield\ \ p_c'}\right]^{\alpha}$ equals 1 regardless of the value of α. As cyclic loading progresses, the ratio $\left[\frac{Sub-yield\ \ p_c'}{Yield\ \ p_c'}\right]$ decreases and is always less than 1 so increasing α results in less plasticity. Thus, the "butterfly" profile in the effective stress path corresponding to $\alpha = 10$ is less pronounced. With less plasticity, the stress-strain loops also show more severe flattening by the 10th load cycle because more elastic behaviour leads to less variation in stiffness.

Another potential effect of a higher value of α is the observed increase in peak cyclic deviator stress from the first to second load cycle due to the elliptical shape of the Modified Cam Clay bounding surface. The same limitation can also be observed in the Zienkiewicz's (1985) "generalized plasticity" model that assumes elliptical yield surface (see Figure 7.19). This means that the secant shear modulus had increased from the 1st load cycle to the 2nd load cycle, which is inconsistent with the current experimental trend and literature data reported earlier in Chapter 5 (e.g. Figure 5.6). This issue can be overcome by limiting the value of α to less than 4. For both Marine Clay and kaolin, $\alpha = 2$ is found to provide a reasonable fit with the empirical data. A detailed comparison of the model results with the experimental data will be discussed in the following Section 7.5.

From Figure 7.18, an increase in β from 0.1 to 0.4 leads to more significant degradation in the deviator and mean effective stresses after 10 load cycles. This is because the unloading plastic strain increment is assumed to be directly proportional to β (refer to Equation7.34). A recommended range of $0.1 \le \beta \le 0.5$ is proposed for

the current model since $\beta < 0.1$ leads to model instability and increasing β beyond 0.5 has negligible influence on the simulation results.

Lastly, unlike α and β, the unloading material constant μ has little influence on the overall degradation in the deviator and mean effective stresses. μ only affects the unloading phase of the first or sometimes the initial few cycles as long as the reversal stress ratio (η_r) is less than the critical state friction coefficient (M). As demonstrated in Figure 7.20, increasing μ from 1 to 10 leads to a more elastic unloading response for the 1st load cycle. As explained earlier, the unloading phase of the first load cycle is almost elastic though the subsequent cycles show more degradation in mean effective stress (Figure 7.13). A recommended range of $5 \le \mu \le 20$ is proposed for the current model since $\mu < 5$ leads to unrealistic volumetric plastic strains upon unloading for the 1st load cycle and increasing μ beyond 20 results in model instability. For both Marine Clay and kaolin, $\mu = 10$ is found to provide a reasonable fit with the empirical data.

7.5 Comparison with Experimental Data

7.5.1 Model Response to Cyclic Loading

The model is used to simulate the behaviour of two-way strain-controlled undrained cyclic triaxial tests with the applied cyclic strain amplitude of 1.4%. Comparisons of the model simulations and the experimental data are presented in Figures 7.21 and 7.22. The bounding surface parameters were prescribed to provide the best fit of the experimental data. The predicted trend of the effective stress paths for both Marine Clay and kaolin are reasonably similar to the experimental data. The progressive reduction in mean effective stress is in good agreement although the reduction in deviator stress is more pronounced in the model. By the 30th load cycle, the peak deviator stresses are under-predicted by 3kPa and 2kPa for Marine Clay and kaolin respectively. Consequently, the model yields slightly conservative secant shear modulus. Similar to the experimental observations, the model exhibits alternating phases of dilation and contraction which manifest as the “butterfly” effective stress paths after 30 load cycles. The stress-strain relationships, however, could not be modelled accurately for both clay types. For the first load cycle, the non-linearity in the stress-strain profile of the unloading phases (i.e. both compression and extension) could not be reproduced. The predicted stress-strain loops show a progressive

flattening with increasing load cycles, indicating more elastic behaviour. This implies that the damping ratio becomes grossly underestimated. This limitation in the model lies in the assumption of ideal isotropic elasticity within the yield surfaces (Equation 7.6) and a constant value of Poisson's ratio. By combining Equations 7.6 and 7.7, the shear modulus (G') is then directly proportional to the mean effective stress (p'):

$$G' = \frac{3(1-2\upsilon')}{2(1+\upsilon')}\left(\frac{1+e_0}{\kappa}\right)p' \qquad [7.38]$$

Since the variation in the mean effective stress is limited during the unloading phases, the shear modulus will be approximately constant such that the stress-strain behaviour approaches that of linear elastic for the first load cycle. As cyclic loading progresses, the change in mean effective stress within each cycle reduces as the excess pore pressure stabilizes. This explains the flattening stress-strain loops in the model.

As highlighted in Chapter 6, overconsolidated kaolin exhibit phase transformation while Marine Clay does not. Hence, phase transformation cannot be defined for Marine Clay. For this reason, the definition of the phase transformation line in the model was altered for overconsolidated Marine Clay. From Figure 7.23, overconsolidated Marine Clay tends to exhibit contractive behaviour in the compression loading and unloading phases. Dilative behaviour is observed in the extension loading phase followed by contractive behaviour upon extension unloading. To model this behaviour, the stress ratio of the phase transformation line (η_{PT}) in the compression zone (q > 0) is assigned a large value such that the stress state is always within the contractive regime below the phase transformation line ($\eta_{PT} = 2$ in this simulation). For the extension zone (q < 0), a small value is prescribed for η_{PT} so that there is early onset of dilative behaviour ($\eta_{PT} = -0.4$ in this simulation; $\eta_{PT} < -0.4$ leads to model instability). At the end of 30 load cycles, the predicted profile of the effective stress path for overconsolidated Marine Clay is quite similar to the experimental data (Figure 7.24). The progressive reduction in the mean effective stresses is slightly underestimated by 3kPa. Due to the different phase transformation stress ratios prescribed for the compression and extension zones, the degradation in deviator stress is more pronounced for the extension zone. Thus, the peak deviator stress corresponding to the 30th load cycle is under-predicted by 7kPa and 22kPa in the compression and extension zones respectively. This indicates that the model

yields conservative secant shear modulus for overconsolidated clays. Similar to the model predictions for normally consolidated Marine Clay, the predicted stress-strain loops also show a progressive flattening with increasing load cycles.

As Figure 7.25 shows, the predicted stress path for overconsolidated kaolin is reasonably similar to the experimental data. The overall reduction in mean effective stress at the end of 30 load cycles is in good agreement but the reduction in deviator stress is more pronounced in the model. This is because the effective stress path is limited by the Mohr Coulomb bounding surface. As explained earlier, this Mohr Coulomb criterion that assumes no cohesion will underestimate the peak strength of clays at low values of mean effective stress. Thus, the peak deviator stress corresponding to the 30^{th} load cycle is grossly underestimated by 14kPa. The progressive flattening of stress-strain loops that leads to low damping ratios can also be observed in the predicted behaviour of overconsolidated kaolin.

Lastly, the model is applied to simulate the behaviour of normally consolidated Marine Clay subjected to higher cyclic strain amplitude of 4.2%. As Figure 7.26 shows, the predicted effective stress path is capable of crossing the critical state line which is more representative of the observed clay behaviour (refer to Figure 6.1). This is the advantage of introducing the Mohr Coulomb bounding surface to the proposed model; which is an improvement over the "generalized plasticity" model by Zienkiewicz et al. (1985). Although the model prediction for the effective stress path is rather accurate compared to the empirical data, the model's limitation in grossly underestimating the damping ratio describing the stress-strain behaviour still persists at higher cyclic strain amplitude.

One possible method of overcoming this limitation is to adopt a hysteretic stress-strain model such as the MIT-E3 model (Whittle and Kavvadas 1994). In their model, the Poisson's ratio is assumed constant while the slope of the elastic unloading-reloading line (κ) in the $v - \ln p'$ space becomes a variable as follows:

$$\kappa = \kappa_0 (1 + \delta) \qquad [7.39]$$

Where:

κ_0 = Initial unloading slope in the $v - \ln p'$ space. κ_0 corresponds to the value of the small-strain shear modulus (G_{max}) and can be determined by:

$$\kappa_0 = (1+e_0)p'\left(\frac{3(1-2\upsilon')}{2G_{\max}(1+\upsilon')}\right) \qquad [7.40]$$

$\delta = Cn(\ln \xi)^{n-1}$ where C and n are material constants. ξ relates the current stress state (p') to the reversal stress state (p_{rev}') as defined in Figure 7.27.

However, incorporating a varying κ using this perfectly hysteretic stress-strain model requires an additional 3 parameters - $G_{\max}$, C and n. This will increase the complexity of the proposed model. In order to retain the basic simplicity requirement, this stress-strain model will not be included into the present formulation. Due to time constraint in the present study, efforts in overcoming the model's limitation in predicting accurate stress-strain behaviour will be left as future work.

7.5.2 Model Response to Monotonic and Post-Cyclic Loading

As discussed in Section 6.2, the post-cyclic effective stress paths of clays with apparent overconsolidation induced by cyclic loading are similar to those of clays overconsolidated by real unloading. Consequently, the undrained strength of a cyclically loaded specimen may be predicted based on the apparent overconsolidation ratio induced by the end of the cyclic loading phase. Hence, to simulate post-cyclic behaviour, two assumptions were made:

(i) The preconsolidation pressure (p_c') in the model is a user-defined input that is back-calculated using the compression and swelling indices (Figure 7.28).

$$p_c' = e^{\frac{v_\lambda - v_\kappa}{\lambda - \kappa}} \qquad [7.41]$$

Where:

$$v_\kappa = (1+e_0) + \kappa \ln p_0' \qquad [7.42]$$

(ii) The apparent overconsolidation ratio is then given by (Figure 7.28):

$$AOCR = \frac{p_c'}{p_0'} \qquad [7.43]$$

Subsequently, this apparent overconsolidation ratio is used as the overconsolidation ratio of the specimen at the start of post-cyclic loading in the model.

The comparisons of the model simulations against the experimental data for Marine Clay and kaolin are presented in Figures 7.29 and 7.30 respectively. The monotonic stress paths, i.e. obtained without prior cyclic loading, are designated by N=0. Based on the experimental results, the post-cyclic stress paths for normally consolidated Marine Clay specimens do not exhibit phase transformation regardless of the normalized mean effective stress at the start of the post-cyclic monotonic loading. To model this behaviour, the stress ratio of the phase transformation line (η_{PT}) in the compression zone (q > 0) is assigned a large value such that the stress state is always within the contractive regime below the phase transformation line ($\eta_{PT} = 2$ in this simulation). This is consistent with the assumed value for cyclic loading of overconsolidated Marine Clay.

From Figure 7.29, the maximum deviator stress achieved for Marine Clay is under-predicted by the model, which indicates that both monotonic and post-cyclic undrained shear strength estimated by the model is conservative. As reported in Section 6.2.1, at high normalized mean effective stress, the effective stress of Marine Clay decreases throughout the loading phase of the cycle, indicating contractive tendency. When the normalized mean effective stress decreases to between 0.5 and 0.6, the post-cyclic effective stress path becomes approximately vertical, indicating a transition zone between contractive and dilative post-cyclic behaviour. Similarly, the model is capable of producing post-cyclic effective stress paths which are consistent with these behavioural changes. Furthermore, like the experimental data, the simulated effective stress paths converge to the critical state line at the same point in the effective stress space (Figure 7.29a). In terms of the stress-strain relationship, the model results show good agreement with the experimental data until the predicted maximum deviator stress is achieved (Figure 7.29b). The reduction in the initial stiffness of Marine Clay as the number of applied load cycles increases (from 0 to 100) is also reflected in the model results.

In contrast, the post-cyclic behaviour of kaolin is different. Kaolin exhibits phase transformation throughout the entire range of possible normalized mean effective stress (p'/p_c'), from 0 to 1. As Figure 7.30 shows, the monotonic effective stress path produced by the model is remarkably similar to the experimental data. However, for the post-cyclic stress paths, the contractive behaviour of kaolin below the phase transformation line could not be accurately modelled. This is because the Modified Cam Clay model predicts contractive behaviour only for the range of normalized

mean effective stress (p'/p_c') greater than 0.5 while the Mohr Coulomb model always predicts dilative behaviour. Despite this limitation, the model is capable of producing post-cyclic effective stress paths that not only cross the critical state line but also terminate at the same critical stress state as the experimental data. In terms of the stress-strain relationship, the similarities in the maximum deviator stress achieved between the model and experimental results indicate that the post-cyclic undrained strength of kaolin can be reasonably predicted. Similar to Marine Clay, the reduction in initial stiffness of kaolin as the number of applied load cycles increases (from 0 to 100) is reflected in the model results.

In conclusion, the model introduced in this chapter accounts reasonably well for the salient features of the stress paths of Marine Clay and kaolin under cyclic loading. The model is able to simulate the cyclic mobility observed in the effective stress paths although the flattening of the stress-strain loops will lead to under-estimation of damping ratio. This is a reasonable compromise given the simplicity of the model in terms of the number of input parameters required. Furthermore, the model shows good qualitative agreement with the monotonic and post-cyclic behaviour of both clay types. The predicted undrained shear strengths err generally on the conservative side.

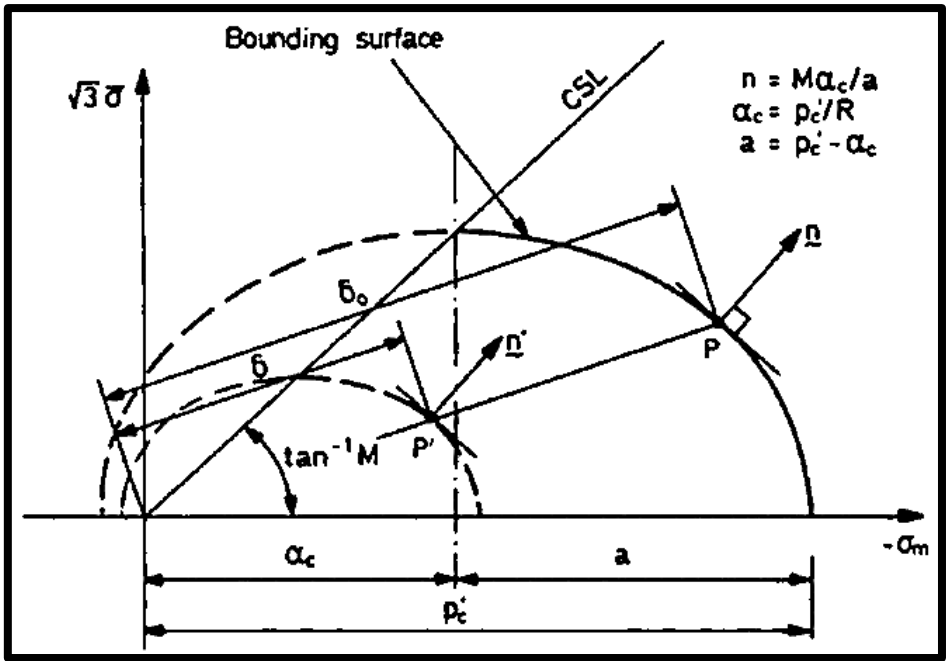

Figure 7.1 Schematic illustration of the bounding surface model in the space of stress invariants (Zienkiewicz et al. 1985).

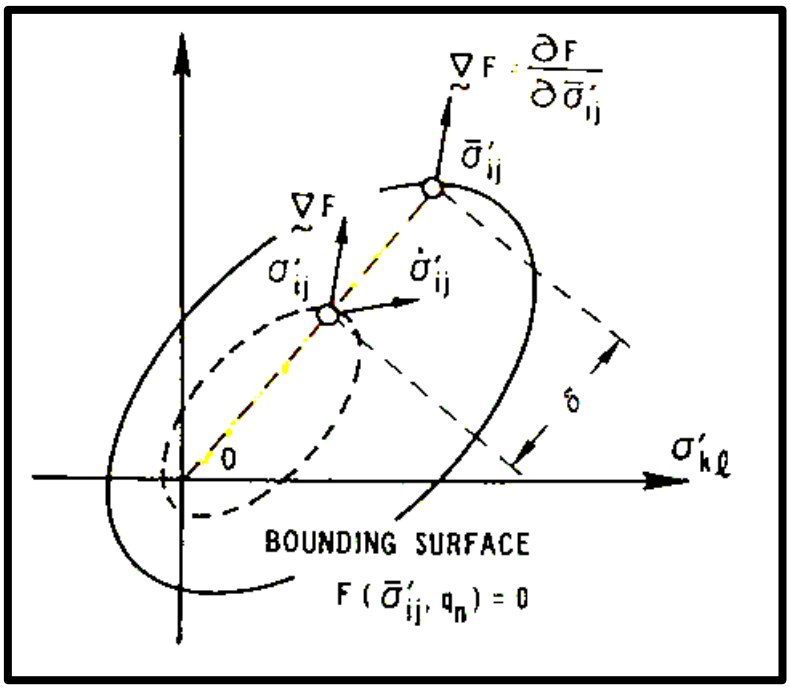

Figure 7.2 Schematic illustration of the bounding surface model in a general stress space (Dafalias and Herrmann 1982).

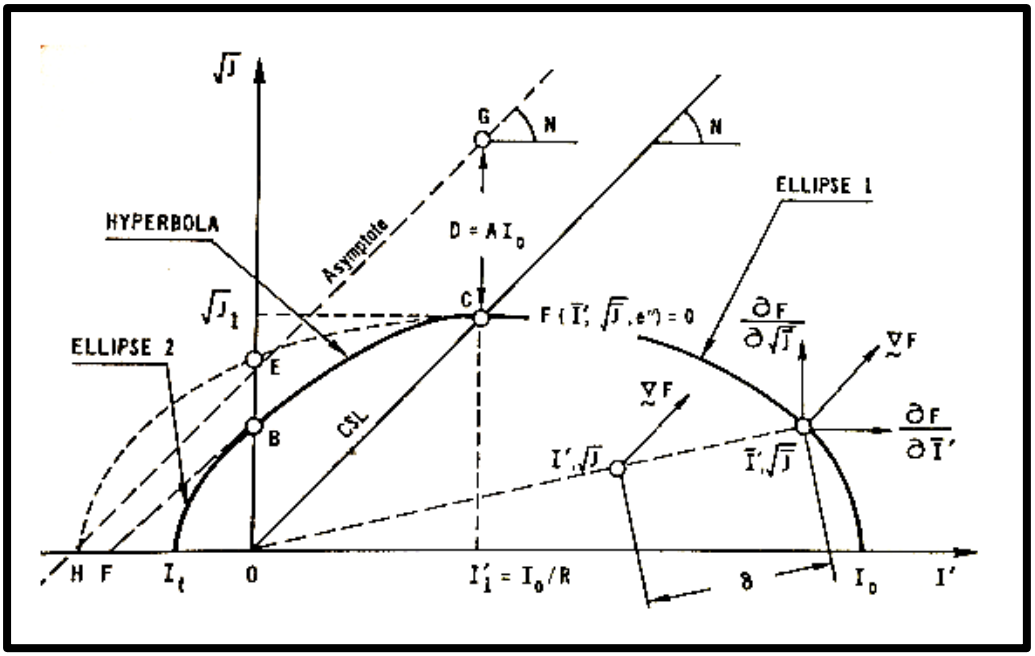

Figure 7.3 Bounding surface model in the space of stress invariants (Dafalias and Herrmann 1982).

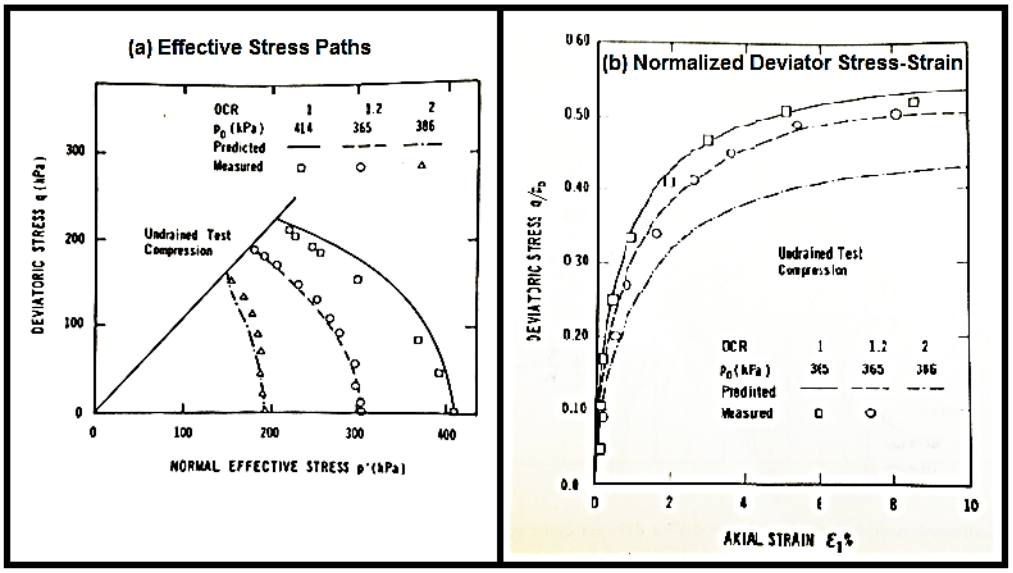

Figure 7.4 Comparison of model predictions for lightly overconsolidated clays against experimental data (Dafalias and Herrmann 1982).

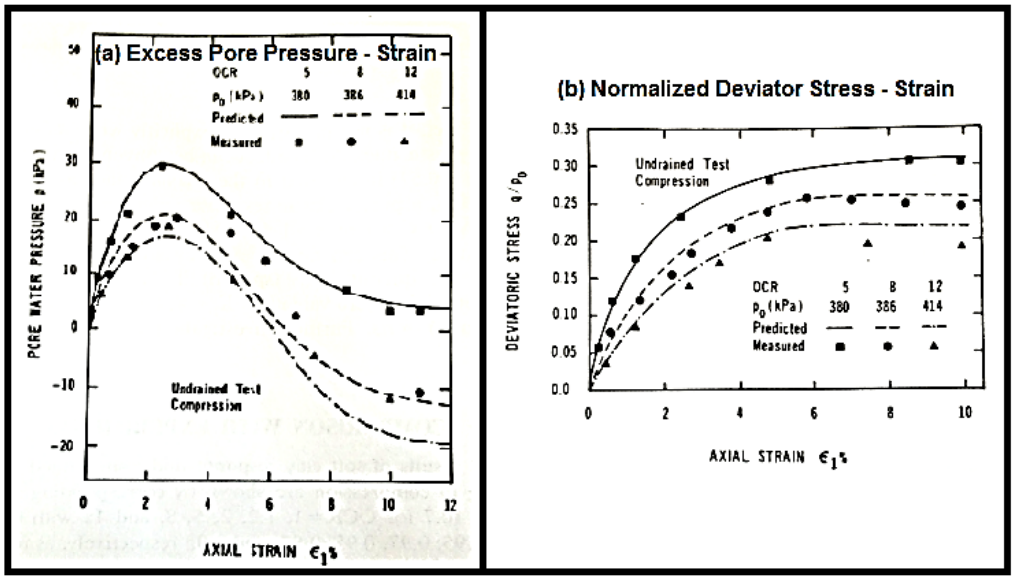

Figure 7.5 Comparison of model predictions for heavily overconsolidated clays against experimental data (Dafalias and Herrmann 1982).

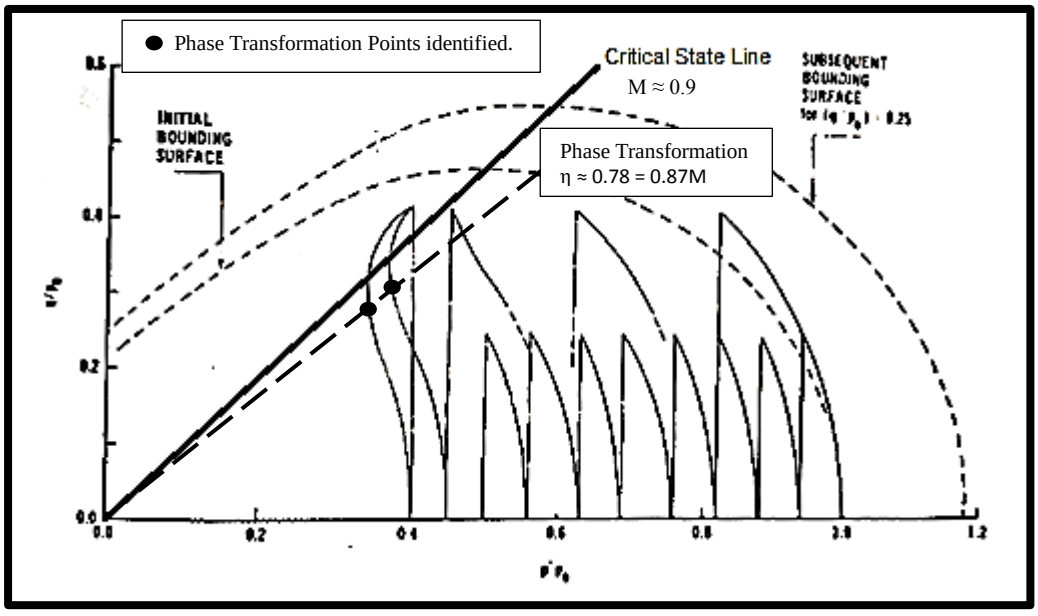

Figure 7.6 Undrained cyclic behaviour of the model for cyclic compression stress amplitudes, q / p_0' of 0.25 and 0.42 (Edited from: Dafalias and Herrmann 1982).

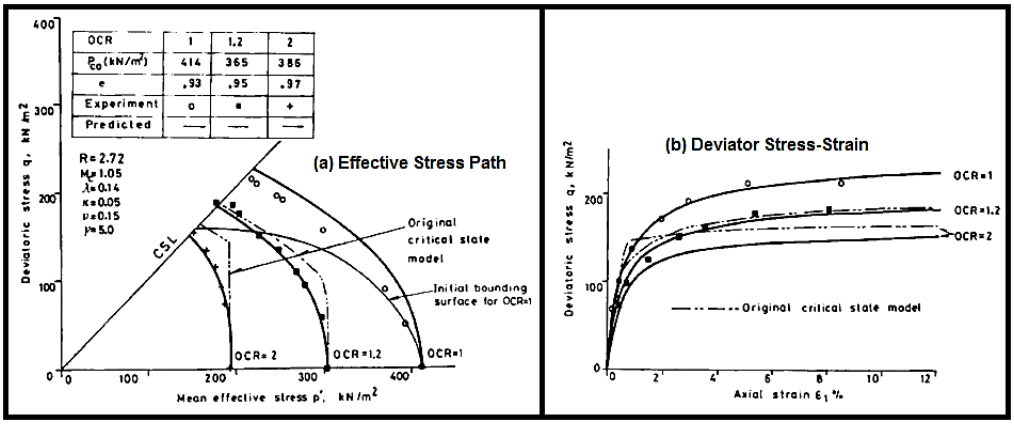

Figure 7.7 Comparison of model predictions for lightly overconsolidated clays against experimental data (Zienkiewicz et al 1985).

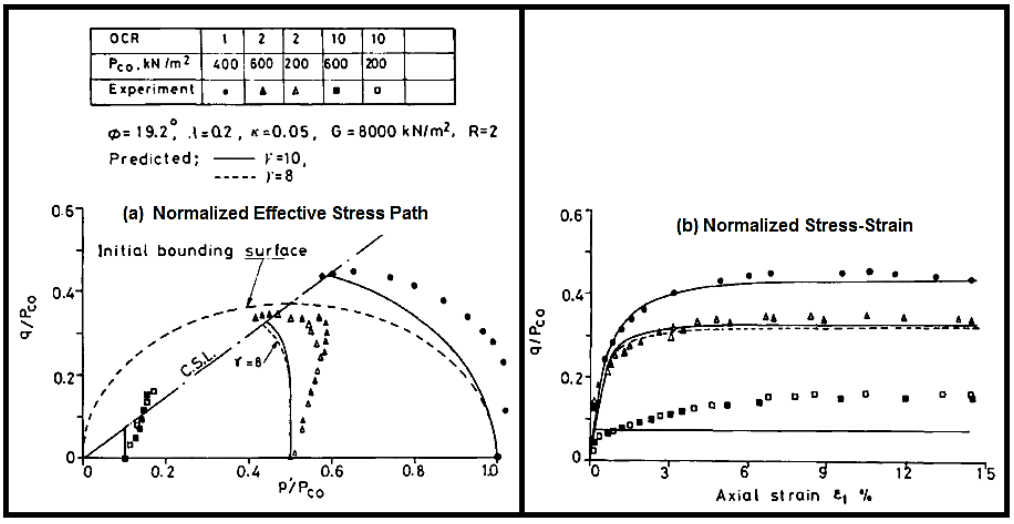

Figure 7.8 Comparison of model predictions for heavily overconsolidated clays against experimental data for Kaolin clay (Zienkiewicz et al 1985).

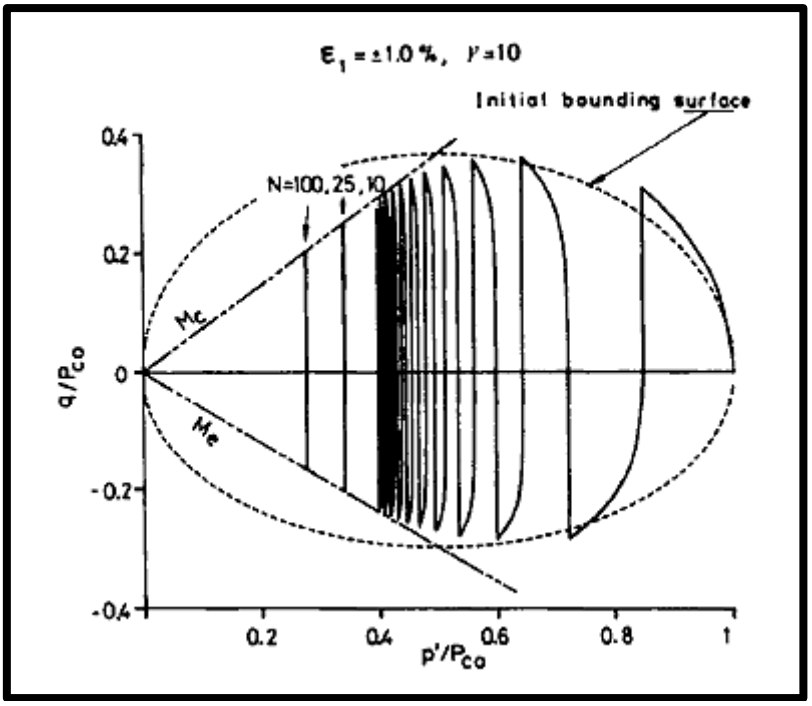

Figure 7.9 Model simulation for cyclic effective stress path of Kaolin Clay under two-way strain-controlled cyclic triaxial loading (Zienkiewicz et al 1985).

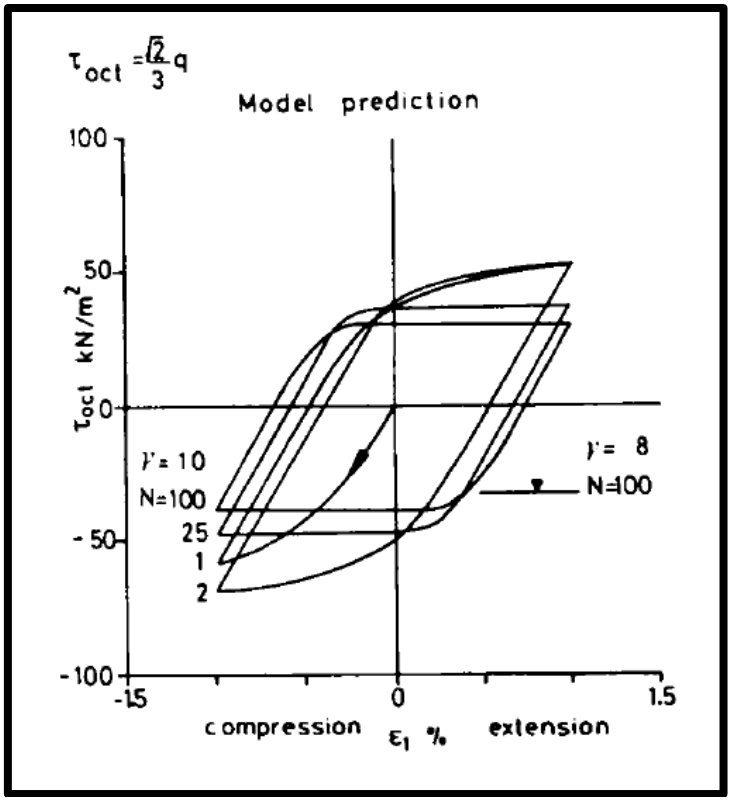

Figure 7.10 Model simulation for cyclic stress-strain curve of kaolin ($\varepsilon = 1\%$, $\gamma = 8$) under two-way strain-controlled cyclic triaxial loading (Zienkiewicz et al 1985).

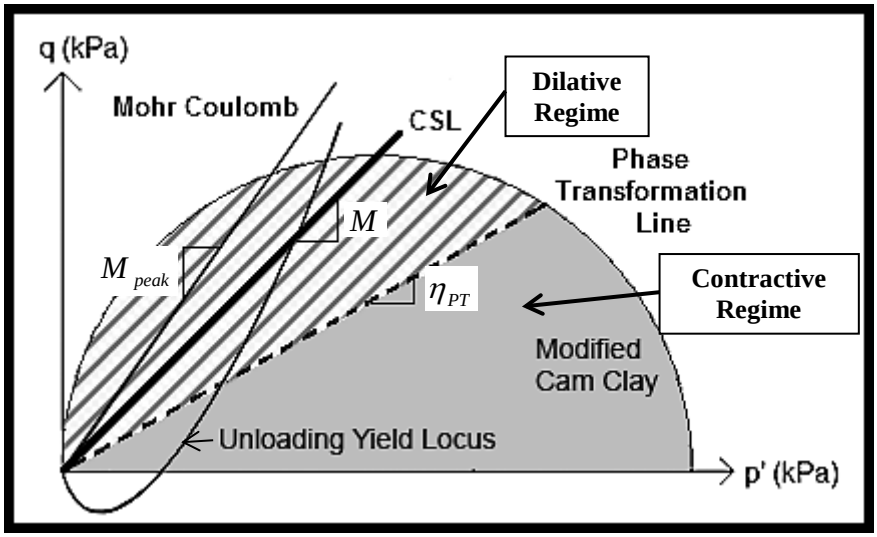

Figure 7.11 Schematic diagram of the bounding surfaces in the proposed model.

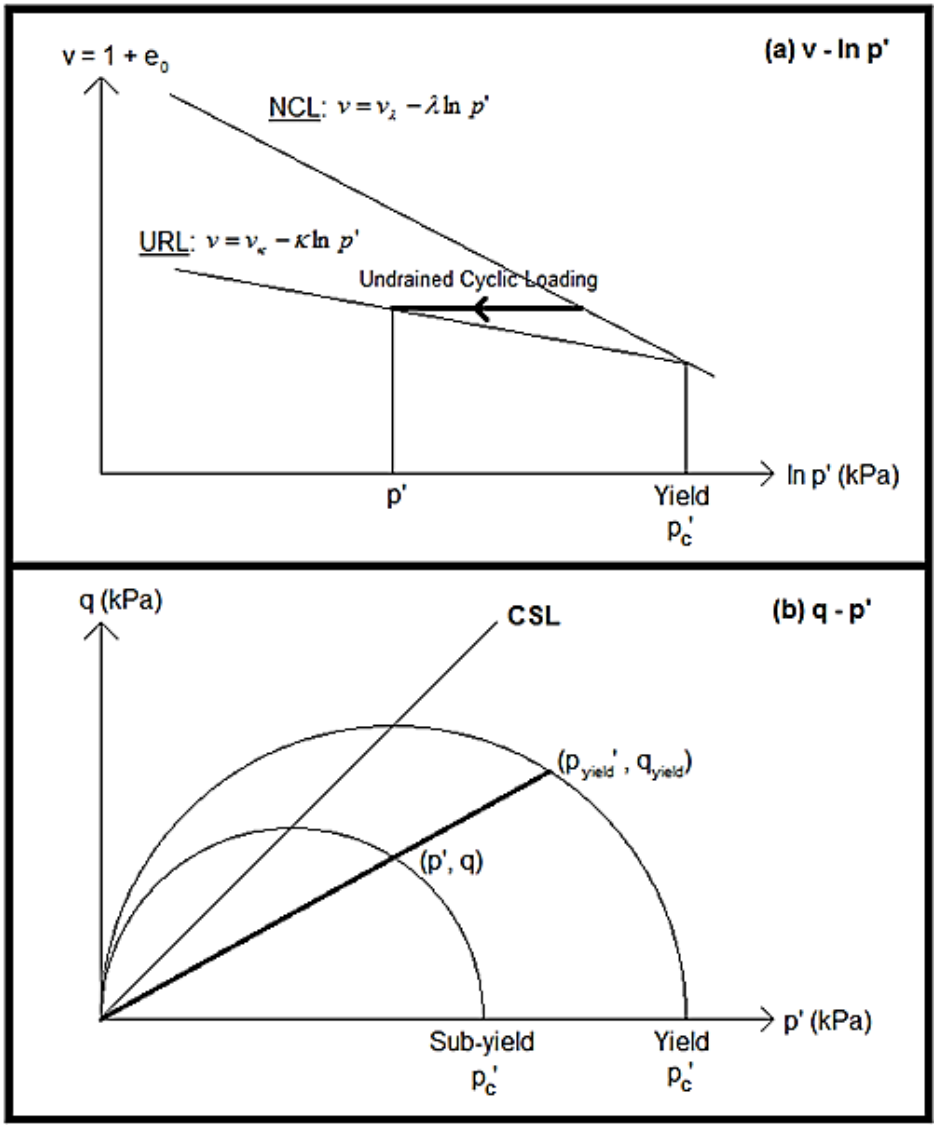

Figure 7.12 Interpolation rule for Modified Cam Clay bounding surface.

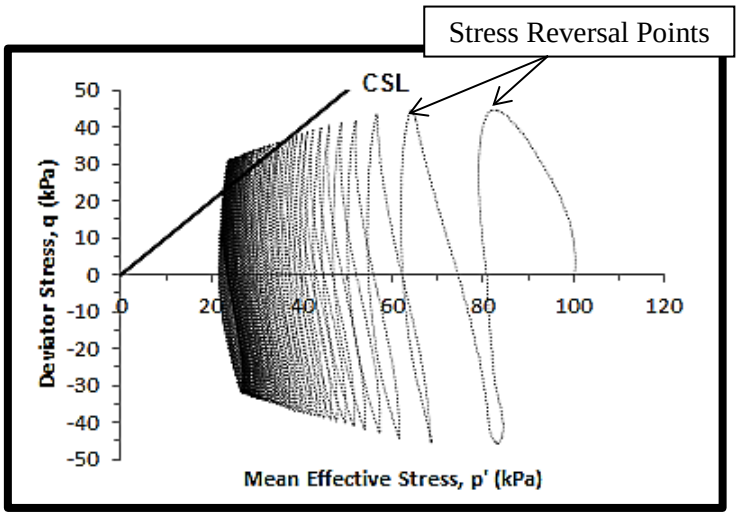

Figure 7.13 Effective stress path for Singapore Upper Marine Clay under cyclic loading (OCR = 1, p_c' = 100kPa, ε = 1.4%).

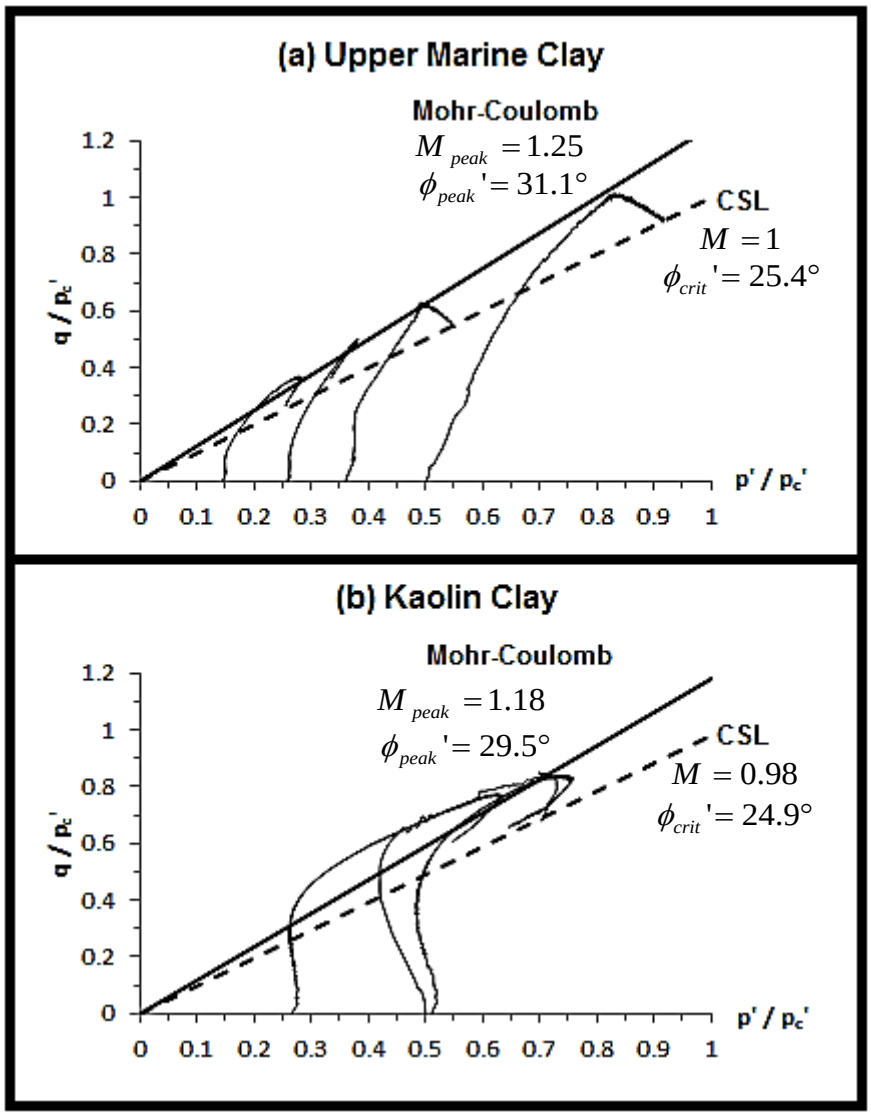

Figure 7.14 Mohr-Coulomb friction coefficient (M_{peak}) obtained for specimens consolidated to 200kPa, swelled to different confining stresses, and sheared under undrained triaxial conditions.

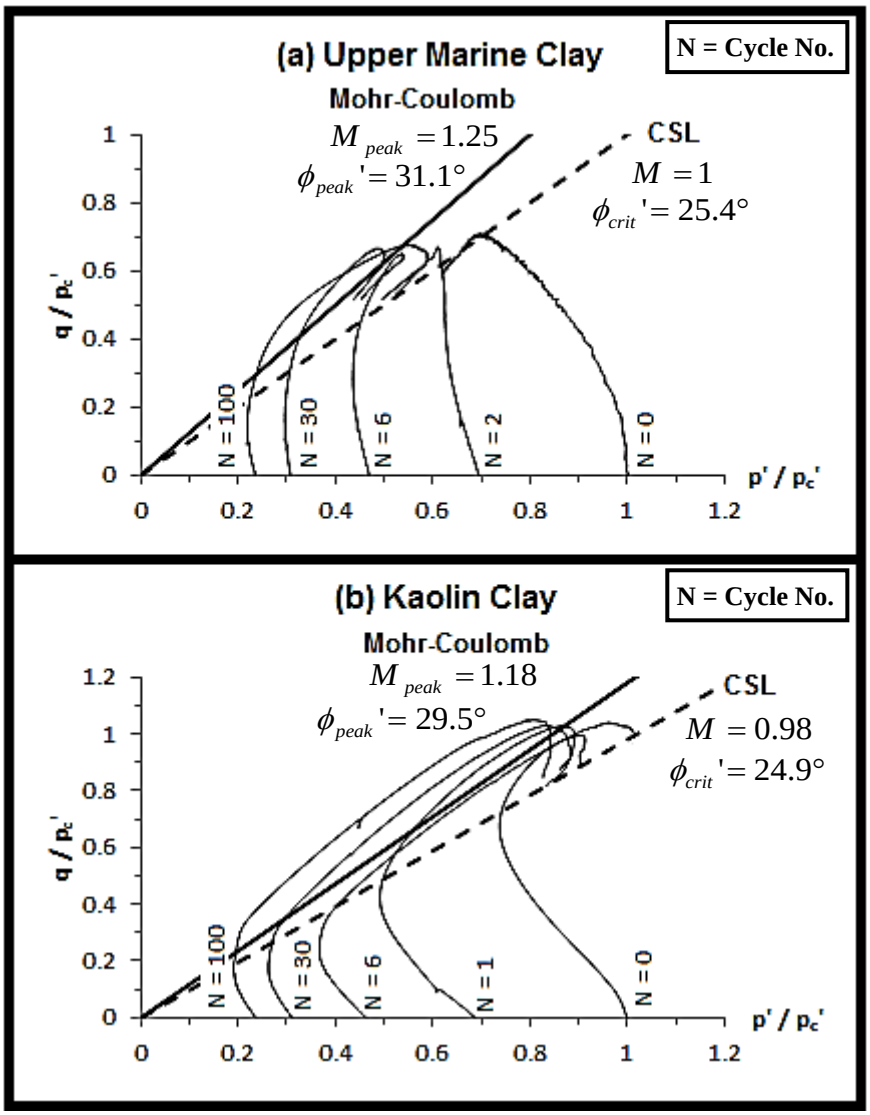

Figure 7.15 Comparison of M_{peak} with the post-cyclic effective stress paths.

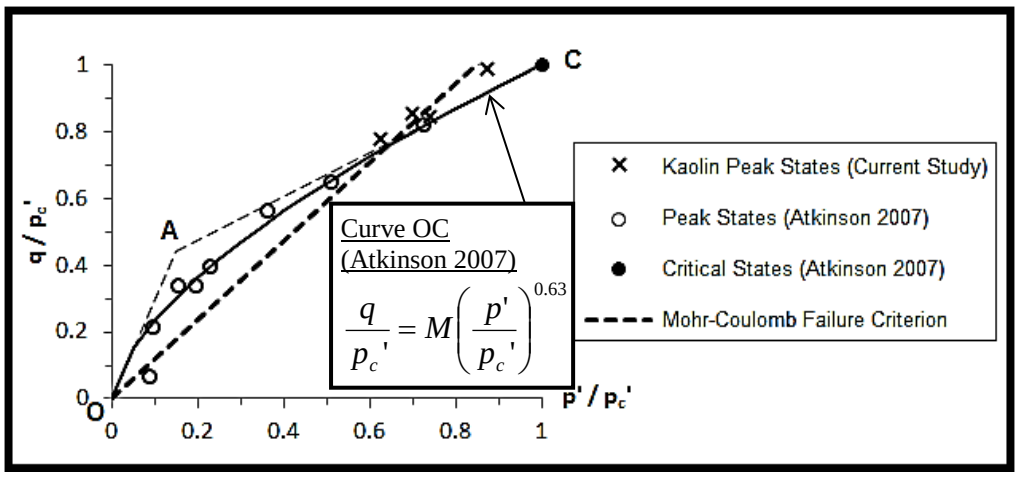

Figure 7.16 Comparison of Kaolin Clay peak effective stress states against Atkinson's data (2007).

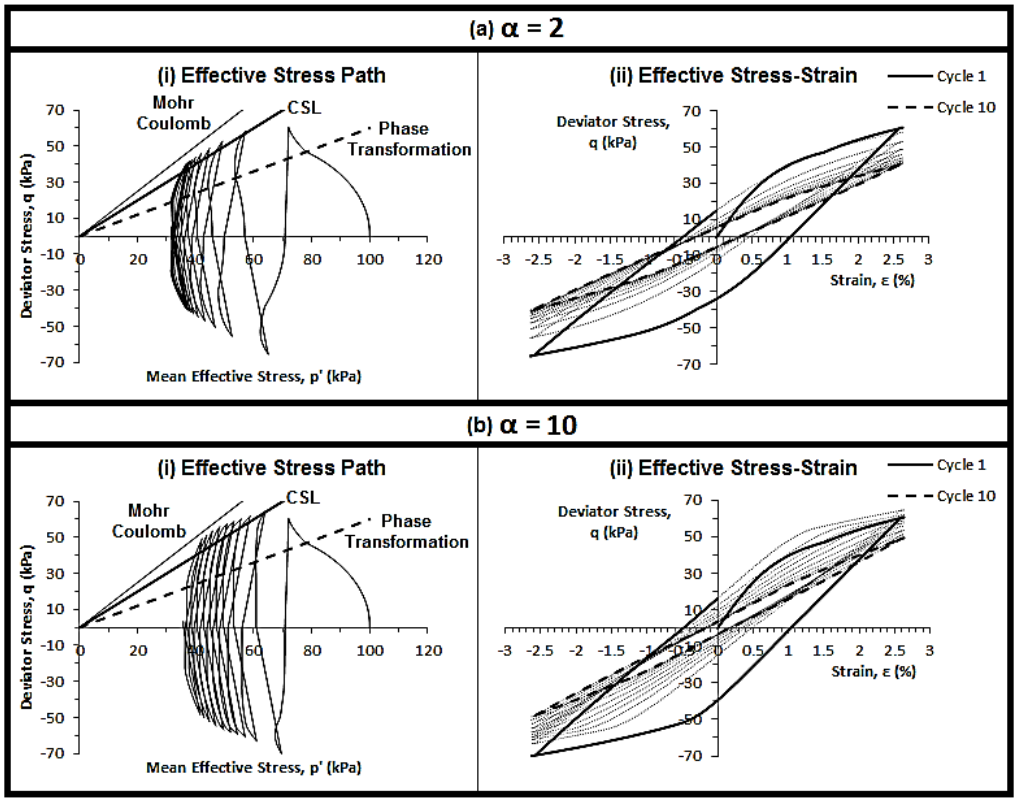

Figure 7.17 Effect of material constant α in the proposed model.

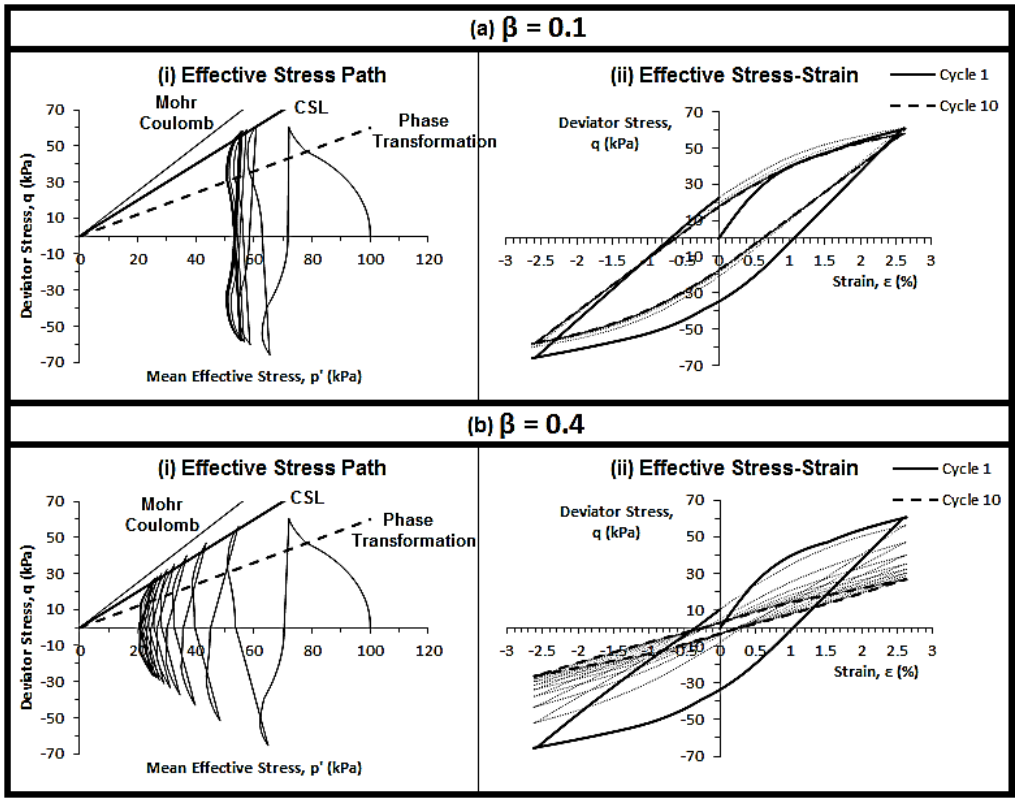

Figure 7.18 Effect of material constant β in the proposed model.

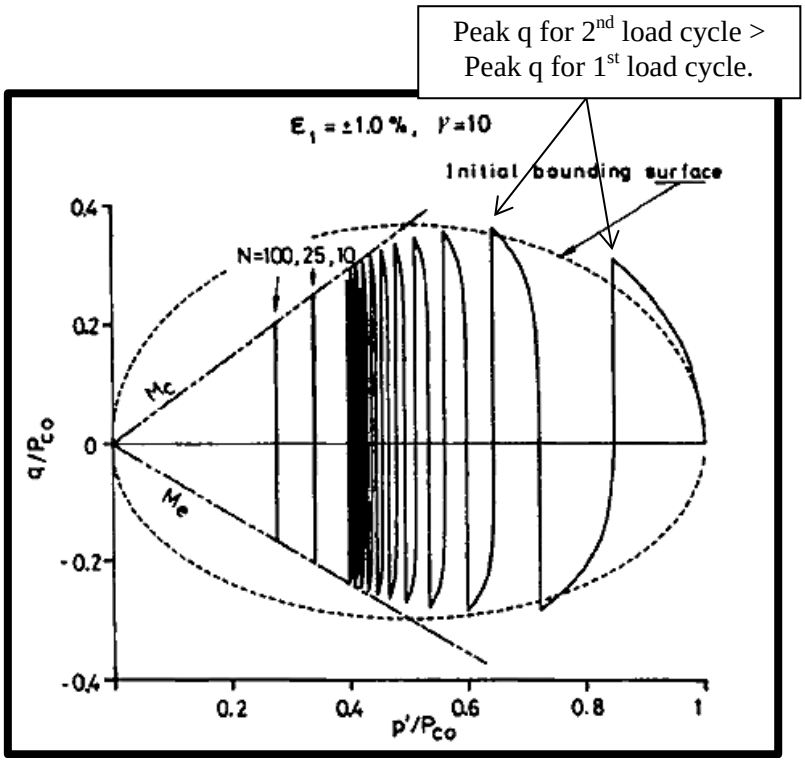

Figure 7.19 "Generalized plasticity" model prediction of two-way, strain-controlled undrained cyclic triaxial test on Kaolin Clay (Zienkiewicz et al. 1985).

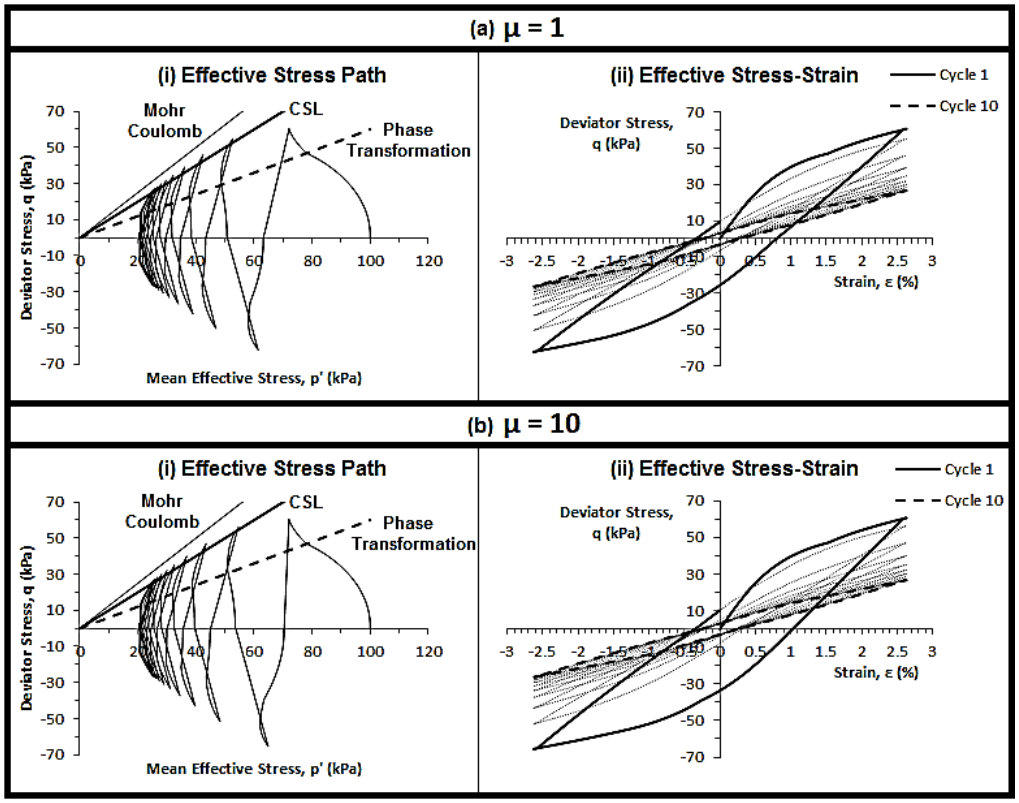

Figure 7.20 Effect of material constant μ in the proposed model.

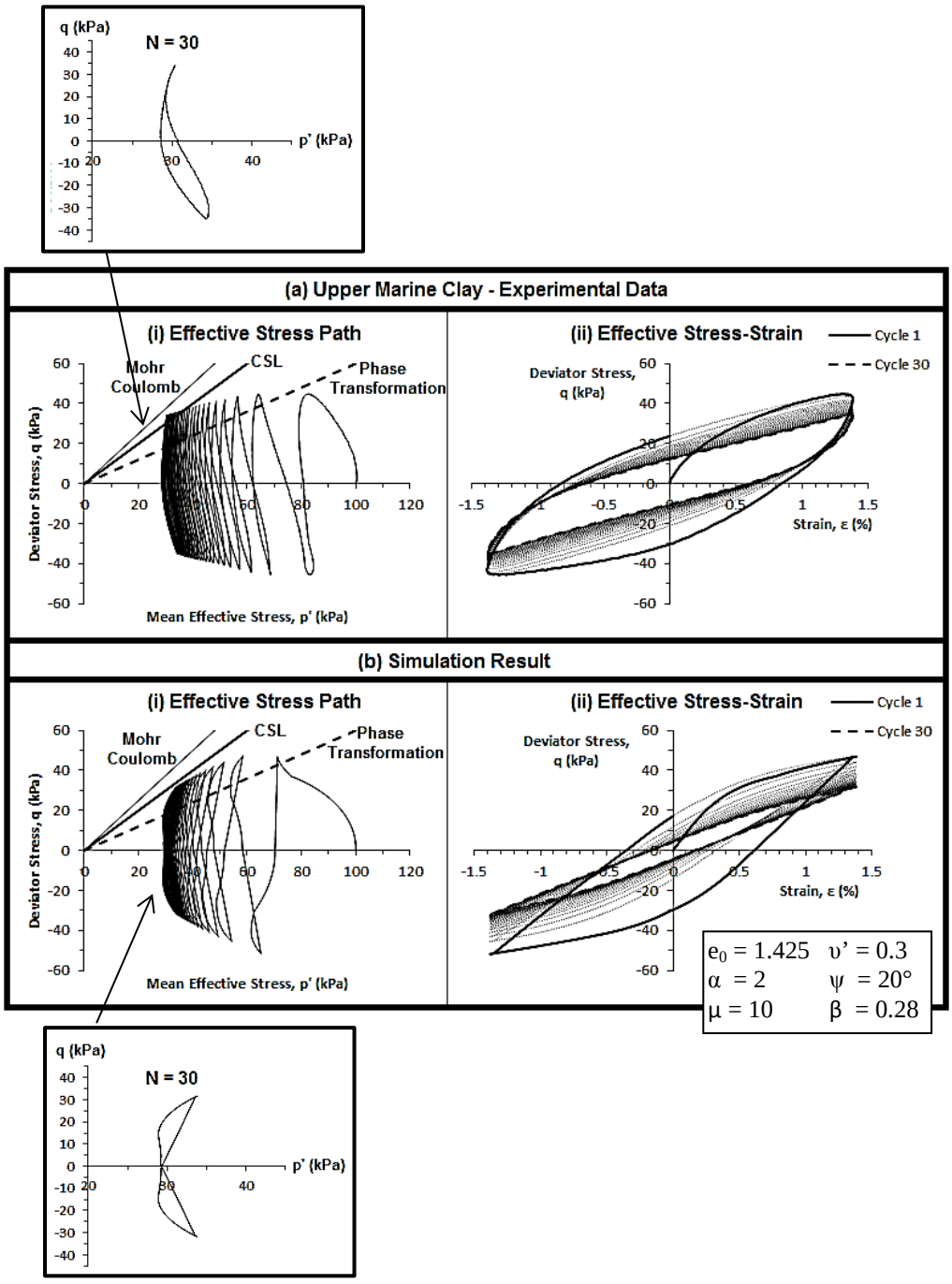

Figure 7.21 Comparison of model simulation against experimental results for Singapore Upper Marine Clay (OCR = 1, p_c' = 100kPa, ε = 1.4%, N = 30 Cycles).

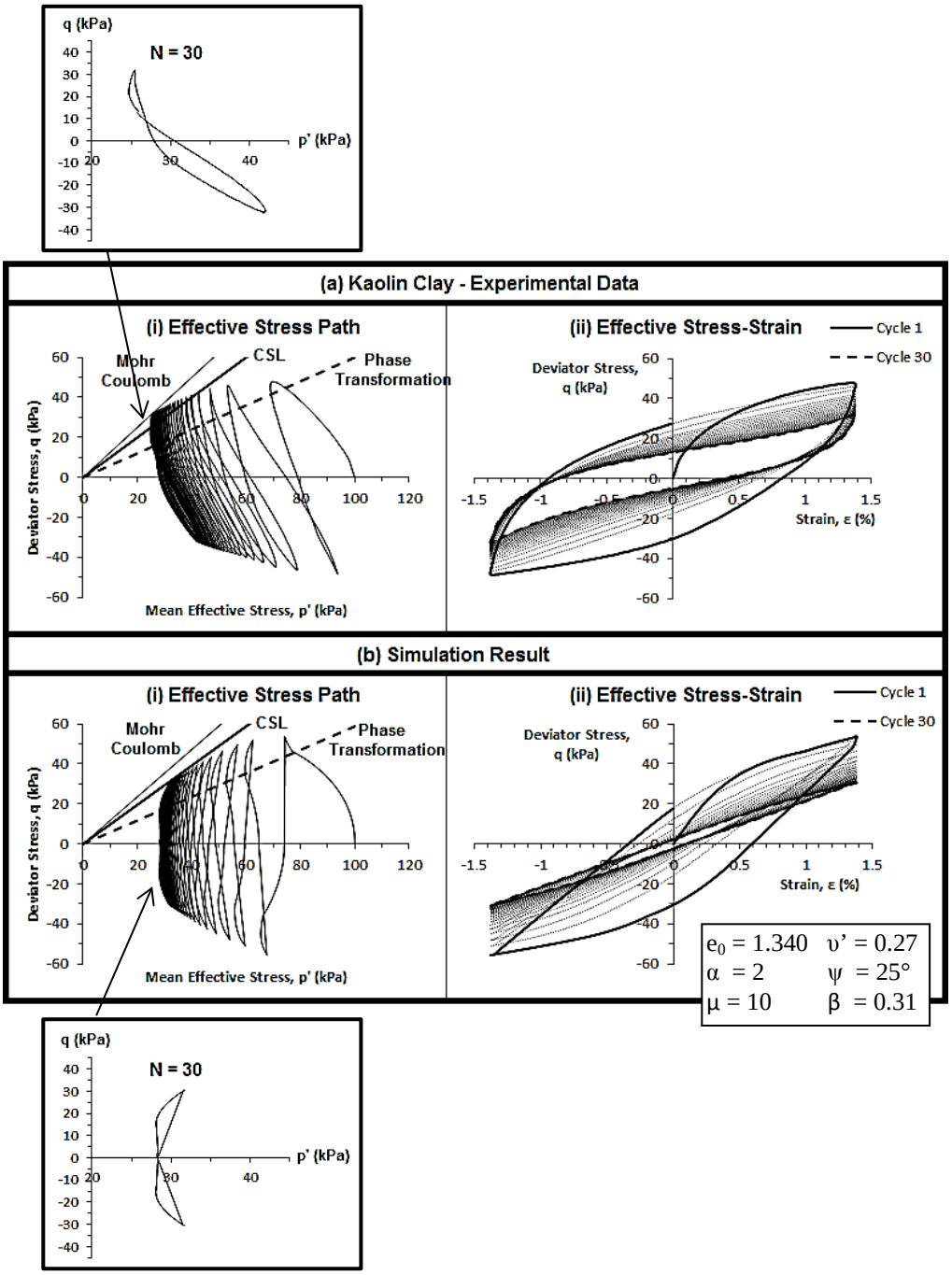

Figure 7.22 Comparison of model simulation against experimental results for Kaolin Clay (OCR = 1, p_c' = 100kPa, ε = 1.4%, N = 30 Cycles).

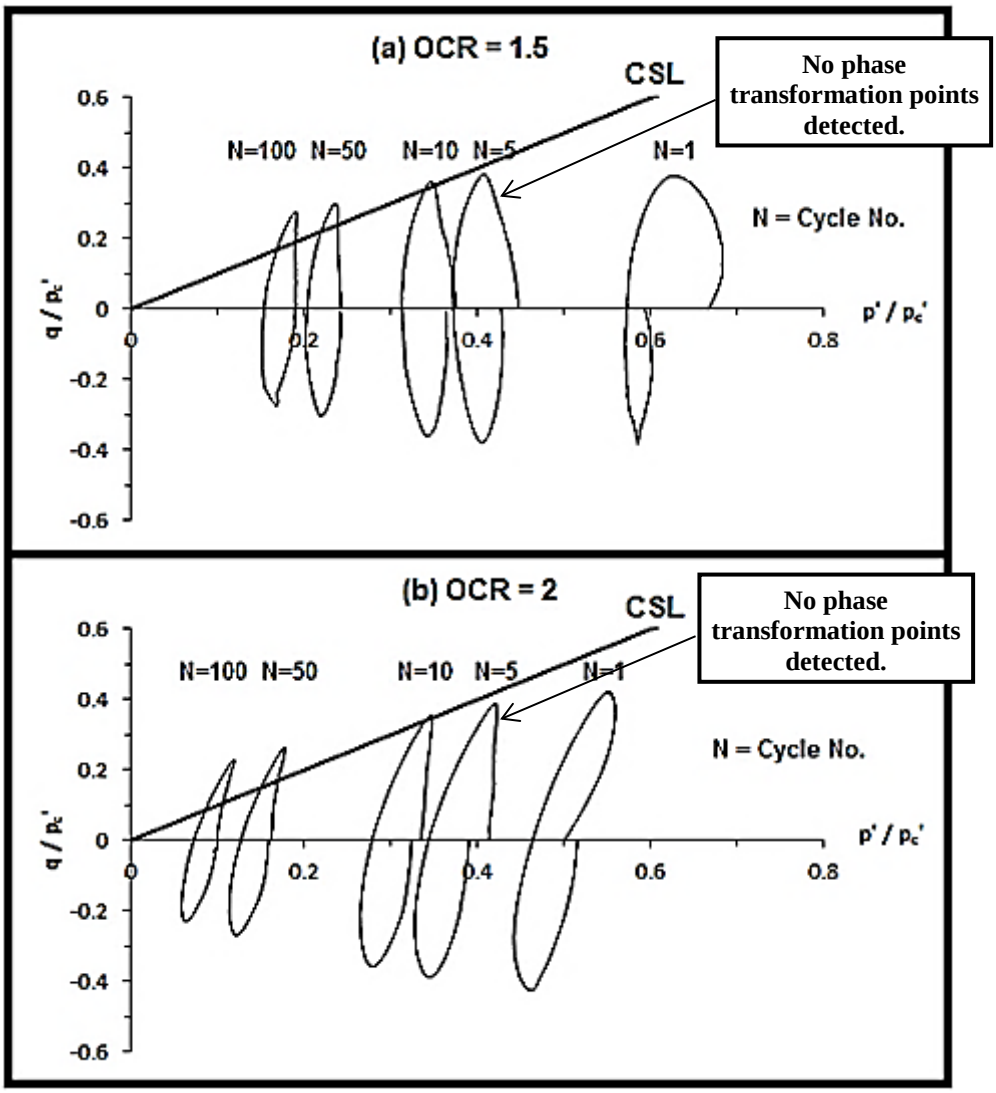

Figure 7.23 Typical normalized effective stress path of overconsolidated Singapore Upper Marine Clay specimens (p_c' = 100kPa, ε = 1.4%).

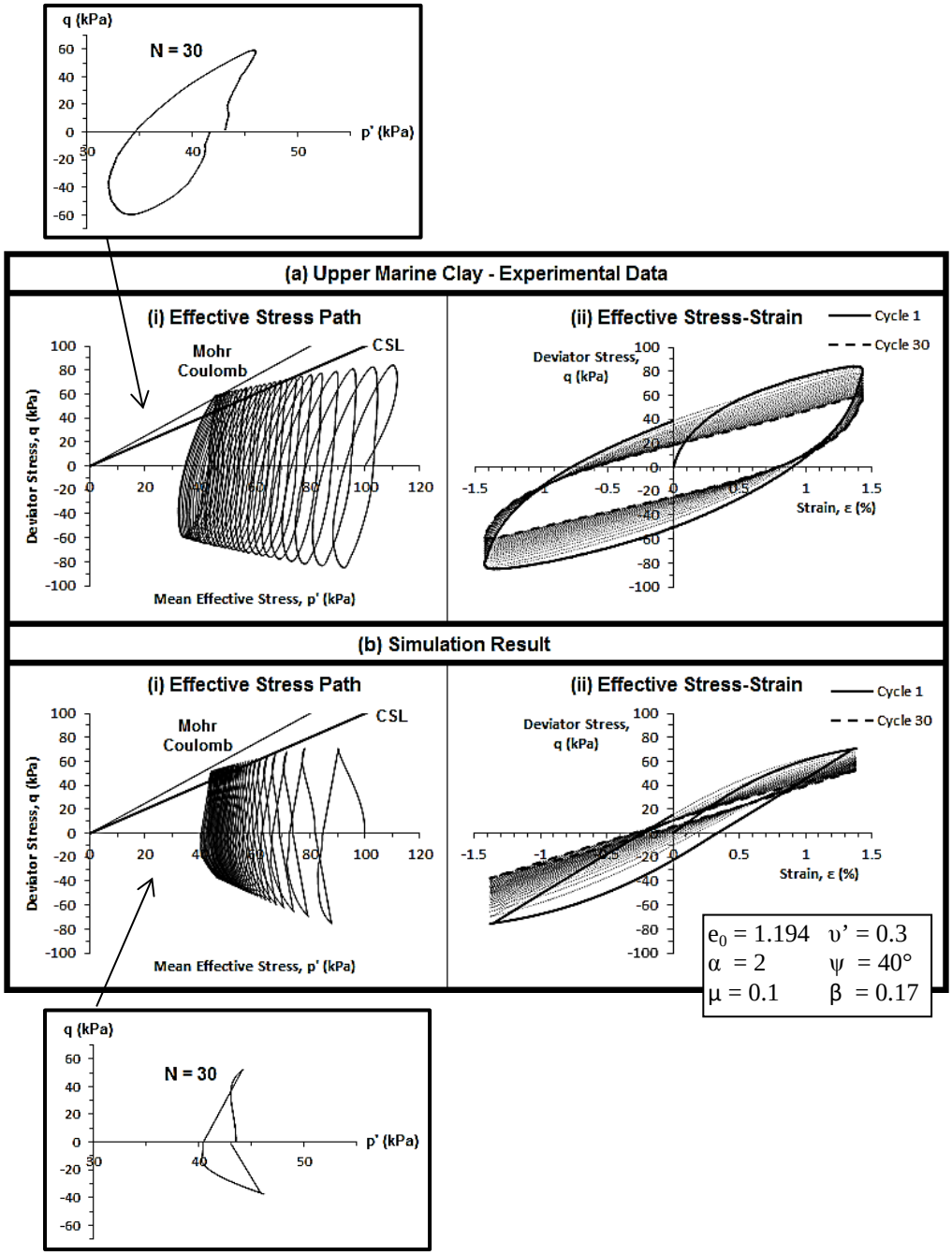

Figure 7.24 Comparison of model simulation against experimental results for Singapore Upper Marine Clay (OCR = 2, p_c' = 200kPa, ε = 1.4%, N = 30 Cycles).

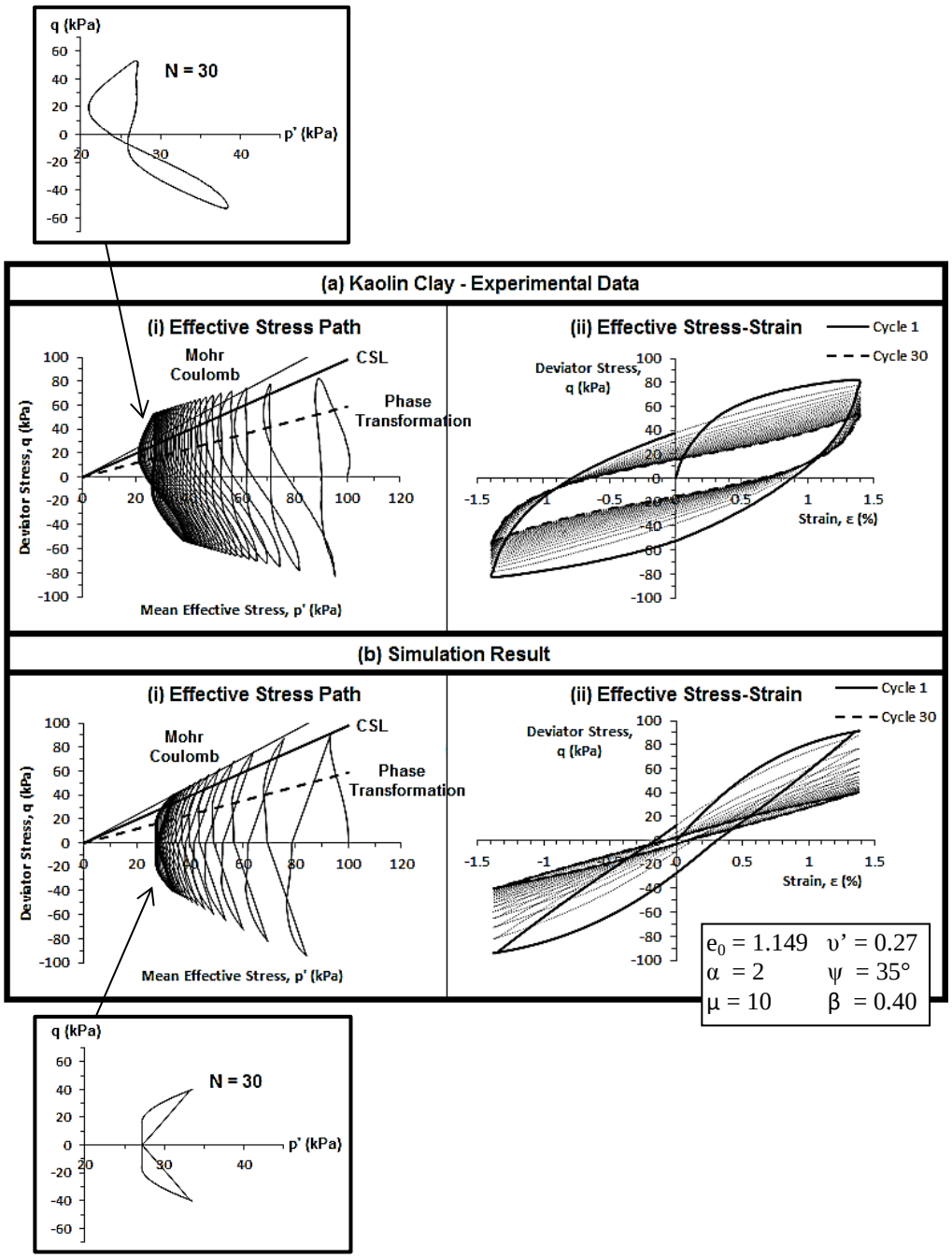

Figure 7.25 Comparison of model simulation against experimental results for Kaolin Clay (OCR = 2, p_c' = 200kPa, ε = 1.4%, N = 30 Cycles).

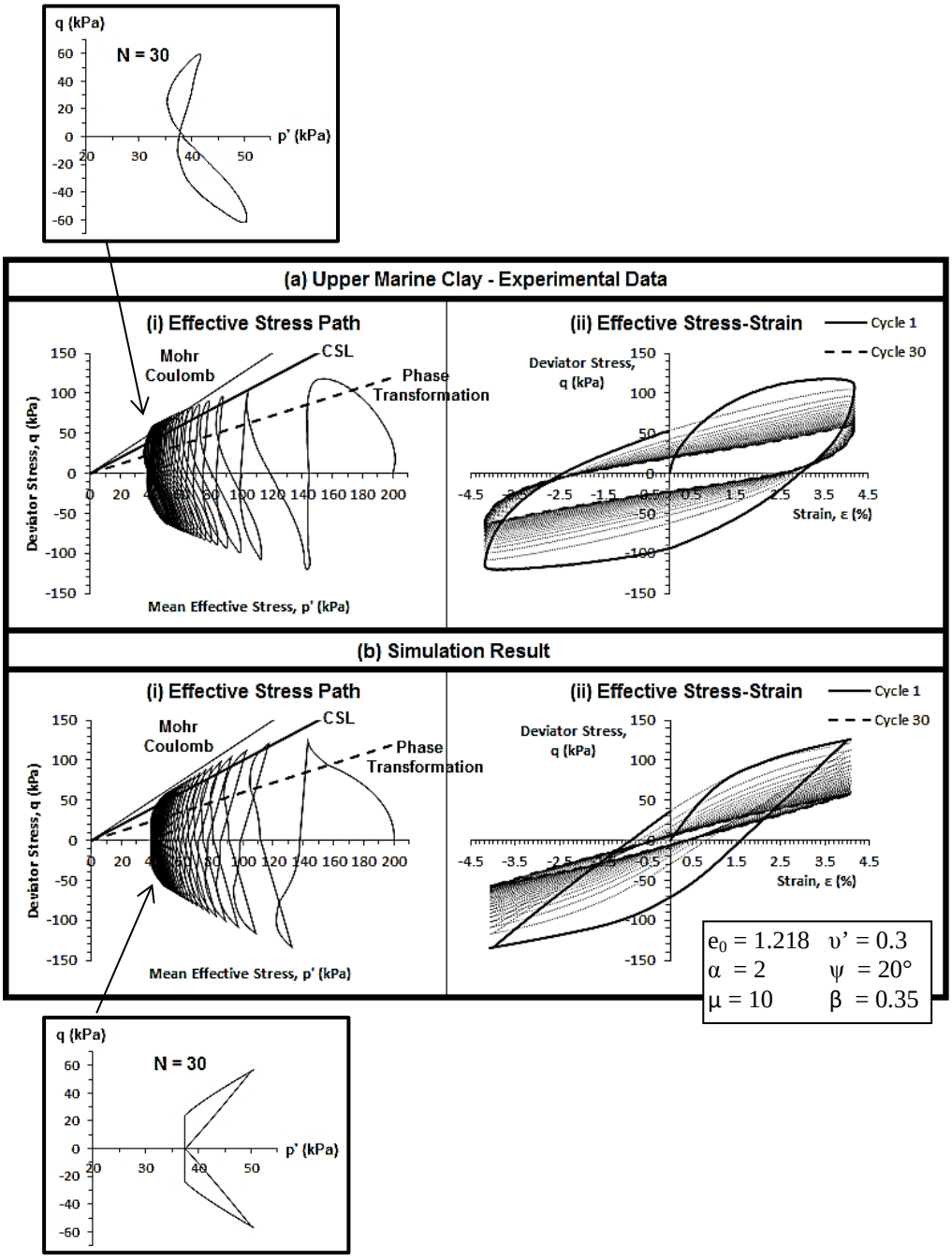

Figure 7.26 Comparison of model simulation against experimental results for Singapore Upper Marine Clay (OCR = 1, p_c' = 200kPa, ε = 4.2%, N = 30 Cycles).

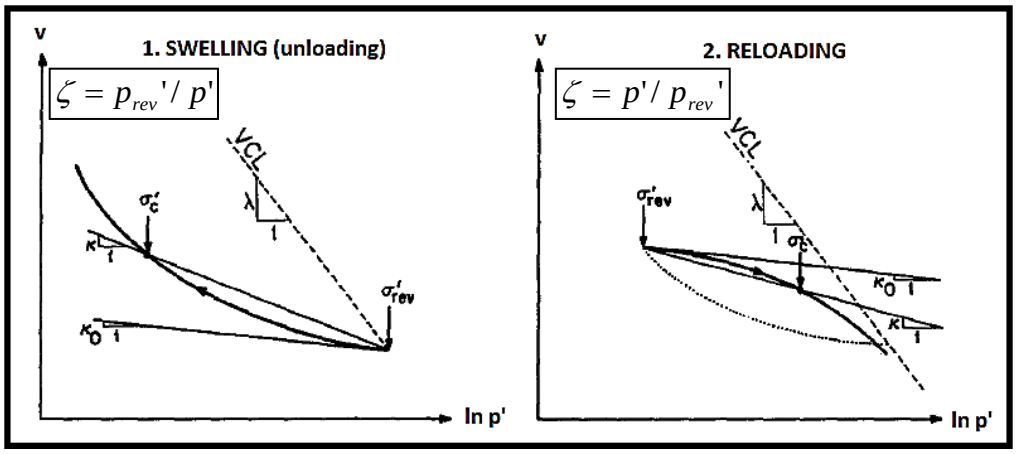

Figure 7.27 Definition of parameter ξ for hydrostatic compression (Whittle and Kavvadas 1994).

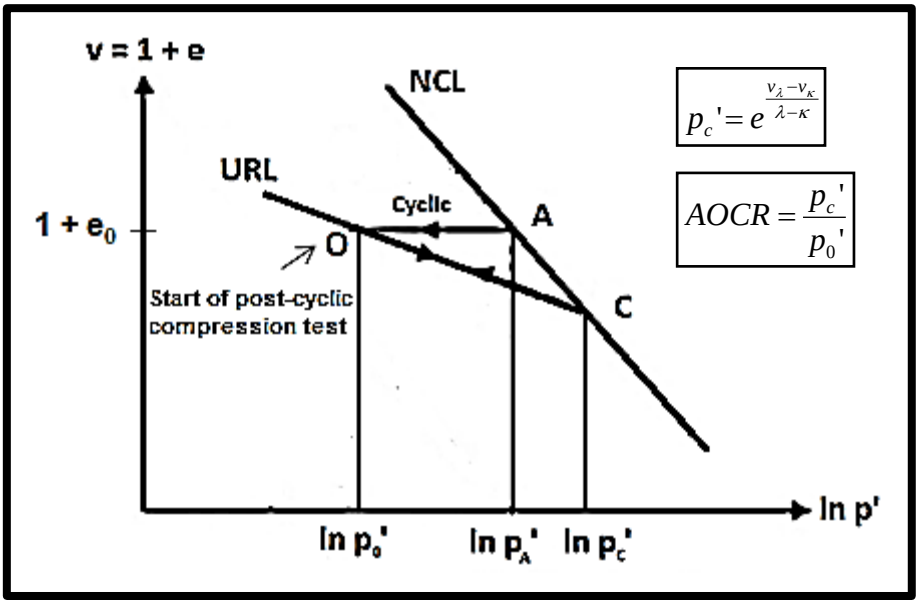

Figure 7.28 Definition of model inputs, p_c' and *AOCR*, for post-cyclic compression loading.

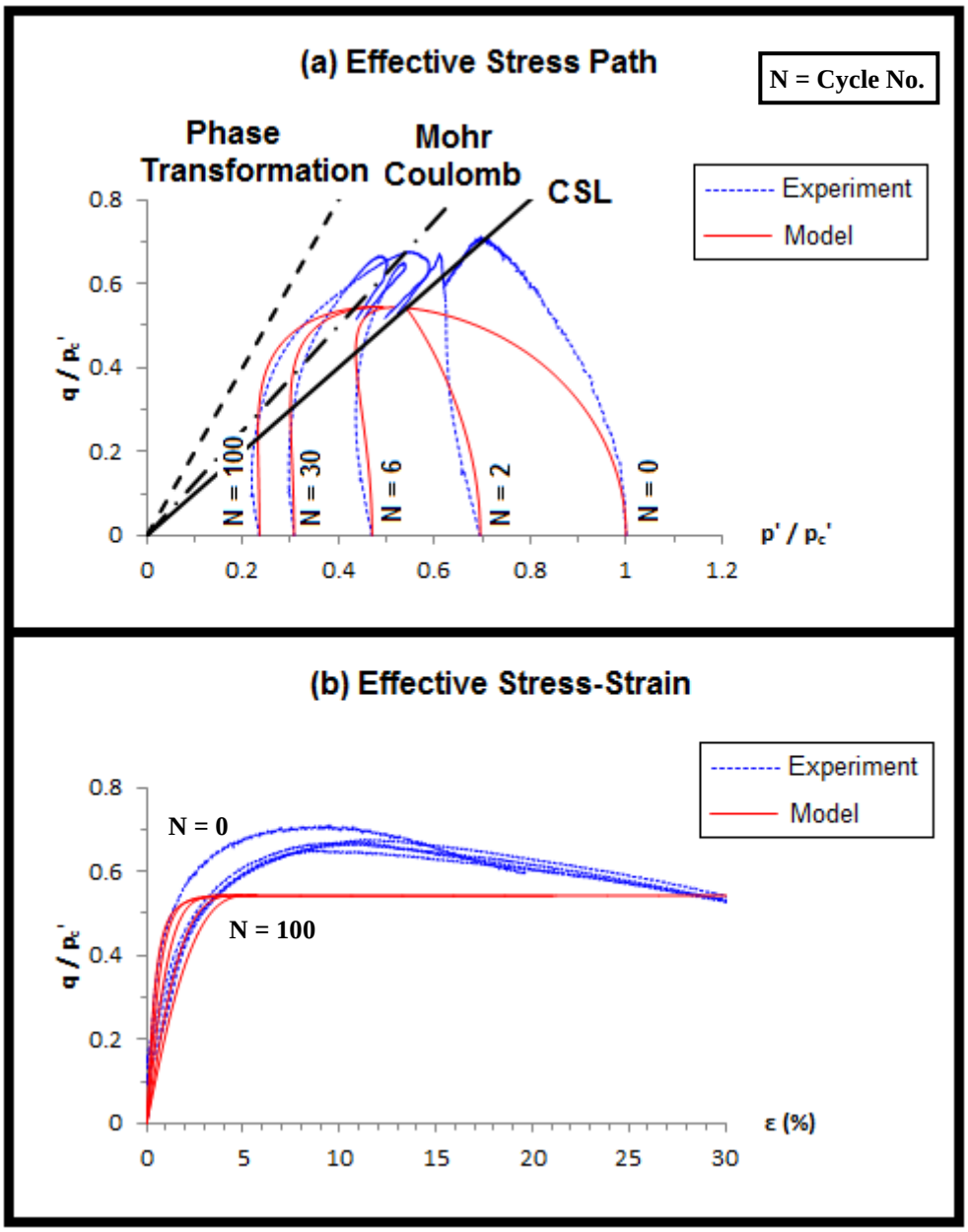

Figure 7.29 Comparison of model simulation against experimental results for post-cyclic behaviour of Singapore Upper Marine Clay.

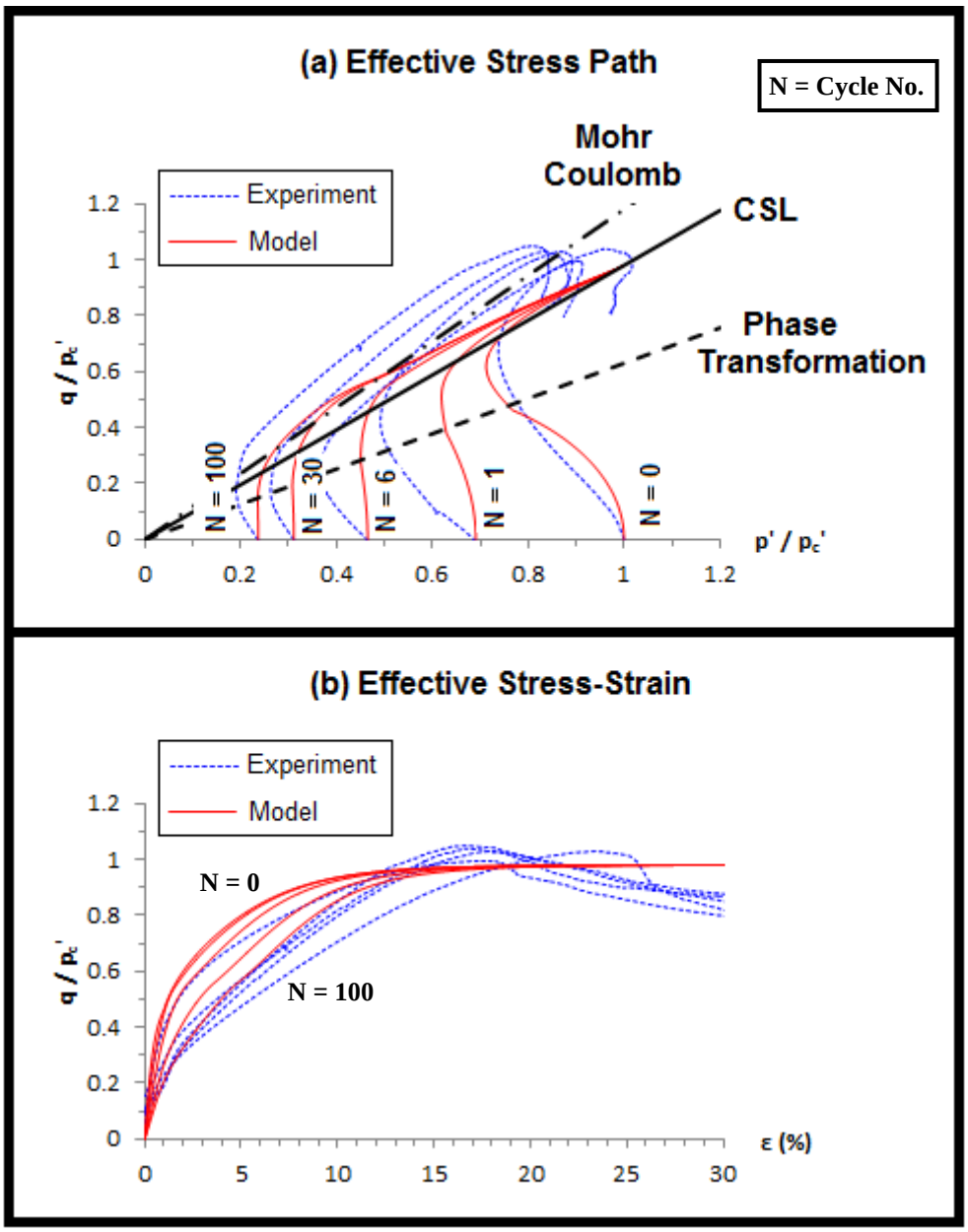

Figure 7.30 Comparison of model simulation against experimental results for post-cyclic behaviour of Kaolin Clay.

Chapter 8 – Conclusion

8.1 Overview

As discussed in Chapter 1, Singapore is challenged with dynamic problems posed by far-field earthquake effects due to its geological proximity to the Great Sumatran Fault and the Sunda Arc subduction zone. Aside from far-field earthquakes, Singapore also faces dynamic problems arising from construction vibrations. Despite the ongoing major construction works, design criteria for road and rail systems still take little or no account of dynamic loading. One of the main reasons is that there is a scarcity of information on the cyclic loading behaviour of local clays. Previous characterization studies on Singapore Marine Clay (e.g. Tan 1983; Dames and Moore 1983; Tan et al. 1999; Tan et al. 2002; Chu et al. 2002; Chong 2002) have been largely restricted to monotonic loading behaviour. Furthermore, published findings on the behaviour of different soft clays (e.g. San Francisco Bay Mud, Venezuelan Clay, Bangkok Clay, Vancouver Marine Clay etc.) may not be applicable to Singapore Marine Clay due to the differences in plasticity and mineralogy. As the findings of this thesis show, even amongst clays, such as kaolin and Marine Clay, there can still be significant differences in behaviour. As reviewed in Chapter 2, the conflicting conclusions in previous studies (e.g. strain rate effects) also make their findings difficult to apply directly to Singapore Marine Clay. In addition, many of the previous studies did not take into account pore pressure equilibrium time. As a result, questions remain over the accuracy of previously observed stress paths.

This current research is an attempt to examine the cyclic and post-cyclic response of Singapore Marine Clay and present a detailed characterization of its cyclic behaviour. Apart from Singapore Marine Clay, commercially available Kaolin Clay was tested and used as a “reference” soil against which the behaviour of Singapore Marine Clay can be compared. Since the evaluation of test results in terms of total stresses are generally not very helpful for understanding soil behaviour, special attention is paid to obtaining reliable pore pressure measurements for calculating effective stresses. Through this, a much better understanding of the cyclic and post-cyclic behaviour of Singapore Marine Clay has been achieved.

8.2 Summary of Research Findings

The key findings from this research are summarized as follows:

8.2.1 Effect of Cyclic Strain Rate on Pore Pressure Measurement

(i) During slow undrained cyclic triaxial testing of Marine Clay and kaolin, intrinsic strain rate effects on the excess pore pressure measurements, effective stress paths and stress strain plots are negligible once pore pressure equilibration is achieved.

(ii) In cases when pore pressure equilibration did not occur, the pore pressure non-uniformity affects the effective stress paths much more significantly than the stress-strain curve. The decrease in mean effective stresses is grossly underestimated (~75% for Marine Clay and ~41% for kaolin) while the percentage errors in the deviator stresses for the initial cycle were considerably small (~11% for Marine Clay and ~5% for kaolin). Thus, strain rate effect on the stress-strain behaviour of clays is negligible.

(iii) The strain rate specifications stipulated in BS1377:1990 and Eurocode ISO/TS 17892:2004 for undrained monotonic triaxial compression are conservative when applied to undrained cyclic triaxial testing. Their recommended strain rates for pore pressure equilibration are at least one order in magnitude slower than the required experimental rates.

(iv) Modifications were made to BS1377 and TS17892 strain rate specifications to cater to cyclic loading. The modified relations are listed in Equations 4.10 and 4.11. These equations are applicable for both normally consolidated and overconsolidated (up to OCR = 2) Marine Clay and kaolin specimens with preconsolidation pressures ranging 50kPa to 200kPa and within an applied strain range of 0.7% to 4.2%.

8.2.2 Shear Modulus and Damping Ratio

(i) The small-strain shear modulus for Marine Clay and kaolin are adequately described via Equations 5.13 and 5.14.

(ii) For both Marine Clay and kaolin, the normalized shear modulus degradation and damping curves are independent of the mean effective stress (over the range of 50 to 200kPa) and overconsolidation ratio (up to OCR = 2).

(iii) For shear strain amplitudes less than 0.15%, no pore pressure accumulation occurred during and after cyclic loading for both Marine Clay and kaolin specimens.

(iv) The degradation cyclic strain threshold marks the beginning of significant degradation of the clay structure where excess pore pressure generation becomes apparent. For all Marine Clay and kaolin specimens subjected to different stress histories (i.e. effective mean principal stress and over-consolidation ratio), the degradation cyclic strain threshold is ~0.2% and ~0.17% respectively. $\gamma_{td} \approx 0.2\%$ $\gamma_{td} \approx 0.17\%$

(v) The Hyperbolic, Ramberg-Osgood and Modified Hyperbolic models can reasonably capture the variation in normalized shear modulus with strain. However, none of the three models are able to predict the damping ratio variation over the entire range of strain. For strain level exceeding 0.4%, the Hyperbolic and Modified Hyperbolic Cycmodels over-predict the damping ratio while the Ramberg-Osgood model under-predicts the damping characteristics of Marine Clay. The differences between the model results and empirical data, however, were more prominent for Kaolin Clay specimens. The Ramberg-Osgood model consistently under-predicts the damping ratio by a significant margin. The other two models under-predict the damping ratio at strain levels up to about 0.3%. At higher strain levels exceeding 0.4%, they appear to over-predict the damping ratio. All three relations are based on total stress and make no prediction on effective stress path or excess pore pressure.

8.2.3 Cyclic and Post-Cyclic Behaviour

(i) An elliptical yield locus (corresponding to the state boundary and critical state boundary surfaces) was found to provide a reasonably good envelope to the monotonic and post-cyclic effective stress paths for Marine Clay and kaolin.

(ii) Phase transformation behaviour (marking a change from contractive to dilative behaviour) was observed in the cyclic effective stress paths for normally consolidated Marine Clay and kaolin. Similar to the cyclic mobility of saturated dense sands, the cyclic oscillations in effective stress and shear stiffness in Marine Clay and kaolin specimens result in distinctive "butterfly" stress paths after about 100 cycles.

(iii) For normally consolidated Marine Clay, phase transformation generally initiates when the normalized mean effective stress (p'/p_c') decreases to about 0.5. This initiation of phase transformation also marks the onset of dilative post-cyclic behaviour. These observed behavioural changes are

consistent regardless of the effective preconsolidation pressure and applied strain amplitude. The cyclic effective stress paths for all overconsolidated Marine Clay specimens, however, do not exhibit phase transformation.

(iv) The behaviour of kaolin is different. Phase transformation occurs throughout the entire range of possible normalized mean effective stress (p'/p_c'), from 0 to 1. This phase transformation behaviour observed in kaolin is independent of its stress history (i.e. effective preconsolidation pressure and overconsolidation ratio).

(v) For both Marine Clay and kaolin, a unique straight line of phase transformation can be defined within the effective stress space. The equation of this phase transformation line can be expressed via Equations 6.1 and 6.2. Effective stress paths below the phase transformation line do not lead to phase transformation.

(vi) For overconsolidated Marine Clay and kaolin specimens, cyclic loading generally results in undrained shear strength degradation. For normally consolidated specimens, the undrained strength is largely independent of its cyclic stress history except for specimens consolidated under 200kPa effective confining pressure, which shows a post-cyclic strength decrease of about 24%. For these specimens, the undrained strength degrades approximately linearly with respect to decreasing normalized mean effective stress. This relation was observed to be independent of the cyclic strain amplitude.

(vii) The post-cyclic effective stress paths and stress-strain curves of both Marine Clay and kaolin specimens lie close to those of corresponding specimens with the equivalent swelling-induced overconsolidation ratio. The similarities in the maximum deviator stress achieved indicate that the undrained strength of a cyclically loaded specimen may be predicted based on the apparent over-consolidation ratio induced by the end of the cyclic loading phase.

8.2.4 Constitutive Model for Cyclic Loading

(i) A new three-bounding surface constitutive model was developed to describe the cyclic behaviour of Marine Clay and kaolin. In order to model phase transformation, both Modified Cam Clay and Mohr Coulomb yield surfaces were used for the cyclic loading phase. For the cyclic unloading phase, a non-hardening unloading yield locus derived by Lee and Foo (1991) based

on the combination of Taylor's energy equation with an associated flow rule was used as the unloading bounding surface. In spite of the apparent complexity brought about by the three bounding surfaces, only three new parameters were needed.

(ii) This proposed model is able to capture the cyclic mobility and subsequent "butterfly" stress paths observed in normally consolidated Marine Clay and normal and overconsolidated kaolin under undrained cyclic triaxial loading. For overconsolidated Marine Clay that does not exhibit phase transformation, the effective stress path can be reasonably modelled by prescribing a high stress ratio (i.e. $\eta_{PT} = 2$) for the phase transformation line.

(iii) In all cases, however, this model is unable to reproduce accurately the nonlinear cyclic stress-strain responses of Marine Clay and kaolin after a large number of cycles. Although the reduction in the peak cyclic deviator stresses can be reasonably modelled, the predicted stress-strain loops show progressive flattening with increasing load cycles, indicating more elastic behaviour. Consequently, the damping ratio becomes grossly underestimated.

(iv) The model also shows good qualitative agreement with the monotonic and post-cyclic behaviour for both clays. The predicted undrained shear strengths are generally on the conservative side.

8.3 Recommendations for Future Work

Based on the current study, some recommendations for future research are provided as follows:

(i) One important finding in this study is the presence of phase transformation behaviour for both Marine Clay and kaolin under cyclic loading. For Marine Clay, phase transformation behaviour was restricted to normally consolidated specimens. In contrast, kaolin shows phase transformation regardless of its stress history. Furthermore, even the monotonic loading response of kaolin shows phase transformation contrary to the compressive behaviour commonly assumed in constitutive models. Based on the foregoing discussions, the occurrence of phase transformation may be dependent on plasticity index or microstructure. More research efforts are required to find out and understand the reasons causing this phenomenon.

(ii) As highlighted previously, the main limitation in the proposed model is its inability to capture the nonlinear cyclic stress-strain responses of Marine Clay and kaolin. Although the cyclic degradation in the secant shear modulus can be reasonably predicted, the damping ratio is grossly underestimated. As suggested in Chapter 7, incorporating a varying swelling index (κ) may be feasible. However, unlike the perfectly hysteretic stress-strain model defined by Equations 7.39 and 7.40, a simpler formulation for κ should be developed such that the number of model parameter is still kept to a minimum.

(iii) The study described in this thesis is confined to remoulded specimens of Singapore Marine Clay that were isotropically consolidated under specified pressure prior to cyclic and post-cyclic tests. While this is suitable for laboratory study, it differs from the in-situ condition of Singapore Marine Clay which is generally anisotropic. Thus, the cyclic behaviour of natural Singapore Marine Clay could be investigated and the results would serve as a benchmark for the proposed model.

(iv) In the local context, cement is commonly used for ground improvement works due to its low cost and abundance relative to other chemicals (Broms 1984). With an increasing demand for underground space due to rapid urbanization and land scarcity, there is rising need for cement-stabilization of soft clays. Hence, further study is also necessary to explore the cyclic behaviour of cement treated Singapore Marine Clay.

References

Aggour M.S., Tawfiq K.S. and Amini F. (1987), "Effects of frequency content on dynamic properties for cohesive soils", Proc. of 3rd International Conference on Earthquake Engineering and Soil Mechanics, 31-39.

American Society for Testing and Materials D3999-91(2003), "Standard test methods for the determination of the modulus and damping properties of soils using the cyclic triaxial apparatus".

Anderson D.G. and Richart F.E. (1976), "Effects of straining on shear modulus of clays", Journal of Geotechnical Engineering Division, Vol. 102 (9), 975-987.

Andersen K.H., Pool J.H.; Brown S.F. and Rosenbrand W.F. (1980), "Cyclic and static laboratory tests on Drammen clay", Journal of the Geotechnical Engineering Division, ASCE, Vol. 106 (GT5), 499

Andrianopoulos K.I. (2006), "Numerical modeling of static and dynamic behavior of elastoplastic soils. PhD Thesis, National Technical University of Athens.

Ansal A., Iyisan R. and Yildirim H. (2001), "The cyclic behaviour of soils and effects of geotechnical factors in microzonation", Soil Dynamics and Earthquake Engineering, Vol. 21 (5), 445-452.

Atkinson J.H. and Richardson D. (1985), "Elasticity and normality in soil-experimental examinations", Géotechnique, Vol. 35 (4), 443-449.

Baldi G., Hight D.W., and Thomas G.E. (1988). "A reevaluation of conventional triaxial test methods", Advanced triaxial testing of soil and rock, ASTM STP, 977, 219-263.

Banerjee S. (2009). "Centrifuge and numerical modelling of soft clay-pile-raft foundations subjected to seismic shaking", PhD Thesis, National University of Singapore.

Bazant Z.P., Ansal A.M. and Krizek R.J. (1982), "Endochronic models for soils. In: Soil mechanics – Transient and cyclic Loads", eds. Pande G.N. and Zienkiewicz O.C., John Wiley & Sons Ltd, 418-438.

Bishop A.W. and Henkel D.J. (1962), "The measurement of soil properties in the triaxial test", 2nd ed. Edward Arnold, London, 164-166.

Bjerrum L., Simons N. and Torblaa I. (1958), "The effect of time on the shear strength of soft marine clay", Proc. Brussels Conference on Earth Pressure Problems, Vol. 1, 148 - 158.

Blight G.E. (1964), “The effect of non-uniform pore pressure on laboratory measurements of the shear strength of soils”, Laboratory Shear Testing of Soils: A Symposium sponsored by the National Research Council Canada and the American Society for Testing and Materials, Ottawa, Canada , 173-191.

British Standards BS1377 (1990), “Methods of test for soils for civil engineering purposes”.

Broms B.B. (1984), “Stabilisation of soft clay with lime columns”, Proc. Seminar on Soil Improvement and Construction Techniques in Soft Ground, Singapore.

Brown S.F., Lashine A.K.F. and Hyde A.F.L. (1975), “Repeated load triaxial testing of a silty clay”, Géotechnique, Vol. 25 (1), 95-114.

Burland J.B. (1989), “Small is beautiful – the stiffness of soils at small strains”, 9th Laurits Bjerrum Memorial Lecture, Canadian Geotechnical Journal, Vol. 26, 499-516.

Burland J.B. (1990), “On the compressibility and shear strength of natural clays”, Géotechnique, Vol. 40 (3), 329-378.

Carter J.P., Booker J.R. and Wroth C.P. (1982), “A critical state soil model for cyclic loading. In: Soil mechanics – Transient and cyclic loads”, eds. Pande G.N. and Zienkiewicz O.C., John Wiley & Sons Ltd, 219-252.

Castante G., Vanderkooy J. and Chung W. (2003), “Difference between current and voltage measurements in resonant-column testing”, Canadian Geotechnical Journal, Vol. 40 (4), 806-820.

Cavallaro A. and Maugeri M. (2004), “Modelling of cyclic behaviour of a cohesive soil by shear torsional and triaxial Tests”, Cyclic Behaviour of Soils and Liquefaction Phenomena, 109-114.

Cekerevac C. and Laloui L. (2010), Experimental analysis of the cyclic behaviour of kaolin at high temperature, Géotechnique, Vol. 60 (8), 651–655.

Chen A.T.F and Stokoe K.H. (1979), “Interpretation of strain dependent modulus and damping from torsional soil tests”, U.S. Geological Survey.

Chen W.F. and Baladi G.Y. (1985), “Soil plasticity: theory and implementation”, Elsevier, Amsterdam, New York.

Chiaro G., Sato T., Kiyota T. and Koseki, J. (2011), “Effect of initial static shear stress on the undrained cyclic behavior of saturated sand by torsional shear loading”, 5th International Conference on Earthquake Geotechnical Engineering, Santiago, Chile.

Chong P.T. (2002), “Characterization of Singapore lower marine clay”, PhD Thesis, National University of Singapore.

Chu J., Bo M. W., Chang M. F. and Choa V. (2002), “Consolidation and permeability properties of Singapore marine clay”, Journal of Geotechnical and Geoenvironmental Engineering, Vol. 128 (9), 724-732.

Chua T.S. (1990), “Some considerations in undrained triaxial testing of very soft clay”, MEng Thesis, National University of Singapore.

Crawford C.B. (1959), “The influence of rate of strain on effective stresses in a sensitive clay”, ASTM STP 254, 36-61.

Crouch R.S. and Wolf J.P. (1994), “Unified 3D critical state bounding-surface plasticity model for soils incorporating continuous plastic loading under cyclic paths. Part I: constitutive relations”, International Journal for Numerical and Analytical Methods in Geomechanics, Vol. 18, 735-758.

Dafalias Y.F. and Herrmann L.R. (1982), “Bounding surface formulation of soil plasticity. In: Soil mechanics – Transient and cyclic loads”, eds. Pande G.N. and Zienkiewicz O.C., John Wiley & Sons Ltd, 253-282.

Dafalias Y.F. and Popov E.P. (1977), “Cyclic loading for materials with a vanishing elastic region”, Nuclear Engineering and Design, Vol. 41, 293-302.

Dames and Moore (1983), “Singapore Mass Rapid Transit system: detailed geotechnical study - interpretative report”, Provisional Mass Rapid Transit Authority, Singapore.

Dasari G.R. (1996), “Modelling the variation of soil stiffness during sequential construction”, PhD Thesis, Cambridge University.

Díaz- Rodriguez J.A. and Lopez-Molina J.A. (2008), “Strain thresholds in soil dynamics”, Proc. 14th World Conference on Earthquake Engineering, Beijing, China.

Diaz-Rodriguez J.A., Moreno P. and Salinas G. (2000), “Undrained shear behavior of mexico city sediments during and after cyclic loading”, Proc. 12th World Conference on Earthquake Engineering, 1652-1660.

Diaz-Rodriguez J.A. and Santamarina C. (2001), “Mexico City soil behavior at different strains: observation and physical interpretation”, Journal of Geotechnical and Geoenvironmental Engineering, Vol. 127 (9), 783-789.

Dobry R. and Vucetic M. (1987), “State-of-the-art report: dynamic properties and response of soft clay deposits”, Proc. International Symposium on Geotechnical Engineering of Soft Soils, Vol. 2, 51-87.

Drucker D.C. and Prager W. (1952), “Soil mechanics and plastic analysis for limit design”, Quarterly of Applied Mathematics, Vol. 10 (2), 157-165.

Duncan J.M. and Chang C.Y. (1970), “Nonlinear analysis of stress and strain in soils”, Journal of the Soil Mechanics and Foundations Division, ASCE, Vol. 96 (5), 1629-1653.

Ejezie S.U. and Harrop-Williams K. (1987), “Reliability of cyclic load deformation models for cohesive soil”, Soil Dynamics and Earthquake Engineering, Vol. 6 (2), 108-115.

Elgamal A., Yang Z., and Parra E. (2002), “Computational modelling of cyclic mobility and post-liquefaction site response”, Soil Dynamics and Earthquake Engineering, Vol 22 (4), 259-271.

Erken A. and Ulker B.M.C. (2007), “Effect of cyclic loading on monotonic shear strength of fine-grained soils”, Engineering Geology, Vol. 89, 243-257.

Eurocode ISO/TS 17892 (2004), “Geotechnical investigation and testing – laboratory testing of soil”.

Frost J. D. (1989), “Studies on the monotonic and cyclic behavior of sands”, PhD Thesis, Purdue University.

Georgiannou V.N., Rampello S. and Silvestri F. (1991), “Static and dynamic measurement of undrained stiffness of natural overconsolidated clays”, Proc. 10th European Conference on Soil Mechanics, Vol. 1, 91-96.

Germaine J.T., and Ladd C.C. (1988), “Triaxial testing of saturated cohesive soils”, ASTM STP 977, 421-459.

Goto S., Tatsuoka F., Shibuya S., Kim Y.S. and Takeshi S. (1991), “A simple gauge for local small strain measurements in the laboratory”, Soils and Foundations, Vol. 31 (1), 169-180.

Guha, S. (1995), “Dynamic characteristics of Old Bay clay deposits in the East San Francisco Bay Area. PhD Thesis, Purdue University, Indiana.

Hardin B.O. (1978), “The nature of stress-strain behavior for soils”, Proc. Earthquake Engineering and Soil Mechanics Conference, ASCE, Pasadena, California, Vol. 1, 3-90.

Hardin B.O. and Black W.L. (1968), “Vibration modulus of normally consolidated clay”, Journal of the Soil Mechanics and Foundation Division, Vol. 94 (2), 353-369.

Hardin B.O. and Drnevich W.L. (1972a), “Shear modulus and damping in soils; measurement and parameter effects”, Journal of the Soil Mechanics and Foundation Division, Vol. 98 (6), 603-624.

Hardin B.O. and Drnevich W.L. (1972b), “Shear modulus and damping in soils; design equations and curves”, Journal of the Soil Mechanics and Foundation Division, Vol. 98 (7), 667-692.

Hirschfeld R.C. (1958), “Factors influencing the constant volume strength of clays”, PhD Thesis, Harvard University.

Houston W.N. and Herrmann, H.G. (1980), “Undrained cyclic strength of marine soils”, Journal of the Geotechnical Engineering Division, Vol. 106 (6), 691-712.

Hwang S.K. (1997), “Dynamic properties of natural soils”, PhD Thesis, University of Texas, Austin.

Hyde A.F.L. and Ward S.J. (1985), “A pore pressure and stability model for a silty clay under repeated loading”, Géotechnique, Vol. 35 (2), 113-125.

Hyodo M., Yamamoto Y. and Sugiyama M. (1994), “Undrained cyclic shear behaviour of clay with initial static shear stress”, Soil Dynamics and Earthquake Engineering, 299-313.

Idriss I.M., Dobry R. and Singh R.D. (1978), “Nonlinear behavior of soft clays during cyclic loading”, Journal of Geotechnical Engineering, Vol. 104 (12), 1427-1447.

Ishibashi I. and Zhang X. (1993), “Unified dynamic shear moduli and damping ratios of sand and clay”, Soils and Foundations, Vol. 33 (1), 182-191.

Isenhower W.M. (1979), “Torsional simple shear/resonant column properties of San Francisco bay mud. M.Sc. Thesis, University of Texas, Austin.

Isenhower W.M. and Stokoe K.H. (1981), “Strain rate dependent shear modulus of San Francisco bay mud”, Proc. International Conference on Recent Advances in Geotechnical Earthquake Engineering and Soil Mechanics, Vol. 2, 597-602.

Ishihara K. (1993), “Dynamic properties of soils and gravels from laboratory tests”, Soil Dynamics and Geotechnical Engineering, 1-17.

Ishihara K. (1996), “Soil behavior in earthquake geotechnics”, Clarendon Press, Oxford.

Ishihara K., Tatsuoka F. and Yasuda S. (1975), “Undrained deformation and liquefaction of sand under cyclic stresses”, Soils and Foundations, Vol. 15 (1), 29-44.

Jardine R.J., Symes M.J. and Burland J.B. (1984), “The measurement of soil stiffness in the triaxial apparatus”, Géotechnique, Vol. 34 (3), 323-340.

Jastrzebska M. (2010), “The external and internal measurement impact on shear modulus distribution within cyclic small strains in triaxial studies into cohesive soil”, EPJ Web of Conferences, Vol. 6, 22014..

Kagawa T. (1992), “Moduli and damping factors of soft marine clays”, Journal of Geotechnical Engineering, Vol. 118 (9), 1360-1375.

Kim D.S. (1991), “Deformational characteristics of soils at small to intermediate strains from cyclic tests”, PhD Thesis, University of Texas, Austin.

Kim T.C. and Novak M. (1981), “Dynamic properties of some cohesive soils of Ontario”, Canadian Geotechnical Journal, Vol. 18, 371-389.

Kim D.S., Stokoe K.H. and Hudson W.R. (1991),”Deformational characteristics of soils at small to intermediate strains from cyclic tests”, Report to Texas Department of Transportation, Transportation Planning Division, University of Texas, Austin.

Kim D.S., Stokoe K.H. and Roesset J.M. (1991), “Characterization of material damping of soils using resonant column and torsional shear tests”, Proc. 5th International Conference on SDEE.

Kokusho T. (1980), “Cyclic triaxial test of dynamic soil properties for wide strain range”, Soils and Foundations, Vol. 20 (2), 45-60.

Kokusho T., Yoshida Y. and Esashi Y. (1982), “Dynamic properties of soft clay for wide strain range”, Soils and Foundations, Vol. 22, 1-18.

Koutsoftas D. C. (1978), “Effect of cyclic loads on undrained strength of two marine clays”, ASCE Vol. 104 (5), 609-620.

Krishnan R. (2000), “Tunnelling and underground projects in Singapore”, Proc. International Conference on Tunnels and Underground Structures, Singapore, 89-96.

Lade P. V. and Ibsen L. B. (1997), “A study of the phase transformation and the characteristic lines of sand behaviour”, Proc. International Symposium on Deformation and Progressive Failure in Geomechanics, 353-359.

Lam N.T.K., Balendra T., Wilson J.L. and Venkatesan S. (2009), “Seismic load estimates of distant subduction earthquakes affecting Singapore”, Engineering Structures, Vol. 31 (5), 1230-1240.

Land Transport Authority (LTA). (2009), “Civil design criteria for road and rail transit systems”, Singapore.

Larkin T.J. and Donavan N.C. (1979), "Sensitivity of computed nonlinear effective stress soil response to shear modulus relationships", Proceedings of 2nd U.S. National Conference on Earthquake Engineering, 573-582.

Lee F.H. and Schofield A.N. (1988), "Centrifuge modelling of sand embankments and islands in earthquakes", Géotechnique, Vol. 38 (1), 45-58.

Lee F.H. and Foo S.L. (1991), "Cyclic mobility response of a dense sand stratum", Computers and Geotechnics, Vol. 11 (1), 59-81.

Lee F.H., Lee Y., Chew S.H. and Yong K.Y. (2005), "Strength and modulus of marine clay-cement mixes", Journal of Geotechnical and Geoenvironmental Engineering, Vol. 131 (2), 178-186.

Lefebvre G.S., Leboeuf D. and Demers B. (1989), "Stability threshold for cyclic loading of saturated clay", Canadian Geotechnical Journal, Vol. 26 (1), 122-131.

Li L., Dan H. and Wang L. (2011), "Undrained behaviour of natural marine clay under cyclic loading", Ocean Engineering, Vol. 38, 1792-1805.

Liu H. and Ling H.I. (2006), "Modeling cyclic behavior of geosynthetics using mathematical functions combined with masing rule and bounding surface plasticity. Geosynthetics International, Vol. 13 (6), 234-245.

Lodde P.F. (1980), "Shear moduli and material damping of San Francisco bay mud", M.Sc. Thesis, The University of Texas, Austin.

Low H.E. (2004), "Compressibility and undrained behaviour of natural Singapore marine clay: Effect of soil structure", MEng Thesis, National University of Singapore.

Luong M.P. (1982), "Stress-strain aspects of cohesionless soils under cyclic and transient loading", International Symposium on Soils under Cyclic and Transient Loading, 315-324.

Marcuson W.F. and Wahls H.E. (1972), "Time effects on the dynamic shear modulus of clays", Journal of Soil Mechanics Foundation Division, ASCE, Vol. 98 (12), 1359-1373.

Martin G.R., Tsai C.F., Lam I.P. and Anderson D.G. (1979), "Seismic response of soft offshore soils – a parametric study", Proc. of 2nd U.S. National Conference on Earthquake Engineering, 583-592.

Masing G. (1926), "Eigenspannungen und verfestigung beim messing", Proc. 2nd International Congress of Applied Mechanics, Zurich, Switzerland, 332–335.

Matasovic N. and Vucetic M. (1995), “Generalized cyclic-degradation-pore-pressure generation model for clays”, Journal of geotechnical engineering, Vol. 121 (1), 33-42.

Matesic L. and Vucetic M. (2003), “Strain-rate effect on soil secant shear modulus at small cyclic strains”, Journal of Geotechnical and Geoenvironmental Engineering, Vol. 129 (6), 536-549.

Matsui T., Bahr M.A. and Abe N. (1992), “Estimation of shear characteristics degradation and stress-strain relationship of saturated clays after cyclic loading”, Soils and foundations, Vol. 32 (1), 161-172.

Matsui T., Ohara H. and Ito T. (1980), “Cyclic stress-strain history and shear characteristics of clay”, Journal of Geotechnical Engineering, Vol. 106 (10), 1101-1120.

Meng J. and Rix G.J. (2003), “Reduction of equipment-generated damping in resonant column measurements”, Géotechnique, Vol. 53 (5), 503-512.

Menzies B., Hooker P., Snelling K. and Sutton J. (2002), “GDS software-based dynamic and seismic laboratory soil testing systems”, GDS Instruments Ltd.

Monkul M. M. and Yamamuro J. A. (2011), “Influence of silt size and content on liquefaction behavior of sands”, Canadian Geotechnical Journal, Vol. 48 (6), 931-942.

Moses G.G., Rao S.N. and Rao P.N. (2003), “Undrained strength behaviour of a cemented marine clay under monotonic and cyclic loading”, Ocean Engineering, Vol. 30 (14), 1765-1789.

Mroz Z., Norris V.A. and Zienkiewicz O.C. (1978), “An anisotropic hardening model for soils and its application to cyclic loading”, International Journal for Numerical and Analytical Methods in Geomechanics, Vol. 2, 203-221.

Mroz Z. and Pietruszczak S.T. (1983), “A constitutive model for sand with anisotropic hardening rule”, International Journal for Numerical and Analytical Methods in Geomechanics, Vol. 7 (3), 305-320.

Oka F., Kodaka T. and Kim Y.S. (2004), “A cyclic viscoelastic-viscoplastic constitutive model for clay and liquefaction analysis of multi-layered ground”, International Journal for Numerical and Analytical Methods in Geomechanics, Vol. 28, 131-179.

Okur D.V. and Ansal A. (2007), “Stiffness degradation of natural fine grained soils during cyclic loading”, Soil Dynamics and Earthquake Engineering, Vol. 27 (9), 843-854.

O'Neill H.M. (1962), "Direct-shear test for effective-strength parameters", Proc. ASCE, Vol. 88 (SM4), 109-137.

Pan T.C., Karim K.R., You X.T., Lim C.L. and Leong C.L. (2006), "Far-field motions in Singapore during the December 2004 and March 2005 Great Sumatra Earthquake and the March 2005 Nias-Simeulue Earthquake", Earthquake Spectra, 22, S403-S417.

Pan T.C., Megawati K. and Lim C.L. (2007), "Seismic shaking in Singapore due to past Sumatran earthquakes", Journal of Earthquake and Tsunami, Vol. 1 (1), 49-70.

Parmelee R.A., Penzien J., Scheffey C.F., Seed H.B. and Thiers G.R. (1964), "Seismic effects on structures supported on piles extending through deep sensitive clays", Report to California State Division of Highways, University of California, Berkeley.

Parra-Colmenares E. J. (1996), "Numerical modelling of liquefaction and lateral ground deformation including cyclic mobility and dilation response in soil systems", PhD thesis, Rensselaer Polytechnic Institute, New York.

Pastor M., Zienkiewicz O.C. and Chan A.H.C. (1990), "Generalized plasticity and the modelling of soil behaviour", International Journal for Numerical and Analytical Methods in Geomechanics, Vol. 14 (3), 151-190.

Penzien J.C., Scheffey C.F. and Parmelee R.A. (1964), "Seismic analysis of bridges on long piles", Journal of the Mechanics Division, ASCE, Vol. 90 (EM3), 223-254.

Pestana J. M., and Whittle A. J. (1999), ''Formulation of a unified constitutive model for clays and sands'', International Journal for Numerical and Analytical Methods in Geomechanics, Vol. 23, 1215-1243.

Pillai R.J., Robinson R.G. and Boominathan A. (2011), "Effect of microfabric on undrained static and cyclic behaviour of kaolin clay", Journal of Geotechnical and Geoenvironmental Engineering, Vol. 137 (4), 421-429.

Pitts J. (1992), "Landforms and geomorphic evolution of the islands during the quaternary. Physical adjustments in a changing landscape: the Singapore story", Eds. Gupta A. and Pitts J., Singapore University Press, Singapore, 83–143.

Prevost J.H. (1977), "Mathematical modelling of monotonic and cyclic undrained clay behaviour", International Journal for Numerical and Analytical Methods in Geomechanics, Vol. 1, 195-216.

Prevost J.H. (1978), "Plasticity theory for soil stress-strain behaviour", Journal of Engineering Mechanics, Vol. 104 (5), 1177-1194.

Puzrin A., Frydman S. and Talesnick M. (1995), “Normalising degrading behavior of soft clay under cyclic simple shear loading. Journal of the Geotechnical Engineering Division, Vol. 121 (12), 836-843.

Pyke R. (1979), “Nonlinear soil models for irregular cyclic loadings”, Journal of the Geotechnical Engineering Division, ASCE, Vol. 105 (6), 715–726.

Rao S.N. and Panda A.P. (1999), “Non-linear analysis of undrained cyclic strength of soft marine clay. Ocean Engineering, Vol. 26 (3), 241–253.

Ray P.R. and Richart D.W. (1988), “Modulus and damping due to uniform and variable cyclic loading”, Journal of the Geotechnical Engineering Division, ASCE, Vol. 114 (8), 861-876.

Richart F.E. (1975), “Some effects of dynamic soil properties on soil-structure interaction”, Journal of the Geotechnical Engineering Division, ASCE, Vol. 101 (12), 1193-1240.

Richardson A.M. (1963), “The relationship of the effective stress-strain behaviour of a saturated clay to the rate of strain”, ScD Thesis, Massachusetts Institute of Technology.

Richardson A.M. and Whitman R.V. (1963), “Effect of strain-rate upon undrained shear resistance of a saturated remoulded fat clay”, Géotechnique, Vol. 13 (4), 310-324.

Romo M. P., Jaime, A. and Resendiz, D. (1988), “The Mexico earthquake of September 19, 1985-General soil conditions and clay properties in the Valley of Mexico”, Earthquake spectra, Vol. 4 (4), 731-752.

Roscoe K.H. and Burland J.B. (1968), “On the generalized stress-strain behaviour of “wet” clay. In: Engineering Plasticity”, eds. Heyman J. and Leckie F.A., Cambridge University Press, 535-610.

Saada A.S. and Macky T.A. (1985), “Integrated testing and properties of a Gulf of Mexico clay”, ASTM STP 883, Philadelphia, 363-380.

Sangrey D.A., Henkel D.J. and Esrig M.I. (1969), “The effective response of a saturated clay soil to repeated loading”, Canadian Geotechnical Journal, Vol. 6 (3), 241-252.

Sangrey D.A. and France J.W. (1980), “Peak strength of clay soils after a repeated loading history”, Proc. International Symposium on Soils Under Cyclic and Transient Loading, 421-430.

Schofield A. N. and Wroth P. (1968). Critical state soil mechanics. McGraw-Hill, London, England.

Shibuya S., Mitachi T., Fukuda F. and Degoshi T. (1995), "Strain rate effects on shear modulus and damping of normally consolidated clay", Geotechnical Testing Journal, Vol. 18 (3), 365-375.

Shirlaw J.N., Tan T.S. and Wong K.S. (2006), "Deep excavations in Singapore marine clay", Proc. 5th International Conference of TC28 of the ISSMGE, the Netherlands, 13-28.

Simpson B., O'Riordan N.J. and Croft D.D (1979), "A computer model for the analysis of ground movements in London clay", Géotechnique, Vol. 29 (2), 149-175.

Stokoe K.H., Hwang S.K. Lee J.N. and Andrus R. (1995), "Effects of various parameters on the stiffness and damping of soils at small to medium strains", Proc. of the International Symposium, Japan, 785-816.

Stokoe K.H. and Lodde P.F. (1978), "Dynamic response of San Francisco bay mud", Proc. ASCE Earthquake Engineering and Soil Dynamics Conference, Vol. 2, 940-959.

Streeter V.L., Wylie E.B. and Richart F.E. (1975), "Soil motion computations by characteristics method", Journal of the Geotechnical Engineering Division, ASCE, Vol. 100 (3), 247–263.

Sun J.I., Golesorkhi R. and Seed H.B. (1988), "Dynamic moduli and damping ratios for cohesive soils", Report No. UCB/EERC-88/15, University of California, Berkley.

Takahashi M., Hight D.W. and Vaughn P.R. (1980), "Effective stress changes observed during undrained cyclic triaxial tests on clay", Proc. International Symposium on Soils under Cyclic and Transient Loading, Vol. 1, 201-209.

Tanaka H., Locat J., Shibuya S., Soon T. T. and Shiwakoti D. R. (2001), "Characterization of Singapore, Bangkok, and Ariake clays", Canadian Geotechnical Journal, Vol. 38(2), 378-400.

Tan S.L. (1983), "Geotechnical properties and laboratory testing of soft soils in Singapore", Proc. 1st International Seminar on Construction Problems in Soft Soils, Nanyang Technological Institute, Singapore, 1–47.

Tan T.S., Chong P.T., Lee F.H., Yong K.Y., Tanaka H., Somkiat L., Yang K.S., Lim J.M. and Chiam S.L. (1999), "Characterisation of Singapore Lower Marine clay by in-situ and laboratory tests", Proc. Dr. Tan Swan Beng Memorial Symposium, Singapore, 181-187.

Tan T.S., Phoon K.K., Lee F.H., Tanaka H., Locat J. and Chong P.T. (2002), "A characterization study of Singapore Lower Marine clay. Proc. International Workshop on Characterisation and Engineering Properties of Natural Soils, Singapore, Vol 1, 429-454.

Tatsuoka F., Muramatsu M., and Sasaki T. (1982), "Cyclic undrained stress-strain behaviour of dense sands by torsional simple shear test", Soils and Foundations, Vol. 22 (2), 55-70.

Tatsuoka F. and Shibuya S. (1992), "Deformation characteristics of soils and rocks from field and laboratory tests", Proc. 9th Asian Regional Conf. on SMFE, Vol. 2, 101-170.

Tatsuoka F., Teachavorasinskun S., Dong J., Kohata Y., and Sato T. (1994), "Importance of measuring local strains in cyclic triaxial tests on granular materials", ASTM STP 1213, 288-304.

Taylor P.W. and Bacchus D.R. (1969), "Dynamic cyclic strain tests on a clay", Proc. 7th International Conference on Soil Mechanics and Foundation Engineering, Vol. 1, 401-409.

Teachavorasinskun S., Thongchim P. and Lukkunaprasit P. (2002), "Stress rate effect on the stiffness of a soft clay from cyclic, compression and extension triaxial tests", Géotechnique, Vol. 52 (1), 51-54.

Thammathiwat A. and Weeraya C. (2004), "Behavior of strength and pore pressure of soft Bangkok clay under cyclic loading", Thammasat International Journal of Science and Technology, Vol. 9 (4), 21-28.

Thiers G.R. and Seed H.B. (1968), "Cyclic stress–strain characteristics of clay. Journal of the Soil Mechanics and Foundations Division, ASCE, No. 94 (2), 555–569.

Thiers G.R. and Seed H.B. (1969), "Strength and stress-strain characteristics of clays subjected to seismic loading conditions", ASTM STP 450, 3-56.

Towhata I. (2008), "Geotechnical earthquake engineering", eds. Wu W. and Borja R.I., Springer.

Valanis K.C. and Read H.E. (1982), "A new endochronic plasticity model for soils. In: Soil mechanics – Transient and cyclic Loads", eds. Pande G.N. and Zienkiewicz O.C., John Wiley & Sons Ltd, 375-417.

Viggiani G. and Atkinson J.H. (1995), "Stiffness of fine-grained soil at very small strains. Géotechnique, Vol. 45 (2), 249-265.

Vucetic M. and Dobry R. (1988), "Degradation of marine clays under cyclic loading", Journal of Geotechnical Engineering, Vol. 114 (2), 133-149.

Vucetic M. and Dobry R. (1991), “Effect of soil plasticity on cyclic response”, Journal of Geotechnical Engineering, Vol. 117 (1), 89-107.

Wan R.G. and Guo P.J. (2001). “Drained cyclic behaviour of sand with fabric dependence”, Journal of Engineering Mechanics, Vol. 127(11), 1106-1116.

Wang Y.H., Cascante G. and Santamarina J.C. (2003), “Resonant column testing: the inherent counter EMF effect”, Geotechnical Testing Journal, Vol. 26 (3), 342-352.

Whitman R.V. (1960), “Some considerations and data regarding the shear strength of clays”, Proc. ASCE Research Conference on Shear Strength of Cohesive Soils, 581-614.

Whittle A.J. (1993), “Evaluation of a constitutive model for overconsolidated clays”, Géotechnique, Vol. 43 (2), 289-313.

Whittle A.J. and Kavvadas M.J. (1994), “Formulation of the MIT-E3 constitutive model for overconsolidated clays”, Journal of Geotechnical Engineering, Vol. 120 (1), 173-198.

Whittle A.J., Degroot D.J., Seah T.H. and Ladd C.C. (1994), “Model prediction of the anisotropic behaviour of Boston blue clay”, Journal of Geotechnical Engineering, Vol. 120 (1), 199-224.

Wijewickreme D. (2010), “Cyclic shear response of low plastic Fraser River Silt”, Proc. 9th U.S. National and 10th Canadian Conference on Earthquake Engineering, Canada.

Wilson N.E., and Greenwood J.R. (1974), “Pore pressures and strains after repeated loading of saturated clay”, Canadian Geotechnical Journal, Vol. 11, 269-277.

Wood D.M. (1982), “Laboratory investigations of the behaviour of soils under cyclic loading: a review. In: Soil mechanics – Transient and cyclic Loads”, eds. Pande G.N. and Zienkiewicz O.C., John Wiley & Sons Ltd, 513-582.

Wood D. M. (1990), “Soil behaviour and critical state soil mechanics”,150-153, Cambridge University Press.

Yamada S., Hyodo M., Orense R., Dinesh S. and Hyodo T. (2008), “Strain-dependent dynamic properties of remoulded sand-clay mixtures”, Journal of Geotechnical and Geoenvironmental Engineering, Vol. 134 (7), 972-981.

Yang J., and Sze H. Y. (2011), “Cyclic behaviour and resistance of saturated sand under non-symmetrical loading conditions”, Géotechnique, Vol. 61 (1), 59-73.

Yasuhara K. (1994), “Post-cyclic undrained strength for cohesive soils”, Journal of Geotechnical Engineering, Vol. 120 (11), 1961-1979.

Yasuhara K., Hirao K. and Hyde A.F.L. (1992), “Effects of cyclic loading on undrained strength and compressibility of clay”, Soils and Foundations, Vol. 32 (1), 100-116.

Yasuhara K., Yamanouchi T. and Hirao K. (1983), “Cyclic stress-strain and strength performance of soft clay”, Proc. Symposium on recent developments in laboratory and field tests and analysis of geotechnical problems, 206-229.

Yin Z. Y., Chang C. S. and Hicher P. Y. (2010), “Micromechanical modelling for effect of inherent anisotropy on cyclic behaviour of sand”, International Journal of Solids and Structures, Vol. 47 (14), 1933-1951.

Yong R.N. and Townsend F.C. (1986), “Consolidation testing and evaluation: problems and issues. In: Consolidation of soils: testing and evaluation”, eds. Yong R.N. and Townsend F.C., ASTM STP 892, 713-718.

Yoon S.B. (2007), “Modeling soil behaviour in large strain resonant column and torsional shear tests”, PhD Thesis, Utah State University.

Yu H.S., Khong C. and Wang J. (2007), “A unified plasticity model for cyclic behaviour of clay and sand”, Mechanics Research Communications, Vol. 34, 97-114.

Zavoral D.Z. and Campanella R.G. (1994), “Frequency effects on damping/modulus of cohesive soil”, ASTM STP 1213, 191-201.

Zen K., Umehara Y. and Hamada K. (1978), “Laboratory tests and in-situ seismic survey on vibratory shear modulus of clayey soils with various plasticities”, Proc. of 5th Japan Earthquake Engineering Symposium, Tokyo, Japan, 721-728.

Zergoun M. and Vaid Y.P. (1994), “Effective stress response of clay to undrained cyclic loading”, Canadian Geotechnical Journal, Vol. 31 (5), 714-727.

Zhou J. and Gong X. (2001), “Strain degradation of saturated clay under cyclic loading”, Canadian Geotechnical Journal, Vol. 38 (1), 208-212.

Zienkiewicz O.C., Leung K.H. and Pastor M. (1985), “Simple model for transient soil loading in earthquake analysis. I. Basic model and its application”, International Journal for Numerical and Analytical Methods in Geomechanics, Vol. 9, 453-476.

Appendix A – Calibration of Resonant Column

A.1 Equipment Data

Based on ASTM D4015-07:

Polar Moment of Inertia of Calibration Rod,

$$I_p = \left(\pi d^4\right)/32 \qquad \text{[A.1]}$$

Where:

d = Diameter of rod (m).

Torsional Stiffness of Calibration Rod,

$$\left(K_{rod}\right)_T = \left(I_p G\right)/L \qquad \text{[A.2]}$$

Where:

G = Shear modulus of rod (kPa),

L = Length of rod (m).

Rotational Inertia of Active End Platen System,

$$J_A = \frac{\left(K_{rod}\right)_T}{\left(2\pi\right)^2\left[\left(f_{rod}\right)_T^2 - f_{OT}^2\right]} \qquad \text{[A.3]}$$

Where:

$\left(f_{rod}\right)_T^2$ = Apparatus torsional resonant frequency.

Since there is no torsional spring used for active end platen, $f_{OT}^2 = 0$. Hence, we have

$$J_A = \frac{\left(K_{rod}\right)_T}{\left(2\pi\left(f_{rod}\right)_T\right)^2} \qquad \text{[A.4]}$$

A standard aluminium calibrating rod used at Soil Dynamics Instuments, Inc is first used on NUS Resonant Column System for calibration.

Based on this standard rod:

Given: $d = 0.375in$; $L = 2.95in$; $\left(f_{rod}\right)_T = 48.12Hz$

Using Equations A.1, A.2 and A.4, we have:

$$I_p = \left(\pi \times \left(0.375in \times 0.0254m/in\right)^4\right)/32 = 8.081\times10^{-10}\,m^4$$

$$\left(K_{rod}\right)_T = \left(8.081\times10^{-10}\,m^4\right)\times\left(2.37\times10^{10}\,Pa\right)/\left(2.95in\times0.0254m/in\right) = 255.6Nm/radian$$

$$J_A = \frac{255.6 Nm/radian}{(2\pi \times 48.12 Hz)^2} = 2.796 \times 10^{-3} kgm^2$$

Using this value of J_A tabulated from the standard rod, the torsional stiffness $(K_{rod})_T$ of the NUS calibration road is back-calculated since J_A is a constant independent of the calibration rod used.

Based on the NUS calibration rod:

The calibration performed in the NUS geotechnical laboratory gives the following:

$(f_{rod})_T = 52.44 Hz$

By applying $J_A = 2.796 \times 10^{-3} kgm^2$ to Equation A.4, $(K_{rod})_T = 303.54 Nm/radian$.

This value of J_A is inclusive of the $3.57cm$ diameter aluminium top platen which is used together with the calibration rod. However, during the resonant column tests on soil specimens, the aluminium top platen is replaced with a $3.57cm$ diameter stainless steel top platen and a $3.57cm$ diameter porous bronze stone. Hence, the J_A will have to be re-calculated based on the ASTM D4015-07.

Given: $J_{(3.57cm\ aluminium\ top\ platen)} = 2.33 \times 10^{-5} kgm^2$;

$J_{(3.57cm\ stainless\ steel\ top\ platen)} = 4.49 \times 10^{-5} kgm^2$;

$J_{(3.57cm\ porous\ bronze\ stone)} = 0.52 \times 10^{-5} kgm^2$

$J_A = 2.796 \times 10^{-3} kgm^2 - J_{(3.57cm\ aluminium\ top\ platen)} + J_{(3.57cm\ stainless\ steel\ top\ platen)} + J_{(3.57cm\ porous\ bronze\ stone)}$

$= 2.823 \times 10^{-3} kgm^2$

The accelerometer was then calibrated using a portable shaker at frequency of 100Hz and peak acceleration of 1g. The output of the charge amplifier was measured with a voltmeter and found to be 1.218 V_{rms}/g. The displacement calibration factor for the accelerometer is then given by:

$$LCF_A = \frac{9.80 m/\sec^2/g}{(1.218 V_{rms}/g)(2\pi f)^2} = 0.203/f^2 \qquad [A.5]$$

Since the accelerometer is mounted at a distance of 0.0316m from the axis of rotation, using Equation A.5, the equivalent rotational calibration factor can be calculated as follows:

$$RCF_A = \frac{0.2038/f^2 (m/V_{rms})}{0.0316m} = 6.45/f^2 (radian/V_{rms}) \qquad [A.6]$$

Using the calibration procedures stipulated in ASTM D4015-07, the torque calibration factor *TCF* was obtained as follows:

(i) The current supplied to the torsional coils was adjusted so that the accelerometer output was at least 10 times of its output due to ambient vibrations and electrical noise when no power is applied to the torsional coils. The rotational calibration factor when the input frequency was set at 0.707 times the resonant frequency $(f_{rod})_T$ is given by:

$$RCF_1 = 6.45/(0.707 \times 52.44)^2 = 4.692 \times 10^{-3}\, radian/V_{rms}$$

Given that the accelerometer output $TO1 = 0.099 V_{rms}$ and the input current to the torsional coils $CR1 = 0.995 V_{rms}$,

$$C_1 = 0.5(RCF_1)(TO1)/CR1 = 2.334 \times 10^{-4}\, radian/V_{rms}$$

(ii) By keeping the supplied current constant, the input frequency was then set at 1.414 times the resonant frequency $(f_{rod})_T$. Consequently, we have

$$RCF_2 = 6.45/(0.414 \times 52.44)^2 = 1.173 \times 10^{-3}\, radian/V_{rms}$$

Given that the accelerometer output $TO2 = 0.183 V_{rms}$ and the input current to the torsional coils $CR2 = 0.991 V_{rms}$,

$$C_2 = 0.5(RCF_2)(TO2)/CR2 = 2.166 \times 10^{-4}\, radian/V_{rms}$$

Check: C_1 and C_2 should agree within 10%. **OK!**

(iii) Since $(K_{rod})_T = 303.54 Nm/radian$,

$$TCF = 0.5(C_1 + C_2)(K_{rod})_T = 6.830 \times 10^{-2}\, Nm/V_{rms}$$

A.2 Torsional Motion Data

Based on ASTM D4015-07:

Soil Mass Density,

$$\rho = M/V \qquad [A.7]$$

Where:

M = Total specimen mass (kg),

V = Volume of specimen (m^3).

Specimen Rotational Inertia,

$$J = Md^2/8 \qquad [A.8]$$

Where:

d = Diameter of specimen (m).

Active-end Inertia Factor (Torsional Motion),

$$T_T = \frac{J_A}{J}\left[1-\left(\frac{f_{OT}}{f_T}\right)^2\right] \qquad \text{[A.9]}$$

Where:

f_T = System resonant frequency (*Hz*).

Since no torsional spring is used for the active-end platen, $f_{OT} = 0$. Thus, Equation A.9 becomes

$$T_T = \frac{J_A}{J} \qquad \text{[A.10]}$$

By using the free-vibration decay curve, the logarithmic decrement is given by

$$\delta_T = (1/n)\ln\left(A_1 / A_{n+1}\right) \qquad \text{[A.11]}$$

Where:

A_1 = Amplitude of vibration for the first cycle after power is cut off,

A_{n+1} = Amplitude of vibration for the (n+1)th cycle after power is cut off.

Apparatus Damping Coefficient,

$$ADC_{OT} = 2\left(f_{rod}\right)_T J_A \delta_T \qquad \text{[A.12]}$$

Based on the NUS calibration rod:

$$\delta_T = (1/5.40132)\ln(8.2/4.4) = 0.115$$

$$ADC_{OT} = 2(52.44Hz)\left(2.824\times10^{-3}kgm^2\right)(0.115) = 0.0341kgm^2/s$$